

ISSN: 1737-9334
-PET-Vol. 44



Proceedings of Engineering & Technology
-PET-

Special Issue on Renewable energy & Applications
Anglophone issue

Editors:

Dr. Ahmed Rhif (Tunisia)

Dr. Georges Descombes (France)

International Centre for Innovation & Development

-ICID-



ISSN: 1737-9334

-PET- Vol.44

Proceedings of Engineering & Technology -PET-

Special Issue on Renewable energy & Applications

Anglophone issue

Editors:

Dr. Ahmed Rhif (Tunisia)

Dr. Georges Descombes (France)

International Centre for Innovation & Development

-ICID-

Editeurs en chef

Dr. Ahmed Rhif (**Tunisia**)

Dr. Georges Descombes (**France**)

Comité de rédaction

Abdelfettah Barhdadi (**Maroc**)

Djamila Rekioua (**Algérie**)

Nachida K. Merzouk (**Algérie**)

Youcef Soufi (**Algérie**)

Sara Zatir (**Algérie**)

Brahim Berbaoui (**Algérie**)

Sylvie Faucheux (**France**)

Tahar Bahi (**Algérie**)

Aillerie Michel (**France**)

Arouna Darga (**France**)

Abdellah Mechaqrane (**Maroc**)

Brahim Berbaoui (**Algérie**)

Djamila Rekioua Ziani (**Algérie**)

Driss Youssfi (**Maroc**)

Hana Boudjedir (**Algérie**)

Hamadi Foudil (**Algérie**)

Houria Siguerdidjane (**France**)

Mohamed E.Djeghlal (**Algérie**)

Philippe Guibert (**France**)

Pierre-Olivier Logerais (**France**)

Rafika Boudries (**Algérie**)

Said Zouhdi (**France**)

Fathi Mohammed (**Algérie**)

Hassane Mahmoudi (**Maroc**)

Olivier Riou (**France**)

Samira ChaderKerdjou (**Algérie**)

Youssef Errami (**Maroc**)

Missoum abdelkrim (**Algérie**)

Abdelaziz Hamzaoui (**France**)

Abdelhamid I.Hassane (**Tchad**)

Adnan Yassine (**France**)

Bassouabde Islam (**Algérie**)

Beladram Mohamed (**Algérie**)

Belboukhari Naceur (**Algérie**)

Belhachemi Meriem (**Algérie**)

Bousserhane Smail (**Algérie**)

Cheikh Nawel (**Algérie**)

Cheriti Abdelkrim (**Algérie**)

Cheriti Abdelkrim (**Algérie**)

Dahou Zohra (**Algérie**)

Dennai Brahim (**Algérie**)

Dhini Rachid (**Algérie**)

Ernest Matagne (**Belgique**)

Fabien Delaleux (**France**)

Fawaz Massouh (**France**)

Fezioui Naima (**Algérie**)

Hamouinabde Imajid (**Algérie**)

Kadri Boufelja (**Algérie**)

Khalfaoui rachid (**Algérie**)

Khenfer Nabil (**Algérie**)

Khouloud Beddoud (**Algérie**)

Manar Slimane (**Maroc**)

Mohamed Benbouzid (**France**)

Mohamed Ben Braika (**Algérie**)

Mustapha Hatti (**Algérie**)

Olena lurevych (**France**)

Rahmani lakhdar (**Algérie**)

Sallam Mebrouk (**Algérie**)

Touati Boumedienne (**Algérie**)

Toufik Madani Layadi (**Algérie**)

Toufik Rekioua (**Algérie**)

Tounzi Abdelmounaïm (**France**)

Zohra Ameur (**Algérie**)

Summary

- Power flow and Short circuit with different load and contingency scenarios of an electrolysis plant. Page 5
Amine Zeggai, Farid Benhamida.
- Structural study and electrical properties of Bi_{1.5-x} Cax Sb_{1.5}CuO₇ Pyrochlore-type solid solution series. Page 12
Rafik E.A. Dra, Ahmed Bekka, Robert E. Dinnebier, Bounekref Boukerma.
- Contribution to the valorization of clay composite materials in Algeria: Application Building materials. Page 19
BOUSSAK HASSINA.
- Programming interface in Matlab to estimate solar radiation in Algeria: Application to M'sila Page 22
Younes Kherbiche , Nabila Ihaddadene, Razika Ihaddadene, Marouane Mostefaoui.
- A new approach of Sliding mode observer for sensorless control applied in Induction machine. Page 28
Mohammed Zakaria Kari, Abdelkader Mechernene, Sidi Mohammed Meliani.
- Multivariable Predictive Control in the Form of State Space for a Chemical Multivariable System. Page 34
Ibrahim El Khalil MEKKI.
- Realization of Dip-Coating technology to prepared the Fe-doped ZnO and Al-doped ZnO thin films for Solar Cells. Page 40
C.ZEGADI, A.ABDELKADER and S. HAMZAOUI, M. ADNANE, N.HAMDADOU.
- Comparative studies between Lithium-Ion ,Nickel Cadmium and Nickel Metal hydride Batteries for wireless sensor Networks. Page 46
Boubakeur Hamlili, Khelifa Benahmed, Brahim Gasbaoui.
- Reconciliation of the objective and the subjective bioclimatic architectural parts; the contribution of schematization and CBR. Page 54
BENABDELFATTAH Mohamed , HAMRANI Saida.
- Predictive MRAS Sensorless Vector Control of Induction Motor Drives. Page 60
Moustafa zair, Abdeldejjbar Hazzab.
- Extraction of Zn (II) in acetate medium by 8- Hydroxyquinoline. Page 66
Fatiha.Zaoui, Mohamed Amine .Didi , Didier Villemin.
- Fuzzy Direct Power Control of Voltage Source Rectifier (VSR). Page 72
CHAKAR Abdeselem, ABDELKHALEK Othmane, TEDJINI Hamza, GASBAOUI Brahim, HAFSI Ossama, SOUMEUR Mohammed amine.

Analysis and Evolution of Solid and Leachates Residues at the Level of the Gas Complex. <i>HADDAR Mabrouk, ALLAOUA Boumediene.</i>	Page 78
The controlling of the DFIG Based Wind Energy Conversion System modeling and simulation <i>HADDAR Mabrouk, ALLAOUA Boumediene.</i>	Page 91
Power loss reduction in power system using optimal location of STATCOM. <i>F.Z.Messaoud, H.Tédjini, M. Boudiaf.</i>	Page 97
Valorization Of Sand Dune Of Taghit (South-Western Algeria) In The Construction: Technical And Eco-Environmental Aspect. <i>Makani, F.Z. Rennani, A. Tafraoui, F. Benmerioul, S. Zaoiai.</i>	Page 102
The fp-lapw calculations of structural, electronic and thermodynamic properties of alkaline earth oxides cao, sro and their alloys. <i>M. Slimani, N. Chouit, H. Meradji and S. Ghemid.</i>	Page 105
Determination of The Tg, Td and the Refractive Index (n) of the Poly (PEA) Network as A Function of the Degree of Crosslinking. <i>N. Benmessaoud, T. Bouchaour, U. Maschke.</i>	Page 110
A Green Catalyst “Maghnite Na ⁺ ” For Synthesis and Anionic Polymerization of Methacrylamide. <i>Samira Derkaoui, Mohammed Belbachir and Fatima Zohra Zeggai.</i>	Page 116
Wind turbine generator based on PMSG connected to DC microgrid system. <i>Hafsi Oussama, Abdelkhalek Othmane, Chakar Abdeselem, Hartani Mohammed Amine.</i>	Page 120
Development of the renewable electricity generation in Algeria: Impact of oil Price using a Vector Error Correction Model (VECM). <i>Widad Berriche , Meriam Bougueroua.</i>	Page 124
Study of the Evolution of Mechanical Properties of Laminated Composites. <i>Mansouri Lilla, Djebbar Arezki, Samir Khatir and Magd Abdel Wahab.</i>	Page 132
Application of sand dunes in the machining of molds of composite materials. <i>CHAOUFI, A. TAFRAOUI, M. ZAOUI, S. TAFRAOUI, M. DAHMANI.</i>	Page 139
Modelling and simulation of a gypsum decomposition process by carbon monoxide. <i>Hasna Soli, Bassem Jamoussi.</i>	Page 143
Efficient Receiver of Parabolic Trough Collector for Indirect Steam Production. Applications. <i>Karima Ghazouani, Safa Skouri, Salwa Bouadila, AmenAllah Guizani.</i>	Page 148
A Flexible Active and Reactive Power Control Strategy of a LV Grid Connected PV System. <i>Hamrouni Nejib, Younsi Sami.</i>	Page 153
Analysis of the pv efficiency according to the characteristics of silicon solar cells. <i>Souad Merabet, Bilal Djelil, Boubekour Birouk.</i>	Page 164

Power flow and Short circuit with different load and contingency scenarios of an electrolysis plant

Amine Zeggai

Irecom laboratory, dept. of electrotechnics
UDL university of Djilali Liabes , Sidi Bel Abbes, Algeria
zeggai-amine13@hotmail.com

Farid Benhamida

Irecom laboratory, dept. of electrotechnics
UDL university of Djilali Liabes , Sidi Bel Abbes, Algeria
farid.benhamida@yahoo.fr

Abstract—This This paper presents a power flow and voltage profile analysis of an electrolysis plant power system with a power supply of 30 MW and a distribution level of 63 kV / 20 kV/ 5.5 kV / 0.4 kV and a 5 MVA steam turbine at the 5.5 kV level. The purpose of the simulation is to predict the behavior of a real system of an HV customer through the power flow and the short circuit with different load and contingency scenarios in order to know and to control its operation, the simulation is carried out using Electrical Transient Analyzer Program (ETAP). The effectiveness of results are proven by comparison to hand calculation and real measures taken in electrolysis plant.

Keywords— *Load Flow Analysis, electrical Transient Analyzer Program (ETAP), Real Industrial Enterprise, Short circuit Analysis, Different load scenarios.*

I. INTRODUCTION

Large industrial process plants like oil and gas, fertilizers and petro-chemical etc. needs electrical as well as steam energy. These plants demand high reliability as well as economic costs for power and steam generation. In many areas where reliable power is costly or difficult to access, these industries have developed their own captive power plants to meet their needs. This increases the complexity of industrial power systems due to distributed generation and grid interconnection. The power system deployed must be capable of meeting the load requirement under defined contingencies. To monitor, to maintain stability under various operating conditions and to manage these complex industrial power systems, different additional sophisticated simulation software's are used. To facilitate the supply of reliable power, operation team needs to create different scenarios for power flow, short circuit and stability studies in advance to check the constrains in the system, if any. Proactive actions can be taken based on these simulation study results to minimize disruption to process plant operations. A continual and comprehensive analysis of a power system is required to evaluate current status of the system and to evaluate the optional plans for system expansion[1].

Electrical power system in large-scale industry has inherent discrimination in itself as far as the system is concerned. In

addition, sizes of power source and load are large; considering its complexity of power generation is the same as other power generation of electrical power system. Large numbers of medium and low-voltage motors are considered. Due to electrical power system of the whole plant involving with the requirements of power source, distribution network, a great deal of motor loads, manufacturing and technical management, it is higher than power supply companies in medium-sized industry under controlled conditions [2] [3].

The power system model of an industrial complex is presented here uses NR method based power flow analysis (1) simulation using ETAP software version 16.0.0. The acceptable voltage limits are as per the standard IS-12360-2006. The power flow simulations are carried out for identifying best operating conditions provided under the guidelines of process requirements, and (2) simulation of short circuit analysis to check the rating of electrical devices under fault condition and to establish the fault levels of the system at various voltage levels for various operating conditions of the plant the effect of 3-phase, line-to-ground, line-to-line, and line-to-line-to-ground faults on electrical distribution systems. The program calculates the total short circuit currents as well as the contributions of individual motors, generators, and utility ties in the system. Fault duties are in compliance with the latest editions of the ANSI/IEEE Standards (C37 series) and IEC Standards (IEC 60909 and others).

The ETAP software performs numerical calculations of large integrated power system with fabulous speed besides generating output parameters.

II. NETWORK DETAILS

The power supply of an electrolysis plant is from the Algerian electricity company (Sonelgaz) 220/63 kV source station located about 3 km away. From the Sonelgaz substation, two 63 kV lines supply two 63 kV / 20 kV, 39 MVA step-down transformers each

The main Factory Unit is divided to six principal zone:

- **Zone 1 (Central):** supplied by (1) two 20 kV / 5.5 kV, 5 MVA transformers, one transformer operated in emergency, (2) two 5.5 kV / 380 V, 2.5 MVA transformers, one transformer operated in emergency and (3) a 380/380 V, 400 kVA transformer for lighting.
- **Zone 2 (Lixi-purif):** supplied by (1) two 20 kV / 380 V, 2.5 MVA transformers with one transformer operated in emergency and (2) a 380/380 V, 400 kVA transformer for lighting.
- **Zone 3 (Electrolysis):** supplied by (1) two 20 kV / 380 V, 2.5 MVA transformers with one transformer operated in emergency and (2) a 380/380 V, 400

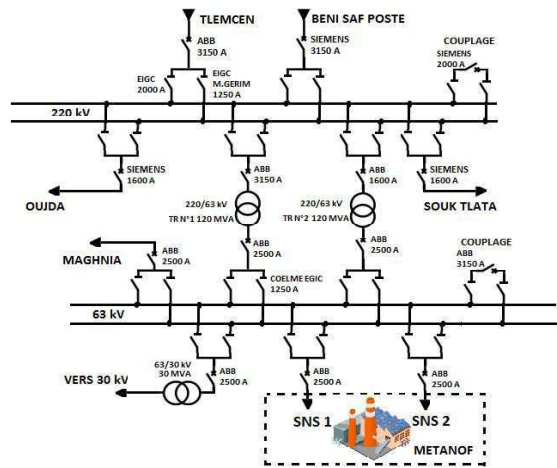


Fig. 1. Single line diagram GHAZAOUET 220/63/30 kV

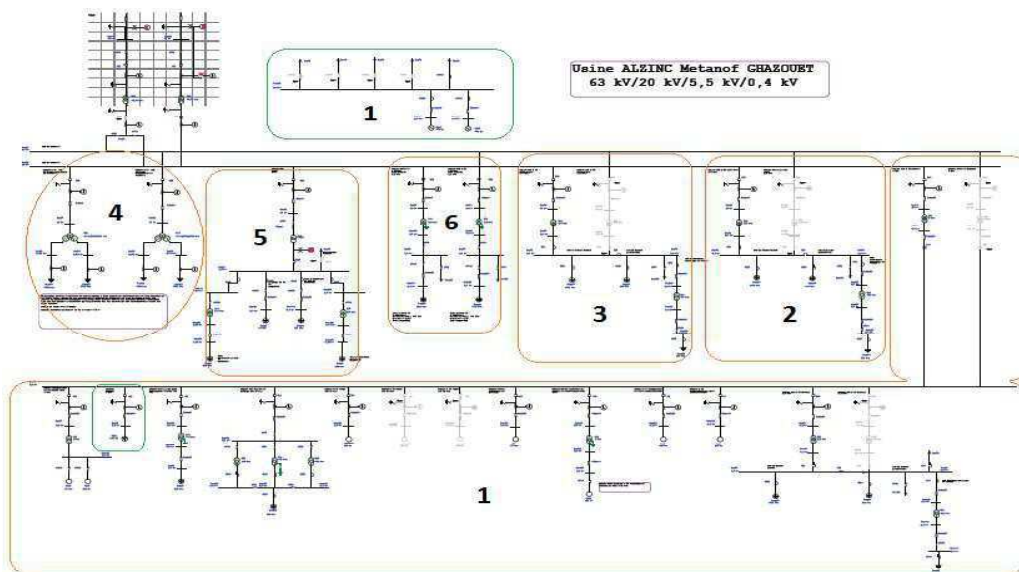


Fig. 2. Distribution network of electrolysis plant

kVA transformer for lighting.

- **Zone 4 (Zinc Electrolysis):** supplied by two rectifiers connected in series with two 20 kV / 380 V, 11.1 MVA transformer.
- **Zone 5 (Refonte):** two furnaces are supplied by two 20 kV / 225, 330, 350, 400, 450, 500, 550, 600 V, 1.2 MVA transformers.
- **Zone 6 (Zamac):** four furnaces supplied by a 20 kV / 380 V, 1 MVA transformer.

The electrolysis plant contain three generators:

- **Zone 1 (Central):**
 - Two identical diesel group 1100 kVA, 380 V, 1590 A, %PF = 70, 50 Hz.
 - Steam turbine 5 MVA, 5,5 kV, 535 A, 50 Hz.

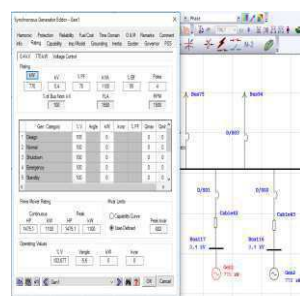


Fig. 3. Two Diesel group 1100 kVA

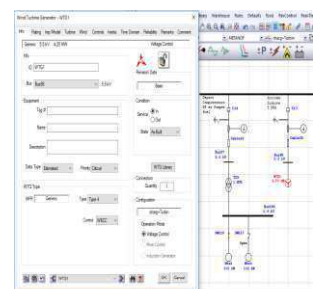


Fig. 4. Steam turbine 5 MVA

III. TEST CASE STUDY

A. Methodology

Electrical system network data is modeled in the software for system analysis. Important inputs to an effective system study are:

Identification of all loads specifically split of motive and non-motive loads.

- Power sources, including voltage and short circuit levels and their operational constrains.
- Bus, Nominal kV, Initial/Operating Voltage (Magnitude and Angle), Diversity Factors (Maximum and Minimum), FDR Tag, and Equipment Name and Description.
- Generators, including MVA, voltage, impedances and grounding methods.
- Transformer sizes, their ratings, tap ratios, voltages, impedances, connections and grounding methods.
- Protective devices and their ratings.
- Length, number of conductors per phase, Sizes and types of overhead lines and underground cables.
- Future planned additions / provisions.
- Grid interconnection provision.

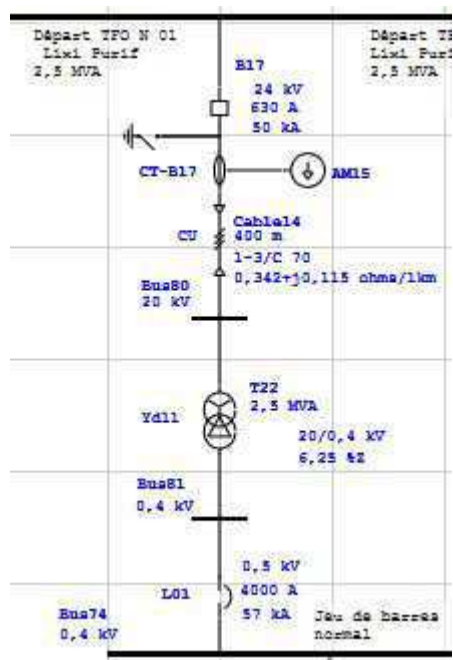


Fig. 5. Departure N° 01 of Zone 2

B. Assumptions & Operating conditions for Power Flow study

Following are the assumptions and network operating conditions for the simulation and analysis carried out.

Load flow calculations are based on Newton Raphson method.

- ❖ **Low Load:** the company is on standby for maintenance or rehabilitation for example, the majority of the loads is stopped except the lighting, the catch, the furnace inductor... ex and all its consumption through the networks sonelgaz line 63 kV
- ❖ **Full Load:** the factory operates normal all the areas in service and all its consumption through networks sonelgaz line 63 kV.
- ❖ **Full Load + Steam Turbine :** the plant normally operates all areas in service and its consumption through the 63 kV line sonelgaz networks with a power of 5 MVA from the steam turbine that inject into 5.5 kV bar set which can supply little power to any Zone 1
- ❖ **Diesel Group (normal switch-off 63 kV):** In this case, the diesel group feed only the 400V priority bus bar of each zone (induction furnaces, lighting, capacitor batteries, etc.)

Note:

- A steam turbine is a machine that recuperates the thermal energy of the pressurized steam in the main furnace boiler elements (the temperature at which the blende is roasted oscillates between 950 ° C and 980 ° C, This gas is cooled in the boiler up to 315 ° C) and uses it to produce a mechanical work of rotating the output shaft and transferring electrical energy through the alternator.
- charge controller (63/20 kV transformer) is a device for adding or removing turns to the main winding of the transformer can thus be adapted to the load conditions on the network to maintain the voltage at an optimal level at 20 kV bus bar
Voltage tolerences

Table I lists the voltage tolerances as per IS 123602006.

C. General Description of Calculation Methodology

In IEC short-circuit calculations; an equivalent voltage source at the fault location replaces all voltage sources. A voltage factor c is applied to adjust the value of the equivalent voltage source for minimum and maximum current calculations. All machines are represented by their internal impedances. Transformer taps can be set at either the nominal position or at an operating position, and different schemes are available to correct transformer impedance and system voltages if off-nominal tap setting exists. System impedances are assumed to be balanced 3-phase, and the method of symmetrical components is used for unbalanced fault calculations. Zero sequence capacitances of transmission lines, cables and shunt admittances can be considered for unbalanced fault calculations (LG and LLG) if the option in the study case is

selected to include branch Y and static load. This means that the capacitances of static loads and branches are considered based on IEC 60909-0 2001. Calculations consider electrical distance from the fault location to synchronous generators. For a far-from generator fault, calculations assume that the steady-state value of the short-circuit current is equal to the initial symmetrical short-circuit current and only the DC component decays to zero. However, for a near-to-generator fault, calculations count for decaying in both AC and DC components.

The equivalent R/X ratios determine the rates of decay of both components, and different values are taken for generators and loads near the fault.

IV. SIMULATION OF LOAD FLOW ANALYSIS IN ETAP

The Load Flow software module can create and validate system models and obtain accurate and reliable results. It can calculate bus voltages, branch power factors, currents, and

TABLE I
 RESULT COMPARISON OF POWER FLOW ACTUAL MEASUREMENT AND CALCULATION WITH DIFFERENT SCENARIOS OF REAL INDUSTRIAL ENTERPRISE LOAD SCALING

	Calculation ETAP					Actual Measurement			
	N° bus	bus 138	bus 94	bus 88	bus 51	bus 138	bus 94	bus 88	bus 51
Voltage		0,4 kV	0,4 kV	5,5 kV	20 kV	0,4 kV	0,4 kV	5,5 kV	20 kV
FULL LOAD	Voltage %	104,3	101,7	101,9	100,1	104,34	102,7	102,1	100
	cos(φ)		0,889				0,89		
FULL LOAD + TURBINE	Voltage %	104,5	99,72	100	100,1	104	100	100,1	100
	cos(φ)		0,892				0,89		
LOW LOAD	Voltage %	104,5	102,4	102,7	100,2	104,78	102,7	102,1	100
	cos(φ)		0,772				0,78		
DIESEL GROUP	Voltage %	105,2	103,4	/	/	105,65	103	/	/
	cos(φ)		/				/		

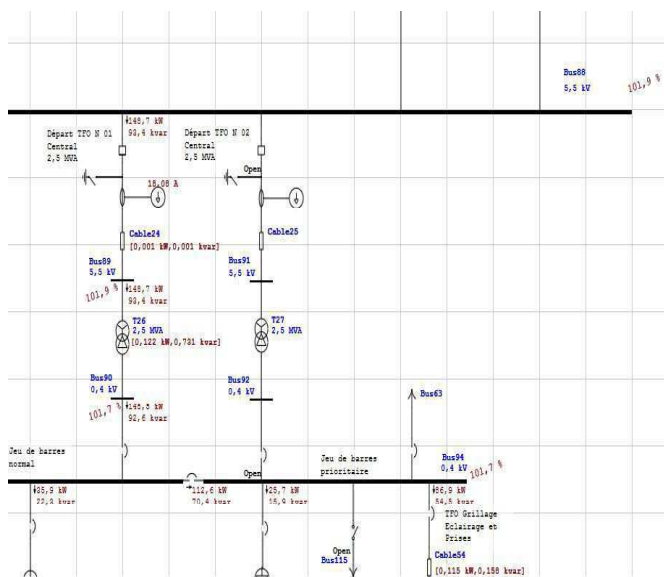


Fig. 6. Load flow analysis of full load scenario "bus 88, 5,5 kV"

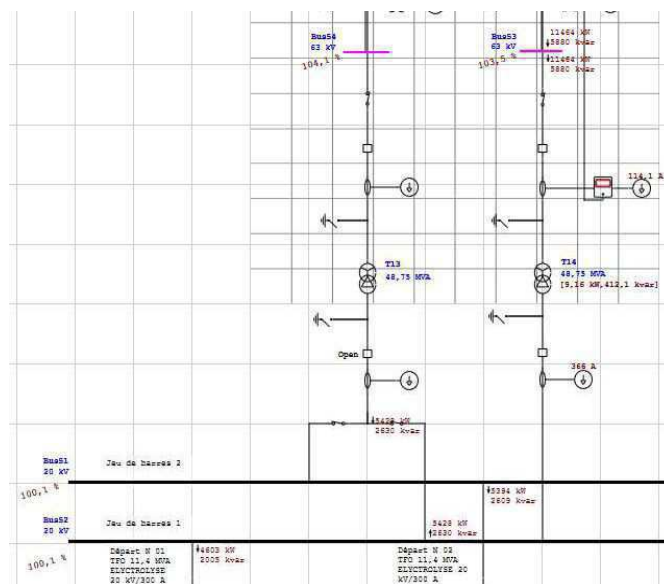


Fig. 7: Load flow analysis of full load scenario "bus 51, 20 kV"

power flows throughout the electrical system.

The comparison between the result of calculation of the hand and the result of the calculation of the software ETAP is given in Table 1. It is noted that the results obtained by ETAP is precise and fast compared and we lose time in the calculations with a lack of precision. The coordinated relay protection modules and the ETAP software insertion errors are used to check the sequence of the relay protection motion sequence. The protective movement conditions of typical lines, power lines and typical equipment (large transformer and motor) are selectively checked.

It is noted that in this plant (24/24 H operation) there is no voltage drop which disrupts the quality of the electrical energy and its normal operation because there is different sources (a normal arrival and an emergency 63 kV, steam turbine 5 MVA, 2 diesel group 1100 KVA) and load regulator with relays which ensure a low voltage at all times and place.
Low load: (20% of the load consumption "zone 1, 2, 3, 5 and 6") the PF is low 74% <in relation to load is more inductive (motor, furnace with induction, lighting, welding station...).
In charge: the PF is increased by 89% when the zone 4 "Zinc Electrolysis" (zone in operation) is put into operation, which consumes a large power of approximately 60% of the total power.
In charge with Turbine: The PF remains 89% ± 1% in the

case of the commissioning of the Turbine which can supply the whole zone 1 "central" which has a power factor the same (89% in charge) therefore no change.

Diesel group (normal switch-off 63 kV): In this case the diesel groups only supply the priority bar set in 400V (induction furnaces, lighting, capacitor batteries, etc.) with a voltage setting of 105% to avoid voltage drop in case of an increase Of the load.

Fast security assessment is of paramount importance in a modern power system to provide reliable and secure electricity supply to its consumers. To perform the contingency screening, which is one of the most CPU time-consuming tasks for on-line security assessment, the computation in a few minutes of many LF scenarios is required simulating the occurrence of several contingencies and different loading conditions

V. SIMULATION OF SHORT CIRCUIT ANALYSIS IN ETAP

ETAP's short circuit analysis software can achieve device duty calculations which allow the determination of fault currents and comparison with manufacturer ratings. Overloaded device alarms are displayed on the one-line diagram and study reports.

Short-Circuit Summary Report

3-Phase, LG, LL, LLG Fault Currents

Bus	ID	kV	3-Phase Fault			Line-to-Ground Fault				Line-to-Line Fault				*Line-to-Line-to-Ground			
			I ¹ k	i _p	I _k	I ¹ k	i _p	I _b	I _k	I ¹ k	i _p	I _b	I _k	I ¹ k	i _p	I _b	I _k
Bus75		0.400	53.326	126.345	33.667	0.000	0.000	0.000	0.000	47.914	109.418	47.914	47.914	47.914	109.418	47.914	47.914
Initial Symmetrical Current (kA, rms)	:		53.326		0.000		47.914			47.914				47.914			
Peak Current (kA), Method C	:		126.345		0.000		109.418			109.418				109.418			
Breaking Current (kA, rms, symm)	:				0.000		47.914			47.914				47.914			
Steady State Current (kA, rms)	:		53.667		0.000		47.914			47.914				47.914			

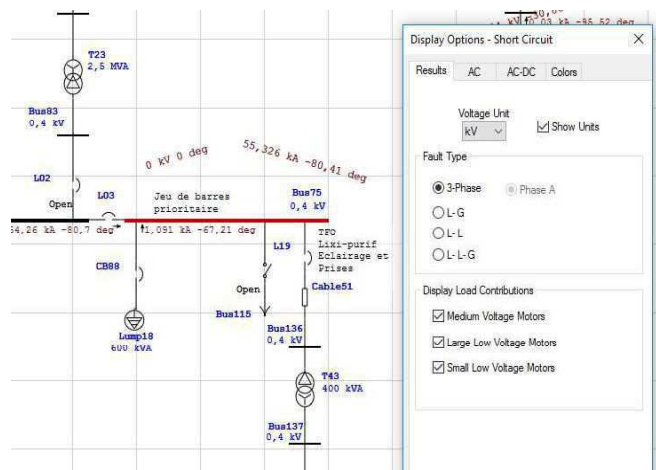
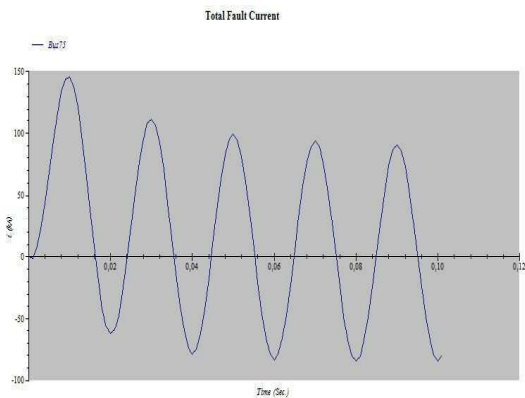


Fig. 8. 3-Phase Fault, bus 75/ 400 V with medium load scenarios

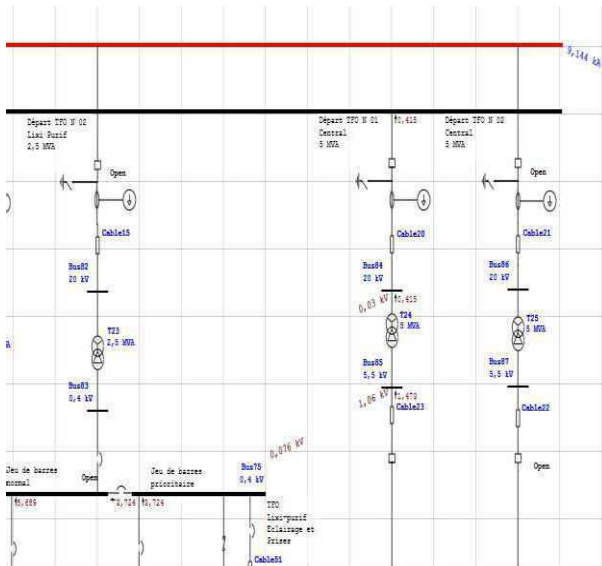


Fig. 9: Short circuit analysis "bus 51, 20 kV" with medium load scenarios

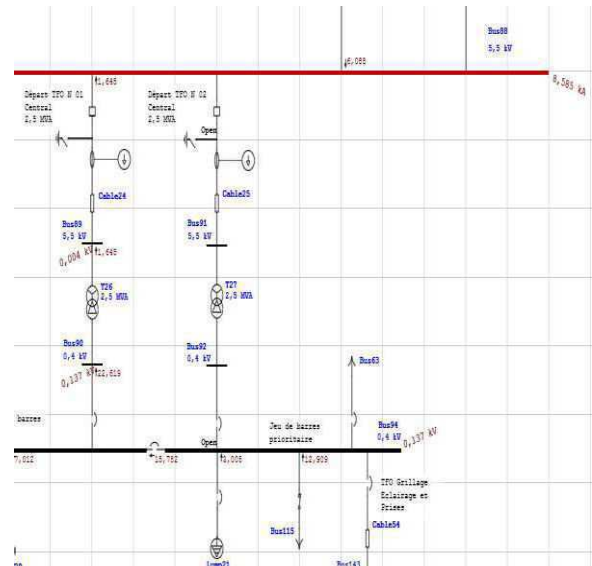


Fig. 10: Short circuit analysis "bus 88, 5,5 kV" with medium load scenarios

TABLE III.

SHORT-CIRCUIT COMPARISON OF HAND CALCULATION RESULT AND ETAP CALCULATED RESULT WITH MEDIUM LOAD SCENARIOS

Icc	At 20 kV	At 5,5 kV	At 400 V Zone 01	At 400 V Zone 02	At 400 V Zone 03	At 400 V Zone 04	At 400 V Zone 05
Device	50	50	57	57	57	50	50
Fault Current (KA)	9,144	8,585	49,348	54,149	54,422	22,867	31,957
Manu Cal (KA)	8,5	8,5	45	48,7	48,7	/	/

TABLE IV.

SHORT-CIRCUIT COMPARISON OF "BUS 88, 5,5 kV" WITH DIFFERENT SCENARIOS OF REAL INDUSTRIAL ENTERPRISE LOAD SCALING

Bus 88 5,5 kV	3-Phse fault (kA)	Line to Grount fault (kA)	Line to line fault (kA)	Line to line to Grount (kA)
LOW LOAD	6,891 L -80,91	0 L 0	3,445 L -81,85	3,445 L -81,85
		0 L 0	3,445 L 98,15	3,445 L 98,15
		0 L 0	0 L 0	0 L 0
FULL LOAD	7,836 L -80,91	0 L 0	3,887 L -81,05	3,887 L -81,05
		0 L 0	3,887 L 98,95	3,887 L 98,95
		0 L 0	0 L 0	0 L 0
FULL LOAD + TURBINE	10,855 L -82,57	3,25 L -81,91	5,437 L -82,22	6,905 L -82,25
		3,25 L -81,91	5,437 L 97,78	3,964 L 97,56
		3,25 L -81,91	0 L 0	2,94 L 98,01

The power system operations are balanced during normal operating conditions. Under irregular condition (fault) the system becomes unbalanced.

The sample short circuit analysis with ETAP is provided in Table 3. The short circuit analysis reveals a clear idea about the system under short circuited conditions and it is helpful in power system estimation. This analysis is very significant when applying relay coordination in the distribution system because it helps to determine the maximum current during the fault to determine the breaking and closing powers of the devices as well as the electromechanical and thermal behavior of the devices equipment and calculate the protection relay settings and the fuse ratings, in order to ensure good selectivity in the electrical network

REFERENCE FOR RELAY CO-ORDINATION

Relay co-ordination plays an important role in the protection of power system. For proper protection, proper coordination of relays with appropriate relay settings is to be done. Relay settings are done in such a way that proper co-ordination is achieved along various series network. However the review of Co-ordination is always essential since various additions / deletion of feeders and equipments will occur after the initial commissioning of plants. As power can be received from generators of captive power plant, the analysis becomes complex. So this study can be a base reference for relay as well as circuit breaker ratings and plug setting of the protective devices.

VI. CONCLUSION

To evaluate various operating states of an existing system, the power flow analysis is essential and short circuit studies are important for planning future expansion of power systems as well as in determining the best operation of protective systems. In order to know how to operate a real system of a HT customer, we simulate the power flow and the voltage profile with different load and contingency scenarios using ETAP software (Electrical Transient and Analysis Program) in order to detect weak points and find the solution, in the form of an application suite consisting of a network editor, analysis modules and customizable template libraries

ETAP Load Flow software performs power flow analysis and voltage drop calculations with accurate and reliable results. . Load flow studies determine if system voltages remain within specified limits under various contingency conditions, and whether equipment such as transformers and conductors are overloaded. This can be used to determine the optimum size and location of capacitors to surmount the problem of an under voltage. Short circuits studies are the most required in a power system in order to adequately size the devices, so that they are capable to handle the short circuit currents. Also these studies provide information regarding the

intensity and the probable damage which can be caused in the event of the short circuit

These studies also help to adequately design the protection system. And, equally important, short circuit study is the prerequisite for Relay Co-ordination and Arc Flash Studies.

REFERENCES

- [1] Smita Acharya, Pragati Gupta, M.A.Mujawa, "Power Flow Analysis Of A Continuous Process Plant: (A Case Study)" International Journal of Electrical, Electronics and Data Communication, ISSN (p): 2320-2084
- [2] Tang Chunhua, "Electrical Power System And Simulation Of Large-Scale Industrial Enterprise," International Conference On Advanced Power System Automation And Protection, 2011, pp. 2076-2081
- [3] K. B Shah, S. K Rathor, Rohan Mehta, " Industrial Grade Power System Study Analysis," International Conference on Electrical, Electronics, and Optimization Techniques (ICEEOT), 2016, pp. 3955-3960.
- [4] Tsai-Hsiang Chen, M.S. Chen, W.-J. Lee, Peter Van Olinda " Distribution system short circuit analysis-A rigid approach" Power Industry Computer Application Conference, 7(1):22-28 · June 1991
- [5] Muhammad Naveed Malik, Ateeb Iftikhar Toor and Muhammad Asim Siddiqui, Nusrat Husain and Akif Nadeem "Load Flow Analysis Of An Eht Network Using Etap®" Journal of Multidisciplinary Engineering Science and Technology (JMEST) ISSN: 2458-940, June - 2016
- [6] Guguloth Ramesh and T. K. Sunil" Optimal Dispatch of Real Power Generation Using Classical Methods"International Journal of Electronics and Electrical Engineering Vol. 3, No. 2, April, 2015, pp 115-120.
- [7] R. S. Maciel, A. Padilha- Feltrin and E. Righeto, "Substitution Newton Raphson Method for the Solution of Electric Network Equations," Transmission & Distribution Conference and Exposition: Latin America, Aug. 2006, pp. 1-6.
- [8] Hui ZHU "The application of the ETAP Software in the Analysis and Simulation of Power Systeme" International Conference on Energy and Power Engennering, 2014, pp 209-213
- [9] Ankita Palod, Vijaya Huchche "Reactive Power Compensation Using DSTATCOM" International Journal of Electrical, Electronics and Data Communication, June-2015 pp 2320-2084
- [10] Mirchevski Slobodan1, Arsov Ljupcho1, Iljazi Iljaz "The Impact of Reactive Power on Energy Efficiency in Electric Drive" Conference: 13th WSEAS International Conference on Electric Power Systems, High Voltages, Electric Machines (POWER '13), At Chania, Crete Island, Greece August 2013
- [11] Kiran V. Natkar1, Naveen Kumar2 "Short Circuit Analysis Of 220/132 kV Substation By Using ETAP" International Journal of Advanced Technology in Engineering and Science. March 2016 ISSN (p): 2348 - 7550,
- [12] S. Thangalakshmi " Planning and Coordination of Relays in Distribution System" Indian Journal of Science and Technology. August 2016, ISSN (p) : 0974-5645
- [13] K.Rajesh, A.Arjunamuthu, M.Karuppasamyandiyan, A.Bhuvanesh "Power Flow Analysis of 230/110 kV Substation using ETAP" International Conference on Emerging Trends in Science, Engineering, Business and Disaster Management, 2014 Feb
- [14] Raj P. Load Flow and Short Circuit Analysis of 400/220 kV Substation. International Journal of Creative Research Thoughts. 2013 Apr; 1(4):1-4.
- [15] Bhagyashri Patil, Swapnil Namekar " Load Flow & Short Circuit Analysis of 132/33/11KV Substation using ETAP" nternational Journal of Applied Engineering Research ISSN 0973-4562 Volume 13, Number 11 (2018) pp. 9943-9952

Structural study and electrical properties of $\text{Bi}_{1.5-x}\text{Ca}_x\text{Sb}_{1.5}\text{CuO}_{7-\delta}$ Pyrochlore-type solid solution series

Rafik E.A. Dra^{#1}, Ahmed Bekka^{#2}, Robert E. Dinnebier^{*3}, Bounekref Boukerma^{#4}

[#] *Laboratoire de Chimie des Matériaux Inorganiques et Applications, Université des Sciences et de la Technologie d'Oran, Faculté de Chimie, BP1505, 31000 Oran El-Mnaouer, Algeria.*

¹aarslene@yahoo.fr (Corresponding author)

²bekkahmed2@gmail.com.

⁴boukerma.houari@gmail.com

^{*} *Max Planck Institute for Solid State Research, Heisenbergstrasse 1, D-70569 Stuttgart, Germany.*

³r.dinnebier@fkf.mpg.de

Abstract- Pyrochlore solid solution $\text{Bi}_{1.5-x}\text{Ca}_x\text{Sb}_{1.5}\text{CuO}_{7-\delta}$ has been prepared by conventional ceramic solid state reaction with $0 \leq x \leq 0.4$. The samples were characterized by X-ray powder diffraction (XRPD), scanning electron microscopy (SEM) and electrical conductivity measurements. The pyrochlore single phase formation was confirmed for all of the x-fractions. The variation of the electrical resistivity versus x of all samples measured by means of a four probe device at room temperature indicates that these still remain insulators. High temperature electrical conductivity measurements at various frequencies using two electrodes device allow us to note the maximum electrical conductivity of $4.7 \cdot 10^{-3} \text{ S.cm}^{-1}$ which has been reached at $x = 0.2$ generating an activation energy of 0.14 eV. For this fraction, Rietveld refinement of the corresponding X-ray powder diffraction pattern confirmed the typical cubic Fd-3m space group with a cell parameter of $a = 10.4089(1) \text{ \AA}$.

Keywords— Pyrochlore, Solid solution, Bismuth, XRPD, Rietveld refinement, SEM, EDX, Electrical conductivity.

I. INTRODUCTION

Materials with pyrochlore like-structure are of interest to chemists as well as to physicists because of properties such as high ionic and electronic conductivity [1], magnetic ordering [2], [3] and luminescence [4], [5]. These properties make them applicable in a variety of areas such as Solid Oxide Fuel Cells (SOFCs) [6], [7], catalysis, nuclear waste immobilization etc. They form over a huge compositional range due to the flexibility of the structure [8]. Within the crystal structure of stoichiometric oxide pyrochlores with general formula $\text{A}_2\text{B}_2\text{O}_7$ a larger 8-coordinated A-site (scalenoedra or distorted cube) and a smaller 6-coordinated B-site (octahedra) exist. The structural formula is often written as $\text{A}_2\text{B}_2\text{O}_6\text{O}'$ in which O and O' occupy the 48f and 8b Wyckoff sites (origin at -3m on the B-site), respectively. The crystal structure could be described as a substructure of the fluorite (CaF_2) structure type (Fm-3m, 225) in which the anionic vacancy and the two A and B cations are ordered. The structure stability of pyrochlores is generally related to the ratio of the two A and B ionic radii and has been observed for R_A/R_B in the range of [1.46 – 1.78].

Smaller ratios lead to the formation of a disordered fluorite structure [8]. The most common charge distributions within the A and B-sites are $\text{A}_2^{+3}\text{B}_2^{+4}\text{O}_7^{-2}$ and $\text{A}_2^{+2}\text{B}_2^{+5}\text{O}_7^{-2}$, the first being however more common than the second one. Bismuth-based pyrochlore compounds are subject of interest because of their particular electric and magnetic properties, which make them promising candidates as electroceramics [9]. Most of them adopt a cubic crystal structure with space group Fd-3m (227) [8]. Non-stoichiometric bismuth zinc niobate, $\text{Bi}_3\text{Zn}_{1.84}\text{Nb}_3\text{O}_{13.84}$ exhibits a high relative permittivity, low dielectric loss and a negative temperature coefficient of capacitance [10]. It has been reported that ruthenate pyrochlore compounds are good oxygen reduction catalysts [11] and potential cathode materials [12]. Pure ceramic pyrochlore compound with chemical formula $(\text{Bi}_{1.524}\text{Cu}_{0.476})(\text{Sb}_{1.524}\text{Cu}_{0.476})\text{O}_{7+\delta}$ exhibits an electrical resistivity of $10^5 \Omega.\text{cm}$ and an effective moment of $\mu_{\text{eff}} = 2.27 \mu_B$ obtained by magnetic susceptibility measurements performed between 300 and 800 K [13]. Magnetic measurements in a temperature range of [4 – 800K] realized on a new pyrochlore compound $(\text{Bi}_{1.56}\text{Co}_{0.44})(\text{Sb}_{1.48}\text{Co}_{0.52})\text{O}_7$ revealed, on one hand, a paramagnetic character of the compound and, on the other hand, the oxidation state «+2» of the cobalt cation. The electrical conductivity of the compound reached $1.88 \cdot 10^{-3} \text{ S.cm}^{-1}$ at 775 K [14]. Magnetic susceptibility of the pyrochlore solid solution $\text{Bi}_{1.5}\text{Sb}_{1.5}\text{Cu}_{1-x}\text{Mn}_x\text{O}_7$ measured between 4 and 300 K revealed a paramagnetic behavior of the solution as well as a «+2» oxidation state of the manganese cation. The lowest electrical resistivity reached was $5 \cdot 10^2 \Omega.\text{cm}$ at 675 K [15].

This study deals with a new pyrochlore solid solution series in which the trivalent cation Bi^{3+} has been partially substituted with the bivalent cation Ca^{2+} . The general formula of the solid solution series can be written as $\text{Bi}_{1.5-x}^{+3}\text{Ca}_x^{+2}\text{Sb}_{1.5}^{+5}\text{Cu}^{+2}\text{O}_{7-\delta}^{-2}$ where δ represents the fraction of oxygen vacancy per formula unit that should be considered to preserve the electro-neutrality of the material. The x-fraction of bismuth exchanged for calcium varies from

0 to 0.4. Polycrystalline samples were prepared by the solid-state reaction route and their properties including crystal structure, microscopic morphology, and electrical conductivity are presented.

II. EXPERIMENTAL PROCEDURES

The solid solution series $\text{Bi}_{1.5-x}\text{Ca}_x\text{Sb}_{1.5}\text{CuO}_{7-\delta}$ was prepared using the conventional solid-state reaction method. The starting materials, with a purity of at least 99.9%, were mixed and well ground for 15 min. Firstly, the mixture underwent a homogenization grinding before being poured into an alumina crucible and calcined at a temperature of 700 °C for 48 hours in a muffle furnace. The calcined powder was reground and recalcined at a temperature of 850 °C for 72 hours. The final product was finely ground in order to prepare disk-shaped samples with a diameter of 10 mm and thickness of 2-3 mm by conventional solid-state powder processing techniques [16]. The disks were sintered in air at 950 °C for 12 hours. The pure phase, the crystal structure and the lattice parameters of the samples were determined using a laboratory X-ray powder diffractometer « Bruker D8 Advance » operating with Cu-K α_1 radiation ($\lambda = 1.540598 \text{ \AA}$) at room temperature. Grain morphology and average stoichiometric composition were characterized by a scanning electron microscope (SEM) « Hitachi 2500 C » equipped with an energy dispersive analysis X-ray system (EDX). The electrical conductivity of the samples was measured by means of four probe device at room temperature in air, as well as two-electrode cell at various frequencies of the external field «GWINSTEK LCR-821», from room temperature up to 300 °C in air.

III. RESULTS AND DISCUSSION

A. Structural Characterization

Fig.1 shows the X-ray powder diffraction (XRPD) patterns of the solid solution series $\text{Bi}_{1.5-x}\text{Ca}_x\text{Sb}_{1.5}\text{CuO}_{7-\delta}$ corresponding to the five x-fractions of calcium. All compounds with $x = 0 - 0.4$, exhibit a single pyrochlore phase characterized by its strongest peak (222) located around $2\theta = 29.6^\circ$. This allows us to confirm the partial substitution of bismuth for calcium. Besides, we can notice the progressive decrease of the intensity of the peak (311) with increasing x-fraction of calcium until it disappears at $x = 0.4$, which is related to the substitution of the heavy bismuth cation in the (311) plans by calcium cation.

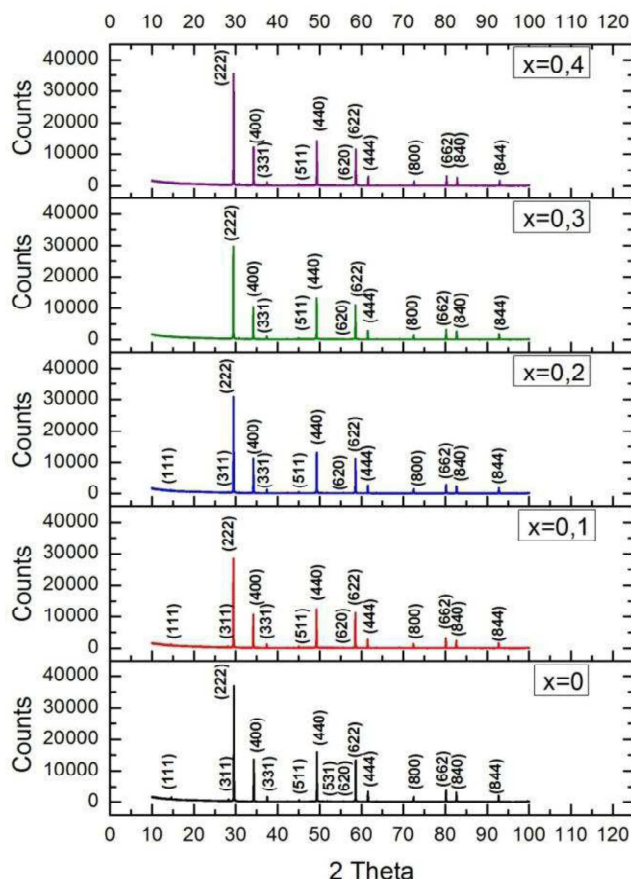


Fig. 1 X-ray diffraction patterns of $\text{Bi}_{1.5-x}\text{Ca}_x\text{Sb}_{1.5}\text{CuO}_{7-\delta}$ solid solution.

The refined lattice parameter variation versus x of the solid solution $\text{Bi}_{1.5-x}\text{Ca}_x\text{Sb}_{1.5}\text{CuO}_{7-\delta}$ series is shown in Fig. 2.

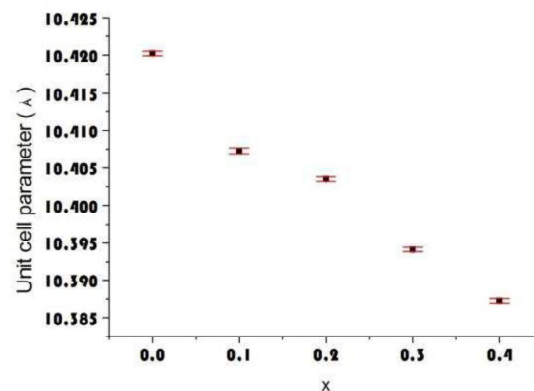


Fig. 2 Lattice parameter of $\text{Bi}_{1.5-x}\text{Ca}_x\text{Sb}_{1.5}\text{CuO}_{7-\delta}$ solid solution as a function of the x-fraction of calcium.

The observed weak decrease (0.12%) of the unit cell parameter with increasing x is possibly not only due to the small difference between the sizes of the two cations involved in the exchange ($R_{\text{VIII}}(\text{Ca}^{2+}) = 1.12 \text{ \AA}$, $R_{\text{VIII}}(\text{Bi}^{3+}) = 1.17 \text{ \AA}$ [17]), but also due to the formation of oxygen vacancies within the pyrochlore crystal structure.

B. Scanning Electron Microscopy characterisation

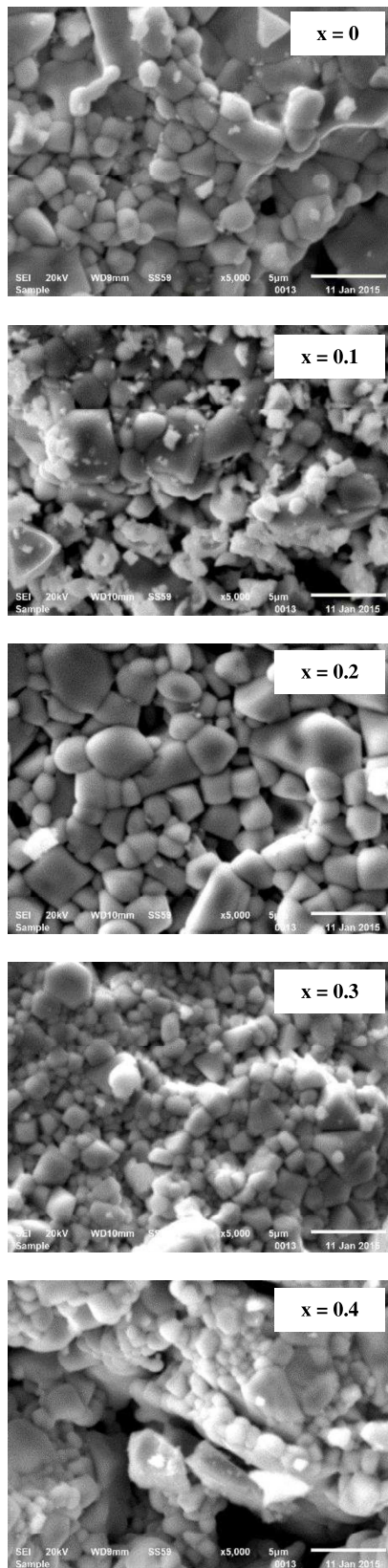


Fig. 3 SEM-pictures of $\text{Bi}_{1.5-x}\text{Ca}_x\text{Sb}_{1.5}\text{CuO}_{7-\delta}$ solid solution.

The scanning electron microscopy (SEM) pictures of the four disk-shaped compounds corresponding to $x = 0 - 0.4$, are shown in Fig. 3.

For the three first x -fractions, the samples exhibit relatively big size particles with relatively well-defined grain boundaries. On the other hand, for $x = 0.3$ and $x = 0.4$, the samples exhibit mixed small ($x = 0.3$) and big ($x = 0.4$) size particles without any apparent grain boundaries. Some areas seem to give evidence of a probable starting fusion of the samples such as that corresponding to $x = 0.4$. It should be noted the sample corresponding to $x = 0.2$ has the most regular grain shapes, relatively large grain sizes, and larger grain boundaries.

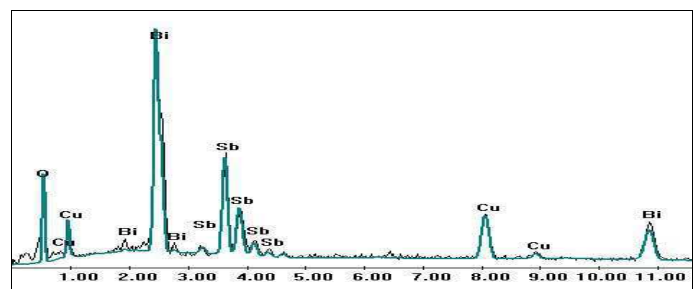
C. Scanning Electron Microscopy characterisation

Table 1 gives the results of EDX analysis as atomic percentage of $\text{Bi}_{1.5-x}\text{Ca}_x\text{Sb}_{1.5}\text{CuO}_{7-(x/2)}$ solid solution series.

TABLE I
 CHEMICAL COMPOSITION OF $\text{Bi}_{1.5-x}\text{Ca}_x\text{Sb}_{1.5}\text{CuO}_{7-(x/2)}$ SOLID SOLUTION SERIES DETERMINED by SEM/EDX ANALYSIS

At%					
Atom	x=0	x=0.1	x=0.2	x=0.3	x=0.4
O	59.64	61.78	66.69	65.46	66.95
Sb	13.55	12.93	12.60	13.58	12.01
Ca	-	2.30	3.03	3.32	3.45
Cu	13.09	12.20	9.72	10.14	11.19
Bi	13.72	10.79	7.96	7.49	6.40

A significant increase of calcium percentage associated with a significant decrease of bismuth percentage when increasing the x -fraction of calcium is in agreement with the substitution of bismuth for calcium process. For $x = 0.2$, the measured stoichiometry is $\text{Bi}_{0.95}\text{Ca}_{0.36}\text{Sb}_{1.5}\text{Cu}_{1.16}\text{O}_{6.53}$. Energy peaks overlap of Ca and Sb could explain the discrepancy between the experimental and theoretical stoichiometry. Fig. 4 shows EDX-diagrams of the solid solution compounds.



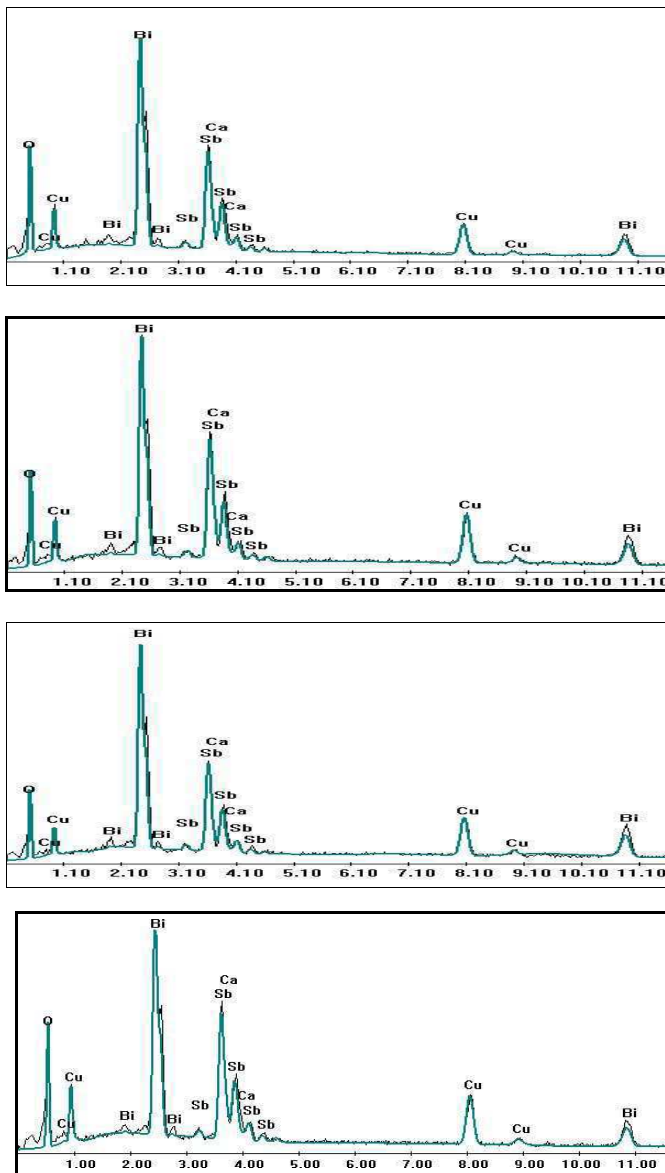


Fig. 4 EDX diagrams of solid solution series $\text{Bi}_{1.5-x}\text{Ca}_x\text{Sb}_{1.5}\text{CuO}_{7-\delta}$ compounds.

D. Electrical Conductivity Characterization

Fig. 5 shows the variation of the electrical resistivity of the pellets versus the x-fraction of calcium of the solid solution series performed with the four probe device at room temperature in air. The increase of the electrical resistivity versus x shows that the calcium doping process does not improve the electrical character of the solid solution. Furthermore, the insulating character of the material tends to increase exponentially starting from $x = 0.2$. Indeed, an average resistivity of $7.3 \times 10^7 \Omega \cdot \text{cm}$ is measured before it suddenly increases up to $44.4 \times 10^7 \Omega \cdot \text{cm}$. Therefore, the loss of the electrical neutrality of the solid solution, due to " $\text{Bi}^{3+}/\text{Ca}^{2+}$ " substitution, is most probably compensated by the loss of oxygen from the structure rather than oxidation of copper. If it is, then the chemical formula of the solid solution would be written as $\text{Bi}_{1.5-x}^{+3}\text{Ca}_x^{+2}\text{Sb}_{1.5}^{+5}\text{Cu}^{+2}\text{O}_{7-\frac{x}{2}}$ so that

when x bismuth-cations are substituted for x calcium-cations, $\delta = x/2$ oxygen-ions vacancies per formula unit would be generated. Consequently, such solid solution could be an oxygen-ion conductor like most of pyrochlore-like compounds. In order to improve the electrical characterization, we performed high temperature electrical conductivity measurements in air, using two electrodes device, within the temperature range of $[25 - 300^\circ\text{C}]$ at various frequencies from 100 Hz to 100 KHz and at 1 Volt.

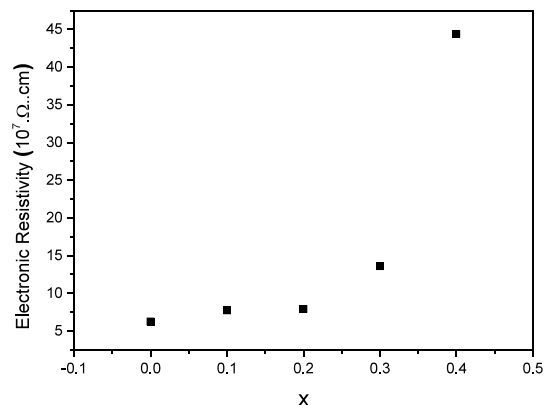
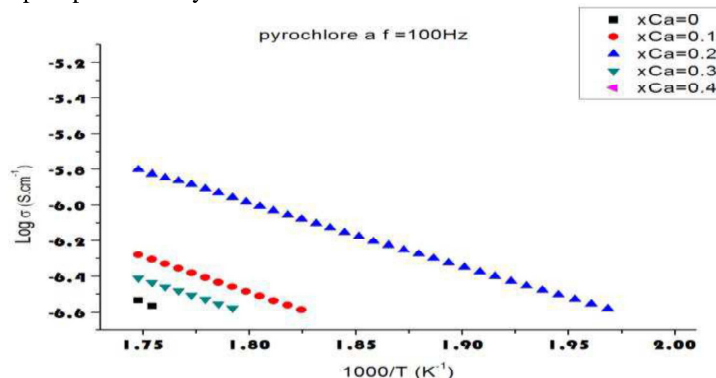


Fig. 5 Electrical resistivity as a function of the x-fraction of calcium of $\text{Bi}_{1.5-x}\text{Ca}_x\text{Sb}_{1.5}\text{CuO}_{7-\delta}$ solid solution

Fig. 6 shows the variation of $\text{Log } \sigma$ versus reciprocal temperature at 100 Hz, 500 Hz, 1 KHz, 10 KHz and 100 KHz for all x-fractions of calcium of the solid solution respectively. It confirms that the electrical conductivity of the samples is thermally activated and follows an Arrhenius law. We note that the maximum calculated conductivity of $4.7 \cdot 10^{-3} \text{ S} \cdot \text{cm}^{-1}$ is that corresponding to $x = 0.2$ at 100 KHz and 300°C . The corresponding activation energy of 0.14 eV was calculated from the slope of the linear fit. This value is too low regarding to the most common values of around 0.3 eV observed with most pyrochlore phases. Consequently, the weak electrical conductivity could be due to only electron displacement, as oxygen displacement cannot be confirmed with maximum measurement temperature not exceeding 300°C . The absence of any breaking slope of the lines show that none of the samples presents any electrical transition.



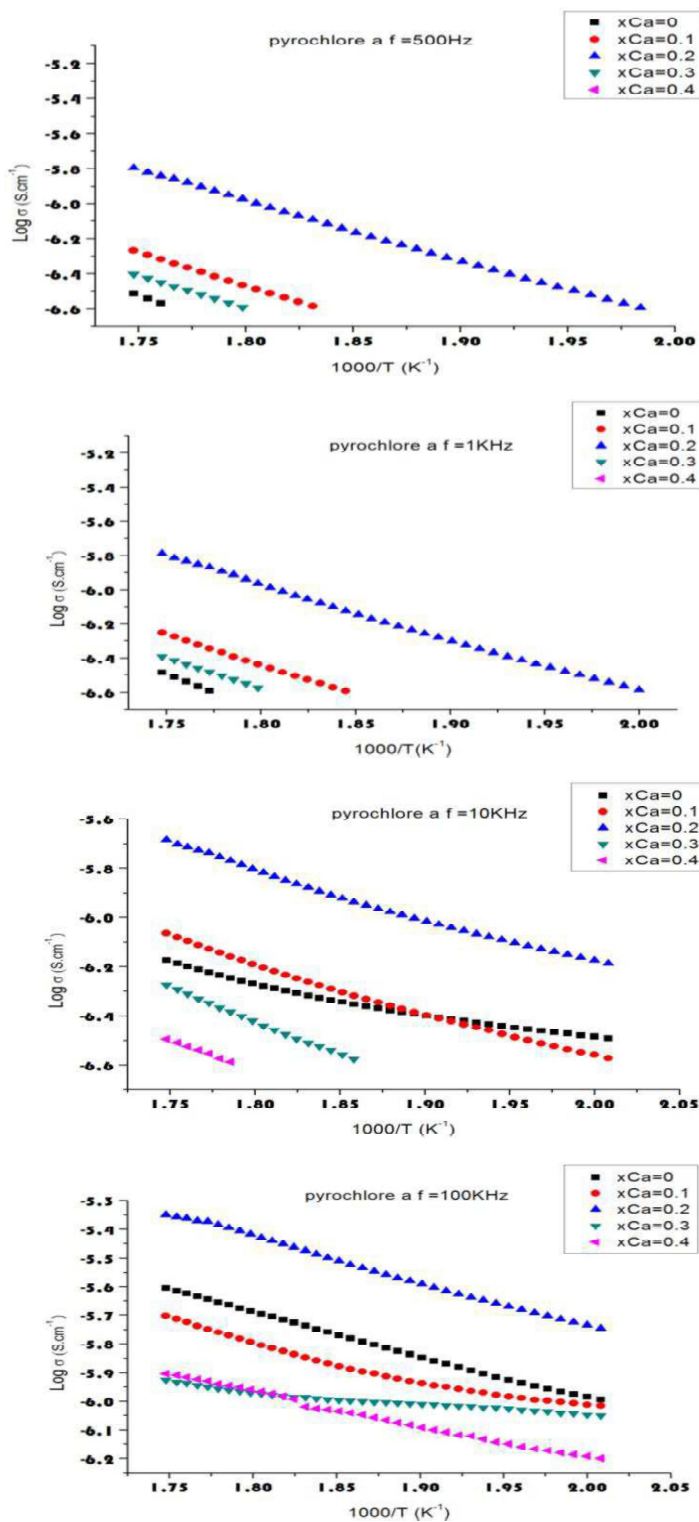


Fig. 6 Variation of $\text{Log } \sigma$ versus $1000/T$ at various frequencies of $\text{Bi}_{1.5-x}\text{Ca}_x\text{Sb}_{1.5}\text{CuO}_{7-\delta}$ solid solution.

E. Rietveld Refinement

In order to confirm the stoichiometry of the compound corresponding to the fraction $x = 0.2$ of calcium, we performed a Rietveld refinement based on a former refined pyrochlore

compound [13] using the Fullprof program [18]. Table 2 gives the refinement parameters.

TABLE II
RIETVELD REFINEMENT PARAMETERS OF THE Bi/Ca ($x = 0.2$)
 $\text{Bi}_{1.5-x}\text{Ca}_x\text{Sb}_{1.5}\text{CuO}_{7-\delta}$ PYROCHLORE

Instrumental parameters	
Diffractometer	Bruker D8-Advance
Wavelength (\AA)	1.54056
Monochromator	Germanium (111)
2θ range ($^\circ$)	10-140
2θ step ($^\circ$)	0.009
Time per step (s)	60
Crystallographic parameters	
Global formula	$\text{Bi}_{1.3}\text{Ca}_{0.2}\text{Sb}_{1.5}\text{CuO}_{6.9}$
Formula units per cell	$Z = 8$
Formula mass (g)	5725.81
Crystal system	Cubic
Space group	$Fd\bar{3}m (227)$
Cell parameter (\AA)	10.4089(1)
Cell volume (\AA^3)	1127.7543(5)
Density (g/cm^3)	10.019
Refinement parameters	
Refinement program	Fullprof
Number of parameters refined	39
Number of reflections	70
Peak shape function	Pseudo-Voigt

Fig. 7 shows the agreement between observed and calculated XRPD profiles for Bi/Ca ($x = 0.2$) pyrochlore compound.

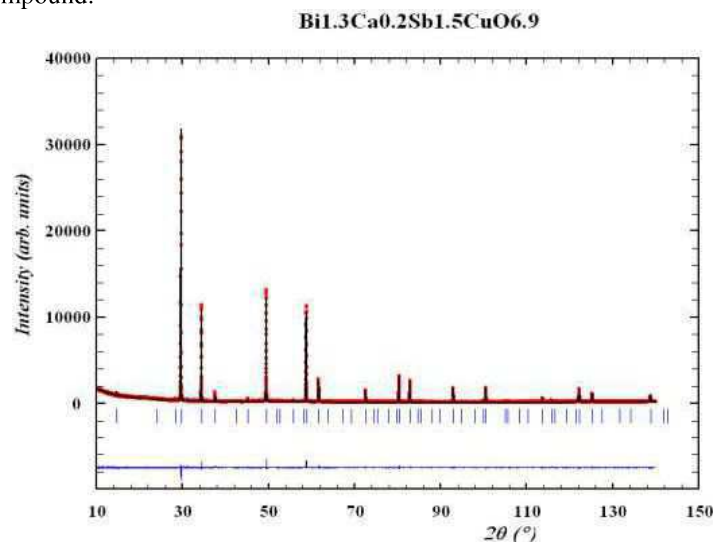


Fig. 7 Rietveld plot of the Bi/Ca ($x = 0.2$) $\text{Bi}_{1.5-x}\text{Ca}_x\text{Sb}_{1.5}\text{CuO}_{7-\delta}$ pyrochlore compound.

Table 3 gives the refined profile parameters of the crystal structure.

TABLE III
REFINED PROFILE PARAMETERS OF THE Bi/Ca (x = 0.2)
Bi_{1.5-x}Ca_xSb_{1.5}CuO_{7-δ} PYROCHLORE STRUCTURE

Scale factor	0.17771(35)10 ⁻⁴
Zero point	0.0002
x(O _{48f}) parameter	0.3212(3)
Gaussian peak half width parameters (Å ²)	U = 0.00857 V = -0.01040 W = 0.00690(1)
R _{wp} (%)	14.6
R _p (%)	19.9
R _{Bragg} (%)	5.37
R _f (%)	6.81
χ ² (R _{wp} /R _{exp}) ²	1.52

Significant interatomic distances and bonding angles are given in Table 4.

TABLE IV
INTER ATOMIC DISTANCES (Å) AND BONDING ANGLES (°) OF THE
Bi/Ca (x = 0.2) Bi_{1.5-x}Ca_xSb_{1.5}CuO_{7-δ} PYROCHLORE STRUCTURE

AO ₈ scalenohedra		
A – O1	6x	2.619(5)
A – O2	2x	2.2536(1)
O1 – A – O2 (a)		80.6(1)
O1 – A – O2 (b)		99.4(3)
A – O1 – A		89.3(2)
BO ₆ octahedra		
B – O1	6x	1.982(1)
B – B	6x	3.6801(2)
O1 – B – O1		93.3(5)
B – O1 – B		105.4(3)

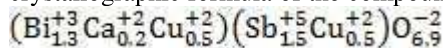
The R-factors values confirm the good agreement between observed and calculated profiles. Refined occupancy, x coordinate of the 48f oxygen atom and isotropic thermal factors of all atoms of the Bi/Ca (x = 0.2) pyrochlore compound are summarized in Table 5.

TABLE V
REFINED ATOMIC PARAMETERS OF THE Bi/Ca (x = 0.2)
Bi_{1.5-x}Ca_xSb_{1.5}CuO_{7-δ} PYROCHLORE STRUCTURE

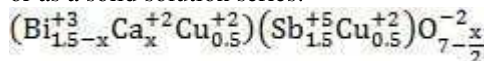
Atom	Site	Occ.	x	y	z	B (Å ²)
Bi	16d	0.65	1/2	1/2	1/2	3.1(4)
Ca	16d	0.1	1/2	1/2	1/2	3.1(4)
Cu(1)	16d	0.25	1/2	1/2	1/2	3.1(4)
Sb	16c	0.75	0	0	0	0.29(5)
Cu(2)	16c	0.25	0	0	0	0.29(5)
O(1)	48f	1.0	0.3209(12)	1/8	1/8	0.5(8)
O(2)	8b	1.0	3/8	3/8	3/8	0.5(8)

Cations on 16d site exhibit a considerably higher atomic displacement parameter (ADP) than those on 16c site. Relatively high atomic displacement parameters on 16d site are very common in pyrochlore structures. This is due to the

fact that the A-site consists of a heavily cube-distorted 8-fold coordination with two sets of “A – O” distances (6 × A – O1 and 2 × A – O2) [9]. This structure relaxation is also caused by the bismuth lone pair which the A-site must accommodate. However, such high values have been obtained only when the A-site is occupied by more than one atom [13]. Taking into account the electrical neutrality of the compound, the crystallographic formula of the compound should be written as:



or as a solid solution series:

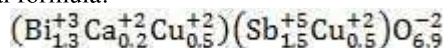


in which « x/2 » oxygen vacancies for x calcium per formula unit are generated. Hence, the more the quantity of calcium substituting the bismuth increases, the more oxygen vacancies will be generated.

IV. CONCLUSION

The solid solution with chemical formula $\text{Bi}_{1.5-x}^{+3}\text{Ca}_x^{+2}\text{Sb}_{1.5}^{+5}\text{Cu}^{+2}\text{O}_{7-\delta}^{-2}$ has been successfully synthesized. XRPD characterization shows that pure and well-crystallized pyrochlore phases were obtained. The unit cell volume of the crystal structure slightly decreases with increasing x. This is not only caused by the smaller size of substituting Ca²⁺ than that of substituted Bi³⁺ but also by the formation of oxygen vacancies, since no electronic conductivity enhancement was found. High temperature conductivity measurements allowed us to find a maximum electrical conductivity of 4.7 10⁻³ S.cm⁻¹ at 100 KHz and 300 °C, and an activation energy of 0.14 eV. This latter, much lower than those of most of pyrochlore compounds (≈ 0.3 eV), and the low maximum measurements temperature of 300°C, let us suggest that the measured conductivity is most probably due to much more electron displacements than oxygen displacements.

These values have been reached when substituting bismuth for optimal fraction x = 0.2 of calcium leading to the following chemical formula:



in which «0.10» oxygen vacancies per formula unit would be required to reach the electrical neutrality of the ionic structure, leading to a non-stoichiometric oxygen pyrochlore compound.

ACKNOWLEDGMENT

We thank Dr Carlos Frontera of the Institute of Material Science of Barcelona (ICMAB) for his samples characterization guidance. The German Academic Exchange Service (DAAD) should be acknowledged for financial support which made possible the publication of this paper.

REFERENCES

- [1] A.G. Krasnov, I.V. Piir, M.S. Koroleva, N.A. Sekushin, Y.I. Ryabkov, M.M. Piskaykina, V.A. Sadykov, E.M. Sadovskaya, V.V. Pelipenko, N.F. Eremeev, *Solid State Ionics*, Volume 302, 118–125 (2017).
- [2] M.A. Subramanian, J.E. Greedan, N.P. Raju, A.P. Ramirez, A.W. Sleight, *Journal de Physique IV*, Vol.7, C1-625 – C1-628, (1997).
- [3] J.E. Greedan, N.P. Raju, A. Maignan, Ch.Simon, J.S. Pedersen, A.M. Niraimathi, E.Gmelin, M.A. Subramanian, *Physical review B – Condensed Matter and Materials Physics*, Vol. 54, Issue 10, 7189 – 7200, (1996).
- [4] L.K. Joseph, K.R. Dayas, S. Damodar, B. Krishnan, K. Krishnankutty, V.P.N. Nampoore, P. Radhakrishnan, *Spectrochimica Acta, Part A: Molecular and Biomolecular Spectroscopy*, Vol. 71, Issue 4, 128 – 1285, (2008).
- [5] J. Yang, Y. Su, *Materials Letters*, Vol. 64, Issue 3, 313-316, (2010).
- [6] S. Khademinia, M. Behzad and H. S. Jahromi, *RSC Advances*, Volume 5, Issue 31, pages 24313–24318, (2015).
- [7] D.W. Jung, K.T. Lee, and E.D. Wachsman, *Journal of the Electrochemical Society*, Volume 163, pages 411–4145, (2016).
- [8] M. A. Subramanian, G. Aravamudan, G. V. S. Rao; *Progress in Solid State Chemistry*, 15, 55, (1983).
- [9] D.P.Cann, C.A.Randall, T.R.Shrouf, *Solid State Commun.*, 100,529,(1996).
- [10] K. B. Tan, C. C. Khaw, C. K. Lee, Z. Zainal, Y. P. Tan, H. Shaari, *Materials Science-Poland*, Vol. 27, No. 3, (2009).
- [11] H.S.Horowitz, J.M.Longo and H.H.Horowitz, *Journal of the Electrochemical Society*, 130(9), 1851-1853, (1983).
- [12] Z. Zhong, *Electrochemical and Solid-State Letters*. 9, A215-A219, (2006).
- [13] M.Sellami, A. Bekka, N. Bettahar, *Comptes Rendus de Chimie*, Volume 8, issues 6-7 1129–1134, (2005).
- [14] M. Sellami, A. Bekka, N. Bettahar, V. Caignaert and Nguyen Ninh; C. R. Chimie, Volume 12, issues 1-2, 276-283 (2009).
- [15] M. Sellami, V. Caignaert, M. Haddad, A. Bekka and N. Bettahar, *Journal of Alloys and Compounds*, Volume 482, issues 1-2, 13-18 (2009).
- [16] J. C. Nino, M. T. Lanagan and C. A. Randall, *J. Mater. Res.* **16**, 1460 (2001).
- [17] R.D Shannon, *Acta cryst.* A32, p. 571, (1976).
- [18] J. Rodriguez-Carvajal, *Physica B* 192,p. 55,(1993).

Contribution to the valorization of clay composite materials in Algeria: Application building materials

BOUSSAK HASSINA

Coatings Laboratory, Materials and Environment University of Science and Technology M'Hamed Bougara-35000-Boumerdes Algeria.

fatia_690@yahoo.fr

Abstract— This work is part of the development of local products such as clays in the Maghnia region, using them in the manufacture of cementitious building materials, such as mortars, to improve their performance. The results of tests on the cementitious products (mortar) after firing show that the compressive and flexural strength (at 7 days) by substituting the sand by the bentonite clay are important compared to the reference material. Adding refractory clay to building materials causes an increase in the mechanical and thermal resistance of the product after sintering. This highlights the diversity of application of this material (boiler coatings, chimneys, flue gas systems, steel plant floors, parts of ovens, .etc up to 1400°C) without forgetting the economic and environmental interest.

Keywords— valorisation des argiles; argiles réfractaire; mortiers; thermomécanique; composite materials.

I. INTRODUCTION

The steel industry requires specific materials capable of meeting a number of requirements including a good ability to withstand repeated mechanical and thermal stress. Indeed, the materials thus solicited are likely to deteriorate prematurely and thus, lead to the ruin of structures in service entailing significant risks for operators and significant production losses. To improve the performance of these materials, it is imperative to have a good vision of the evolution of their thermomechanical properties [1], [2]. This evolution can result from their microstructural state, which is necessarily evolutionary in the conditions of service. The design of the refractory structures must seek the adequacy between the types of stresses undergone in a specific place and the nature of the material to be used [3], [4]. In this context, the research laboratories on materials are working on the development of new cementitious composites, for the economic purpose (reduce the cost of production), ecological (giving importance to local raw materials) and technical (improving the mechanical and thermal properties of mortars or concretes) [5]. The study described in this article aims to take stock of the valorization of refractory clays which are in abundance in cement and brick factories Algerian, and this,

for the manufacture of mortars in order to study and improve certain thermomechanical properties.

II. EXPERIMENTATION

A. Materials and experimental process

The resistance to compression and flexion (three-point bending) of a parallelepiped ($4 \times 4 \times 16$ cm) was achieved using a branded equipment (Zwick / Roell) (reference Z2.5KN), 0.5mm / min of displacement. These tests or experiments consist in placing a test piece between the jaws of a compression or bending machine, the applied force is recorded, which is then converted into deformation and stress. The materials used in this study are: Ain El kbira - Sétif cement, Tébessa standardized sand and Maghnia bentonite. The formulation of the reference mortar is shown in the table below:

TABLE I
CONSTITUENTS OF MORTARS

Formulation	Cement (g)	Sand (g)	Water (g)
Reference	450	1350	225

For mortar mixing, add 225g (+/- 1) of water and 450g (+/- 2) of cement to the mixer and start immediately at low speed. After 30 sec of mixing, add 1350 g (+/- 5) of sand regularly for the next 30 sec. Divide the mortar into pieces and fill the molds in two layers. Put a first coat and start the appliance: 60 shocks will be made to spread the first layer of mortar. Turn off the device and then put the second layer of mortar. Restart the device: 60 shocks will be carried out again, as soon as the operation is carried out and that the mortar is well spread on the mold, equalized with a spatula. When the mortar is solidified, the test piece is removed. Here, the manufactured test pieces were demolded at 2_{days} and 7_{days}.



Fig. 1 Manufacture of mortar specimens

The figure and table below show the composition of the mortars when substituting normalized sand with bentonite.

TABLE II
 DIFFERENT FORMULATIONS SUBSTITUTING NORMALIZED SAND WITH BENTONITE.

Formulation	Cement (g)	Sand (g)	Water (g)	Clay (g)
V1	450	1350	225	0
V2	450	1080	225	270
V3	450	945	225	405

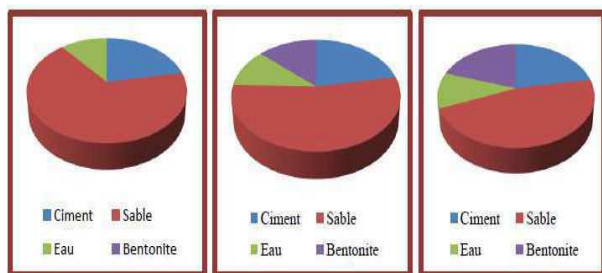


Fig. 2 Different formulations substituting normalized sand with bentonite.

The effect of the temperature will cause a modification of the components (cement paste, sand, and bentonite) as well as the structure of our mortar. Remove the test pieces of the basin after storage under water for 2 days (temperature: 20°C). Leave to air dry, then steam at a temperature of 100 to 105°C. Subject the test pieces to a high temperature (1400 ° C) in an oven, maintain a constant heating rate (V) up to 1400°C and allow this step for 30 minutes so that the test tubes heat homogeneously. Cooling the oven in the opposite direction at a speed (-V) and remove the test pieces. Follow the same steps for 7 day mortars.

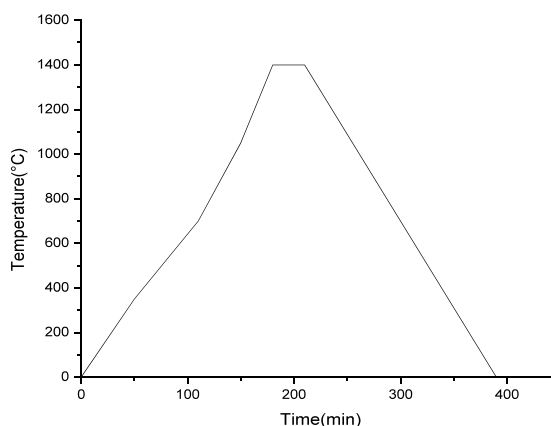


Fig. 3 Thermal cycle of mortar specimens



Fig. 4 Test specimens before heat treatment



Fig. 5 Test specimens after heat treatment at 1400°C.

The tables and figures below show the evolution of the mechanical resistance to compression and bending of the various mortars after firing.

TABLE III
 RESULTS OF MECHANICAL TESTS ON MORTARS BY SUBSTITUTING NORMALIZED SAND WITH BENTONITE.

Formulations	2 days		7 days	
	Flexion (MPa)	Compression (MPa)	Flexion (MPa)	Compression (MPa)
V ₁	3.0	20.1	3.8	24.7
V ₂	2.2	20.6	4.4	21.3
V ₃	1.9	14.15	3.6	14.35

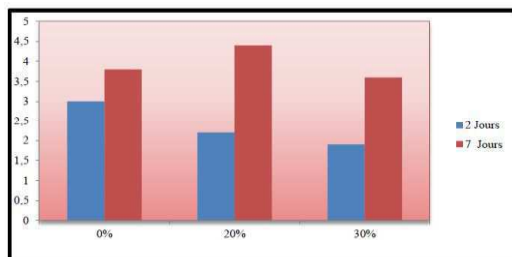


Fig. 6 Results of flexural tests by substituting normalized sand with bentonite

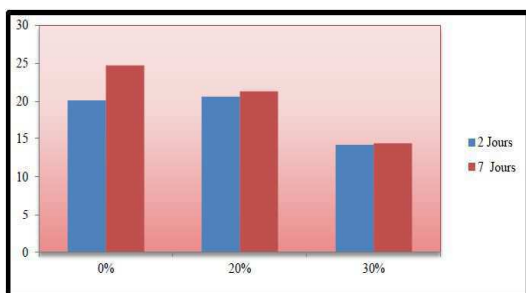


Fig. 7 Compression test results by substituting normalized sand with bentonite

III. RESULTS AND DISCUSSION

The main rule of mechanical strength of mortars is directly related to the ratio (E / C) [6], [7]. Figures 6 and 7 show the evolution of the mechanical resistance to compression and bending of the various mortars formulated. From these histograms, we find that the reference mortar has a higher mechanical strength than those of other mortars containing bentonite, before the heat treatment. In ordinary concrete, during the increase of the temperature, there is a modification of the physicochemical properties of this one [8], [9], it is almost the same case for the mortar; it results from the rise of the temperature a modification of the thermal properties which also influences on a macroscopic point of view. From these histograms, we notice that after cooking, there is a decrease in the resistance of the reference mortars. On the other hand we observe an increase of the resistances of the substituted mortars. From the results obtained, we can deduce that the addition of bentonite positively influences the mechanical behavior of the substituted mortars, so they can be valorised mechanically. Nevertheless, the ordinary mortar remains here, more resistant than the latter.

III. CONCLUSIONS

In conclusion, we can say that clay-substituted mortars can be used in moderately stressed structures, even if this does not bring significant improvements. Nevertheless, these results highlight the influence of clays on the properties of cementitious materials, highlighting the economic and environmental interest of cement substitution by calcined clays. In general, it is possible to exploit refractory clay mortars up to 1400°C.

of this template was provided by courtesy of Causal Productions (www.causalproductions.com)".

ACKNOWLEDGMENT

In my present work I made a substitution of refractory clay Maghnia in the building materials on one side to value the clays of our country and another to lower the cost of return of the raw materials. In a future study we would like to analyze our materials by physical and mechanical analysis.

REFERENCES

- [1] M. ISAAC, O. ISHAI, Engineering Mechanics of Composite Materials, Second Edition Oxford University Press 2006.
- [2] J. Madejeva, P. Komadel, "Baseline studies of the clay minerals society source clays: infrared methods", clay and clays minerals , vol 49, No. 5, pp. 410-432, 2001.
- [3] R. D. Magagi, Y. H. Kerr, "Characterization of surface parameters over arid and semi-arid areas by use of ERS-1 Windscatterometer, Remote Sens. Reviews, vol. 15, pp. 133-155, 1997.
- [4] M. Rigaud, "Trends in the steel industry and developments of new refractory materials", Refractories Application and News, Vol. 10, pp. 26-32, Sep 2005.
- [5] E. Yeugo-Fogaing, "High temperature characterization of refractory materials", T. Doct. Thesis, University of Limoges. France. 2006.
- [6] C. E. Semler, "The sleeping giant (china) has awakened", Refractories Application and News, Vol. 11 No. 4, pp. 6-12, 2006.
- [7] H. Celik, "Technological characterization and industrial application of two Turkish clays for the ceramic industry", Applied Clay Science, Vol. 50, pp 245-254, 2010.
- [8] A. Bessa, J.P. Bigas, J.L. Gallias, Evaluation of the binding contribution of mineral additions to the porosity, the compressive strength and the durability of mortars. 22nd university meetings of civil engineering, P 1-8, 2004.
- [9] M. Savic Ivana; T. Stojiljkovic Stanisa; M. Savic Ivan; B. Sreten Stojanovic. "Modeling and optimization of iron(III) adsorption from water using bentonite clay: comparison of central composite design and artificial neural network", Chemical Engineering & Technology, Vol. 35(11), pp. 2007-2014, 2012.

Programming interface in Matlab to estimate solar radiation in Algeria: Application to M'sila

Younes Kherbiche ^{#1}, Nabila Ihaddadene ^{#2}, Razika Ihaddadene ^{#3} and Marouane Mostefaoui ^{*}

[#] Department of Mechanical Engineering,
Med Boudiaf University-BP 166 M'sila 28000, Algeria

^{*} M'sila Weather Station-M'sila-Algeria

¹Kherbiche_younes@hotmail.com ²MAZ1dz@gmail.com ³tassekurt1@gmail.com

Abstract— The solar energy gives life to humans and all living beings on earth. Solar energy is used to produce thermal as well as electrical power. Solar energy and other renewable sources, allow us to meet the demand for energy while providing a cleaner and greener footprint. In this work, we have developed a software using the programming language MATLAB GUIs (also known as graphical user interfaces or UIs) for the estimation of solar radiation for the different types of the sky in Algeria. The software contains a database (latitude, longitude, and altitude) of all the regions of Algeria. The program gives the opportunity to compare the values estimated by the theoretical models (Perrin de Brichambaut, Lui & Jordon, Hay & Davies, Klucher and Reindl) and the values measured by the meteorological station in the region of M'sila. A good agreement was found between the measured and recorded values.

Keywords- Solar Radiation, Solar Radiation Models, Matlab GUIs.

I. INTRODUCTION

The sun is the source of solar energy, which is the largest member of the solar system compared to other members around it. About 74% of the sun's mass is hydrogen, 25% is helium, and 1% is the residue tracing heavier elements. Solar radiation is radiation emitted by the Sun, whereas solar energy is the energy emitted by the Sun in the form of electromagnetic waves [1].

The quantities and types of aerosols in the atmosphere, water vapour, ozone, and other components affect the total quantity and the spectral distribution of the solar radiation incident on a solar collector surface. The wavelength range of solar radiation available in the terrestrial region for the use of solar energy applications is from 0.29 to 2.3 μm . Due to dispersing in the atmosphere, solar radiation has two components (beam and diffuse radiations) in the terrestrial region [2].

The solar radiation data are used in the development, as well as in the evaluation of the performance of solar systems. It is possible to predict the instantaneous changes of diffuse, direct and global irradiation for different inclinations, even if the sky possesses cloudy perturbation.

For this, we developed an interface written and designed in Matlab GUIs which calculated the position parameters and the solar radiation on any surface using different models and for different sky types. We also present some simplified models for the evaluation of solar energy received on a horizontal and inclined planes.

II. THEORETICAL

A. Solar Radiation Energy

- Solar time is the calculation of time passing refers to the position of the sun in the sky, solar time is of two types, namely, apparent solar time and mean solar time (clock time or standard time). The difference in minutes between solar time and standard time is: [3]

$$\text{Solar time} - \text{standard time} = 4(L_{sm} - L_{loc}) + \xi \quad (1)$$

- ✓ L_{sm} is the standard meridian.
- ✓ L_{loc} is the longitude of the location
- ✓ ξ is the equation of time (in minutes),

Which is given by the expression:

$$\xi = 229.2(0.000075 + 0.001868 \cos B - 0.032077 \sin B - 0.014615 \cos 2B - 0.04089 \sin 2B) \quad (2)$$

$$\text{Where: } B = (N - 1) * 360/365 \quad (3)$$

- The hour angle corresponding to 1 h is 15° ;
Expression for the hour angle is given by:

$$\omega = (ST - 12) * 15^\circ \quad (4)$$

- The declination is calculated by the following relation:

$$\delta = 23.45 \sin[(360/365)(284 + N)] \quad (5)$$

- The angle of incidence (θ_i) can be expressed as:

$$\cos(\theta_i) = (\cos \varphi \cos \beta + \sin \varphi \sin \beta \cos \gamma) \cos \delta \cos \omega + \cos \delta \sin \omega \sin \beta \sin \gamma + \sin \delta (\sin \varphi \cos \beta - \cos \varphi \sin \beta \cos \gamma) \quad (6)$$

- ✓ β surface tilt angle from horizon, °
- ✓ h the height of the sun
- ✓ γ surface azimuth angle, °

For a horizontal plane facing due south:

$$\sin(h) = \cos(\theta_z) = \cos \varphi \cos \delta \cos \omega + \sin \delta \sin \varphi \quad (7)$$

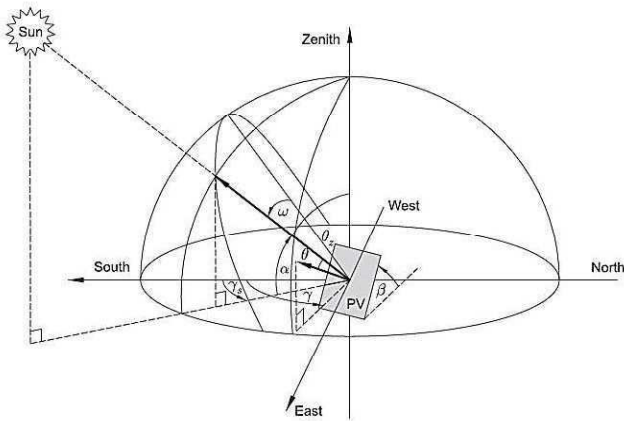


Fig. 1 View of various Sun–Earth angles on an inclined surface. [4]

- The solar intensity on a plane perpendicular to the direction of solar radiation is given by:

$$I_{ext} = I_{SC} [1 + 0.033 \cos(360N/365)] \quad (8)$$

- The solar radiation (I_0) incident on a horizontal plane in the extra-terrestrial the atmosphere in W/m^2 :

$$I_0 = I_{SC} [1 + 0.033 \cos(360N/365)] \cos \theta_z \quad (9)$$

Where (I_{SC}) is the solar constant, the value of solar constant is $1367 W/m^2$, for the N the day of the year.

B. Solar radiation models

- The isotropic sky model is a simple model when the diffuse radiation is uniformly distributed over the sky dome and this reflection spreads over the ground. [5] :

$$I_G = I_{dir} R_b + I_{dif} \left(\frac{1+\cos \beta}{2} \right) + (I_{dir} + I_{dif}) \rho \left(\frac{1-\cos \beta}{2} \right);$$

$$\text{Correction factor for beam radiation } R_b = \frac{\cos \theta_i}{\cos \theta_z} \quad (10)$$

- Klucher found that the isotropic model gave good results for overcast skies but reduces irradiance under clear and partly overcast conditions, the total irradiation on a tilted plane shown in Eq. (11). [6]:

$$I_G = I_{dir} R_b + I_{dif} \left(\frac{1+\cos \beta}{2} \right) \left[1 + k \sin^3 \frac{\beta}{2} \right] \left[1 + k \cos^2 \theta \sin^3 \theta_z \right] + (I_{dir} + I_{dif}) \rho \left(\frac{1-\cos \beta}{2} \right); k = 1 - \left[\frac{I_{dir}}{(I_{dir}+I_{dif})} \right]^2 \quad (11)$$

- In the Hay–Davies model, diffuse radiation from the sky is composed of an isotropic and circumsolar component and horizon brightening is not taken into account. [7]:

$$I_G = (I_{dir} + I_{dif} \tau) R_b + I_{dif} (1 - \tau) \left(\frac{1+\cos \beta}{2} \right) + (I_{dir} + I_{dif}) * \rho \left(\frac{1-\cos \beta}{2} \right); \tau = \left(\frac{I_{on}}{I_{ext}} \right) \quad (12)$$

- The Reindl model also accounts for horizon brightening and employs the same definition of the anisotropy index τ as described in Eq.(12), The total irradiance on a tilted surface can then be calculated using Eq. (13):

$$I_G = (I_{dir} + I_{dif} \tau) R_b + I_{dif} (1 - \tau) \left(\frac{1+\cos \beta}{2} \right) \left[1 + \sqrt{\frac{I_{dif}}{(I_{dir}+I_{dif})}} \sin^3 \frac{\beta}{2} \right] + (I_{dir} + I_{dif}) \rho \left(\frac{1-\cos \beta}{2} \right) \quad (13)$$

- ✓ I_{dir} Direct-normal component of solar irradiance on the horizontal surface, W/m^2
- ✓ I_{dif} Global diffuse horizontal solar irradiance, W/m^2
- ✓ I_{on} Direct-normal solar irradiance, W/m^2
- ✓ I_{ext} Direct extraterrestrial normal irradiance, W/m^2

- The Perrin de Brichambaut model have proposed another correlation to predict direct normal irradiance in the terrestrial region, which is given by: [8]:

$$I_{on} = I_{ext} \cos \theta_i e^{(-T_L * (0.9 + \frac{9.4}{(0.89)^Z} \cos \theta_z)^{-1})} \quad (14)$$

- T_L is the Linke turbidity factor, which is given by the expression: $T_L = \Psi + X + Y$ (15)
- Ψ is the turbidity corresponding to the absorption by the gases of the atmosphere

$$\psi = (0.89)^z \quad (16)$$

- X is the turbidity relative to diffusion by aerosols

$$X = (0.9 + 0.4 A) * (0.63)^z \quad (17)$$

- Y is the turbidity due to gas absorption, by water vapor, which is given by the expression:

$$Y = 2.4 - 0.9 \sin(\varphi) + 0.1(2 + \sin(\varphi))A - 0.2Z - (1.22 + 0.14 A)(1 - \cos \theta_z) \quad (18)$$

- A is the factor as a function of the astronomical

$$A = \sin((360/365)(N - 121)) \quad (19)$$

The model estimates the O_2 components of the global solar radiation on a horizontal plane as follows:

$$I_{dir} = A * \sin(h) * e^{-1*(B*\sin(h+C))^{-1}} \quad (20)$$

$$I_{dif} = D * (\sin(h))^{0.4} \quad (21)$$

Sky condition	A	B	C	D
Normal Conditions Of Clear Sky	1230	3.8	1	125
Clear Sky polluted	1260	2.3	3	166.6
Clear Sky	1210	6	1	93.75
Very Clear Sky	1300	6	2	87
Average Sky	1230	4	2	125
Polluted Sky	1200	5	2	187

Tableau 1. The values of the constants A, B, C and D in terms of the nature of the Sky. [9]

III. SOFTWARE OVERVIEW

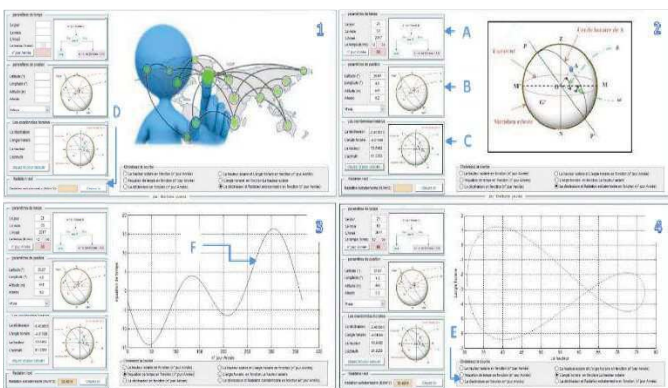
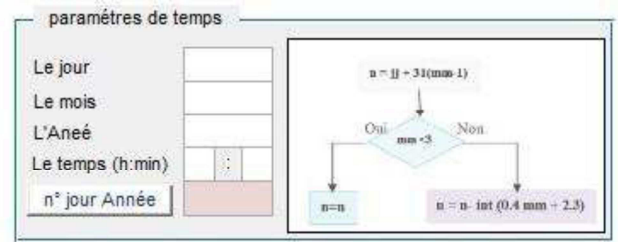


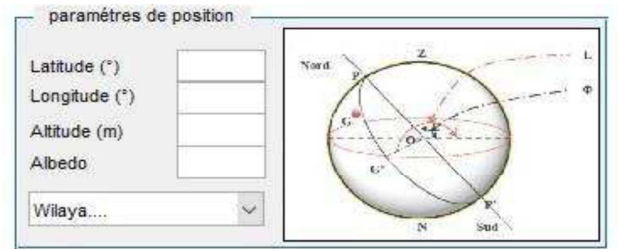
Fig. 2 Graphical interface giving: the position of the earth in relation to the sun, the declination of the sun, the number of the day and the month and the equation of the appropriate time.

The computational software developed has flexible graphical interfaces (two graphical interfaces) as illustrated in FIGURE 2 and

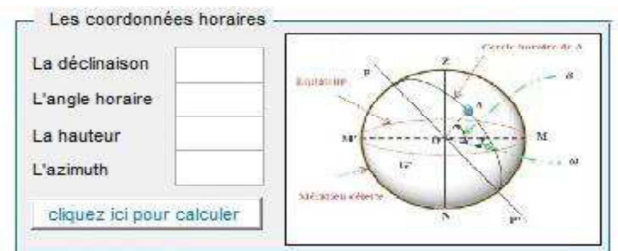
FIGURE 3. It has graphical interfaces and digital data. The first graphical interface is divided into six panels; A, B, C, D, E and F.



Panel A: this panel contains time parameters as the day, the month, the year, the time as illustrated in FIGURE2.



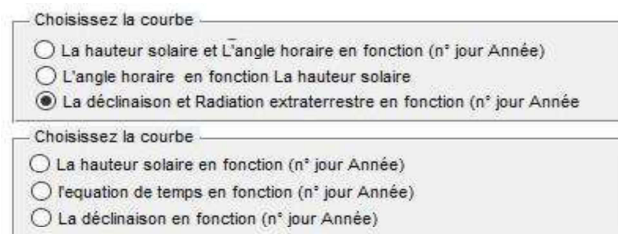
Panel B: this panel covers positional parameters such as latitude, longitude, elevation, albedo and location (Wilayas) as shown in FIGURE2.



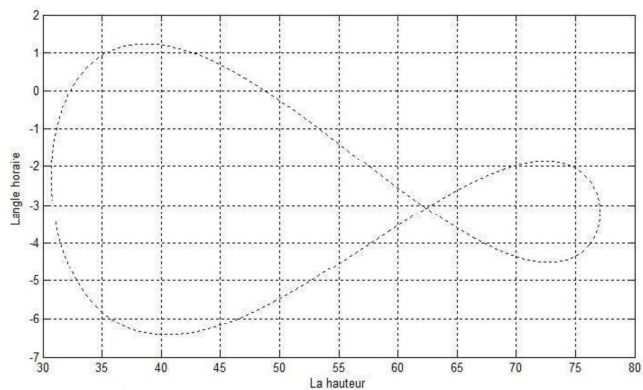
Panel C: this panel contains the time coordinates such as declination, height, time angle, azimuth as noted in FIGURE2;



Panel D: this panel calculate direct extraterrestrial normal radiation I_{ext} as illustrated in FIGURE2;



Panel E: this panel is used to select curves (ex: Analm, the time equation, the declination...etc.) as illustrated in FIGURE2;



Panel F: Custom area for displaying curves as illustrated in FIGURE2.

The second graphical interface is divided into five panels; G, H, I, J and K as noted:

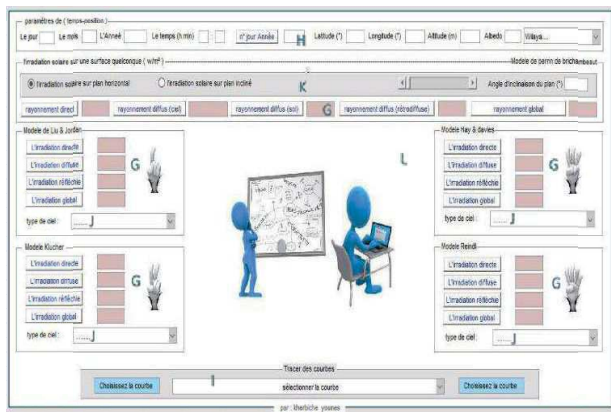
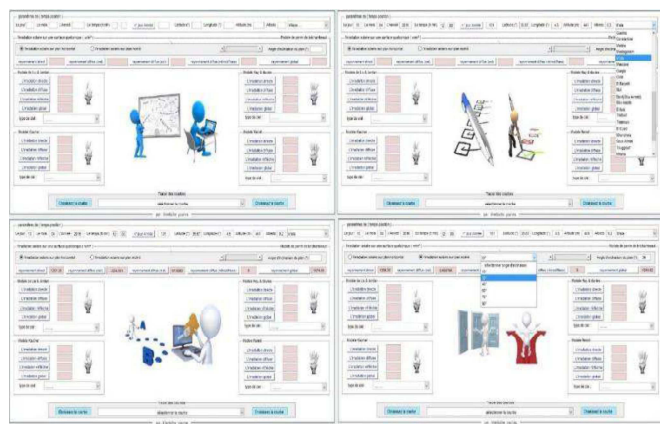
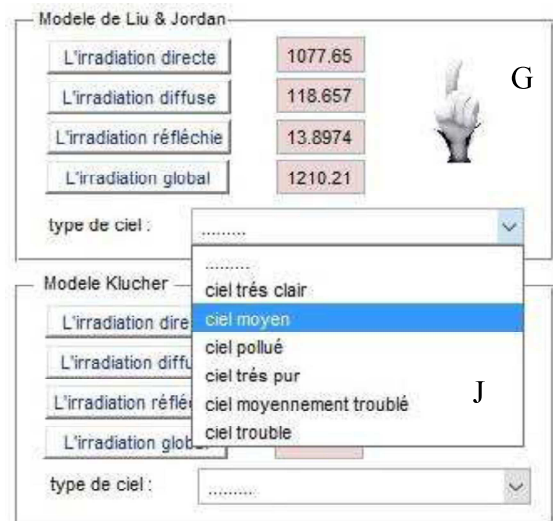


Fig. 3 Interface allowing the daily global, diffuse irradiations and direct timetables, l irradiation measured on any surface and the type of sky and use of several model.



Panel H: this panels contains time-position parameters such as the day, the month, the year, day number, the time ,

latitude, longitude, elevation and albedo for the chosen location as noted in FIGURE3.;



Panel G: this panel covers solar radiations (direct, diffuse, reflected and global) for each models of the five cited models (Perrin de Brichambaut model, Liu & Jordan model, Klucher model, Hay–Davies model and Reindl model) as shown in FIGURE3.

Panel J: this panel contains the sky type as noted in FIGURE3;



Panel I: this panel is used for selecting curves of solar irradiation as illustrated in FIGURE3;



Panel K: this panel contains the plan type; horizontal or inclined with the inclination angle value as illustrated in FIGURE3;

Panel L: Custom area for displaying curves as illustrated in FIGURE3.

IV. RESULTS AND DISCUSSION

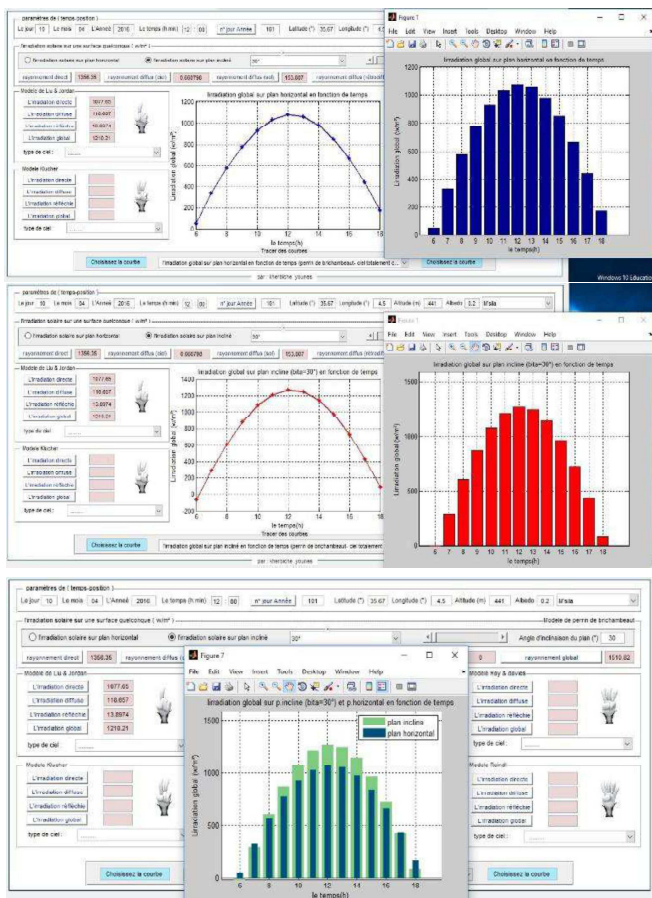


Fig. 4 Graphical interface giving: the solar radiation for the model of “Lui & Jordan” and the type of sky and horizontal surface.

In order to validate our calculation software, a comparison is made between the global solar radiations on a horizontal surface calculated according to Lui and Jordan model and the values noted by M'sila meteorological station for a few days. Four illustrative examples are shown in FIGURE 5 (the days 17/01/2016, 15/05/2016, 09/06/2016) and 11/12/2016).

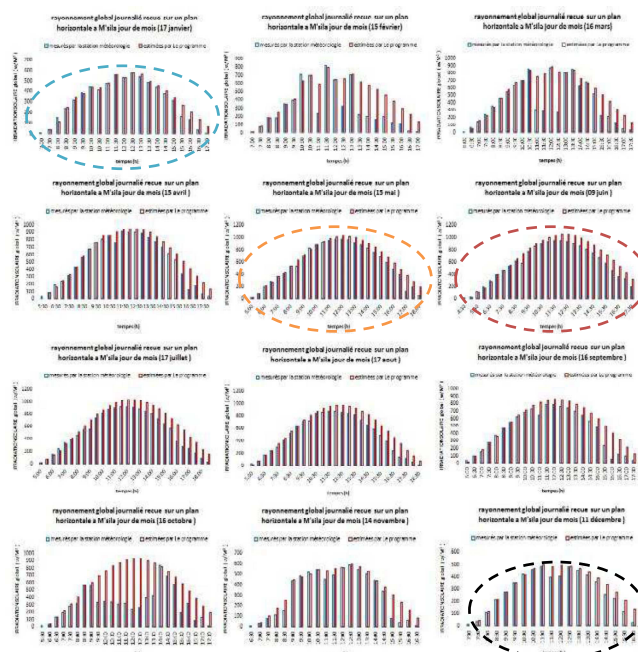
It is found that all the curves of global solar radiation measured and calculated by the model of Lui and Jordan for the region of M'sila follows the same shape of bell shape. They reach their maximum values between 11:30 and 12:30. As an example for 17/01/2016, the maximum value is recorded at 12: 30 with 573 W/m² for the measured value and 575,09 W/m² for the calculated value. It

is also noted that this value varies from one month to the other, which is illustrated in FIGURE 5. The highest values are reached during the summer and lowest values during the winter.

It is also found that Lui and Jordan model is in good agreement with the measured values as illustrated in FIG. 5. It has a coefficient of determination of 0.967 for the 17/01/2016, 0.965 for the 15/05/2016, 0.974 for the 09/06/2016 and 0.942 for the 11/12/2016.

It is noted that the solar radiation values calculated by the Lui and Jordan model are higher than those measured at the meteorological station of M'sila. This difference is usually visible at the end of the day and in the afternoon on 9/06/2016 and 11/12/2016. It is due to the sky state, which is not taken into account in the model of Lui and Jordan, which is taken in the clear sky. This confirms that the Lui and Jordan model is a very good model for estimating global solar radiation on a horizontal surface in the M'sila region.

Therefore, it can be said that our software gives good results in the estimation of global solar radiation on a horizontal surface in M'sila region. We propose to check it for other models (Klucher model, Hay-Davies model, Reindl model and Brichambaut model), to take account the sky condition and to apply it for other regions, which is the subject of another work to confirm its validation.



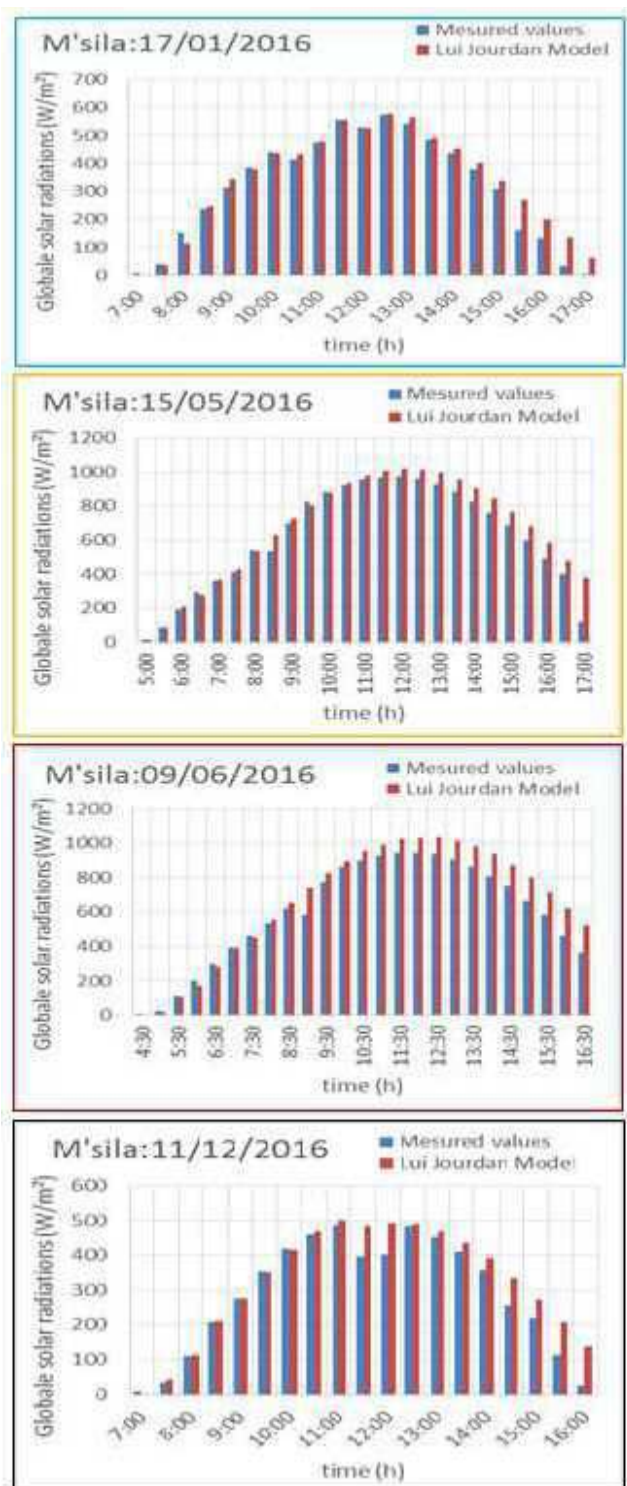


Fig. 5 Compare the values estimated by the theoretical models (program) and the values measured by the metrological station in the region of m'sila (the typical days).

V. CONCLUSIONS

In this work, a solar calculation software was developed using MATLAB. This software can

calculate the solar radiation components (diffuse, direct, and comprehensive refléchi) using five models; Lui and Jordan model, Klucher model, Hay-Davies model, Reindl model and Blichambaut model. The validation of our software was carried out by comparing global solar radiation according to Lui and Jordan model and the global solar radiation recorded by the meteorological station of M'sila region. The results show a good agreement between them which confirms the validation of our calculation software.

REFERENCES

- [1] Dorota Chwieduk D.Sc., Ph.D. M.Sc., Solar Energy in Buildings. Optimizing Thermal Balance for Efficient Heating and Cooling- Elsevier Inc., Academic Press, London (2014).
- [2] T. Stoffel, "Terms and Definitions," Solar Energy Forecasting and Resource Assessment, edited by J. Kleissl, 2013, pp. 12–15.
- [3] G. N. Tiwari, Arvind Tiwari, Shyam, Handbook of Solar Energy_ Theory, Analysis and Applications-Springer Singapore (2016).
- [4] M. Despotovic, V.Nedic, Comparison of optimum tilt angles of solar collectors determined at yearly, seasonal and monthly levels, Energy Conversion and Management 97, 123-124 (2015).
- [5] K. Kerkouche I, F. Cherfa, A. Hadj Arab, S. Bouchakour, K. Abdeladim et K. Bergheul, Evaluation de l'irradiation solaire globale sur une surface inclinée selon différents modèles pour le site de Bouzaréah, Revue des Energies Renouvelables Vol. 16 N°2 (2013) 269 – 284.
- [6] K.N. Shukla, Saroj Rangnekar, K. Sudhakar, Comparative study of isotropic and anisotropic sky models to estimate solar radiation incident on tilted surface: A case study for Bhopal, India, Energy Reports 1 (2015) 96–103.
- [7] P.G. Loutzenhiser, H. Manz , C. Felsmann , P.A. Strachan ,T. Frank a, G.M. Maxwell, Empirical validation of models to compute solar irradiance on inclined surfaces for building energy simulation, Solar Energy 81, 254–267 (2007).
- [8] Ali Mohammad Nooriana, Isaac Moradib, Gholam Ali Kamalia, Evaluation of 12 models to estimate hourly diffuse irradiation on inclined surfaces, Renewable Energy 33 (2008) 1406–1412.
- [9] Mokhtar Ghodbane, Boussad Boumeddane, Estimating solar radiation according to semi empirical approach of PERRIN DE BRICHAMBAUT: application on several areas with different climate in Algeria, International Journal of Energetica (IJECA), Volume 1. Issue 1. 2016.

A new approach of Sliding mode observer for sensorless control applied in Induction machine*

Mohammed Zakaria Kari¹, Abdelkader Mechernene¹, Sidi Mohammed Meliani²

¹ Laboratoire d'Automatique de Tlemcen LAT, Université de Tlemcen, Algeria.

² MELT, Manufacturing Engineering Laboratory of Tlemcen, , Université de Tlemcen, Algeria

Abstract—In this paper, a new idea is proposed to the Sliding Mode Observer for the flux and speed applied to the induction motor and it is also controlled by the Sliding Modes as a function of the orientation of the rotor flux. The error between the measurements of the currents and their estimates converges to zero in finite time, which guarantees the accuracy of the observed flux. The rotor speed and the time constant of the rotor are determined by the estimated stator currents and the rotor flux. The speed estimate is used as feedback to control the rotation of the speed of the induction machine. The control strategy is based on the Sliding Mode approach, while the Lyapunov method is introduced to prove the stability of the system. The results of the numerical simulations verify the validity of the proposed strategy and prove the robustness of the controller despite the disturbances of the load torque and the uncertainties of the parameters. Therefore, this strategy can find practical use in many applications for induction motor drive systems over a wide speed range without the use of mechanical sensor.

Index Terms—Induction motor drive, Field oriented control, Sliding Mode Control, Sensorless control, Non-linear control, Lyapunov function, parameters robustness.

I. INTRODUCTION

THE induction motor is the more used in applications of the variable speed. The main advantages of the speed Sensorless control are the reduction of the costs, the size of the system, and its maintenance, as well as the increase in the reliability of the overall system. The main reasons of its success are its simplicity of conception, its reliability and the absence of collector. But his mathematical model is complex, multivariable, with strong non-linearities, and varying parameters. In some applications, these sensors are often difficult to install and they are sensitive to noise, mechanical vibrations and electromagnetic disturbances [1]. The estimation techniques use estimators or state observers to reconstruct the velocity from exclusively stator currents and voltages, which can be measured. The estimators are designed by solving the equations of the dynamic model, and their structures have no feedback. Therefore, they are open-loop reconstructs. The implementation of their algorithms being simple, whereas their dynamic performances are limited. State observers reconstruct the state variables of an observable system from measurable inputs and outputs. They generally provide a good dynamics and accurate estimation, but their low parametric robustness is still their major disadvantage [2]. Several studies have shown that when the induction machine is associated with a Sensorless control, the quality of estimation of speed is due to some challenges appearing at low speed [3] - [4]. In

fact, if the rotor speed is measured, the performance of the machine is ensured. In fact, the observability space generated by the measured quantities and their derivatives correspond to the rank of the system. The mathematical model of the motor is then locally observable. It is therefore possible to reconstruct the state variable, such as electrical (currents and flux) and mechanical (speed, position, and load torque). When the speed measurement is not allowed, the observability of the model cannot be established if the mechanical velocity is constant and the pulsation of the stator voltages and currents is zero (Necessary condition for loss of observability) [5]. This is due to a low speed operating. On the other hand, at low speed the waking induction phenomena, the electromotive forces decrease and become too weak. The flux obtained by integration is then unusable, so the speed information disappears. In addition, low speed operation means that the inverter generates low voltages (a few tens of Volts), which are then greatly disturbed by switching faults (dead times) and by voltage drops at the terminals of the switches static of the converter [6].

Finally, the dependence on parametric variations can greatly reduce the performance level and considerably affect the convergence and accuracy of the estimate. In the scientific literature, several techniques have been proposed to solve the problems of Sensorless control of induction motor. They are commonly classified in two categories: Methods with mathematical models and Methods without a model. Thus, the methods based on the model of induction motor most often use the MRAS Estimators exploiting the fluxes, the currents or the powers [6] -[7] -[8], the Adaptive Observers [9] -[10], the High-Gain Observers [11], the Sliding Modes Observers [12] or the Stochastic Observers as the Kalman Filter [13]. These techniques offer interesting performance, but they show a few limits at low speed and mostly when the parameters of the motor vary [14]. The main works based on the methods without model involve the artificial intelligence techniques, such as Artificial Neural Network Estimators and Hybrid Fuzzy Logic Estimators [15]- [16]. The Sliding Modes approach is like one of techniques simplest to implement for controlling non-linear systems with an imprecise model[17]. This control has many advantages, such as an excellent trajectory tracking, disturbance rejection and robustness despite modelling uncertainties.

This work is dedicated to the new design of the flux and speed Sliding Mode Observer. A flux surface is added to the Sliding

Mode for better control of the induction machine in low-speed (the major problem of the Sensorless control). The objective is to obtain an accurate estimate with better convergence and robustness against the load torque disturbances and the parameter variations. The error between the actual and estimated currents must converge to zero in finite time and thus guarantee the accuracy of the observed flux. The rotor speed and rotor time constant are determined by the estimated stator currents and rotor flux. Once the flux convergence is guaranteed, the rotor speed and its time constant are estimated and converge to their actual values. Finally, the estimated quantities are used for the speed regulation of IM.

This paper is organized as follows. In section 2, the mathematical models of the induction motor are presented, first in the reference frame rotating at the synchronous speed, and then in the stationary stator reference frame. In Section 3, the principle of rotor flux orientation is presented, Sliding Modes theory and its application to induction motor control are also developed. Section 4 describes the design of the conventional Sliding Mode Observer and the flux and speed observer proposed in this work. In Section 5, some simulation results showing the performances of the proposed observer, associated with motor control are presented and discussed. Finally, Section 6 provides some comments and a conclusion.

II. INDUCTION MOTOR MODELLING

A. Dynamical Model of IM in (d-q) Reference Frame

In a similar way, the mathematical model of the induction motor, expressed in the (α, β) stationary stator reference frame is described by:

$$\begin{cases} \frac{di_{s\alpha}}{dt} = a_1 i_{s\alpha} + a_2 \psi_{r\alpha} - a_3 \omega_r \cdot \psi_{r\beta} + a_6 v_{s\alpha} \\ \frac{di_{s\beta}}{dt} = a_1 i_{s\beta} + a_3 \omega_r \cdot \psi_{r\alpha} + a_2 \psi_{r\beta} + a_6 v_{s\beta} \\ \frac{d\psi_{r\alpha}}{dt} = a_4 i_{s\alpha} + a_5 \psi_{r\alpha} - \omega_r \cdot \psi_{r\beta} \\ \frac{d\psi_{r\beta}}{dt} = a_4 i_{s\beta} + \omega_r \cdot \psi_{r\alpha} + a_5 \psi_{r\beta} \end{cases} \quad (1)$$

where

$$a_1 = -\left(\frac{1}{\sigma \cdot T_s} + \frac{(1-\sigma)}{\sigma \cdot T_r}\right); a_2 = \frac{L_m}{\sigma \cdot L_s \cdot L_r} \cdot \frac{1}{T_r}$$

$$a_3 = -\frac{L_m}{\sigma \cdot L_s \cdot L_r}; a_4 = \frac{L_m}{T_r}; a_5 = -\frac{1}{T_r}$$

$$a_6 = \frac{1}{\sigma \cdot L_s}; \sigma = 1 - \frac{L_m^2}{L_s \cdot L_r}; a_7 = \frac{3}{2} \cdot \frac{n_p^2 \cdot L_m}{J \cdot L_r}$$

The electromagnetic torque is given by the following expression:

$$T_e = \frac{3}{2} \cdot \frac{n_p \cdot L_m}{L_r} \cdot (\psi_{rd} \cdot i_{sq} - \psi_{rq} \cdot i_{sd}) \quad (2)$$

III. SLIDING MODE CONTROL FOR IM

A. Rotor flux orientation

The idea of the vectorial control is to control the stator current in a reference mark $(d-q)$ turning at the speed of synchronism by fixing the axis d on the vector of flux, and he will directly controlled by the component d of the stator current and the couple by the component q . All the strategy of control depends on the good chock of the reference mark $(d-q)$, and thus of the knowledge of the angle of Park.

$$\psi_{rq} = 0 \implies \psi_r = \psi_{rd} \quad (3)$$

-Either by direct measurement of a magnitude enabling direct calculation of the angle by the Hall effect sensors.

-The estimation of the park angle of the oriented model.

B. Sliding Mode Control

The design of the Sliding Mode can be divided into three stages: the choice of the Sliding surface, the establishment of the convergence condition and the definition of the control law. The surface is adjusted according to the error of the variable to be regulated (x) .

$$S(x) = \left(\frac{d}{dt} + \lambda_x\right)^{r-1} \cdot e_x \quad (4)$$

with $e(x) = (x^* - x)$; is the error of the variable to be regulated λ_x : is a positive constant and r : is the relative degree, equal to the necessary number of the derivative to to make appear the control inputs.

C. Sliding Mode Control based IM

The variables to be adjusted are the speed ω_r and the rotor flux ψ_r . The relative degree $r = 2$, thus two surfaces are necessary to obtain the expression of control variant v_{sd} and v_{sq} . The convergence is to assure by a Lyapunov function given by:

$$V(x) = \frac{1}{2} \cdot S^2(x) \quad (5)$$

And its time derivative as:

$$V(x) = \dot{S}(x) \cdot S(x) \quad (6)$$

So to ensure the attractiveness and invariance of the surface $S(x)$, the following condition must be satisfied:

$$\dot{S}(x) \cdot S(x) < 0 \quad (7)$$

Considering the vector $x = [\omega_r \ \psi_r]$:

$$\begin{cases} e(\omega_r) = \omega_r^* - \omega_r \\ e(\psi_r) = \psi_r^* - \psi_r \end{cases} \quad (8)$$

The two surfaces are defined as:

$$\begin{cases} S(\omega_r) = \left(\frac{d}{dt} + \lambda_{\omega_r}\right) \cdot e_{\omega_r} \\ S(\psi_r) = \left(\frac{d}{dt} + \lambda_{\psi_r}\right) \cdot e_{\psi_r} \end{cases} \quad (9)$$

where λ_{ω_r} and λ_{ψ_r} are positive constants. The derivatives of the surfaces are deduced as:

$$\begin{cases} \dot{S}(\omega_r) = \ddot{\omega}_r^* + \lambda_{\omega_r} \dot{\omega}_r^* + \frac{n_p}{J} T_l + (\frac{B}{J} - \lambda_{\omega_r}) \dot{\omega}_r \\ \quad - a_7 \dot{i}_{qs} (a_4 \dot{i}_{ds} + a_5 \psi_r) - a_7 \psi_r (\omega_s \dot{i}_{ds} \\ \quad + a_1 \dot{i}_{qs} + a_3 \omega_r \cdot \psi_r + a_6 v_{qs}) \\ \dot{S}(\psi_r) = (\dot{\psi}_r^* + \lambda_{\psi_r} \dot{\psi}_r^*) - (a_5 + \lambda_{\psi_r}) \dot{\psi}_r \\ \quad - a_4 [a_1 \dot{i}_{sd} + \omega_r \dot{i}_{sq} + a_3 a_5 \psi_r + a_6 v_{sd}] \end{cases} \quad (10)$$

$$\begin{cases} \dot{S}(\omega_r) = \ddot{\omega}_r^* + \lambda_{\omega_r} \dot{\omega}_r^* + \frac{n_p}{J} T_l + (\frac{B}{J} - \lambda_{\omega_r}) \dot{\omega}_r \\ \quad - a_7 \dot{i}_{sq} (a_4 \dot{i}_{sd} + a_5 \psi_r) - a_7 \psi_r (-\omega_s \dot{i}_{sd} \\ \quad + a_1 \dot{i}_{sq} + a_3 \omega_r \cdot \psi_r + a_6 v_{sq}) \\ \dot{S}(\psi_r) = \dot{\psi}_r^* + \lambda_{\psi_r} \dot{\psi}_r^* - (a_5 + \lambda_{\psi_r}) \dot{\psi}_r \\ \quad - a_4 [a_1 \dot{i}_{sd} + \omega_r \dot{i}_{sq} + a_3 a_5 \psi_r + a_6 v_{sd}] \end{cases} \quad (11)$$

During the Sliding Mode, the derivative is equal to zero, hence the equivalent commands $v_{sd,eq}$ and $v_{sq,eq}$ can be written as follow:

$$\begin{cases} v_{sd,eq} = \frac{1}{a_4 a_6} [\dot{\psi}_r^* + \lambda_{\psi_r} \dot{\psi}_r^* - (a_5 + \lambda_{\psi_r}) \dot{\psi}_r \\ \quad - a_4 (a_1 \dot{i}_{sd} + \omega_r \dot{i}_{sq} + a_3 a_5 \psi_r)] \\ v_{sq,eq} = \frac{1}{a_7 a_6 \psi_r} [\dot{\omega}_r^* + \lambda_{\omega_r} \dot{\omega}_r^* + \frac{n_p}{J} T_l \\ \quad + (\frac{B}{J} - \lambda_{\omega_r}) \dot{\omega}_r - a_7 \dot{i}_{sq} (a_4 \dot{i}_{sd} + a_5 \psi_r) \\ \quad - a_7 \psi_r (-\omega_s \dot{i}_{sd} + a_1 \dot{i}_{sq} + a_3 \omega_r \cdot \psi_r)] \end{cases} \quad (12)$$

From the command

$$v = v_n + v_{eq} \quad (13)$$

To check the condition of attractiveness, it is assumed that:

$$\begin{cases} v_{dsn} = -K_d \cdot \text{sign}(S\psi_r) \\ v_{qsn} = -K_q \cdot \text{sign}(S\omega_r) \end{cases} \quad (14)$$

where $K_d > 0$ and $K_q > 0$ are the control gains.

IV. SLIDING MODE OBSERVER

A. Conventional Sliding Mode Observer

The Sliding Mode Observer consists in forcing, using discontinuous functions, the dynamics of the errors in estimation of a nonlinear system of n order having p outputs to converge on a variety of orders ($n-p$) known as Sliding surface. The attractiveness and the invariance of the Sliding surface are ensured by conditions called the Sliding conditions. The dynamics of the Sliding surface are calculated by the method of the equivalent control [12]. Thus, for the nonlinear systems. A structure of observer by Sliding Mode is written:

$$\begin{cases} \frac{d\hat{x}}{dt} = f(\hat{x}, U) - K \cdot \text{sign}(\hat{y} - y) \\ \hat{y} = h(\hat{x}) \end{cases} \quad (15)$$

B. Proposed Sliding Mode Observer

The proposed algorithm guarantees a good estimation of the speed and the rotor constant of the time and a very great robustness especially at low speed. The estimation of the rotational speed and the time constant of the rotor are ensured by the convergence of the currents and the fluxes observes. Ensuring the convergence of the current observer. Then, it is used in the flux observation to produce fluxes along the α and β axes. Once the flux values are found, the equivalent

control is produced by using a low pass filter, then the rotor speed and rotor time constant are estimated by using observed fluxes. For the synthesis of observation, the model of the IM in the reference mark (α, β) is used for the synthesis of the observation, to make the model simpler and for c .

Considering that $a_2 = k \cdot \frac{1}{T_r}$ with $k = \frac{L_m}{\sigma \cdot L_s \cdot L_r}$

$$\begin{bmatrix} \frac{di_{s\alpha}}{dt} \\ \frac{di_{s\beta}}{dt} \end{bmatrix} = k \cdot \begin{bmatrix} \frac{1}{T_r} & \omega_r \\ -\omega_r & \frac{1}{T_r} \end{bmatrix} \begin{bmatrix} \psi_{r\alpha} \\ \psi_{r\beta} \end{bmatrix} - a_1 \cdot \begin{bmatrix} i_{s\alpha} \\ i_{s\beta} \end{bmatrix} + a_6 \cdot \begin{bmatrix} v_{s\alpha} \\ v_{s\beta} \end{bmatrix} \quad (16)$$

$$\begin{bmatrix} \frac{d\psi_{r\alpha}}{dt} \\ \frac{d\psi_{r\beta}}{dt} \end{bmatrix} = \begin{bmatrix} -\frac{1}{T_r} & -\omega_r \\ \omega_r & -\frac{1}{T_r} \end{bmatrix} \begin{bmatrix} \psi_{r\alpha} \\ \psi_{r\beta} \end{bmatrix} + a_4 \begin{bmatrix} i_{s\alpha} \\ i_{s\beta} \end{bmatrix} \quad (17)$$

$$\begin{bmatrix} \frac{d\hat{i}_{s\alpha}}{dt} \\ \frac{d\hat{i}_{s\beta}}{dt} \end{bmatrix} = k \cdot \begin{bmatrix} \phi_{i_{s\alpha}} \\ \phi_{i_{s\beta}} \end{bmatrix} - a_1 \cdot \begin{bmatrix} \hat{i}_{s\alpha} \\ \hat{i}_{s\beta} \end{bmatrix} + a_6 \cdot \begin{bmatrix} v_{s\alpha} \\ v_{s\beta} \end{bmatrix} \quad (18)$$

$$\begin{bmatrix} \frac{d\hat{\psi}_{r\alpha}}{dt} \\ \frac{d\hat{\psi}_{r\beta}}{dt} \end{bmatrix} = \begin{bmatrix} \phi_{\psi_{r\alpha}} \\ \phi_{\psi_{r\beta}} \end{bmatrix} + a_4 \begin{bmatrix} \hat{i}_{s\alpha} \\ \hat{i}_{s\beta} \end{bmatrix} \quad (19)$$

with

$$\begin{aligned} \phi_{i_{s\alpha}} &= h_{sd} \cdot \text{sign}(S_{i_{s\alpha}}); & \phi_{i_{s\beta}} &= h_{sq} \cdot \text{sign}(S_{i_{s\beta}}); \\ \phi_{\psi_{r\alpha}} &= H_{rd} \cdot \text{sign}(S_{\psi_{r\alpha}}); & \phi_{\psi_{r\beta}} &= H_{rq} \cdot \text{sign}(S_{\psi_{r\beta}}); \end{aligned}$$

Where $[h_{sd}, h_{sq}, H_{rd}, H_{rq}]$ are control gains. The convergence of the stator currents estimated $\hat{i}_{s\alpha}$ and $\hat{i}_{s\beta}$ to The actual currents $i_{s\alpha}$ and $i_{s\beta}$ assure the estimation of rotor flux $\hat{\psi}_{r\alpha}$ and $\hat{\psi}_{r\beta}$ and from the esteemed rotor flux can esteem the rotor speed $\hat{\omega}_r$. And \hat{T}_r the rotor constant of time. $\hat{i}_{s\alpha}, \hat{i}_{s\beta}$ and $\hat{\psi}_{r\alpha}, \hat{\psi}_{r\beta}$ are used to generate the Sliding Mode. Furthermore, the surfaces of Sliding Mode are selected in this way:

$$\begin{aligned} S_{i_{s\alpha}} &= \hat{i}_{s\alpha} - i_{s\alpha}; & S_{i_{s\beta}} &= \hat{i}_{s\beta} - i_{s\beta}; \\ S_{\psi_{r\alpha}} &= \hat{\psi}_{r\alpha} - \psi_{r\alpha}; & S_{\psi_{r\beta}} &= \hat{\psi}_{r\beta} - \psi_{r\beta}; \end{aligned}$$

and the Sliding Mode surface is defined as:

$$S_n = [S_{i_{s\alpha}} \ S_{i_{s\beta}} \ S_{\psi_{r\alpha}} \ S_{\psi_{r\beta}}]^T$$

By selecting The gains $[h_{sd}, h_{sq}, H_{rd}, H_{rq}]$ of the attractive commands and they are larger than the errors to ensure the attractiveness of the observed signal around the reference and are found by the condition of existence, Sliding Mode ($S_n = 0$) will occur. To solve the $\frac{dS_n}{dt} = 0$ for discontinuous control, it gives the equivalent continuous command.

However, the equivalent control depends on parameter machine and to be difficult to implement. Consequently, it is reasonable to suppose that an equivalent control is close to the slow component of the real control, which can be diverted by filtering the high Frequency using a low-pass filter. The structure of the low-pass filter is implemented:

$$\phi_{\psi_{r\alpha}}^{eq} = \frac{1}{\mu \cdot s + 1} \quad (20)$$

where μ is the time-constant of the filter and it should be sufficiently weak for Component slow without distortion, but enough large to eliminate the component with high frequency. The exit of the low-pass filter will be equal Controls equivalent on the slip surface [18]. The concept of equivalent control supposes flux observed $\hat{\psi}_{r\alpha}$ and $\hat{\psi}_{r\beta}$ equal to real flux $\psi_{r\alpha}, \psi_{r\beta}$ and in the regime permanent we can written:

$$\begin{bmatrix} \phi_{\psi_{r\alpha}}^{eq} \\ \phi_{\psi_{r\beta}}^{eq} \end{bmatrix} = \begin{bmatrix} -\frac{\hat{1}}{T_r} & -\hat{\omega}_r \\ \hat{\omega}_r & -\frac{\hat{1}}{T_r} \end{bmatrix} \begin{bmatrix} \hat{\psi}_{r\alpha} \\ \hat{\psi}_{r\beta} \end{bmatrix} \quad (21)$$

$$\begin{bmatrix} \frac{d\hat{\psi}_{r\alpha}}{dt} \\ \frac{d\hat{\psi}_{r\beta}}{dt} \end{bmatrix} = \begin{bmatrix} \phi_{\psi_{r\alpha}}^{eq} \\ \phi_{\psi_{r\beta}}^{eq} \end{bmatrix} + \frac{L_m}{\hat{T}_r} \cdot \begin{bmatrix} \hat{i}_{s\alpha} \\ \hat{i}_{s\beta} \end{bmatrix} \quad (22)$$

$$\begin{bmatrix} \phi_{\psi_{r\alpha}}^{eq} \\ \phi_{\psi_{r\beta}}^{eq} \end{bmatrix} = \begin{bmatrix} -\hat{\psi}_{r\alpha} & -\hat{\psi}_{r\beta} \\ \hat{\psi}_{r\beta} & -\hat{\psi}_{r\alpha} \end{bmatrix} \begin{bmatrix} \frac{\hat{1}}{T_r} \\ \hat{\omega}_r \end{bmatrix} \quad (23)$$

$$\begin{bmatrix} \frac{\hat{1}}{T_r} \\ \hat{\omega}_r \end{bmatrix} = \frac{1}{\hat{\psi}_{r\alpha}^2 + \hat{\psi}_{r\beta}^2} \begin{bmatrix} -\hat{\psi}_{r\alpha} & -\hat{\psi}_{r\beta} \\ \hat{\psi}_{r\beta} & -\hat{\psi}_{r\alpha} \end{bmatrix} \begin{bmatrix} \phi_{\psi_{r\alpha}}^{eq} \\ \phi_{\psi_{r\beta}}^{eq} \end{bmatrix} \quad (24)$$

From the above equation, the speed of the estimated rotor is equal to:

$$\hat{\omega}_r = \frac{1}{\hat{\psi}_{r\alpha}^2 + \hat{\psi}_{r\beta}^2} \cdot (\hat{\psi}_{r\beta} \cdot \phi_{\psi_{r\alpha}}^{eq} - \hat{\psi}_{r\alpha} \cdot \phi_{\psi_{r\beta}}^{eq}) \quad (25)$$

In addition, the constant of rotor time is equal to:

$$\frac{\hat{1}}{T_r} = \frac{1}{\hat{\psi}_{r\alpha}^2 + \hat{\psi}_{r\beta}^2} \cdot (-\hat{\psi}_{r\alpha} \cdot \phi_{\psi_{r\alpha}}^{eq} - \hat{\psi}_{r\beta} \cdot \phi_{\psi_{r\beta}}^{eq}) \quad (26)$$

V. SIMULATION RESULTS AND DISCUSSION

To evaluate the performance of the proposed structure, the implementation in the software MATLAB/SIMULINK environment has been considered. The computation numerical method adopted is based on the Runge-Kutta algorithm of order 4 with fixed step.

The parameters of both observer and controller are set in order to fulfil some objectives, such as convergence time and limitation of chattering.

This benchmark was chosen to show the performance and robustness of the proposed observer. These parameters are listed in Tables I, II .

TABLE I
 GAINS OF THE SLIDING MODE CONTROL FOR IM

The gains of the command	λ_{ω_r}	λ_{ψ_r}	K_d	K_q
	70	60	2050	4050

TABLE II
 GAINS OF THE SLIDING MODE OBSERVER FOR IM

The gains of the observer	h_{sd}	h_{sq}	H_{rd}	H_{rq}
	100	100	80	80

The figure below shows the structure of the global system, the Sliding Mode Control and the observer propose in this paper.

The benchmark is chosen to see the response and reaction

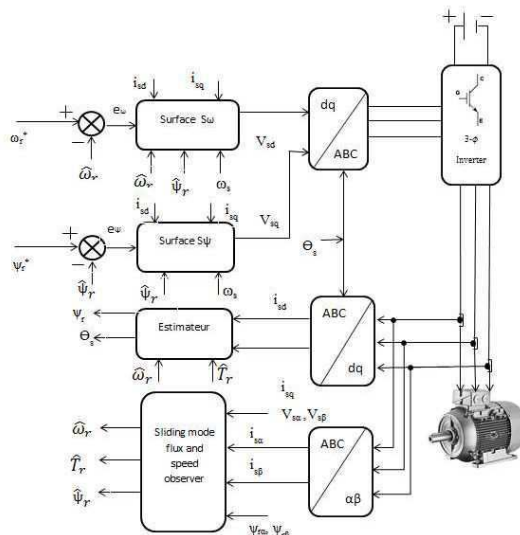


Fig. 1. Global block diagrams of the Sliding Mode Control and the proposed observer of the induction motor

of the system in different cases. The sensorless trajectories of the benchmark are such that: After that, the reference speed is increased to 150 rad/s (figure 2) and at 0.5 to 1.5 s a load torque of 5 N.m is applied. This first step makes it possible to test the robustness of the observer at high speed the estimated speed converge to the actual speed in this step of the benchmark. Then the speed decelerates to 0 rad/s and remains Constant until t = 3 s. This second step is defined to test the controller in low speed (very low frequency). the reference speed equal to zero and the figure 5 shows the phenomenon of unobservability The importance of this test is to see the reaction of the observer in this zone and to see its robustness. Finally, from t=5 to 5.8 s and at 0.5 to 1.5 s a load torque of 5 N.m is applied to test the reaction of the control and if the observer reacts well in this mode. All the estimated variables converge to their and disturbance rejection. Furthermore, all these figures present the best results obtained by the controller and the observer proposes in different modes. Finally, the tested robustness of our observer proposed against the parametric variation, especially the rotor resistance because it is the most influential parameter for the observation and this is conceived for all the specialists of the domain; with an application of restive torque (5N.m) over of duration well presided. Firstly, one made test for nominal values of R_r the reference speed is increased to 100 rad/s and at 1 to 0.7 s a load torque of 5 N.m is applied, then Introducing a 15% error on R_r to see the influence of this parameter for the system, then an error of 20% was introduced to see the reaction and the robustness of the observer, well results are obtained.

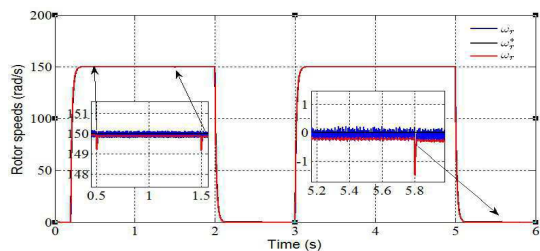


Fig. 2. Rotor speed [rad/s]

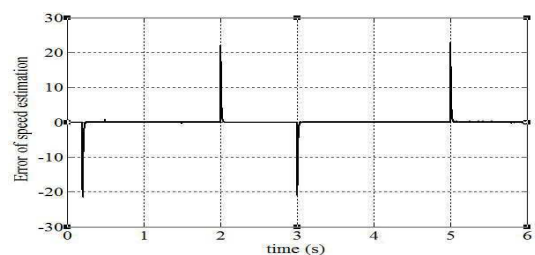


Fig. 3. Error between actual speed and estimated speed [rad/s],

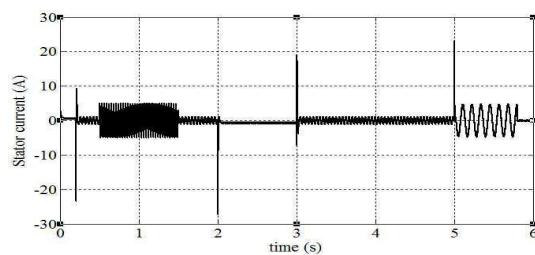


Fig. 4. Stator current of phase A [A]

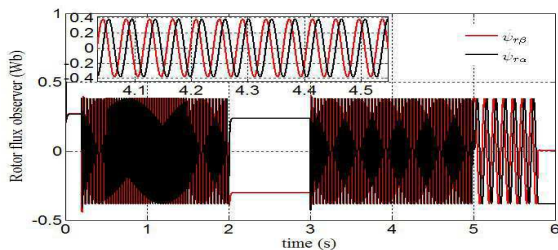


Fig. 5. Observed rotor flux [Wb]

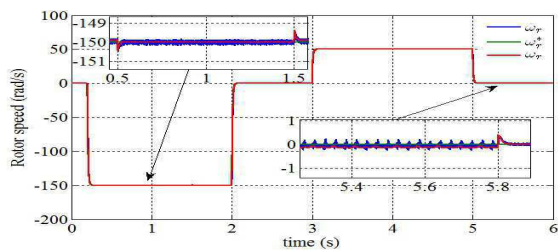


Fig. 6. Reversal rotor speed [rad/s]

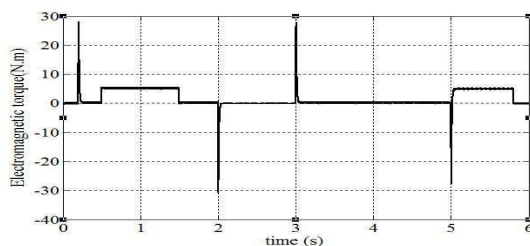


Fig. 7. Electromagnetic torque [N.m]

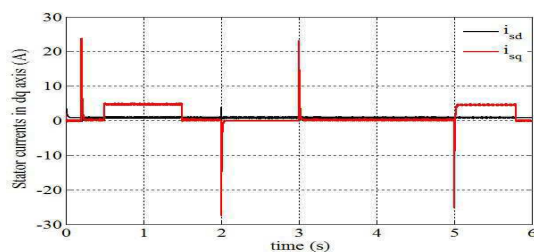


Fig. 8. Direct and quadrature stator current [A]

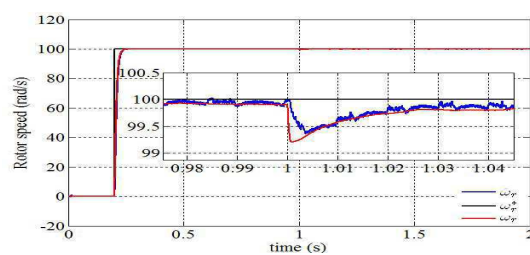


Fig. 9. Rotor speed [rad/s] for $R_r = R_{rn}$

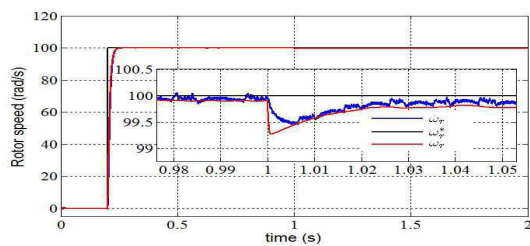


Fig. 10. Rotor speed [rad/s] for $R_r = 1.15 * R_{rn}$

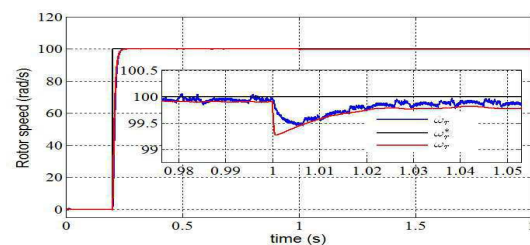


Fig. 11. Rotor speed [rad/s] for $R_r = 1.30 * R_{rn}$

VI. CONCLUDING REMARKS

this paper presents Sliding Mode Control based on the orientation of indirect flux for sensorless control of induction motor. A new structure Sliding-Mode current and flux observer has been proposed for speed, and rotor time constant estimations. The rotor time constant update algorithm will overcome the problem of rotor resistance variation; The proposed scheme is validated through simulation results. It is concluded from the results presented that the proposed scheme performs well and robust for both high and low speeds. It is also important that the new algorithm is robust to parameter changes and the load torques.

REFERENCES

- [1] C. Schauder "Adaptive Speed Identification for Vector Control of Induction Motors without Rotational Transducers," In IEEE Transactions on Industry Applications.1992; vol. 28(no.5): p. 1054-1061.
- [2] V. Vasic, SN.Vukosavic and E.Levi "A Stator Resistance Estimation Scheme for Speed Sensorless Rotor Flux Oriented Induction Motor Drives," In IEEE Transactions on Energy Conversion. 2003; vol. 18(no.4): p. 476-483.
- [3] J. Boker and S. Mathapati, "State of the Art of Induction Motor Control," IEEE International Conference on Electric Machines Drives. 2007 May 3-5; Antalya, Turkey; p. 1459-1464.
- [4] O. Boughazi, A. Boumedienne and O.aymen, "An Efficiency Backstepping Control without Speed Sensor applied to the Induction Motor Voltage Supplied," In Electrotehnica, Electronica, Automatica.2014; vol. 62(no. 1): p. 58-64.
- [5] M. Yahiaoui, A.Kechich and IK.Bouserhane, "Nonlinear Control in PMLSM Positioning by Estimated Load Force by MRAS Method," Electrotehnica, Electronica, Automatica 62.4 (2014): 93.
- [6] V.Vasic, SN.Vukosavic and E. Levi, "A Stator Resistance Estimation Scheme for Speed Sensorless Rotor Flux Oriented Induction Motor Drives,". In IEEE Transactions on Energy Conversion. 2003; vol. 18(no. 4): p. 476-483.
- [7] L. Jia, A. Thapa and K.A .Corzine, "Speed-Sensorless Drive For Induction Machines Using A Novel Hybrid Observer,". IEEE 978-1-5090-5366-2017 IEEE
- [8] H. Echeikh ,R. Trabelsi ,A.I.R. Alammari and M.F. Mimouni "Sensorless Indirect Rotor Flux Oriented Control of a Five-phase Induction Motor Based on Sliding Mode observer," 16th international conference on Sciences and Techniques of Automatic control computer engineering - STA'2015, Monastir, Tunisia, December 21-23, 2015.
- [9] A. Mechernene, M. Zerikat and M.Hachlef, "Fuzzy speed regulation for induction motor associated with field-oriented control," International Journal of Sciences and Techniques of Automatic Control and Computer Engineering, IJ-STA, vol 2, no.2, 2008, pp.804-817.
- [10] Boughazi, Othmane, Abdelmadjid Boumedienne, and Omari Aymen. "An Efficiency Backstepping Control without Speed Sensor applied to the Induction Motor Voltage Supplied," Electrotehnica, Electronica, Automatica 62.1 (2014): 58.
- [11] Y-S. Lai, "Machine modeling and universal controller for vector-controlled Induction Motor drives," IEEE Transactions on Energy Conversion, vol.18, no.5, 2003, pp.23-32.
- [12] Yahiaoui, Maamar, Abdelrahmene Kechich, and Ismail Khalil Bouserhane. " Nonlinear Control in PMLSM Positioning by Estimated Load Force by MRAS Method," Electrotehnica, Electronica, Automatica 62.4 (2014): 93.
- [13] C-C. Lee, "Fuzzy logic in control systems: fuzzy logic controller;". IEEE Transactions on Systems, Man, and Cybernetic, vol.20, no.2, Mar/Apr. 1990, pp.404-418.
- [14] B. Jaballah, "Observateurs robustes pour le diagnostic et la dynamique des véhicules,". Ph.D thesis, University of Paul Czanne Aix-Marseille III, 2011.
- [15] M. Zerikat, S. Chekroun and A. Mechernene, "Development and implementation of high-performance variable structure tracking for induction motor using fuzzy-logic controller," International Review of Electrical Engineering, vol.5 no.1, Jan/Feb. 2010, pp. 160-166.
- [16] M.Z. Kari, A. Mechernene, S.M. Meliani, "Sensorless drive systems for induction motors using a sliding mode observer," in Electrotehnica, Electronica, Automatica (EEA), 2018, vol. 66, nr. 2, pp. 61-68.
- [17] Li, Jia, Anup Thapa, and Keith A. Corzine. "Speed-sensorless drive for induction machines using a novel hybrid observer," Applied Power Electronics Conference and Exposition (APEC), 2017 IEEE. IEEE, 2017.
- [18] Feng, Yong, et al. "Speed Control of Induction Motor Servo Drives Using Terminal Sliding-Mode Controller," Advances in Variable Structure Systems and Sliding Mode Control Theory and Applications. Springer, Cham, 2018. 341-356.

Multivariable Predictive Control in the Form of State Space for a Chemical Multivariable System

Ibrahim El Khalil MEKKI^{#1}

[#] *département de maintenance en instrumentation, Institut de Maintenance et de Sécurité Industrielle (IMSI), Université d'Oran 2 Mohamed Ben Ahmed, Algérie*
¹ *ibrahim_kmekki@yahoo.fr*

Abstract— The main objective in this work is to control design predictive in the form of state space for a chemical multivariable system. Our contribution is to implement this command by introducing the matrix D (input / output coupling matrix) into the control algorithms. This application will allow us to illustrate and concretize the notion of prediction with a continuous binary distillation system having state matrices D different from zero. We simulate the system for different set point changes and disturbance rejection. The obtained results have shown the best of model predictive control performances.

Keywords— Distillation column, modelling, predictive control, chemical process, multivariable system

I. NOMENCLATURE

i : Stage number from bottom
 n : Number of stages, including reboiler
 N_{tot} : Number of stages, including condenser $n + 1$
 N_F : Feed stage
 x, y : Liquid and vapour composition
 y_D : Composition of light component in distillate
 x_B : Composition of light component in bottom
 z_F : Feed composition
 q_F : Fraction of liquid in feed
 M : Liquid holdup on stage i
 M_D, M_B : Liquid holdup in condenser and reboiler
 L : Reflux flow
 V : Boil up flow
 F : Feed flow rate
 D : Distillate product flow rate
 B : Bottom product flow rate
 α : Relative volatility
 τ_L : Time constant for liquid flow dynamics

II. INTRODUCTION

Distillation is a very old separation technology for separating liquid mixtures. It is today the most important technique in chemical process industry, accounting for 90 to 95% of separation operations.

According to [1], distillation is a process in which a liquid or vapour mixture of two or more substances is separated into its component fractions of desired purity, by the application and removal of heat.

Improved control of distillation can have a significant impact on reducing energy consumption, product purification.

The control of a distillation column can be difficult and that due to the feed flow rate, feed composition, from the cooling water etc.

Different strategies of control was proposed in the literatures for many years [2]: internal model control method (IMC) [3], ratio control [4,5], non-interacting control [4-6], fuzzy control [7], μ -synthesis method [8], linear-quadratic Gaussian with loop transfer recovery (LQG/LTR) method [9], Multivariable model predictive control [10], robust control [11] but the proportional Integral derivative (PID) controllers still represent the main of the controllers used in the industry.

There are many types of distillation columns based on different classifications such as: batch, continuous, binary, and multiproduct, extractive and azeotropic.

In this paper, the MPC (model predictive control) control is studied on continuous binary distillation column. However, due to the strong cross coupling and significant time delays inherent to the distillation column, the simultaneous control of overhead and bottom compositions using reflux flow and boil up flow as the control variables is still difficult.

III. MULTIVARIABLE PREDICTIVE CONTROL IN THE FORM OF STATE SPACE

The application of the MPC control law requires the presentation of the model we need to control [10].

A discretization in the form of space of state of the chemical multivariable system, it is written following form:

$$\begin{cases} x(k+1) = A \cdot x(k) + B \cdot u(k) \\ y(k) = C \cdot x(k) + D \cdot u(k) \end{cases} \quad (1)$$

Where:

$x(k) \in \mathfrak{R}^{n \times n}$: contains n variables model states,

$u(k) \in \mathfrak{R}^{m \times 1}$ $u(k) \in \mathfrak{R}^{m \times 1}$: m describes the model inputs,

$y(k) \in \mathfrak{R}^{p \times 1}$ $y(k) \in \mathfrak{R}^{p \times 1}$: p is the output vector.

$k \in \mathbb{N}$: characterizes the discrete time (by definition, if T_e is the sampling period setting the continuous computer controlled system. The matrices A, B and C are the state, input and output respectively. The all-numerical state space matrices in discrete time are given in equation 26 for a sampling period $T_e = 1$ min.

$$u(k) = u(k-1) + \Delta u(k) \quad (2)$$

In which, $\Delta u(k)$ is the control increment and the operator $\Delta = 1 - z^{-1}$ denotes the integral action which ensures static error elimination [10-12].

Taking account of the integral action equation (2), we replace $u(k)$ in the expression equation (1), for the extended condition (x_e) as follows:

$$\begin{cases} x_e(k+1) = A_e \cdot x_e(k) + B_e \cdot u(k) \\ y(k) = C_e \cdot x_e(k) + D_e \cdot u(k) \end{cases} \quad (3)$$

With the following notations:

$$x_e(k) = \begin{bmatrix} x(k) \\ u(k-1) \end{bmatrix}, \quad A_e = \begin{bmatrix} A & B \\ O_{m,n} & I_m \end{bmatrix} \quad (4)$$

$$B_e = \begin{bmatrix} B \\ I_m \end{bmatrix}, \quad C_e = [C \quad D], \quad D_e(k) = D$$

The state of the model is assumed to be available; the starting point for calculating the predicted output vector $\hat{y}(k+i)$ is given by the following expressions:

$$\hat{x}(k+l|k) = A \cdot x(k) + B \cdot u(k) \quad (5)$$

First, we calculate the control $u(k+i)$ iteratively from the equation (2). Predictions of future states from time k are then iteratively calculated [10]:

$$u(k+i) = u(k-1) + \sum_{l=0}^i \Delta u(k+l) \quad (6)$$

Predict the future states of the system, using equation (5) of the instant k to $k+i$ can be written as follows:

$$\hat{x}(k+l|k) = A^l \cdot x(k) + \sum_{j=0}^{l-1} A^{l-j-1} \cdot B \cdot u(k+j) \quad (7)$$

Finally, the future outputs of the system using equations (3), (7) of the instant k to $k+i$ can be written as follows:

$$\begin{aligned} \hat{y}(k+i) &= \hat{y}(k+l|k) = CA^i x(k) \\ &+ \sum_{j=0}^{i-1} CA^{i-j-1} \cdot B \left[u(k-1) + \sum_{l=0}^j \Delta u(k+l) \right] \end{aligned} \quad (8)$$

$u(k+j)$

The cost function J to minimize at each sampling period is to achieve the desired set-point $\hat{y}(k+i)$ following the reference trajectory $y_r(k+i)$ whose minimization provides the vector of future control $\Delta u(k+i)$ [10-13].

$$J = \sum_{i=N_1}^{N_2} \|\hat{y}(k+i) - y_r(k+i)\|_{Q_j(i)}^2 + \sum_{i=0}^{N_u-1} \|\Delta u(k+i)\|_{R_j(i)}^2 \quad (9)$$

Here N_1 and N_2 are respectively the minimum and maximum horizon of prediction; N_u is the control horizon, $\hat{y}(k+i)$ is described in equation (9), $y_r(k+i)$ denotes the set-point at time $k+i$.

The control signals $\Delta u(k)$ result from the minimization of the following quadratic objective function with the weighting matrices Q_j , R_j and the set point Y_r .

The criterion to be minimized can be written in the following matrix form:

$$J = \|Y(k) - Y_r(k)\|_{Q_j(i)}^2 + \|\Delta u(k)\|_{R_j(i)}^2 \quad (10)$$

The next step is to define the vector matrix form $\|\Delta u(k)\|$ predictions output by considering the expression (8) for $i = \overline{N_1, N_2}$ with the condition:

$$\Delta u(k+i) = 0 \text{ for } i \geq N_u$$

The predicted output vector becomes [10-13]:

$$\hat{y}(k) = Y(k|k) = \Psi \cdot x(k) + \Theta \cdot u(k-1) + \Theta_\Delta \cdot \Delta u(k)$$

In which:

$$\begin{aligned} Y(k) &= [\hat{y}(k+N_1|k), \dots, \hat{y}(k+N_2|k)]^T \\ Y_r(k) &= [y_r(k+N_1|k), \dots, y_r(k+N_2|k)]^T \\ \Delta u(k) &= [\Delta u(k), \dots, \Delta u(k+N_u-1)]^T \end{aligned} \quad (11)$$

$$\Psi = \begin{bmatrix} C \cdot A^{N_1} \\ \vdots \\ C \cdot A^{N_2} \end{bmatrix}, \quad \Theta = \begin{bmatrix} \sum_{i=0}^{N_1-1} A^i \\ \vdots \\ \sum_{i=0}^{N_2-1} A^i \end{bmatrix}, \quad \sum_i = C \sum_{i=0}^i A^i \cdot e^{i-j} \cdot B \quad (12)$$

Where the state estimate $\hat{x}_e(k)$ is obtained from the observer (see Fig. 1):

$$\begin{aligned} \hat{x}(k) &= A_e \cdot \hat{x}_e(k) + B_e \cdot \Delta u(k) + K(y(k) - C_e \cdot x_e(k)) \\ \hat{x}_e(k) &= (A_e - K \cdot C_e) \cdot \hat{x}_e(k) + (B_e - KD) \cdot \Delta u(k) + Ky \end{aligned} \quad (13)$$

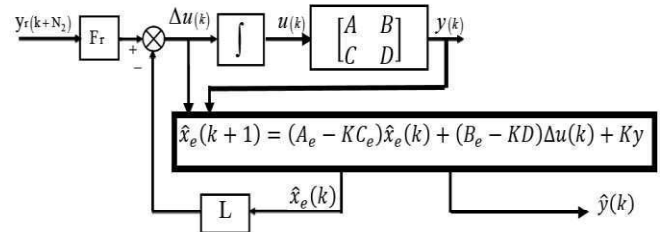


Fig. 1 The Control MPC in the form state based on the observer

The observer gain K is designed through a classical method of eigenvectors, arbitrarily placing the eigenvalues of $A_e - KC_e$ in a stable region, with the same control gain matrix L and a set-point pre-filter (F_r) different that it uses by [10-13]. As shown in Fig. 1, the control signal has the following form:

$$\Delta u(k) = F_r \cdot y_r(k+N_2) - L \cdot \hat{x}_e(k) \quad (14)$$

The matrices set-point pre-filter states are given in the form:

$$\begin{aligned} A_{F_r}(k) &\in \mathfrak{R}^{n \times (N_2 - N_1) \times p(N_2 - N_1)}, \quad B_{F_r}(k) \in \mathfrak{R}^{p \times (N_2 - N_1)}, \\ C_{F_r}(k) &\in \mathfrak{R}^{m \times p(N_2 - N_1)}, \quad D_{F_r}(k) \in \mathfrak{R}^{m \times p} \\ A_{F_r}(k) &= \begin{bmatrix} 0_{p(N_2 - N_1) \times p} & I_{p(N_2 - N_1)} \\ 0_p & 0_{p \times p(N_2 - N_1 - 1)} \end{bmatrix}, \quad B_{F_r}(k) = \begin{bmatrix} 0_{p(N_2 - N_1) \times p} \\ I_p \end{bmatrix} \\ C_{F_r}(k) &= \begin{bmatrix} 0_{p(N_2 - N_1 - 1) \times p} & I_{p(N_2 - N_1)} \\ 0_p & 0_{p \times p(N_2 - N_1 - 1)} \end{bmatrix}, \quad D_{F_r}(k) = \mu \cdot N_2 - N_1 + 1 \end{aligned} \quad (15)$$

IV. CHEMICAL MULTIVARIABLE SYSTEM: MODEL OF THE DISTILLATION COLUMN

The aim of the distillation column is to separate the feed F , which is a mixture of a light and a heavy component with composition z_F , into a distillate product D with composition y_D , which contains most of the light component, and a bottom product B with composition x_B , which contains most of the heavy component [15].

For this objective, the column contains a series of trays that are located along its height. The liquid in the columns flows through the trays from the top to the bottom, while the vapour in the column rises from the bottom to the top. The constant contact between the vapour and liquid leads to increase the concentration of the more volatile component in the vapour, while simultaneously increase the concentration of the less volatile component in the liquid.

The operation of the column requires that some of the bottom product is reboiled at a rate of V to ensure the continuity of the vapour flow and some of the distillate is refluxed to the top tray at a rate of L to ensure the continuity of the liquid flow.

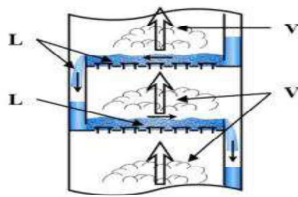


Fig. 2 A series of trays in a distillation column

In general, the distillation column is separated into three sections:

- Rectifying section: The more volatile component is removed through contacting the rising vapour with the down-flowing liquid.
- Feed section.
- Stripping section: the down-flowing liquid is stripped of the more volatile component by the rising vapour.

The nonlinear model equations are [15-16]:

$$\begin{cases} \frac{dM_i}{dt} = L_{i+1} - L_i + V_{i-1} - V_i \\ \frac{d(M_i x_i)}{dt} = L_{i+1} x_{i+1} - L_i x_i + V_{i-1} y_{i-1} - V_i y_i \end{cases} \quad (16)$$

- That yield to:

$$\frac{dx_i}{dt} = \frac{\left(\frac{d(M_i x_i)}{dt} - x_i \left(\frac{dM_i}{dt} \right) \right)}{M_i} \quad (17)$$

- While considering some auxiliary equations

$$\begin{cases} y_i = \frac{\alpha x_i}{(1+(\alpha-1)x_i)} \\ V_i = V_{i-1} \\ L_i = L_0 + (M_i + M_0) / \tau_L + \lambda(V_{i-1} - V_0) \end{cases} \quad (18)$$

- For the feed stage, we have: $i = nf$

$$\begin{cases} \frac{dM_{nf}}{dt} = L_{nf+1} - L_{nf} + V_{nf-1} - V_{nf} + F \\ \frac{d(M_{nf} x_{nf})}{dt} = L_{nf+1} x_{nf+1} - L_{nf} x_{nf} + V_{nf-1} y_{nf-1} - V_{nf} x_{nf} + F z_F \end{cases} \quad (19)$$

- For the total condenser, where: $i = NT = n+1$,

$$\begin{cases} (M_{N+1} = M_D, L_{N+1} = L_D, x_{N+1} = y_D) \\ \frac{dM_B}{dt} = V_n - L_{n+1} - D \\ \frac{d(M_D x_D)}{dt} = V_n y_n - y_D(L_D + D) \end{cases} \quad (20)$$

$M_D = C^{se}$, according to the previous auxiliary equations (18):

$$V_n = (L_D + D)$$

- For the reboiler at $i = 1, (M_1 = M_B, V_1 = V_B = V, x_1 = x_B)$

$$\begin{cases} \frac{dM_B}{dt} = L_2 - V_1 - B \\ \frac{d(M_B x_B)}{dt} = L_2 x_2 - V_1 y_1 - B x_B \end{cases} \quad (21)$$

$M_B = C^{se}$, according to equations (18): $L_2 = (L_1 + B)$

- For the second stage, we have: $i = 2$

$$\begin{cases} \frac{dM_2}{dt} = L_3 - L_2 + V_2 - V_1 \\ \frac{d(M_2 x_2)}{dt} = L_3 x_3 - L_2 x_2 + V_1 y_1 - V_2 x_2 \end{cases} \quad (22)$$

- At Stripping section, we have: $2 \geq i \geq nf-1$

$$\begin{cases} \frac{dM_i}{dt} = L_{i+1} - L_i + V_{i-1} - V_i \\ \frac{d(M_i x_i)}{dt} = L_{i+1} x_{i+1} - L_i x_i + V_{i-1} y_{i-1} - V_i y_i \end{cases} \quad (23)$$

- At rectifying, we have: $nf+1 \geq i \geq n$

$$\begin{cases} \frac{dM_i}{dt} = L_{i+1} - L_i + V_{i-1} - V_i \\ \frac{d(M_i x_i)}{dt} = L_{i+1} x_{i+1} - L_i x_i + V_{i-1} y_{i-1} - V_i y_i \end{cases} \quad (24)$$

- For the stage before last, we have: $i = n$

$$\begin{cases} \frac{dM_n}{dt} = L_{n+1} - L_n + V_{n-1} - V_n \\ \frac{d(M_n x_n)}{dt} = L_{n+1} x_{n+1} - L_n x_n + V_{n-1} y_{n-1} - V_n y_n \end{cases} \quad (25)$$

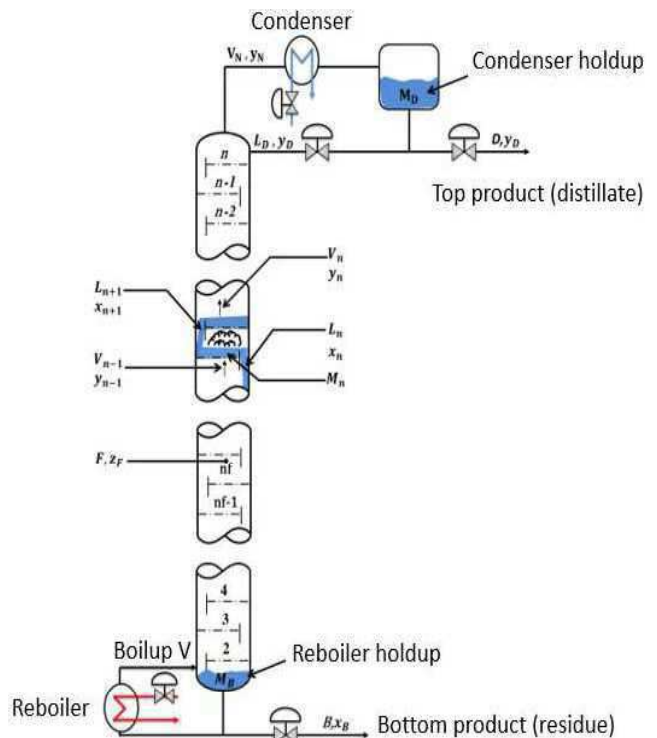


Fig. 3 Distillation unit scheme

In this work, we use a particular high purity distillation column with 40 stages (39 trays and a reboiler) plus a total condenser is considered (Fig. 3).

There are four output variables in the distillation column:

- Composition of distillate (y_D).
- Composition of bottom product (x_B).
- Liquid holdup in condenser (M_D).
- Liquid holdup in reboiler (M_B).

The two outputs liquid holdup in (M_D and M_B) have been controlled by proportional-controllers.

There are seven input variables in the distillation column:

- Reflux flow (L).
- Boil-up flow (v).

These two manipulated variables L and v are independent for composition control.

- Distillate product flow rate (D).
- Bottom product flow rate (B).

We can use the $L-V$ configuration of stabilizing the column system, where we operation D to control M_D and B to control M_B .

- Feed rate (F).
- Feed composition (z_F).
- Fraction of liquid in feed (q_F).

These last three variables are considered as disturbances.

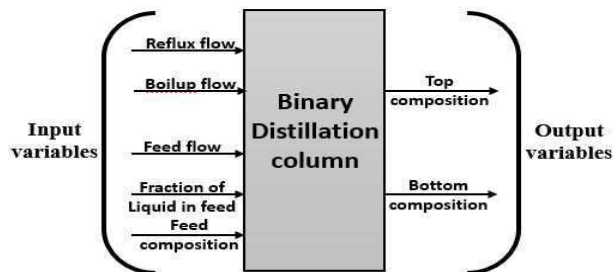


Fig. 4 Distillation process input and output variables

The matrices A , B , C and D are the state, input, output and feedforward respectively.

$$\begin{aligned}
 A &= \begin{bmatrix} 0.1673 & -0.0910 & -0.5766 & 0.1779 & 0.002 & 0.0305 \\ 0 & -0.1541 & 0.4966 & 0.2724 & -0.0012 & -0.0373 \\ 0 & -0.5586 & 0.0807 & -0.2798 & -0.0027 & 0.0828 \\ 0 & 0 & 0 & 0.7760 & 0.0011 & 0.0085 \\ 0 & 0 & 0 & 0 & 0.9948 & -0.0023 \\ 0 & 0 & 0 & 0 & 0 & 0.9274 \end{bmatrix} \\
 B &= \begin{bmatrix} -0.3575 & -0.1985 \\ 0.0322 & -0.0154 \\ 0.6399 & 0.1240 \\ 0.2931 & -0.1355 \\ 0.7093 & -0.6978 \\ -0.0631 & 0.2862 \end{bmatrix} \\
 C &= \begin{bmatrix} 0.1933 & 0.1705 & -0.0333 & 0.0273 & 0.6331 & 0.2664 \\ 1.2511 & -0.0161 & 0.1547 & 0.3080 & -0.7827 & -0.2328 \end{bmatrix} \\
 D &= \begin{bmatrix} 0.0124 & 0.0138 \\ 0.0790 & 0.0055 \end{bmatrix}
 \end{aligned} \quad (26)$$

V. SIMULATION RESULTS AND DISCUSSION

In the design of the MPC controller, a difficult compromise has to be made between the set point tracking and load rejection performance.

The parameters of the MPC: $n = 6, m = 2, p = 2$.

The weighing matrices: $Q_j = 10^9 \cdot I_p, R_j = I_m$.

A. Simulation of a set point change in the distillate

In this part, the set point of the composition in bottom (x_B) is fixed to 0.01 mole fraction.

The simulation was conducted for three set points:

For the first set time point $t = [0-100]$ min, the set point of the composition in distillate (y_D) is equal 0.99 mole fraction.

The second one, $t = [100-200]$ min, the set point of the composition in distillate (y_D) is equal 0.992 mole fraction.

The last one $t = [200-300]$ min, the set point of the composition in distillate (y_D) is equal 0.994 mole fraction.

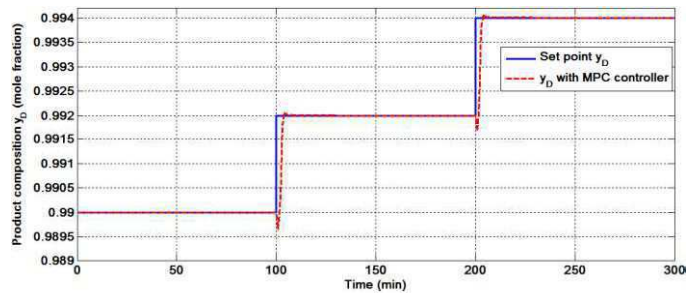


Fig. 5 Composition of light component in distillate

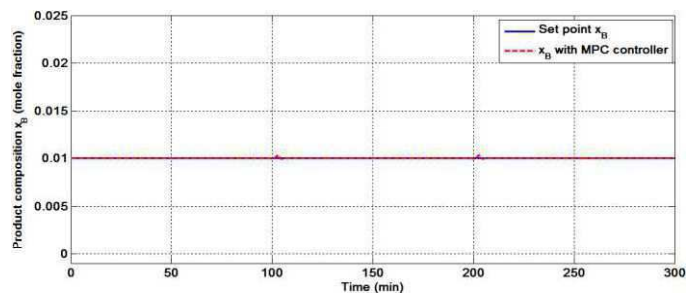


Fig. 6 Composition of light component in bottom

The Fig. 5 shows that the response of Composition of light component in distillate is satisfying in all intervals operation.

B. Simulation of a set point change in the bottom

In this part, the set point of the composition in distillate (y_D) is fixed to 0.99 mole fraction.

The simulation was conducted for three set points:

For the first set time point $t = [0-100]$ min, the set point of the composition in bottom (x_B) is equal 0.01 mole fraction.

The second one, $t = [100-200]$ min, the set point of the composition in bottom (x_B) is equal 0.012 mole fraction.

The last one, $t = [200-300]$ min, the set point of the composition in bottom (x_B) is equal 0.014 mole fraction.

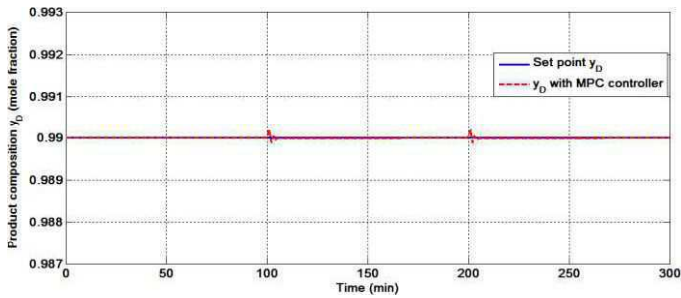


Fig. 7 Composition of light component in distillate

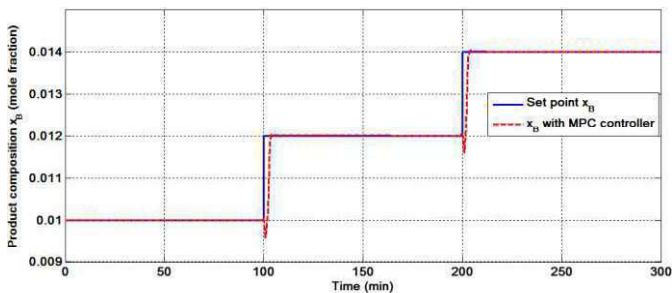


Fig. 8 Composition of light component in bottom

The Fig. 8 shows that the response of Composition of light component in bottom is satisfying in all intervals operation.

Figs. 5-8 illustrate the effect of the multivariable coupling at the instant of change of set points applied to the first (y_D) and the second set point (x_B).

The predictive multivariable controller on the distillation column shows that the interactions between control loops are eliminated (see Figs. 6-7)

C. Simulation with Disturbance Rejection

The system added a continuous disturbance step of 0.1 mole fraction after 150 min, as shown in the Figs. 9, 10.

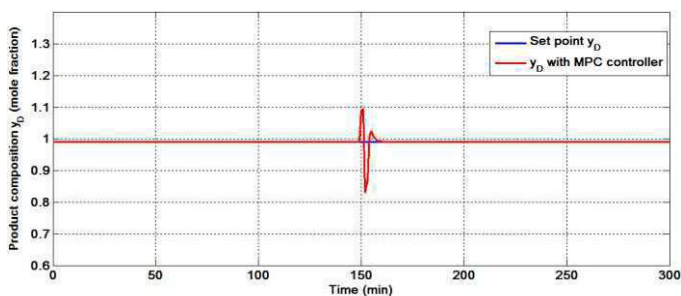


Fig. 9 Composition of light component in distillate

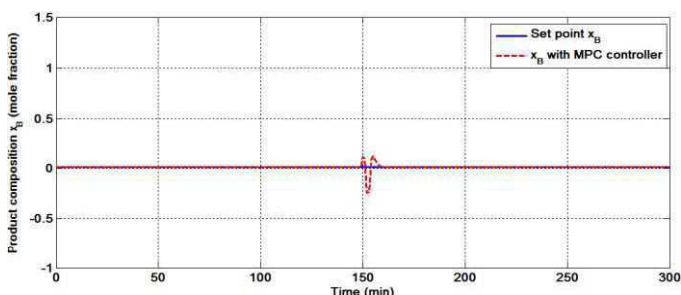


Fig. 10 Composition of light component in bottom

The MPC controller was able to reject the disturbance and has a small overshoot in the distillate and bottom compositions as shown in figs. 9, 10.

Figs. 11, 12 show the variations of the two manipulated variables: reflux flow rate (L) and steam flow rate (v) during the operation using controller to improve the system responses both for set point tracking and disturbance rejection.

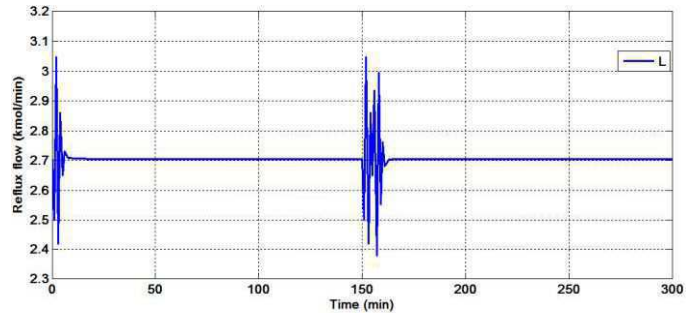


Fig. 11 Reflux flow applied with MPC controller

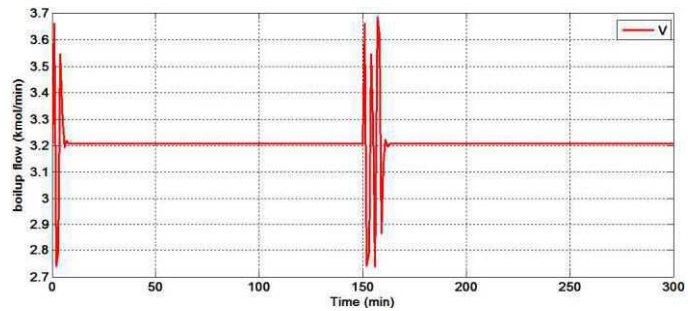


Fig. 12 Boilup flow applied with MPC controller

In Figs. 11-12, the MPC controller has an effect anticipatory on the two outputs of system with minimal future control.

VI. CONCLUSIONS

In this paper, we have used the multivariable MPC controllers to perform reference tracking and disturbance rejection in the distillation column. Changes in the discrete time observer predictive control algorithm have been made in such a way as to take into account that the matrix D is nonzero of the multivariate system of the distillation column.

We show that the two desired set points are exactly satisfied in the presence of disturbance, interaction and time delay, which demonstrates the effectiveness of the controller.

REFERENCES

- [1] N. P. Cheremisinoff, *Handbook of chemical processing equipment*. Elsevier, 2000.
- [2] I. K. MEKKI, M. BOUHAMIDA, M. BENGHANEM and R. KESSAS, "PI Control for Distillation Column". Proceedings of the International Conference on Automation and Mechatronics CIAM'11, 22-24 November 2011, Oran.
- [3] M. Morari and E. Zafiriou, *Robust Process Control*, Prentice Hall, Englewood Cliffs, NJ, 1989.
- [4] D. Seborg, T. F. Edgar, and D. A. Mellichamp, *Process Dynamics and Control*, John Wiley & Sons, New York, NY, 1989.

- [5] R. K. Wood and M. W. Berry, "Terminal composition control of a binary distillation column," *Chemical Engineering Science*, vol. 28, pp. 1707-1717, 1973.
- [6] W. H. Ray, *Advanced Process Control*, McGraw-Hill, New York, NY, 1981.
- [7] R. Stenz and U. Kuhn, Automation of a batch distillation column using fuzzy and conventional control, *IEEE Trans. on Control Systems Technology*, vol. 3, no. 2, pp. 171-176, 1995.
- [8] H. E. Musch and M. Steiner, "Robust PID control for an industrial distillation column," *IEEE Control Systems*, pp. 46-55, August 1995.
- [9] C. Zhou, J. R. Whiteley, E. A. Misawa, and K. A. M. Gasem, "Application of enhanced LQG/LTR for distillation control," *IEEE Control Systems*, pp. 56-63, August, 1995.
- [10] I. K. Mekki, M. Bouhamida, and M. Benghanem, Comparative study of predictive multivariable control and decentralized control for a distillation column, *International Review of Automatic Control (IREACO)* 6.4 (2013): 513-520.
- [11] I. K. Mekki, M. Bouhamida, and M. SAAD, Robust control of a chemical multivariable system in the presence of strong uncertainties in the model parameters. *International Review of Automatic Control*, 2018, vol. 11, no 4, p. 166-173.
- [12] A. K. Abbes, F. Bouani, M. Ksouri, A Microcontroller Implementation of Constrained Model Predictive Control, *International journal of electrical and electronics engineering*, vol. 5(no.3):199-206, summer 2011.
- [13] C. STOICA, Robustification de lois de commande prédictives multivariées, Ph.D. dissertation, Dept. Physic, Paris-Sud Univ., Paris, France, 2008.
- [14] C. Stoica, P. Rodríguez-Ayerbe, D. Dumur, Off-line Method for Improving Robustness of Model Predictive Control Laws, *Control Engineering and Applied, Informatics*, vol. 9(no.3-4):76-83, December 2007.
- [15] D.J.N. Limebeer, The specification and purpose of a controller design study, In *Proceedings of the 30th IEEE Conference on Decision and Control*, Brighton, UK, December 1991, 1579 to 1580.vol.2.
- [16] GU, Da-Wei, PETKOV, Petko, et KONSTANTINOV, Mihail M. *Robust control design with MATLAB®*. Springer Science & Business Media, 2005.

TABLE I
 UNITS FOR COLUMN DATA

Symbol	Quantity	Units
n	40	
N_{tot}	41	
n_F	21	
F	1	(kmol/min)
z_F	0.5	(mole fraction)
D	0.5	(kmol/min)
B	0.5	(kmol/min)
L	2.70629	(kmol/min)
V	3.20629	(kmol/min)
α	1.5	
y_D	0.99	(mole fraction)
x_B	0.01	(mole fraction)
M_i	0.5	(kmol)
τ_L	0.063	(min)

Realization of Dip-Coating technology to prepared the Fe-doped ZnO and Al-doped ZnO thin films for Solar Cells

C.ZEGADI¹, A.ABDELKADER² and S. HAMZAOU², M. ADNANE², N.HAMDADOU²

²Laboratory of Electron Microscopy and Materials Sciences, University of Science and Technology of Oran, P.O. Box 1505,31000 El-Mnaouer Oran, Algeria

¹École nationale polytechnique d'Oran -Maurice Aubin, Ex ENSET, Rue D, Es Sénia, Alegria

E-mail: chouckizegadi@gmail.com

Abstract: The aim of our work is the development of a window layer by "dip-coating" for the "solar cell" based on Zinc Oxide. To do so we realized a mechanism allowing the automation of this technique Dip-Coating and we have chosen a simple interface to control two stepper motors unipolar type from the PC parallel port. The program is written using Borland Delphi Compiler language to control the four soaking substrates parameters: distance, speed, time and number of dipping.

To confirm the system reliability of dipping the substrates and heating of thin films, we chose the Fe-doped zinc oxide (FZO) and zinc oxide doped Al (AZO) as materials for the layers. These thin films were prepared by a sol-gel process using the technique of coating by immersion in an ambient atmosphere with a sink rate of 5 [cm/min] during 60 [s]. After each depositing, the films were preheated in air at 100 C° for 10 min and the coating procedure is repeated ten times. The thin films are characterized by X-ray diffraction and scanning -electron microscopy. The characterization results show that all the compounds are wurtzite with hexagonal structure (2 0 0). They are well crystallized and the grain size is 52 nm for Fe-doped ZnO and 19 nm for Al-doped ZnO. The results of optical transmittance measurement

of (ZnO :Al and ZnO: Fe) thin films reveal a high transmittance (80%) in visible region and exhibit a sharp absorption edge at wavelength about 350 nm.

Keyword: dip-coating, solar cell, simple interface, Fe-doped zinc oxide, zinc oxide doped Al, sol-gel.

1. INTRODUCTION

Electronic and optoelectronic properties of semiconductor oxides have been extensively studied in recent years. Thanks to its semiconducting properties, piezoelectric and optical, zinc oxide (ZnO) thin film has many potential applications; in addition, it plays an important role in the optoelectronic industry. Because of their piezoelectric properties, the ZnO thin films can be used as pressure sensors [1], or in electronic devices such as rectifiers, filters, resonators and to radio communications in the image processing [2]. The thin films of zinc oxide can also be used in chemical sensors highly sensitive gas detectors [3, 4]. Research teams have shown that ZnO thin films, doped with aluminum (Al) and iron (Fe), have very high sensitivity and excellent selectivity for amino gases. The optical properties of ZnO are used in sensors integrated optical waveguides. It can be used as transparent electrode in optoelectronic devices, in solar cells [5, 6, and 7]. The thin films of zinc oxide are also used in the manufacture of smart windows thanks to the possibility of modulation of the transmitted light. Recently, a method the dip-coating sol-gel chemical route has been developed for applications of the photovoltaic devices [8]. The sol-gel method may be considered an adequate procedure for high purity and homogeneous films preparation, based on the hydrolysis and polycondensation of metal organic precursors,

such as metal alkoxides. These last years, this deposition technique has won the scientific interest due to the fact that its advantage mainly related to low temperature of processing, simple and cheap technological equipment, homogeneity on the molecular level in solution allowing a stoichiometry and an excellent compositional control and ability to coat large and complex area substrates. The sol-gel method is one of the most efficient methods for the preparation of nanostructure metal oxides and represents a simple and much low cost processing alternative to the vacuum deposition techniques. [9, 11]

The objective of this work is to consider the deposition of thin films of zinc oxide and Transparent conductors by innovative technology and economy "Dip-Coating" Solar cell for an application. It consists of immersing a substrate into a solution of hydrolysable compounds, and extracting it at constant speed. The film thus formed is subjected to a heat treatment consisting in a drying step, to remove the solvent, followed by a densification step at a higher temperature to crystallize the film. This technique is used commercially to coat surfaces of 10 to 12 m² of various metal oxides including zinc oxide [12, 14] .in this context; we conducted a mechanism to automate this deposition technique. The goal is to obtain materials with desired properties that are put in evidence by this technique. Thus, special attention was paid to the resolution of this goal by methods of simple and reliable deposits. Our study focused on three central pillars

- Creation of a mechanism through technology "Dip-Coating" assisted by a heating system
- Optimization of deposition parameters using the sol-gel process.
- Validation of this method by characterization of the deposits of zinc oxide doped Al and Fe doped.

2. EXPERIMENTAL DETAILS:

Deposition of films Fe-doped and Al-doped ZnO was performed using sol-gel process at room temperature , we used a starting solution of zinc acetated hydrated (Zn(CH₃COO)₂ 2H₂O) with 0.4 molar concentrations dissolved in ethanol (C₂H₅OH) .and iron chloride (FeCl₃)for Fe doped ZnO solution and aluminum chloride (AlCl₃) for Al doped ZnO solution. The concentration of Al and Fe was 2% with respect to Zn. The resultant solution was stirred 250tour /minute at 90 C for 3 h to yield a clear and homogeneous solution The substrates were cleaned Pyrex R _ pieces (75×25×1mm³) that were at first emerged in ultrasonic bath for 10 min and finally rinsed by ethanol Al-doped ZnO (AZO) and Fe-doped ZnO (FZO) films were prepared on glass by repeated coating. .Dip coating was performed with a speed of immersion 5[centimeter / minute] for 60 s. After depositing Each Time, the films were preheated in air at 100 C° for 10 min. After repeating the coating procedure ten times for the final film thickness of

approximately 450 nm, for that we have automated mechanism for this technique that allows control of these parameter The films were finally post heated at 450 C for 4 h in air using an oven furnace a schematic drawn of the dip-coating apparatus (Figure2, 3).

3. AUTOMATON TECHNOLOGY DIP-COATING:

Dip-coating technique is very slow (since depositing a monolayer / cycle, 1 monolayer ~ few nm), thus depositing a thin layer of about 1micromètre, it takes a hundred cycles; So automation this technique is necessary We performed an automatic system controlled by PC via the parallel port and using two stepper motor, the rotation and translation is controlled by software written in a programming language "Borland Delphi". L'interface générale du logiciel est représentée à la Figure 1(b). La Form1 contient un composant TreeView1 qui contient les listes des commandes, quatre boutons « d'insertion » et « enregistrement » pour insérer et enregistrer, respectivement, les commandes à partir du TreeView1 vers un autre composant TreeView2. Le logiciel contient une liste des commandes, et nous pouvons à l'aide de ces derniers programmer un bloc de commandes effectué par le PC. Premièrement, entrer le nombre de cycles ou le nombre d'opérations à effectuer, les positions bas et haut des substrats, le temps d'adsorption, de réaction et de Séchage (Figure 2-(b)) et enfin la rotation (Figure 2-(a)). Nous avons ajouté une autre commande « pause » pour insérer des point d'arrêt et cela pour pouvoir enlever ou placer les substrats, ou pour le Sécher avec l'air chaud, le programme ne tient pas compte de cette commande si nous ne la fait pas appeler par le Bouton «Pause » (Figure 3). Nous pouvons entrer plusieurs blocs de commandes à répéter c.à.d. nous pouvons insérer plusieurs fois la commande « répéter l'opération »

Pour lire et écrire sur ce port en utilisant ce programme nous avons opté a réalisé une carte électronique. Cette interface électronique (Figure 1(a)) permet d'actionner deux moteurs pas à pas de type unipolaire à partir du port parallèle du PC. Les signaux qui entraînent chaque moteur en rotation sont délivrés directement par les huit lignes de données du port de sortie ce qui constitue une configuration matériel suffisamment pratique pour que l'essentiel du travail soit reporté vers la programmation. Notre maquette reste simple et parfaitement efficace. Les deux circuits intégrés représentent la fonction commande et la fonction puissance. En effet, le 74HC573 [15] transmet les niveaux logiques qui correspondent à la mise sous tension ou pas de chaque enroulement des moteurs. Les valeurs sont verrouillées sur les sorties Q1 à Q8 grâce au transistor T via le signal STROBE (C0) provenant du port de contrôle de l'imprimante [16]. Chaque moteur pas à pas nécessitant une tension de 12V pour fonctionner correctement, un ULN 2803A [17] (qui constitue l'étage de puissance) est intercalé directement entre les sorties du 74HC573 et les enroulements. Le courant délivré par le port parallèle est très petit (2,5 mA) donc nous ne pouvons pas utiliser directement ses pins. Donc le choix du C.I. 74HC573 qui fonctionne avec un courant très petit (The 74HC573 is pin compatible with Low-power Schottky TTL [1118]). Le schéma

équivalent du 74HC573 est représenté sur la figure 2. (a). et le diagramme logique sur la figure 2 (b).

Une fois que nous avons terminé le circuit nous avons passé à la réalisation du notre mécanisme .Le système obtenu est représenté à la (Figure 2(a ,b)) L'équipement est constitué de quatre béciers de 75 ml contenant les solutions précurseurs Les substrats sont attachés verticalement sur les quatre bras. Les deux moteurs pas à pas entraînent le mouvement vertical et le mouvement de rotation. Le nombre de pas du moteur 1, c.à.d. la distance de la montée et de la descente, le nombre de pas du moteur 2, c.à.d. le degré de rotation ainsi que le temps d'immersion dans les différent béciers et la vitesse de la montée et le temps de séchage sont contrôlés via PC par le logiciel écrit sous « Borland Delphi. » Pour voir la fiabilité de notre mécanisme nous avons utilisé seulement 3 bécier et deux déplacements transversaux pour la déposition du : (ZnO : AL et ZnO : Fe)

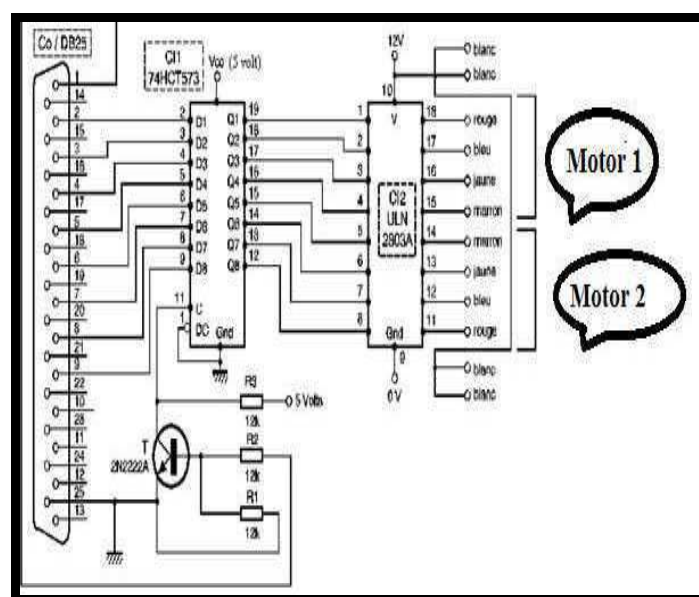


Fig 1(a).Schéma de l'interface électronique qui commande les deux moteurs pas à pas.

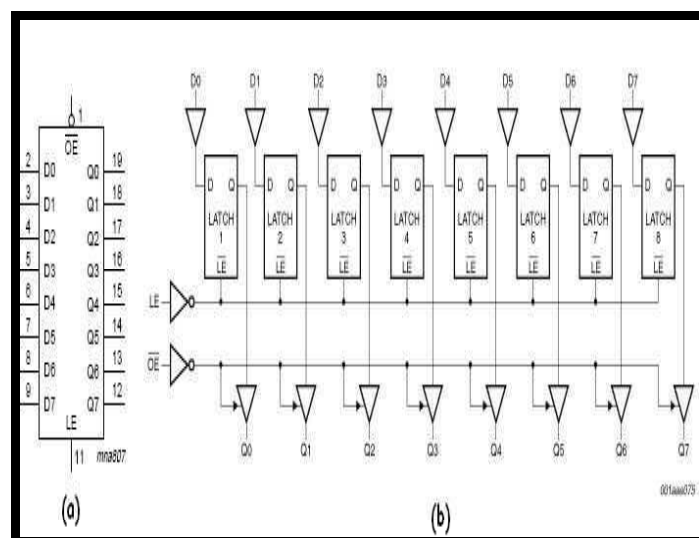


Fig.2.(a) schéma logique du C.I. 74HC573, (b) diagramme logique du C.I. 74HC573.

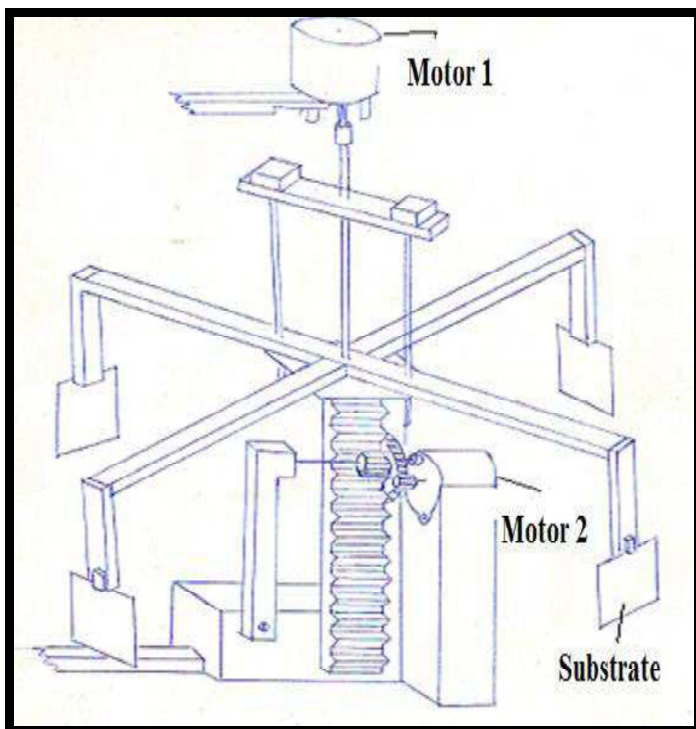


Fig 2(a).Schéma simplifié de l'automatisation du processus Dip-Coating.

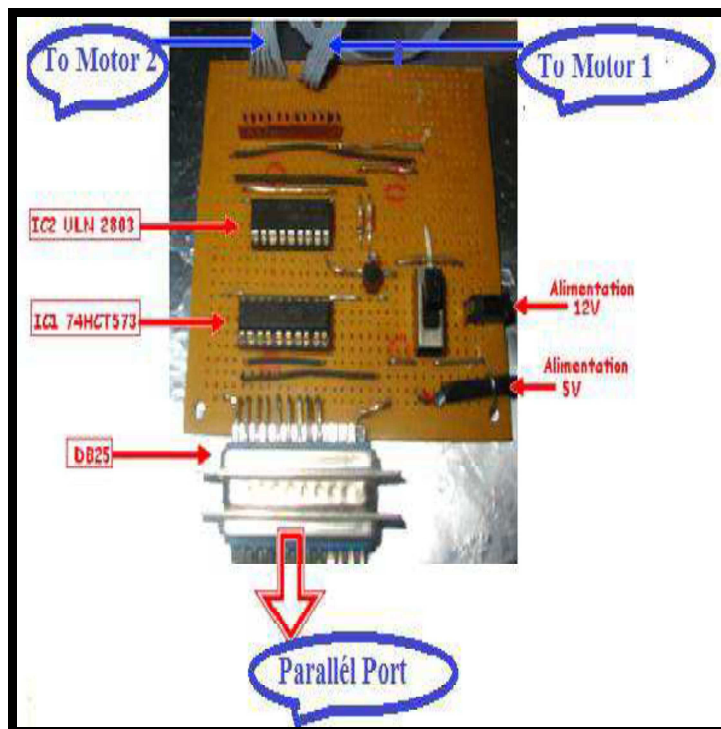


Fig 1.(b).Interface electronic control of two stepper motors

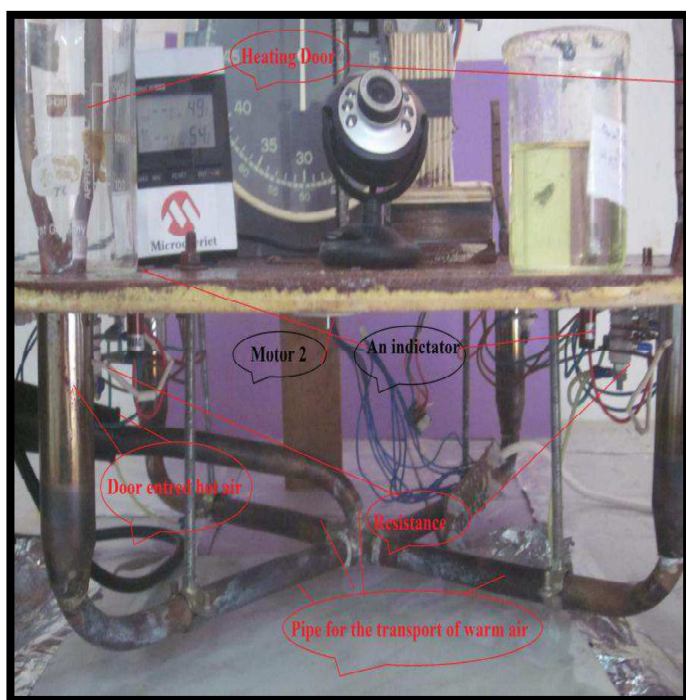


Fig -2 .(b) the final system of heating used for the technical dip-coating .

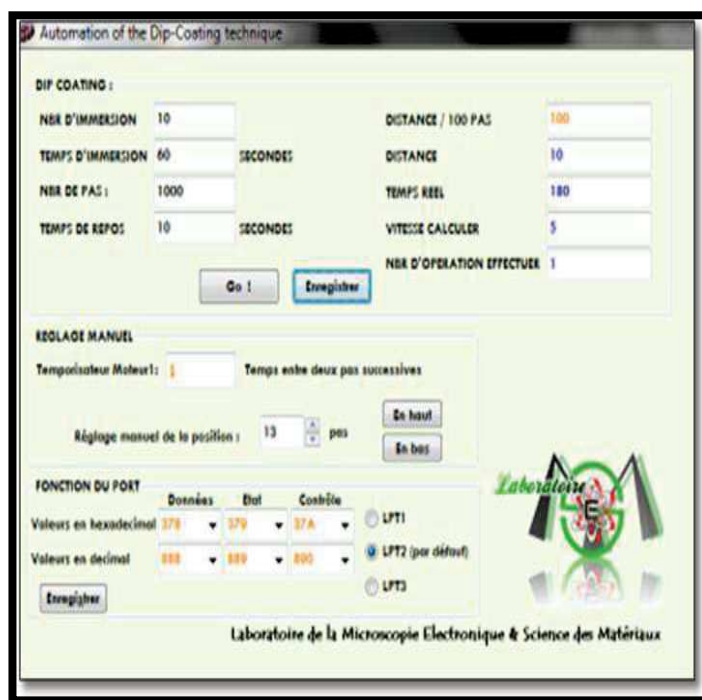


Fig.3. An overview of the main window

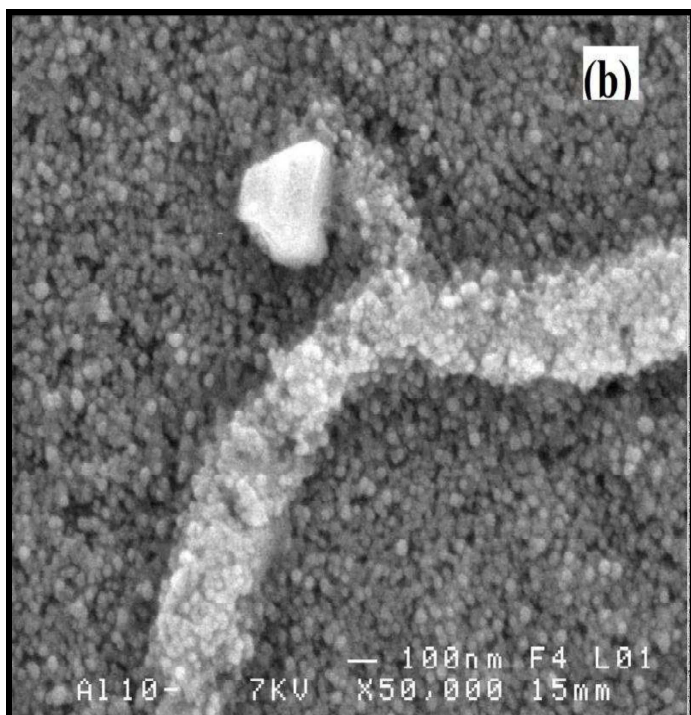


Fig. 5. (b).SEM images of: thin film Al-doped ZnO thin films

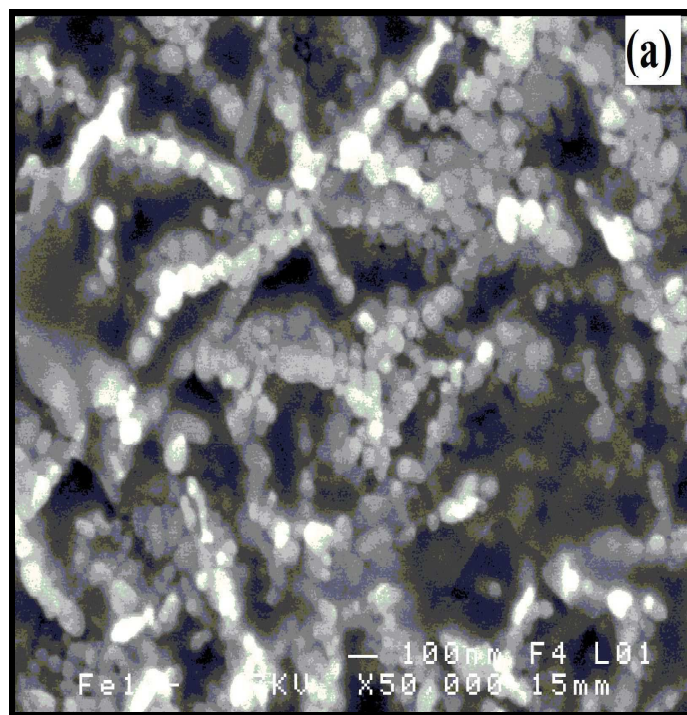


Fig-5.(a).SEM images of thin film Fe-doped ZnO thin films

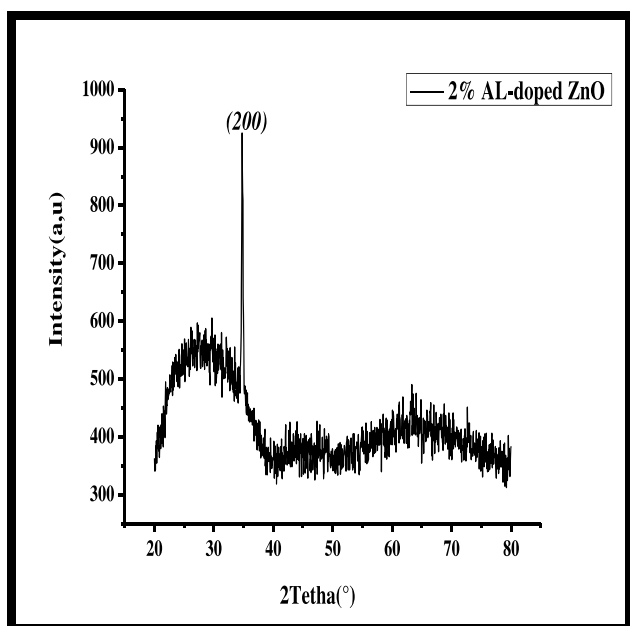


Fig.6.XRD patterns of Al-doped ZnO thin film

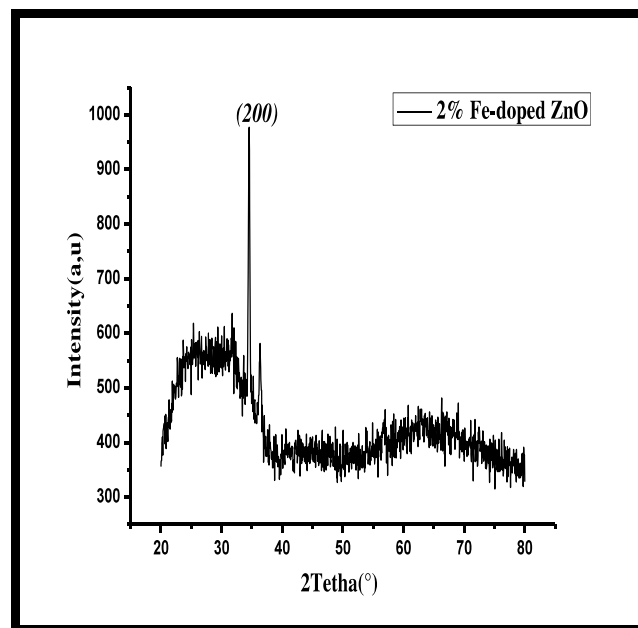


Fig.7.XRD patterns of Fe-doped ZnO thin film4.

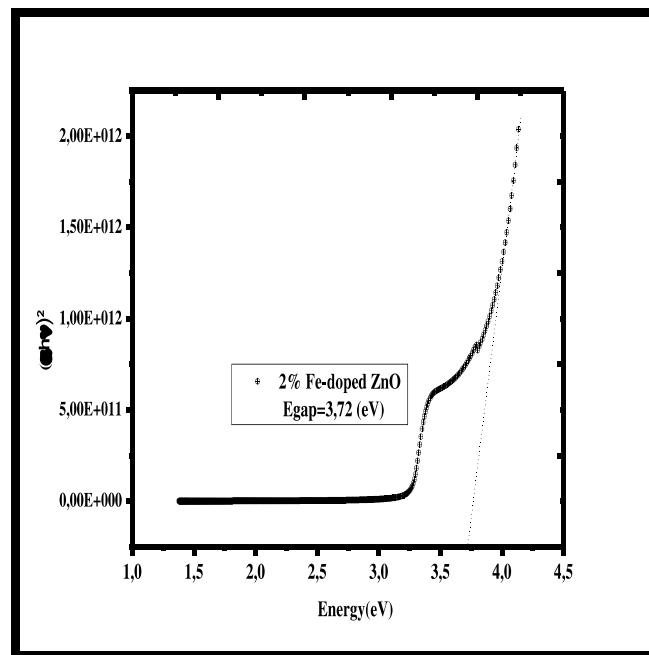
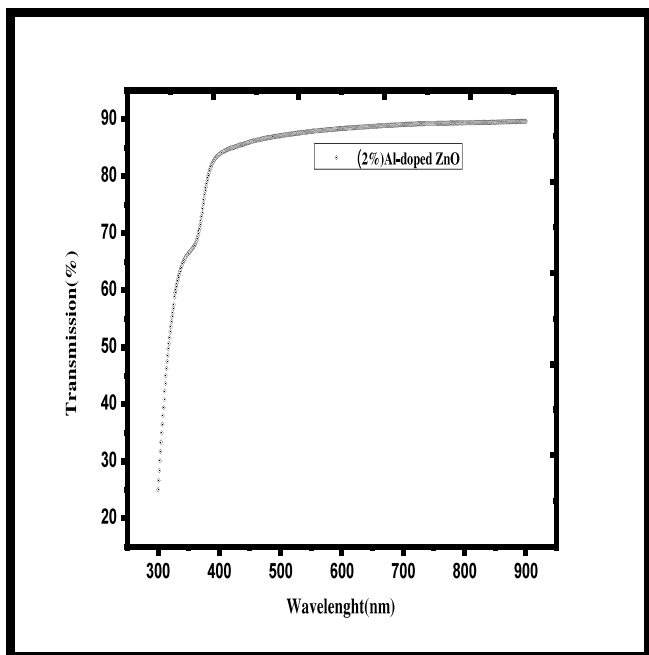


Fig. 8.(a). Transmittance spectra of Fe-doped ZnO thin films

Fig. 8.(a). Plot of $(\alpha h\nu)^2$ versus $(h\nu)$ of Fe-doped ZnO.

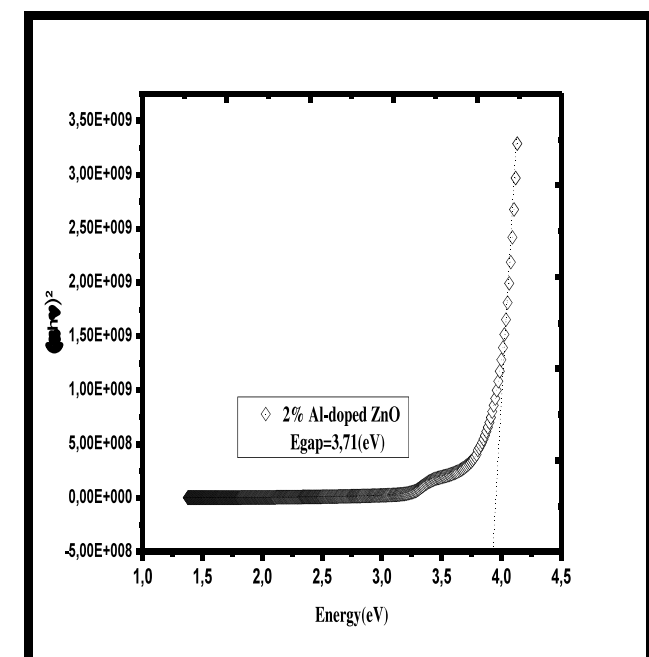
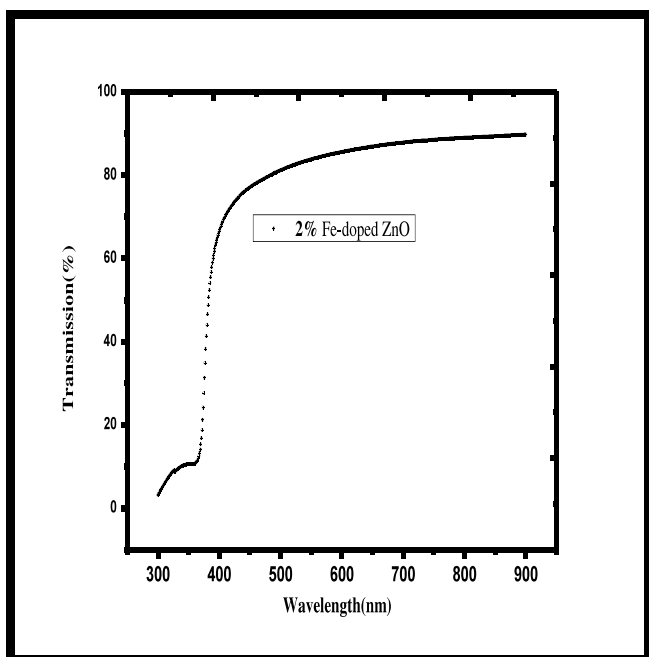


Fig.7. (b). Transmittance spectra of Al-doped ZnO thin films

Fig. 8.(b). Plot of $(\alpha h\nu)^2$ versus $(h\nu)$ of Fe-doped ZnO.

4. CHARACTERIZATIONS

To confirm our experimental procedures (automation technology Dip-Coating) we characterized our samples of ZnO: Al and ZnO: Fe the surface morphologies of films were examined by electronic microscopy (SEM) (VEGA3). The structural characterization of the films was analyzed using X-ray diffract meter (XRD) (Siemens D500) with Cu K α radiation. instrument. The optical transmittance measurements of the films were performed with a UV-Visible spectrophotometer (Shimadzu 1200) and calculated the optical band gap energy.

5. RESULTS AND DISCUSSION

5.1 Scanning electron microscopy (SEM):

Figure 5 shows the scanning electron microscope (SEM) images for 2%Fe-doped (Fig. 5a) and 2% Al-doped ZnO (Fig. 5b) films. The surface of the film displayed a homogeneous appearance in all scanned areas of the sample as shown in Figure 5a. The Al-doped ZnO films showed an increase in the crystallite size, which is in good agreement with the calculated values from the XRD a pattern widths at half maximum of the peaks by Scherrer's formula [19] (0.5 μ m for Fe-doped and 0.4 μ m for Al-doped). The grain size in Al-doped case is smaller than in Fe-doped films, and it is well known that the growth of the materials is easier around the defects [20]

6. CONCLUSIONS

Fe-doped and Al-doped ZnO thin films have been prepared by dip-Coating technique in ambient atmosphere. The advantages of this technique derive from the simplicity of the sol-gel process, short duration, and available auxiliary materials. We have realized a mechanism to control and operate the parameters of this technique that helped us to obtain structures with high efficiency for Solar Cells application. the analysis of X-ray diffraction of samples shows that its structure is hexagonal the crystallite Size of the particles of thin films. The SEM results are consistent with the XRD data obtained as a function of the Fe and Al doped. The optical transmission studies demonstrate that the average optical transmittance in the visible region is above 80% for all of the films.

ACKNOWLEDGMENT

This work is included in supported by Oran University of sciences and technology. The authors would like to thank the generous assistance of Pr Hamzaoui USTO Oran-Algeria and there researchers, Physics Dpt. The authors also acknowledge the support of Denis Chaumont University of Dijon- France.

5.2 X-ray diffract

Figures 6 and 7 show the XRD patterns of Fe-doped and Al-doped ZnO films. For all samples, the peak position agrees well with the reflections of hexagonal structure of ZnO (JCPDS Card No. 36-1451). The diffraction peaks arise at, (0 0 2) 34.46° and (1 0 1) 36.31° [15] for Fe-doped and (0 0 2)

34.28° for Al-doped ZnO without any other phases detected. The diffraction peaks can be well indexed to pure hexagonal phase ZnO with lattice constants $a = 3.249 \text{ \AA}$ and $c = 5.191 \text{ \AA}$ which are in good agreement with the literature values [20, 21]. The crystallite size of the thin films was determined using the peak (0 0 2) by Scherrer's formula [19]: $D = K\lambda / \beta \cos \theta$ (hk l), (1) Where D is the crystallite size, $\lambda = 0.154060 \text{ nm}$ the mean wavelength of Cu K α radiation and β the full-width half maximum (FWHM) of Bragg peak observed at Bragg angle θ (rad), $K = 0.9$, the values of D obtained, it is obvious that the crystallites increase, it is 19 nm for 2% doping with Al and 52 nm for 2% doping with Fe. The crystallite size agrees with the SEM observation. Furthermore, the orientation of crystallites in Al-doped ZnO films the orientation of (only (0 0 2) peak) is better than in Fe-doped ZnO films (two orientations).

5.3 Optical transmissions

The transmittance spectra of Fe-doped and Al-doped ZnO films are shown in Figures 8 (a) and 8 (b). It is found that the transmissivity is above 80%. Based on the transmittance spectra in Figures 9 (a) and 9 (b), the optical band gap E_g was obtained by extrapolating the linear portion of the plot $(ah\nu)^2$ versus $(h\nu)$ to $\alpha = 0$ according to the following equation: $\alpha = A(h\nu - E_g)^n$, [22] where $h\nu$ is the photon energy, E_g is the band gap, A is the edge parameter and $n = 1/2$ for direct gap material. The optical band gap E_g of Fe-doped Al-doped ZnO films are illustrated in Figures 10 and 11. While the band gap is 3.72(eV) for the Fe-doped ZnO film, it rises to 3.71 (eV) for Al-doped ZnO, and the Burstein-Moss effect explains this difference.

REFERENCES

- [8] SOL-GEL TECHNOLOGY OR THIN FILMS FIBERS, PREFORMS, ELECTRONICS AND SPECIALITY SHAPES EDITED BY LISA C. KLEIN CENTER FOR CERAMICS RESEARCH; COLLEGE OF ENGINEERING RUTGERS-THE STATE UNIVERSITY OF NEW JERSEY PISCATAWAY, NEW JERSEY , HANDBOOK OF THERMOSET PLASTICS: EDITED BY SIDNEY H. GOODMAN
- [9] OPTICAL CHARACTERIZATION OF ER-IMPLANTED ZNO FILMS FORMED by sol-gel method T. Fukudome *, A. Kaminaka, H. Isshiki, R. Saito, S. Yugo, T. Kimura B 206 (2003) 287–290 (2003)
- [10] Optical and photoluminescent properties of sol-gel Al-doped ZnO thin films Mingsong Wang a, Ka Eun Lee b, Sung Hong Hahn , Shin Chinho Park c Materials Letters 61 (2007) 1118–1121
- [11] HANDBOOK OF SOL-GEL SCIENCE and TECHNOLOGY Processing , Characterization and Applications VOLUME I SOL-GEL PROCESSING edited by Sumio Sakka

Comparative studies between Lithium-Ion , Nickel Cadmium and Nickel Metal hydride Batteries for wireless sensor Networks

Boubakeur Hamlili*, Khelifa Benahmed**, Brahim Gasbaoui*

* Department of electrical engineering, faculty of technology tahri mohamed University, Bechar - 08000 Algeria.

** Department of mathematics and computer science, faculty of exact sciences tahri mohamed University, Bechar - 08000
Algeria.

boubakeur.adel@yahoo.fr, benahmed_khelifa@yahoo.fr, gasbaoui_2009@yahoo.com

Abstract — Energy in Wireless Sensor Networks (WSNs) is of paramount importance for the remotely deployed energy stringent sensor nodes. These nodes are typically powered different batteries technologies via an efficiency bidirectional DC-DC (BDC) converter. In this purposed, this article deals with comparative studies between three different technologies Lithium-Ion, Nickel-Metal hydride and nickel-Cadmium, their capacity depends on the state of charge (SOC) of the battery. Energy is considered as a scarce resource for a sensor node, specifically when a node is deployed in a remote region and once it depletes the available energy, it is almost impossible to provide supplant energy. The purpose of energy conservation in wireless sensor networks is primarily to increase the lifetime of a sensor node and subsequently the entire network, which ensures availability of the various services provided by each node. The result obtained is satisfactory for our (WSNs) simulated in a MATLAB / SIMULINK environment. Moreover, the obtained results prove the robustness of the proposed control law against variations in load resistance in the studied converter .The most cost effective battery and subsequently better manage the power consumption in a wireless sensor network. The proposed control law increases the utility of (WSNs) autonomous under several power variations.

Keywords— Wireless Sensor Networks, SOC, Power management, SOC bidirectional DC-DC converters.

I. INTRODUCTION

In recent years, technical advances in terms of performance and miniaturization in electromechanical Microsystems (MEMS) and the technological advancement of information and communication have led to the development of a communicating micro component called sensor, and their deployment in several monitoring applications (Environmental, habitat, industrial, agriculture, intelligent transport, military, medical, domestic automation etc.) allow the use of a new strategy. Wireless Sensor Networks (WSNs),

which represent cost-effective solutions for remote monitoring and data processing in complex and distributed environments [1].

Wireless sensor networks are made up of several sensors (nodes) and can communicate with each other wirelessly and which are generally powered by a battery of very limited and almost never renewable energy, the objective of optimizing Energy consumption in wireless sensor networks aims primarily at increasing the lifetime of a sensor node and the long-term operation of the network, which ensures the availability of the various services provided by these networks [2].

A node often keeps a set of low-maintenance maintenance-free devices such as microcontroller, memories, one or more sensors, battery and a radio module for communication, the goal is to increase the lifespan of these small appliances , It is a problem of energy management (the stack), in the literature the researchers have made a lot of efforts to find methods trying to optimize the energy consumption at the level of the sensor and the good quality of service of the network, based either on the manufacture of the hardware (circuits and / or the battery of physical matter), or used the approach of the rechargeable batteries, or used techniques (algorithms) touching protocol layers for example The MAC layer and / or the NETWORK layer [3].

In this article we are interested in the first strategy, that is to say exactly the choice of type of battery suitable for the nodes in an WSN, therefore it is necessary that the only source of energy provided by the stack Must be replaced or collaborated by another energy source by proposing a comparative technique to contribute to the improvement of performance and optimization of energy conservation in the network in order to extend the energy This study consists in using the control of a Buck Boost DC-DC converter for three types of battery during three phase of service of (WSNs), evaluating the performance of the proposed stack, a test

of Simulation is carried out during the service phases of the node.

The remained of this paper is organized as follows. In section 2, the design of wireless sensor network. Section 3 shows the basic operation of a lithium-Ion battery. Section 4 describes the bidirectional DC-DC converter. Section 5 five some simulation results and discussion carried in MATLAB/. Finally, the conclusion is drawn in section 6.

II. BASIC CONCEPTS OF A WIRELESS SENSOR NETWORK AND DISSIPATION OF ENERGY IN SENSOR NODES

The technological advances in information and communications have given rise to a new generation of computer network adapted to a wide range of application very varied are the networks of sensors wireless, that is composed by a great number of nodes which are micro-sensors Capable of collecting and transmitting data in an autonomous manner Figure 1 [1].

The sensor is a measuring instrument that transforms an observed physical or chemical quantity (temperature, humidity, acceleration, vibration, etc.) into an electrical signal, this transformation must be a reflection as perfect as possible of these quantities , In recent years the concept of intelligent sensor [3] (smart sensor), a system composed of several subsystems whose functions are distinct, combines between the acquisition of data (signal converter of the signal) , Information processing (microcontroller and memory), communication (radiofrequency), a location system (GPS) and an energy generator.

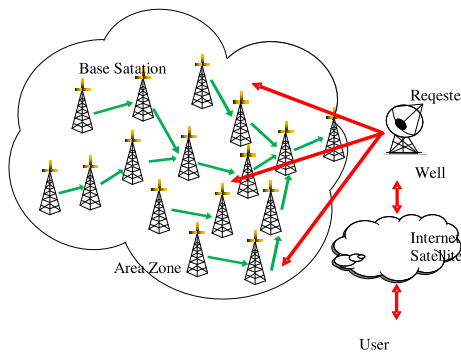


Figure 1. Wireless Sensor Network [1]

The energy consumption generally depends on the type of sensor and its deployment in its application, in order to design efficient solutions in energy, it is important to first analyze the various factors causing the dissipation of energy Of a sensor node which takes place in a general manner in several modes as it is consumed during the capture, processing and transmission (transmission, reception and listening of the channel), the latter is determined by the quantity The data to be communicated and the transmission distance, as well as by the physical properties of the radio module[3]. The emission of a signal is characterized by its power, when the transmission power is high, the signal will have a large range and the energy consumed will be higher, note

that the communication energy represents the largest portion of the energy consumed by a sensor node.

III. PRINCIPLE OF BATTERY OPERATION (LITHIUM-ION)

Li-ion technology consists in using the electrochemical circulation of the lithium ion in two materials and at different potential values. The positive electrode and the negative electrode constitute the two redox potentials, and the potential difference creates the voltage within the battery. In use (the accumulator discharges), the negative electrode releases lithium in ionic form Li^+ ; Li^+ ions migrate to the positive electrode via the ion conductive electrolyte; The passage of each Li^+ ion within the accumulator is compensated by the passage of an electron in the external circuit, in the opposite direction: this is what creates the electric current making the noued work. Figures. 2 and 3 The shows des charging and the discharge digramme lithim-Ion respectively [4]-[8].

Figure 4 describes the equivalent circuit of a lithium-ion battery or, E is the voltage of the battery without charge voltage; E_0 is the idle voltage; K is the polarization constant or the polarization resistance; Maximum capacity of the battery; Q is the exponential tension; B is the exponential capacitance. All parameters of the equivalent circuit are based on the characteristic circuit in discharge.

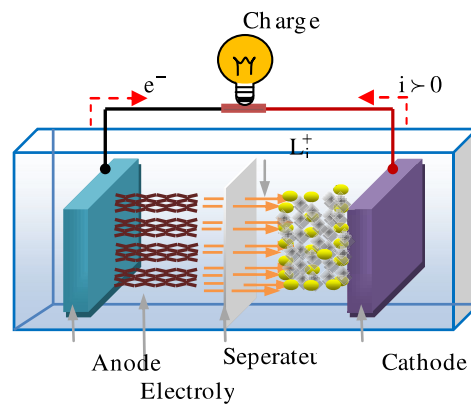


Figure 2. Diagram of a Lithium-Ion battery in discharge.

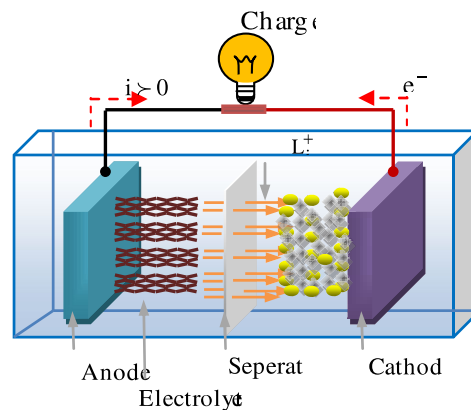


Figure 3. Diagram of charged lithium-ion battery.

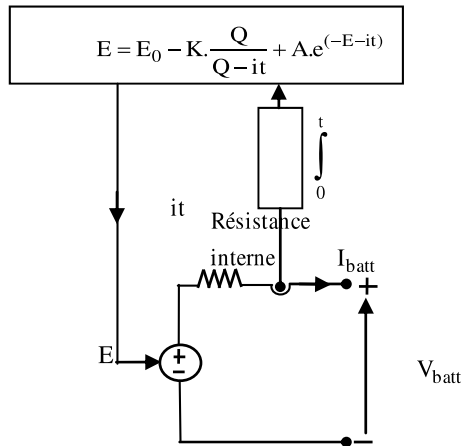


Figure 4. The equivalent circuit of a lithium-ion battery.

IV. THE BIDIRECTIONAL CONVERTER FOR WIRELESS SENSORLESS NETWORKS

The bidirectional converter changes the current flow direction of the battery according to the node power requirement. The BDC boosts up the battery voltage during the high power state and the start-up state. The BDC buck mode is activated for the battery charging state. The non-isolated PWM controlled power converter is selected for the BDC designing process.[9] The BDC circuit diagram is shown in Figure 5. V_{bat} is the battery voltage and the C_1 is the LV side capacitor. L is denoted by the BDC inductor and Q_2 and Q_3 are MOSFET switches. The capacity of the DC bus capacitor bank is denoted by C_2 [10]

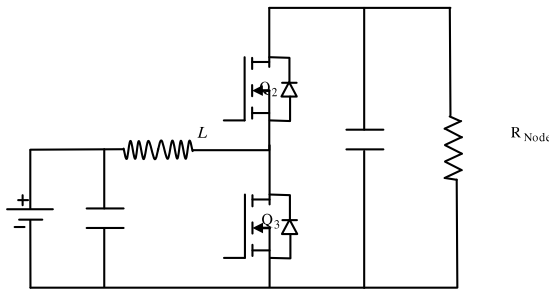


Figure 5 . Bidirectional converter circuit diagram.

When the energy flows from the LV to the HV side during the boost mode, Q_3 operates as the active switch and the Q_2 is passive switch. The BDC current flow diagram during the boost mode is shown in Figure 6. The BDC boost mode operation is similar to the UDC boost mode operation. The Q_2 switch is operated as a diode[11].

Figure 7 shows the power flow during the buck operation. The Q_2 switch is the active switch in the buck mode operation and the Q_3 in the passive state. When the Q_2 is ON state, the current flow from the HV side to the LV side and the energy is accumulated in the inductor. Figure 8 shows the power flow during the Q_2 is OFF mode[9]-[12].

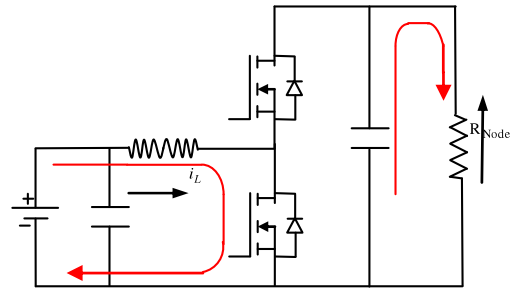


Figure 6. BDC current flow during the boost mod.

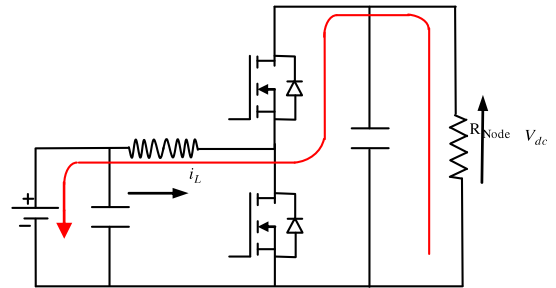


Figure 7. BDC during the Q_2 ON state.

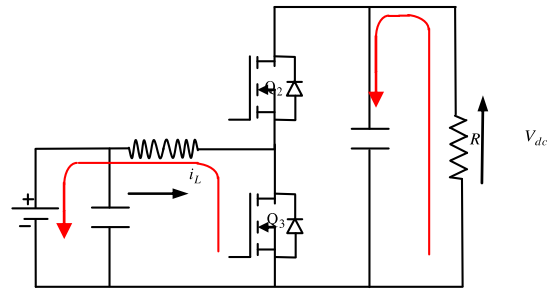


Figure 8. BDC during the Q_2 OFF state

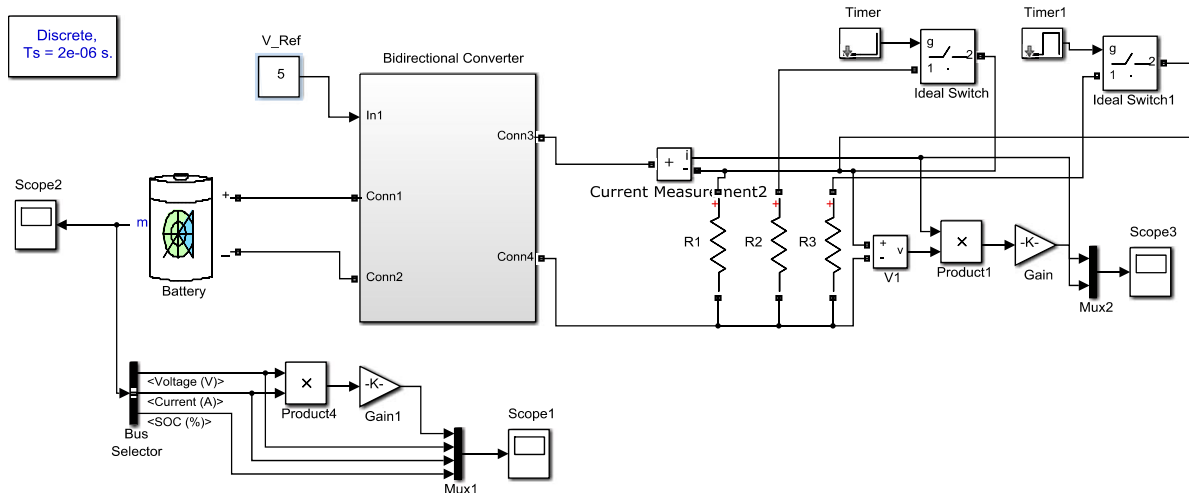


Figure 9. Model of wireless sensor Networks in MATLAB/Simulink.

V. SIMULATION RESULTS

In order to characterize the behaviour of wireless sensor Networks, simulations were carried out using the model in Figure 9. This model uses a sensor node connecting to a lithium-ion battery through the DC-DC Buck Boost bidirectional converter that ensures an output constant voltage 5V. The following results were simulated in MATLAB / SIMULINK. And the simulation is divided into two cases, the first one present a performance test of Lithium-Ion for wireless sensor Networks and a second cases show the comparative studies between three battery technologies

Case 1: Lithium-Ion for wireless sensor Networks:

This case are divided by three phases topologies the first one stand for the beginning phase's the wireless sensor Networks are in data acquisition and processing phase ($P_{node}=10mW$). The second phase correspond to Listening to the transmission channel phase where the power is equal($P_{node}=40mW$), and finally the wireless sensor Networks is in several transmission and reception of data phases , in this phase the node consumes more and more energy ($P_{node}=60mW$), when the power constraints are illustrated in the Table 1 and Figure 10.

Table 1. Specified topology of wireless sensor networks .

Phases	Event information	Power [mW]
Phase 1	Acquisition	10
Phase 2	Processing	40
Phase 3	transmission	60

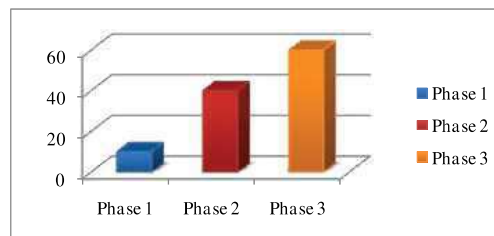


Figure 10. Energy consumption [mW] during the three phases.

The simulated results identified by Figure. 11 show the variations of the battery power, and Figures. 12 and 13 describe variation of current and voltage respectively in different scenarios. Figure 14 describe evaluation of state of charge during all seniors (it was initialized to 70 % at the beginning of the simulation). Figure 15 describe the battery duty cycle of bidirectional DC- DC converter.

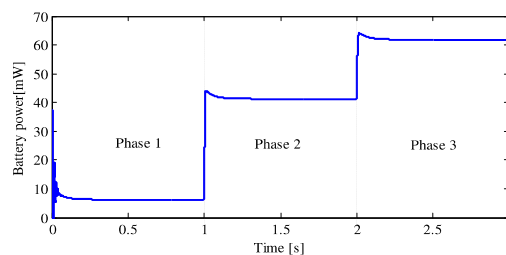


Figure 11. Variation of battery power in different phases

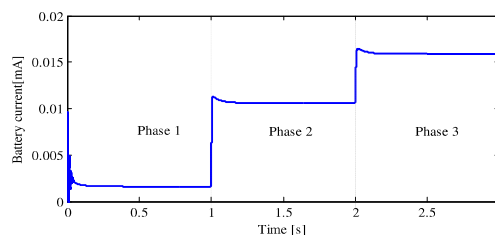


Figure 12 . Variation of battery current in different phases.

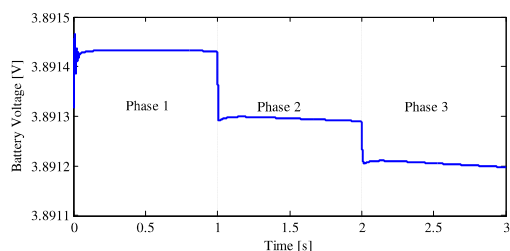


Figure 13 . Variation of battery voltage in different phases.

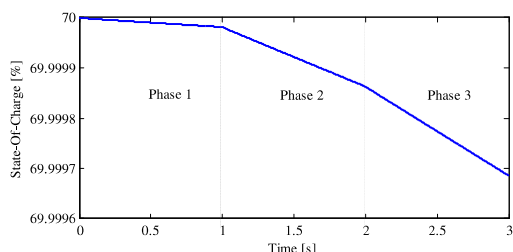


Figure 14. State of charge of battery in different phases.

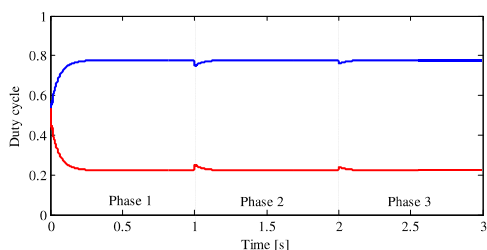


Figure 15. Duty cycle of bidirectional DC-DC converter in different cases.

Figure 16 and 17, demonstrate the variation of nodal power and nodal current correspondingly.

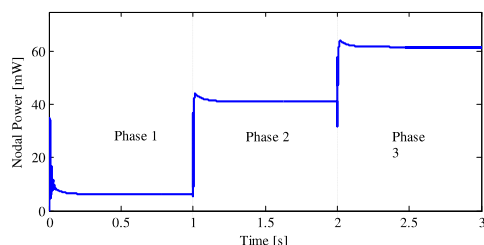


Figure 16 . Variation of nodal power in different phases.

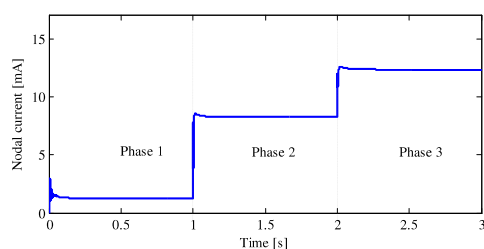


Figure 17. Variation of nodal current in different phases.

It is observed that the power and current nodal variation are almost the same variations in the different phases and form different battery technologies.

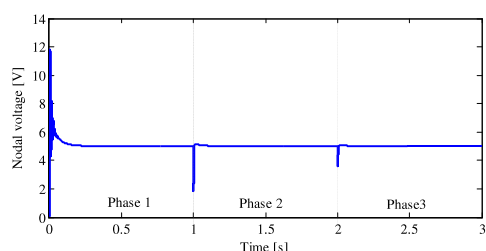


Figure 18. Variation of nodal voltage in different phases.

According to Figure. 10, the bidirectional DC-DC converter is tested by varying the output node resistor, the variation of the voltage in the node still remains around 5V Figure 18. The disturbances do not affect the performance of the buck-boost DC-DC converter output voltage.

Case 2: Comparative studies:

In the node the large energy consumption is during transmission, so a comparative study between the three types of stack will be more concrete during the third phase and one can observe a different observable in the representation of the state of charge of three types of battery technology as a function of time Figure 19, such as the rate of lithium battery Ion rapidly reduced than that of the Nickel Metal Hydride battery and itself as the Nickel Cadmium battery.

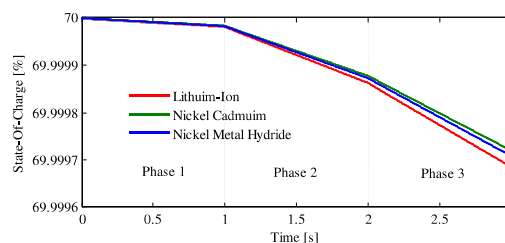


Figure 19. Comparative State of charge of different battery in different phases.

It is interesting to show the variation of SOC is inspired as a function of time equations for each type of battery Figure 18.

Fiting formula for lithium Ion battery:

$$SOC = 2e-006*t^{7} - 1.4e-005*t^{6} + 1.7e-005*t^{5} + 7.7e-005*t^{4} - 0.00026*t^{3} + 0.00023*t^{2} - 8.3e-005*t + 70 \quad (1)$$

Fiting formula for Nickel Cadmium battery:

$$SOC = 1.8e-006*t^{7} - 1.2e-005*t^{6} + 1.5e-005*t^{5} + 6.9e-005*t^{4} - 0.00023*t^{3} + 0.0002*t^{2} - 7.4e-005*t + 70 \quad (2)$$

Fiting formula for Nickel Metal Hydride battery:

$$SOC = 1.9e-006*t^{7} - 1.3e-005*t^{6} + 1.6e-005*t^{5} + 7.2e-005*t^{4} - 0.00024*t^{3} + 0.00021*t^{2} - 7.7e-005*t + 70 \quad (3)$$

These equations have allowed us to calculate the SOC rate for each type of battery at any time, in addition we note that there are small variations for each coefficient of variable x from one equation to another as in The ascending order of equation 2, equation 3 then equation 1, the battery Nickel Cadmium, Nickel Metal Hydride and then lithium Ion. It can be said that the Nickel Cadmium battery gives a slight improvement compared with other batteries, the equations (1), (2) and (3) given, and even the results of the table 2. The SOC value at the beginning and end of phase 3 demonstrated that the Nickel Cadmium battery is more cost effective for the sensor node against Nickel Metal Hydride and lithium Ion batteries

In the transmission phases, table 2 describe the change of SOC value of beginning and end of phase for each materiel battery type.

Table 2. Comparison SOC between three battery types in each start and end of the third phase.

Type	Phase 3		
	Begin	End	Difference
Lithium-Ion	69.99987	69.99996	0.00018
Nickel Cadmium	69.99988	69.99972	0.00016
Nickel Metal Hydride	69.99989	69.99972	0.00017

According to the table above there is a difference between the beginning and the end of the phase for each battery type, so there is a addition energy consumption in the transmission phases, but variation was different from one type of battery to another In order from smallest to largest, the Nickel Cadmium battery, the Nickel Metal Hydride and then the lithium Ion.

The control of the bidirectional DC-DC converter, switching from one phase to another phase a peak power change at the end of each phase (1 and 2 respectively). Figures 20 and 21 shows that the Nickel Metal Hydride batteries present a less peak power compared with others batteries (Lithium Ion and Nickel Cadmium).

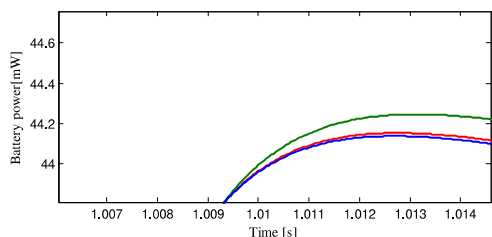


Figure 20. Comparative of peak power in different battery technologies at the end of treatment phases.

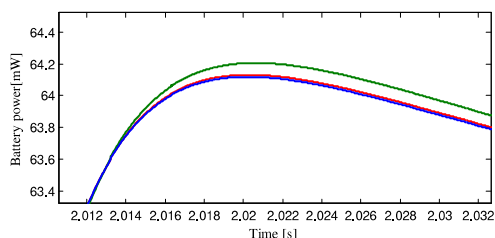


Figure 21. Comparative of peak power in different battery technologies at the end of transmission phases.

The exact values of the power peaks in mW inspired by the curves are given in Table 3 and their graphical representations respectively in Figures. 22 and 23, these values are classified in the order of lowest value to the highest of the Most suitable battery for our Nickel Metal Hydride node with 44.13mW in phase 1 to 2 and 64.10mW in phase 2 to 3 against the Lithium-Ion and Nickel Cadmium battery.

Table 3. Power comparison between three battery types in the end of the second phase.

Type	Pick of power [mW]	
	1	2
Lithium-Ion	44.15	64.11
Nickel Cadmium	44.25	64.21
Nickel Metal Hydride	44.13	64.10

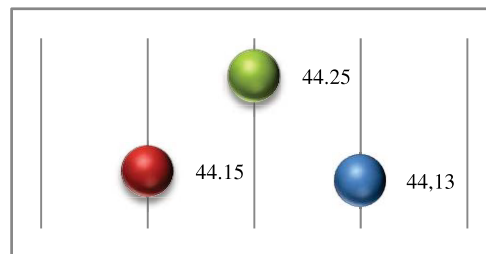


Figure 22. Power [mW] comparison between three battery types in the end of the second phase.

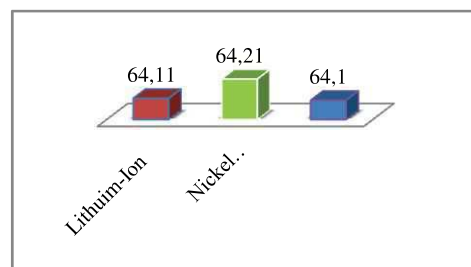


Figure 23. Power [mW] comparison between three battery types in the end of the third phase.

In addition, the results of power peak variations in the sensor node of the end of phase 2 to 3 and are given respectively in Figures. 22 and 23 and in table. show that the power peaks of the stacks Nickel Cadmium give poor results as the batteries and lithium Ion and Nickel Metal Hydride and lithium but with a more or less negligible differences of 0.12 mW that is to say without risk for our node.

Finally, the results of simulation of the discharges curves as a function of time for each type of battery technologies applied to a current of 100 mA and 200 mA respectively in Figures. 24 and 25 shows that the discharge of the lithium ion battery is fast as the discharge of the Nickel Metal Hydride battery and that is even faster than the Nickel Cadmium battery.

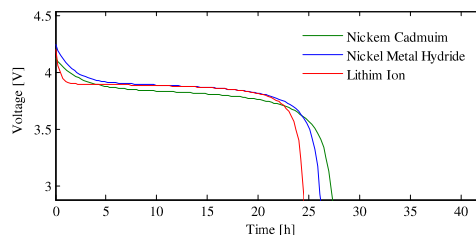


Figure 24. Discharge curve for 100 mA current.

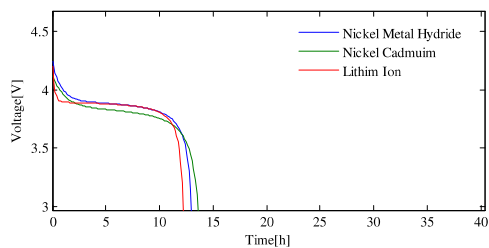


Figure 25. Discharge curve for 200 mA current.

Simulation results in Figures 24 and 25 prove that Nickel Cadmium batteries have a long discharge duration compared to Nickel Metal Hydride and Lithium-Ion batteries.

Due to the importance of the energy management problem in the wireless sensor networks and following all these assumptions it can be concluded that the Nickel Cadmium battery technology is the most suitable and battery candidate applied to the wireless sensor network node, a holistic approach to energy conservation in (WSNs) is essential. However, such an approach is still difficult to find due to the diversity of applications and differing requirements, such as techniques for optimizing energy consumption.

VI. CONCLUSION

This study demonstrates the robustness of dynamic performance of bidirectional DC-DC converter for wireless sensor networks. In the present work, comparative studies of three battery technologies lithium-Ion Nickel Cadmium and Nickel Metal hydride are presented. Three fitting formula are proposed that permit the relationship between state of charge and the timing. Nickel cadmium is the battery candidate for wireless sensor networks compared with Lithium-Ion and Nickel metal battery technologies.

The power variation phases do not affect the performance of the bidirectional DC-DC converter. Moreover, the future industrial transmission and communication sector must take into consideration the paper results studies into design steps.

REFERENCES

- [1] Mohd Fauzi Othmana , Khairunnisa Shazalib "Wireless Sensor Network Applications: A Study in Environment Monitoring System" International Symposium on Robotics and Intelligent Sensors Volume 41, 2012, Pages 1204-1210 2012
- [2] Joseph Polastre , Robert Szewczyk, Alan Mainwaring, David Culler, and John Anderson "ANALYSIS OF WIRELESS SENSOR NETWORKS FOR HABITAT MONITORING" chapitre 18 page 1 to 23 2004
- [3] S. E. Abdellaoui, Y. Fakhri, S. Saoudi et D. Aboutajdine, "Energy Efficiency of MIMO Cooperative Networks with Energy Harvesting Sensor Nodes", International Journal of Ad hoc, Sensor and Ubiquitous Computing (IJASUC), Vol.4, No.2 (2013).
- [4] https://fr.wikipedia.org/wiki/Batterie_d%27accumulateurs consulted 20-04-2017
- [5] Jia-Min S, Hurng-Liahng J, Jinn-Chang W, Kuen-Der W. "Single-phase three-wire grid-connected power converter with energy storage for positive grounding photovoltaic generation system". Electr Power Energy Syst 2014.

- [6] Ngok-Man Sze, Feng Su, Yat-Hei Lam, Wing-Hung Ki, and Chi-Ying Tsui. Integrated single-inductor dual-input dual-output boost converter for energy harvesting applications. In Circuits and Systems, 2008. ISCAS 2008. IEEE International Symposium on ,pages 2218–2221, 2008.
- [7] Ko Ko Win, Xinhui Wu, S. Dasgupta, Wong Jun Wen, R. Kumar, and S.K. Panda. Efficient solar energy harvester for wireless sensor nodes. In Communication Systems (ICCS), 2010 IEEE International Conference on , pages 289–294, nov. 2010
- [8] B. Gasbaoui, A.Nasri, A.Laoufi and Y.f Mouloudi. ,” 4 WD Urban Electric Vehicle Motion Studies Based on MIMO Fuzzy Logic Speed Controller ”, International Journal of Control and Automation Vol. 6, No. 1, February, 2013 105 .
- [9] Anasuya. N. Jadagerimath, Battery Capacity Management in Wireless Sensor Network Rechargeable Sensor Nodes International Journal Of Engineering And Computer Science ISSN:2319-7242 Volume - 3 Issue -9 September, 2014 Page No. 8129-8135.
- [10] B. Khiari, A. Sellami and R. Andoulsi, 'MPPT Control Of Photovoltaic Pumping System Based on Discrete Sliding Mode', International Renewable Energy Congress, pp. 66 – 72, Sousse, Tunisie, November 5-7, 2010.
- [11] E. Benkhilil et A. Gharbi, 'Modélisation et Simulation d'un Générateur Photovoltaïque avec un Étage d'Adaptation DC/DC', The First International Conference on Energy and Sustainable Development, ICESD'2011, 29-30 November 2011, University of Adrar, Algeria.
- [12] Anane, R., K. Raoof, et al. (2015). "On the Evaluation of GMSK Scheme with ECC Techniques in Wireless Sensor Network." arXiv preprint arXiv:1505.05755.

ACKNOWLEDGMENT

The authors would like to thank the laboratory of energy in arid region (ENERGARID) Bechar University and laboratory of smart grids & renewable energy (SGRE) faculty of technology, department of electrical Engineering, Tahri Mohamed university Bechar Algeria.

LITHIUM-ION PARAMETER

NOMINAL VOLTAGE	3.6 V
RATED CAPACITY	2500e-3 Ah
INITIAL STATE OF CHARGE	70%
INTERNAL RESISTANCE	0.0144 Ω

BIOGRAPHY



Boubakeur Hamlili received the Diplôme de computer engineer from the University ES-SENIA of ORAN - Algeria in 1993 and the Master degree of computing and mathematical sciences in 2012 from Tahri Mohamed Bechar University - Algeria, and in 2016 PhD student in Laboratory of Energy in Arid Region (ENERGARID) Tahri Mohamed

Bechar University, Algeria has done his research in Energy management in wireless sensor networks in the Faculty of technology, Department of Electrical Engineering, Tahri Mohamed Bechar University.

e-mail address: boubakeur.adel@yahoo.fr



Khelifa Benahmed has done his research for Ph.D. degree in the field of sensor networks wireless at the school of computing and mathematical sciences at Liverpool John Moores University, UK. He has 26 years of experience in education and research at the University Tahri Mohamed Bechar,

Algeria. Khelifa has also several international publications in the fields: wireless sensor networks, security, surveillance, smart grid, Internet of things, and smart irrigation. Khelifa holds Engineer, Magister degrees and PhD in Computer sciences in University of Oran Algeria.

e-mail address: benahmed_khelifa@yahoo.fr,



Brahim Gasbaoui received the electrical engineering diploma from the University Ibn-Khaldoun of TIARET (UIT) Algeria, in 1993 and the MS degree in 2008 from Bechar University - Algeria, and the Ph.D. degree from the Faculty of the Sciences and the Technology of the Bechar University Currently ,in 2017 professor degree

management, and Artificial and intelligence system optimisation.

e-mail address: gasbaoui_2009@yahoo.com

He is a Professor of electrical engineering at Bechar University. His research interests include power electronics robust control for electric vehicle and propulsion system, power electronics, antilock brake systems, anti-skid control for electric vehicles drive, power

Reconciliation of the objective and the subjective bioclimatic architectural parts; the contribution of schematization and CBR

BENABDELFATTAH Mohamed^{#1}, HAMRANI Saïda^{*2}

[#] Université Africaine d'Adrar ;

Ecole polytechnique d'architecture et d'urbanisme, EPAU d'Alger ;

Laboratoire Architecture et Environnement, LAE/EPAU d'Alger, Algérie

¹Benabdelfattah_med@univ-adrar.dz

^{*} Department of Architecture, University of Sciences and Technologies, Oran, Algeria,

²Hamranisana@gmail.com

Abstract— *During the process of architectural design, architects often face problems to which suitable solutions are required. To carry out this task a multitude of software programs were developed. Nevertheless, it has been noticed that an important number of architects do not use any bioclimatic device tools during the design process, at least in the present case. The inadequacy of these tools, to the professionals implied in the designing process especially the architects, is very probable. In this regard, the researchers aim to give the designer and the various actors a practical tool for help in order to understand and integrate the bioclimatic passive concepts as to the hot climate. The researchers tried to develop a bioclimatic sketching book based on decree n° 14-27 and case based reasoning method. This novel tool offers concrete illustrations to the actors, and assists the architects in the architectural bioclimatic design. It may contribute to the decisive insertion of building in its desert area during various stages of designing.*

Keywords— Architectural design process, desert climate, integration, sketching book, schematisation

I. INTRODUCTION

Architectural projects sometimes are seen as a problem solving activity, and the result of a long complex multidisciplinary process of planning [1]. It is not only a non-linear procedure but also a dynamic one. The emergence of the conceptual solution is the result of various actions. It embraces different sorts of interactions between the actors and their subject-fields. [2]. Pierre Fernandez sees that the major character that renders the act of modeling the design process awkward is the diversity of the methods of project elaboration. This feature of diversity can be interpreted via several ways of conciliating both the objective (program, site, regulations...) and subjective (composition, reference...) parts during the process of design [3]. The architect has to get the maximum amount of information concerning the project, and call for his own experience in terms of knowledge and know-how [4].

Several approaches are suggested to integrate this established fact into an intelligent device which will help the architects to find solutions for the problems. This could be achieved by providing the machine with the necessary

knowledge that would enable it to find the most suitable solution.

The Case based reasoning (CBR) can be considered as the closest one to the human reasoning based satisfaction among all the various approaches related to artificial intelligence. Additionally, it is the most adopted in the activity of designing [5]. Indeed, it can help architects overcome the problem of the lack of information concerning bioclimatic field issues and find optimal solutions.

In its work on the reasoning base references Roger Schank proposes [6] that a problem resolution system based on the CBR must be guided by the experiment. The CBR is a form of reasoning by analogy. It consists in solving a new problem, called target problem, and by using a whole of already solved similar precedents [7], [8].

From this perspective, this paper concerns itself with:

- Gathering and conceiving a set of conceptual strategies related to earthquake resistance design.
- Trying to find a way to take them into account during the early stages of designing.
- Finally, developing a sort of tool based on the schematization and case based reasoning method to assist architects during the designing process.

II. THE ARCHITECTURAL BIOCLIMATIC DESIGN REQUIREMENTS

In Algeria and since 2000, the public authorities put the issue of the elaboration of legislative code for sustainable design as one of its priorities in order to take into account the natural and climatic variables. This is clearly stated in the various promulgated legislative decrees (laws: 01-20; 02-02; 02-08; 04-05; 04-09; 09-99; executive decree number 14-27) [9].

However, to interpret suitably the spirit of the code the designer's experience has to be up to the level, without this a contrary result might occur especially in the case of bad interpretations [10]. Moreover, the majority of the available

bioclimatic help tool devices are used as enhancers, they check the feasibility of the overall architectural forms and intervene at stages in which the architectural part is already done.

On the other hand, the architectural bioclimatic design requires a very close cooperation between both the technical and the architectural bioclimatic aspects as from the early stages of the designing process. By experiment this approach allows a great deal of reconciliation between the architectural aspect and the technical design of the architectural project.

Practically speaking, the implementation of such methods is the result of the interaction of extremely complex factors such as: the current regulation, the economic situation, the technical know-how, the aptitudes, and even the different actors' behavior.

Additionally, the majority of designers do not use a decision advice tool during the early stages of bioclimatic design process. This is mainly due to the inadequacy of these tools to the professionals implied in the design process, especially architects [11]. This absence can be explained on various levels as:

- They are not used until the last phases of the design process.
- Designers are heavily short of training in terms of using these tools.
- Their knowledge about bioclimatic designing concepts is quite poor.
- Architects consider that bioclimatic active strategies are in charge of treating the sustainable aspect of buildings.
- The fact of knowing the existence of an under state control subsidy for the residences energy consumption is compulsory make designing intervenors lazy in considering bioclimatic aspects during the early stages.
- The current software devices are beyond the mastery of architects because of their highly specialized character.
- They require relatively a long training period of time, which professionals can not actually afford.

The use of these support tools varies according to the mode of implication of the bioclimatic aspects in the architectural design process:

In case of post-implication, the support tools will assume the control, validation, or sanction mission. And hence, the amendments have to be limited with regard to the schedule and project budget. Indeed, great deal of rectifications during very advanced state of project design might imply revising a considerable work of design on various scales. On the other hand, in case of very early engagement, as of the draft stage, they will be involved as assistance in the bioclimatic design (see figure 01).

The current simulation tools of bioclimatic aspects of building available form part of the specialized codes, and they are not usually employed in architectural practice. During the early designing phases, architects do not need any validation

but rather an enriching and assistant tool ; as affirmed by the head of CLOA-Adrar (Local Council of the Architects Order), Mr. LAZRAG A. : «...when conceiving we always seek nutritive sources for the project and which stimulates the architectural creativity...»

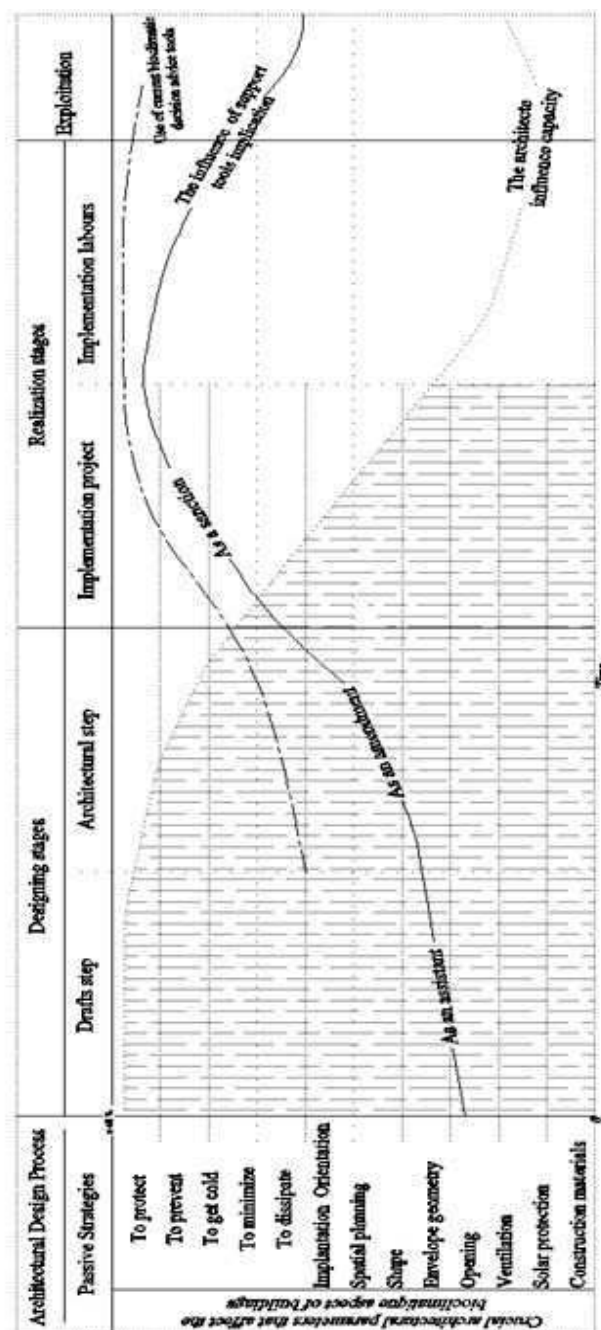


Fig. 1. Implication of current helper bioclimatic device tools in bioclimatic design process (Algerian case study)

Admittedly, the designing act is a rather complex activity; it is technical and sensitive labour at the same time. It often requests a search for ideas and information which can assist the designer in the development of his project. This idea was

developed by many researchers, such as Leplat (2002) [12]; Bignon (2004) [13]; [Kacher (2005) 14]; and other... They explain why during the architectural design process, the recourse to the images (diagrams, sketches, pictures, photographs... etc.) is essential. They consider also that the information transmitted by the image is easier to include/understand than that transmitted by the text. This probably results owing to the fact that the image requires fewer interpretations than the text. Moreover, the image presents information which can be directly integrated in the corpus of the ideas, the constraints or of the solutions of a project. The architectural design process is regarded as a chain made up of several couples of problem/solution formulations which each one called upon specific representations, see figure 02.

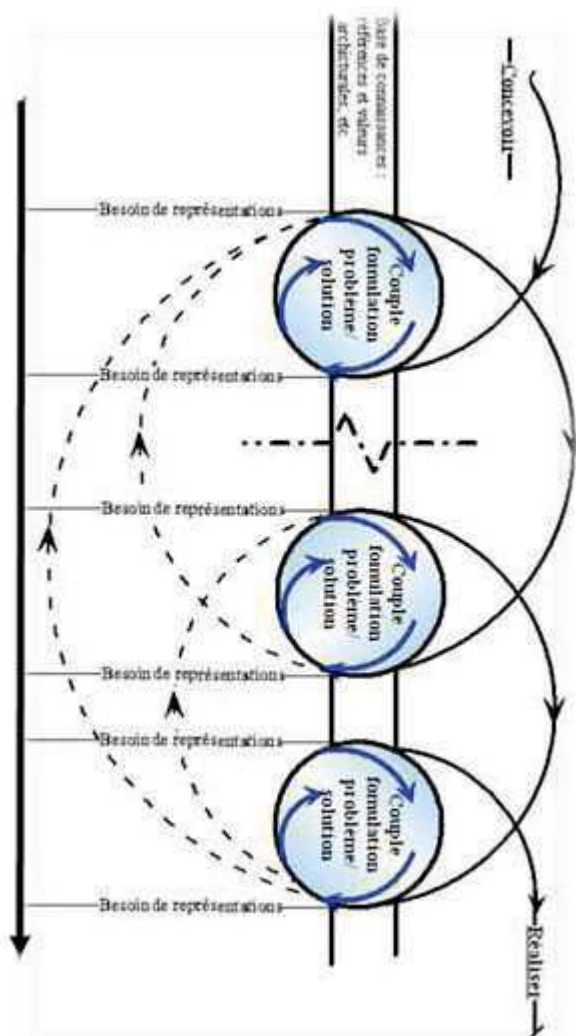


Fig. 2. The role of the couple problem formulation/solution in the advance of the architectural design process (Djafi 2005) [15].

The need for schematizations is a necessity which appears on the various level of the dynamic articulation of this couple. It gives the possibility of expressing the idea of the project which one wishes to carry out, and to communicate it. In architecture, the representation can be considered as a tool of studies making it possible to simulate the various assumptions, a means of anticipation, description, information, dialogue, decision-making aid, control and validation lasting the development process of the architectural project, and also a tool of communication towards a public not specialized.

III. EXPERIMENTAL THE PROPOSED DESIGN PROCEDURE

The designing act is a highly complex activity; it is technical and emotional at the same time. It often requests a search for ideas and information which can assist the designer in the development of his project. This idea has been developed by several researchers and designers, such as Bignon, Halin, and Kacher in his article « A method to index images in the wooden architecture domain » [13], and S. Kacher in her doctoral thesis [14] among others..., they explain that during the conceptual process the need to return back to visual illustration (images, pictures, drawings, etc.) is essential. They consider that the information transmitted by image is easy to understand if compared to written texts. This is due to the fact that the image has a limited number of interpretations. And it presents information which can be directly integrated into the corps of ideas, constraints or solutions for the project. In other terms, the image that supports the architectural creation before and after the design of the project in the conceptual, architectural and even economic order. It clarifies the various situations “analysis / development” of the designing process, and also simulates the comprehension of the bioclimatic architectural concepts. Moreover, it provides a clear illustration to the actors about how to include the formal relationships between the various attributes influencing the bioclimatic aspects of the building. [16].

In this piece of research, our aim is to suggest a tool that facilitates a sort of reconciliation between the objective and the subjective parts of the design. More precisely, enhance the communication between the different actors, and hence ensure a tight collaboration between them as it is the fundamental principle of any architectural design. The proposed tool is composed of two types of structures: a linear structure and in loop one (Figure 03).

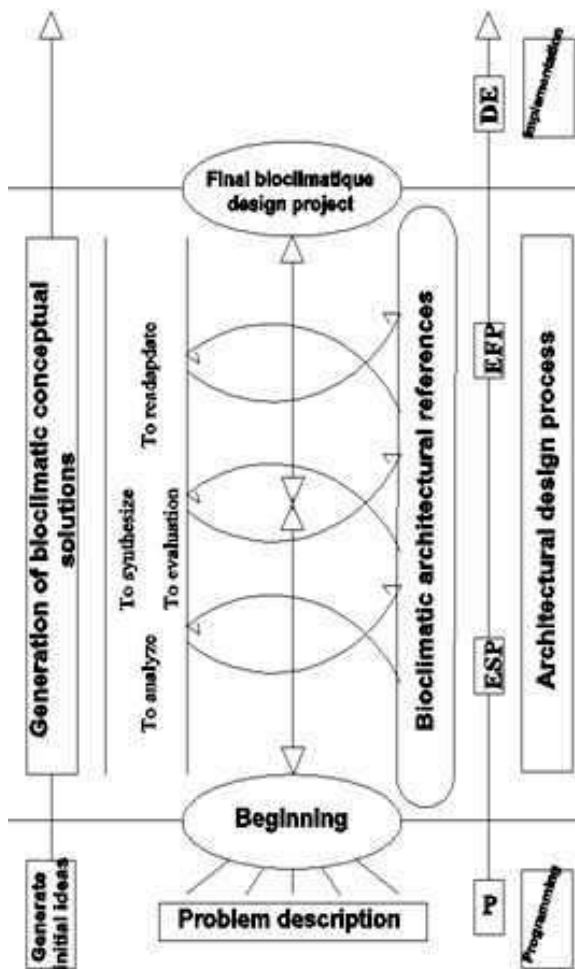


Fig. 3. The proposed design procedure

The linear structure is vertical and it defines the requirements, of the bioclimatic design concerned as well as the different developing phases of the project. The loop structure is concerned with generating alternative solutions and allowing the repetition of all the activities and phases of the linear structure in an iterative way. The loop structure divides the vertical linear into loops of five successive stages. The first one examines the project candidates. The second stage selects bioclimatic concepts from the given data.

Next, an analytic phase was carried out in order to suggest the various possible conceptual solutions. Then a synthetic step generates a potential solution through the exploration of various combinations of the primitive elements.

Finally, the results were evaluated, at times readjusted and reused. These phases were repeated until a satisfactory designing solution was obtained.

IV. THE BIOCLIMATIC SKETCHING BOOK

During the process of design, architects usually use their previous knowledge conceptualized in terms of references and schematized cases so that to feed their new artistic products. They do not have predetermined ways of resolution, but instead they know a certain number of technics and methods,

among which relying on similar projects or existing prototypes. However, it is necessary for designers to reinvent and recombine some strategies to elaborate an adequate solution each time.

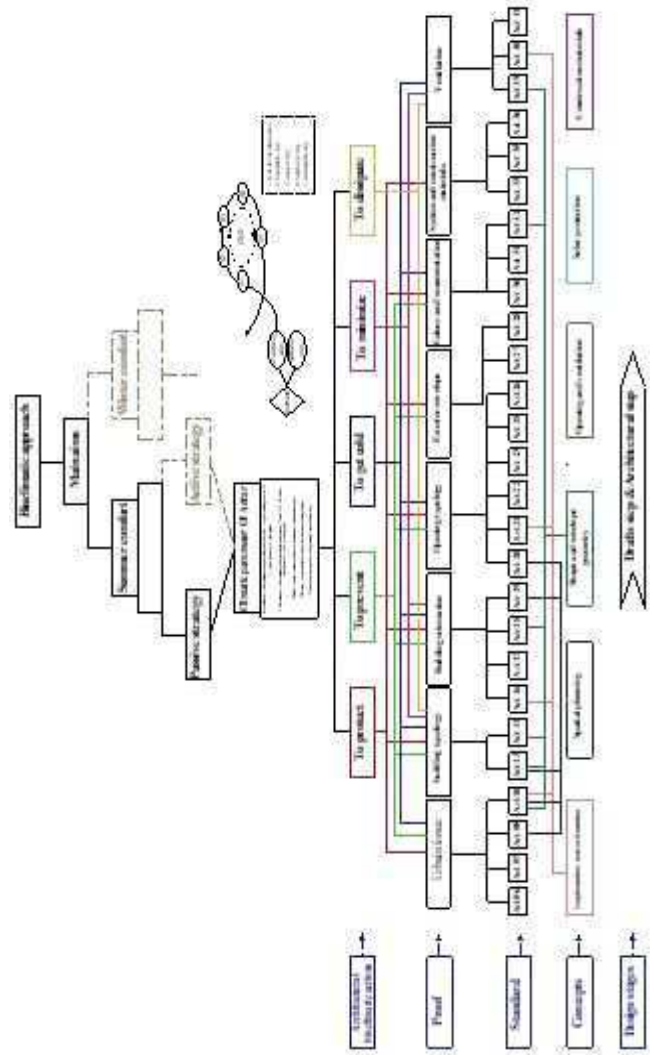


Fig. 4. Diagram of the bioclimatic sketching book

The need for rules related to bioclimatic designs proves to be essential as they offer the architect the conceptual bases for the architectural project. They enable also the guarantee, integration, and insertion of climatic variables as from the early phases of the design process. The reasoning based case is by far the most suitable resolution approach to the problems adopted in the act of designing. Indeed, it implies the use of artificial intelligence “AI” which helps the architect in the bioclimatic design and to find optimal solutions.

The diagram shown in figure 4 recapitulates the bioclimatic sketching book. This last is the result of the superposition of the obtained bioclimatic, urban, architectural, and functional indicators. It is also the outcome of analyzing the executive decree n^o 14-27 and the synthesis of

bibliographical study which fixes the various actions defining the bioclimatic cold passive strategy.

V. RESULTS AND DISCUSSION

The main aim of the present experiments is to contribute to the reflection by focusing on two essential points. The first one is to check the association concept-image which allows a correct interpretation and a performance appropriation of the bioclimatic concepts. The second one is to validate the practical, economic and creative benefits of a schematized navigation in standard referential of bioclimatic architecture of the Algerian southern provinces.

The results of the experiments are supported by 42 architects from CLOA-Adrar (Local Council of the Architects Order) who have received lessons in academic master in architecture at Adrar University in partnership with the University of Sciences and Technologies of Oran. Work proceeds in exercise form of design before and after the use of the developed sketching book. All the drawings and written traces produced during the experimentation are also reserved. The first step of designed tool is given in figure 5.


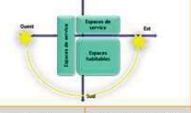

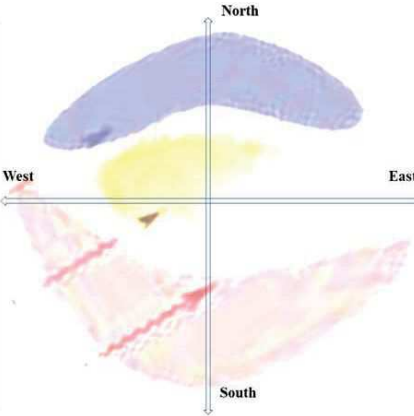


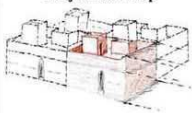
Sketch step	Architectural projet		Final projet		
Process	Implantation and orientation				
Main aims	To protect	To prevent	To get cold	To dissipate	To minimize
Optimal orientation	Climatic zoning		Morphology		
					
Examination, Decree: 14-27 Art: 16, 17, 39, 18,19	Examination, Decree: 14-27	Art: 19, 13, 27, 40	Examination, Decree: 14-27	Art: 13, 14, 18, 27, 28, 30, 40	
La végétation					
					
Examination, Decree: 14-27 Art: 13, 17, 39, 30, 40					
Protection provision					
					
Examination, Decree: 14-27 Art: 06, 07, 08, 14, 17, 39					
The joint ownership					
					
Examination, Decree: 14-27 Art: 27, 28, 31, 40, 13, 10, 14					
Recommendations	Work space				

Fig. 5. sketch step page of designed tool

Thanks to this experiment that we succeeded to improve our sketching book, determine architects' needs in terms of bioclimatic knowledge, and also define the main features of

the suggested approach. It enabled us to check our assumption concerning:

- The presence of several loops of feedback makes it possible to return back in order to take into account the new information generated during the designing process.
- The distinction between the various phases of the design processes especially the beginning and the end with loops between them implies the existence of objective criteria. This illustrates the fact that the objective and its properties guide the mechanism of assistance to generate bioclimatic forms as from the early phase.
- The reliance on the CBR concept and the graphic demonstrations at each level of the design situation enables the possibility to express the idea of the project that one wishes to carry out, or to communicate.

VI. CONCLUSION

The architectural form is remarkably the most significant element in the bioclimatic aspect of any building. The requirements of a bioclimatic design can appear during the first examination as an impoverishing constraint. In fact, in the professional space, we should seek shape of buildings adapted as much as possible with naturel variables, as well in architectural as of technical aspects. Many successful projects on the aesthetic level prove however that a bioclimatic architecture of quality is possible.

Thus, beyond the "thermomechanical behavior" aspect, we can integrate the bioclimatic concerns within the architectural intention, and it is possible to use the bioclimatic concept as an element of architectural expression.

The present model shows two sorts of information framing the representation and the progress of the architectural project; the first is meant to answers the question: « *what is to be done?* ». The answer could be considered as a source of bioclimatic conceptual ideas. And the second is an esthetic answer to the question: « *how it will look like?* ». Its role is to seek conceivable solution forms. The suggested tool can be is conceived to be a tool of assistance and for decision-makers during early stages of the design process. Additionally, it can be used as a tool of communication with the common public.

REFERENCES

- [1] K. pal SANKAR, SIMON c.k.Shui, Foundation of soft case-based-reasoning, vol 2, 150, 2004.
- [2] R. Prost, " conception architecturale une investigation méthodologique," l'Harmattan (ed), French, 1992.
- [3] P. Fernandez, " stratégie d'intégration de composante énergétique dans la pédagogie du projet d'architecture," Ph.D. dissertation, école des mines de Paris, French, 1996.
- [4] M. Benabdefattah, Y. Kehila, H. Khelafi, and N. Djarfour, "Intégration du "RBC" à la prise de decision pour assister l'architecture parasismique; contribution méthodologique," *African Review of Science, Technology and Development*, vol. 3, no. 1, pp. 07-17, 2018.
- [5] S. Mazouz and M. S. Zeouala, "The integration of environmental variables in the process of architectural design; the contribution of

- expert systems,” *Elsevier, J. Energy and Buildings*, vol. 33, pp. 699-710, 2001.
- [6] A. Bendeddouch, “Le processus d’élaboration d’un projet d’architecture,” *L’Harmattan ed.* Montréal, French, 1998, p327.
- [7] C.K. Riesbeck, and R.C. Schank,, (1989), “*Inside Case-Based Reasoning*,” Lawrence Erlbaum Associates, Inc.: Hillsdale, New Jersey.
- [8] B. Fadi, “*Extraction de connaissances d’adaptation en raisonnement à partir de cas*,” Thèse de doctorat : informatique, Ecole doctorale IAEM Lorraine UFR STMIA : Département de formation doctorale en informatique, 2009.
- [9] S. Hamrani, “ L’insertion passive des bâtiments dans un climat désertique ; État de lieu et recommandations ; Cas de la wilaya d’Adrar – Algérie,” M.D. dissertation, University of Sciences and Technologies, USTO, Oran Algeria, 2017.
- [10] M. BRET, “ Image de synthèse : méthodes et algorithmes pour la réalisation d’images numériques,” St-Jean/Richelieu, Dunod (ed), Bo-Pré, Paris, French, 1988.
- [11] Benabdelfattah M., Kehila Y., Makhloufi A. (2018) Meeting Paraseismic Knowledge Needs of Algerian Architects. In: Kallel A., Ksibi M., Ben Dhia H., Khélifi N. (eds) Recent Advances in Environmental Science from the Euro-Mediterranean and Surrounding Regions. EMCEI 2017. Advances in Science, Technology & Innovation (IEREK Interdisciplinary Series for Sustainable Development). Springer, Cham.
- [12] Leplat, J., (2002), De l’étude de cas à l’analyse de l’activité, In :PISTES, perspectives interdisciplinaires sur le travail et la santé, 4(2), DOI : 10.4000/pistes.3658.
- [13] Halin G., Chaabouni S., et Bignon J-C. (2007), Recherche de références par l’image dédiée à l’assistance à la conception architecturale. In : SCAN’07, Séminaire de Conception Architecturale Numérique, 20 novembre 2007.
- [14] S. KACHER, “ proposition d’une méthode de référencement d’images pour assister la conception architecturale : Application à la recherche d’ouvrages,” Ph.D. dissertation, l’Institut National Polytechnique de Lorraine Discipline, Sciences de l’architecture, 2005.
- [15] Djafi, F., (2005), *L’apport du réalisme visuel à la représentation de l’image de synthèse dans un contexte de conception architecturale assistée par ordinateur (CAAO)*, Mémoire de maîtrise : Sciences de l’architecture, Université Laval QUÉBEC : Faculté des études supérieures.
- [1] L. Khelifi, “ Contribution méthodologique à la conception bioclimatique en architecture; développement de modèles génériques,” M.D. dissertation, Ecole polytechnique d’architecture et d’urbanisme, EPAU d’Alger-Algérie, 2006.

Predictive MRAS Sensorless Vector Control of Induction Motor Drives

Moustafa zair¹, Abdeldejbar Hazzab²

^{1,2}Departement of Electrical Engineering, Tahri Mohammed Bechar University

Street of independence, BP 417, Bechar, Algeria.

¹zairm29@yahoo.fr

²hazzab@yahoo.fr

Abstract—In this paper presents the predictive model reference adaptive system (PMRAS) rotor speed observer, This observer developed from the classical MRAS rotor flux scheme associated with predictive adaptation mechanism designed from the Finite Control Set Model Predictive Control (FCS–MPC) by using a search optimization algorithm for calculate the rotor position which guarantee a minimum speed tuning error signal at each sampling period. The effectiveness of the proposed observer proved with the simulation results, show high dynamic performance speed and position observed in sensorless vector control process at low and zero speed as well robustness against motor parameter variation with different loading conditions.

Keywords— Sensorless, IFOC, Classical and Predictive MRAS

I. INTRODUCTION

For many years, lots of efforts have been made in ac drives to eliminate the speed sensor mounted on the machine shaft this technology is referred as sensorless control [1]. In this study presented, the predictive MRAS speed observer based from the classical MRAS rotor flux scheme associated with the adaption mechanism designed from the Finite Control Set Model Predictive Control (FCS–MPC) by using a search algorithm developed to ensure the rotor position each sampling time and minimizing the speed tuning error signal to solve the problems associated with the adaption mechanism design.

II. MATHEMATICAL MODELS IM AND VECTOR CONTROL

A. THE IM MODEL

After use the vector control, the induction machine can be represented as a two-phase motor in a stationary reference frame (α, β) and then convert in synchronously dynamic reference frame (d, q) by applying Park transformation. The mathematical models of an IM can be described by the following state equations [2], [3], [4], [5].

$$\begin{aligned} \dot{X} &= AX + BU \\ Y &= CX \end{aligned} \quad (1)$$

With X : state variables, A : system evolution matrix, B : control vector, U : input vector it is represented by the tension vector.

$$X = \begin{bmatrix} i_{sd} \\ i_{sq} \\ \phi_{rd} \\ \phi_{rq} \end{bmatrix}, \quad U = \begin{bmatrix} V_{sd} \\ V_{sq} \end{bmatrix}, \quad B = \begin{bmatrix} b & 0 \\ 0 & b \\ 0 & 0 \\ 0 & 0 \end{bmatrix}, \quad C = \begin{bmatrix} 1 & 0 & 0 & 0 \\ 0 & 1 & 0 & 0 \end{bmatrix},$$

$$A = \begin{bmatrix} a_1 & \omega_s & a_2 & a_3 \\ -\omega_s & a_1 & -a_3 & a_2 \\ a_4 & 0 & a_5 & \omega_{sl} \\ 0 & a_4 & -\omega_{sl} & a_5 \end{bmatrix}$$

$$a_1 = -\frac{1}{\sigma L_s} \left(R_s + \frac{L_m^2}{T_r L_r} \right), \quad a_2 = \frac{L_m}{\sigma T_r L_r L_s}, \quad a_3 = \frac{L_m}{\sigma L_s L_r} \omega_r,$$

$$a_4 = \frac{L_m}{T_r}, \quad a_5 = -\frac{1}{T_r}, \quad b = \frac{1}{\sigma L_s}, \quad \omega_{sl} = \omega_s - \omega_r,$$

$$\sigma = 1 - \frac{L_m^2}{L_s L_r}, \quad T_r = \frac{L_r}{R_r}, \quad T_s = \frac{L_s}{R_s}$$

The mechanical equation is

$$J \frac{d\Omega}{dt} = C_e - C_r - f \Omega \quad (2)$$

Where the electromagnetic torque is

$$C_e = \frac{3PL_m}{2L_r} (\phi_{rd} i_{sq} - \phi_{rq} i_{sd}) \quad (3)$$

B. Indirect Rotor Flux Orientation control

The purpose of the flux rotor orientation is to decouple the stator current into flux and torque producing components, regulated separately, to obtain a good performance IM drive [3], [6], [7]. For vector control, the rotor flux is oriented in the d-axis

$$\phi_{rq} = 0, \quad \phi_{rd} = \phi_r \quad (4)$$

$$\text{The slip frequency is obtained as } \omega_{sl} = \frac{L_m}{\phi_r T_r} i_{sq} \quad (5)$$

The electromagnetic developed torque equation is given by

$$C_e = \frac{3PL_m}{2L_r} \phi_{rd} i_{sq} \quad (6)$$

III. THE ROTOR FLUX MRAS OBSERVER

The conventional rotor flux MRAS speed observer shown in figure 1. It usually consists of two mathematical models, the reference and adaptive models, and an adaptation mechanism to generate the observer speed.

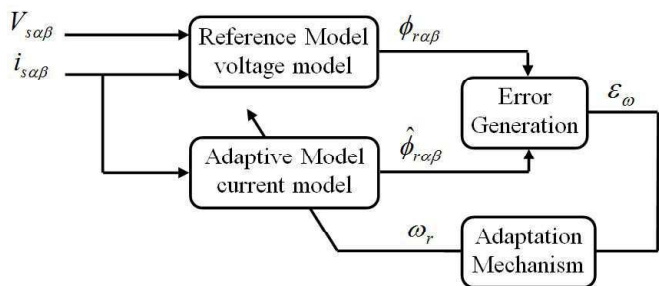


Fig. 1 The classical rotor flux MRAS observer

The reference model represents the stator voltage equation in the stator reference frame. It generates the reference value of the rotor flux component from the monitored stator voltage and current components which can be written as [1], [8], [9], [10].

$$p\phi_{r\alpha} = \frac{L_r}{L_m}(V_{s\alpha} - R_s i_{s\alpha} - \sigma L_s p i_{s\alpha}) \quad (7)$$

$$p\phi_{r\beta} = \frac{L_r}{L_m}(V_{s\beta} - R_s i_{s\beta} - \sigma L_s p i_{s\beta}) \quad (8)$$

where $\phi_{r\alpha}$, $\phi_{r\beta}$ are the alpha and beta reference rotor flux components; $i_{s\alpha}$, $i_{s\beta}$ are the stator current; $V_{s\alpha}$, $V_{s\beta}$ are the stator voltage, all expressed in a stationary reference; p is the laplacian.

The adaptive model represents the current model, describes the rotor voltage equations in the stator reference frame where the rotor flux components are expressed in terms of stator current components and the rotor speed. The rotor flux components are given by [1], [8], [9], [10].

$$p\hat{\phi}_{r\alpha} = \frac{L_m}{T_r} i_{s\alpha} - \frac{1}{T_r} \hat{\phi}_{r\alpha} + \omega_r \hat{\phi}_{r\beta} \quad (9)$$

$$p\hat{\phi}_{r\beta} = \frac{L_m}{T_r} i_{s\beta} - \frac{1}{T_r} \hat{\phi}_{r\beta} + \omega_r \hat{\phi}_{r\alpha} \quad (10)$$

where $\hat{\phi}_{r\alpha}$, $\hat{\phi}_{r\beta}$ are the alpha and beta adaptive rotor flux components;

The adaptation mechanism generates the value of the observer speed. It is based mainly on the hyperstability theory the conventional rotor flux MRAS scheme, this is performed by defining a speed tuning signal ε_ω to be minimized by a PI controller, which generates the observer speed that is feedback to the adaptive model. The error speed is the difference among the product of rotor flux of reference and adaptive model. The expressions for the speed tuning signal and the observer speed can be given as [1].

$$\varepsilon_\omega = \phi_{r\beta} \hat{\phi}_{r\alpha} - \phi_{r\alpha} \hat{\phi}_{r\beta} \quad (11)$$

$$\omega_r = \left(k_p + \frac{k_i}{p} \right) \varepsilon_\omega \quad (12)$$

The velocity variant cross coupling due to speed rotor dependent components in the adaptive model can guide to an instability issue. Therefore, it is common for the rotor

flux equation represented in the rotor reference frame to be used [11].

$$\hat{\phi}_{rd} = \frac{L_m}{1+T_r p} i_{sd} \quad (13)$$

$$\hat{\phi}_{rq} = \frac{L_m}{1+T_r p} i_{sq} \quad (14)$$

where $\hat{\phi}_{rd}$ and $\hat{\phi}_{rq}$ are the rotor flux components all expressed in the rotor reference frame. The implementation of the rotor frame-based flux model is shown in Figure 2.

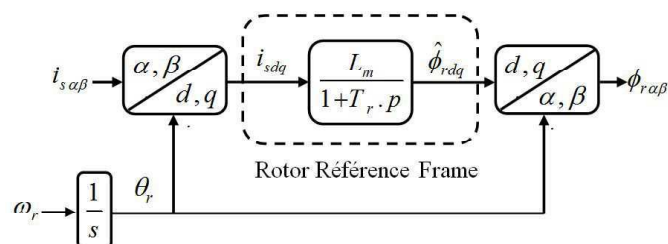


Fig. 2 The Adaptive model in the rotor reference frame

IV. THE PREDICTIVE MRAS SPEED OBSERVER

The predictive MRAS speed observer (PMRAS) is developed from the Finite Control Set Model Predictive Control (FCS-MPC). The MPC is a modern digital control technique that offers a powerful tool to deal with control problems of power converters and electric drives. The main prominences of FCS-MPC are its compact design and flexibility to include many additional control targets. By considering only finite possible states of the inverter, solving the cost function would be straightforward.

The FCS-MPC use to design the adaptation mechanism in MRAS speed observer. An optimization problem is formulated to find the rotor position in order to minimize the speed tuning signal ε_ω . The rotor position varied between 0 and 2π continuously; a search technique discretized the rotor position into a limited number of positions to allow calculating the cost function at each of these discrete positions. The predictive MRAS observer is shown in Figure 3 [12] [13].

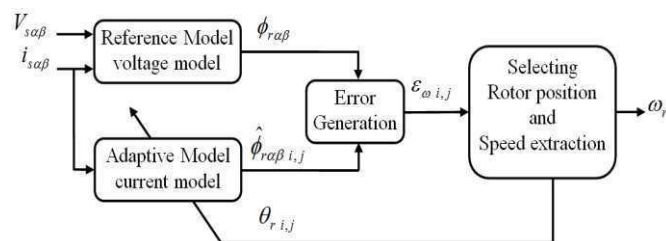


Fig. 3 The predictive MRAS speed observer

The search algorithm is shown in Figure 4 starts by calculating the reference model outputs $\phi_{r\alpha}$, $\phi_{r\beta}$, also initializing the base angle θ_{base} and the error speed ε_ω , and calculating a displacement ($\Delta\theta_i$) can be given as

$$\Delta\theta_i = \frac{\pi}{4} \cdot 2^{-i} \quad (15)$$

where i is the order of the current iteration.

The discrete rotor position as follows

$$\theta_{i,j} = \theta_{base} + \Delta\theta_i \cdot (j-4) \quad (16)$$

Where j is the order of the displacement.

Each discrete position $\theta_{i,j}$ used to calculate the adaptive model outputs corresponding to each individual position $\hat{\phi}_{r\alpha}, \hat{\phi}_{r\beta}$. Therefore, the cost function $\varepsilon_{i,j}$ is calculated for each position as follows:

$$\varepsilon_{i,j} = \phi_{r\beta} \hat{\phi}_{r\alpha i,j} - \phi_{r\alpha} \hat{\phi}_{r\beta i,j} \quad (17)$$

After each iteration, the search algorithm gets closer to the optimal solution, which produces the minimum cost function throughout the search space, is selected as the output rotor position of the observer. The speed signal get by the average value of the change in rotor position, dividing by the simple period as follows [14].

$$\omega_r = \frac{2\pi}{60} \frac{\Delta\theta_{average}}{t_s} \quad (18)$$

$$\Delta\theta_{average} = \frac{1}{x} \sum_{n=1}^x (\theta_{rotor}(k) - \theta_{rotor}(k-1))_n \quad (19)$$

$\Delta\theta_{average}$: The average value of the change in rotor position,

x : Recorded of the change in rotor position,

t_s : Simple period.

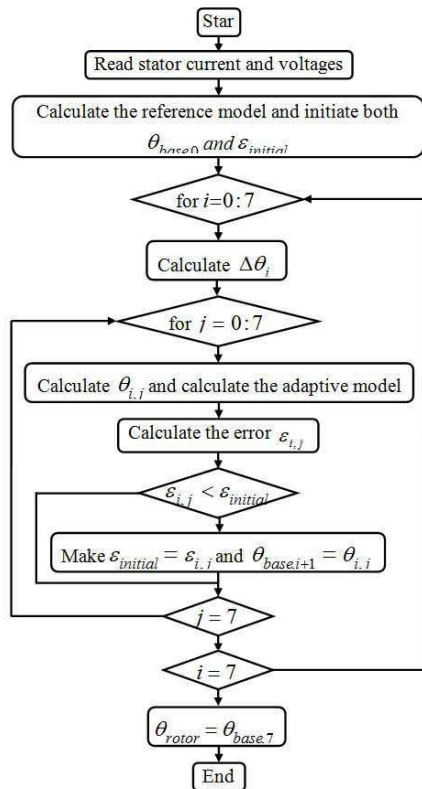


Fig. 4 The rotor position search algorithm

V. SIMULATION RESULTS AND DISCUSSIONS

In this section, the simulate system used the induction machine, the IFOC scheme for vector control is driven by two observers speed, the classical rotor flux MRAS with PI controller, the gains are set to $K_p=1000$ and $K_i=10000$ which are tuned using trial error method to obtain the optimal dynamic performance, and the predictive MRAS with a search algorithm to ensure the sensorless and evaluate the comparative. Simulation results obtained in MATLAB/Simulink environment. The block diagram of sensorless induction motor drive with CMRAS/PMRAS speed observers show in figure 5. The motor parameters are presented in Table1.

Table 1. Induction Motor Parameters

Designation	Quantity
Rated power	1.5kW
Rated voltage	220V
Rated speed	1428rpm
Nominal frequency	50Hz
Stator resistance	4.85Ω
Rotor resistance	3.805Ω
Cyclic stator inductance	0.274H
Cyclic rotor inductance	0.274H
Mutual inductance	0.258H
Number of pole pairs	2
Moment of inertia	0.031kg/m2
Friction coefficient	0.00114Nm.s/rd

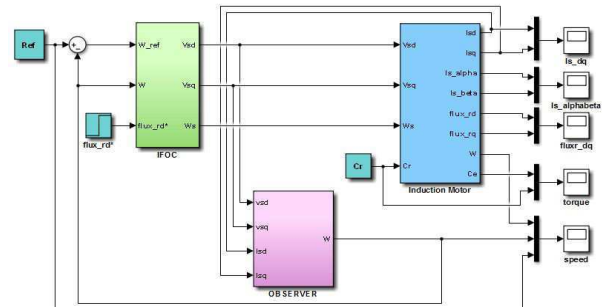


Fig. 5 Block diagram of sensorless induction motor drive with CMRAS/ PMRAS speed observers

The simulation results presented and discussed from testes the performance of both observers under the following conditions:

- The speed reference star between times 0.5 and 1.5s augmented from 0 to 100rad/s, then between times 3.5 and 4.5s reduced from 100 to 0rad/s, next between times 5.5 and 6.5s reversed from 0 to -100rad/s and finally between times 8.5 and 9.5s augmented from -100 to 0rad/s.
- Zero speed between times 0 and 0.5s, also between times 4.5 and 5.5s, moreover between times 9.5 and 10s.
- The load torque applying 10 Nm between times 2 and 3s
- The change of rotor resistance up to 50% at time 2s.
- The change of stator resistance up to 50% at time 2s.

In figure 6, illustrates the sensorless performance of induction motor drive with PMRAS observer, the rotor speed observer and reference depicted in (a), the rotor position generate from the search optimization algorithm depicted in

(b), phase current depicted in (c), d & q axis stator currents depicted in (d), alpha & beta axis rotor fluxes depicted in (e), the electromagnetic and load torque depicted in (f).

According to these satisfactory results, the proposed observer show a high dynamic performance, the FOC control technique ensures a good regulation also a dynamic torque response and full decoupling between flux and torque. The rotor speed observed precise tracking the reference including low and zero speed, moreover robustness against a reversal speed, the load torque disturbance variation and very rapid rejection.

In figure 7, illustrates the comparative sensorless performance of induction motor drive between CMRAS and PMRAS observers, the rotor speed observer of CMRAS, measured and reference depicted in (a), the rotor speed observer of PMRAS ,measured and reference depicted in (b), speed error of CMRAS depicted in (c), speed error of PMRAS depicted in (d).

For this important results obtained, the PMRAS show superiority in comparison with CMRAS. The predictive observer proved a better tracking between the reference and the adaptive model; also reject the load torque three times faster than the CMRAS.

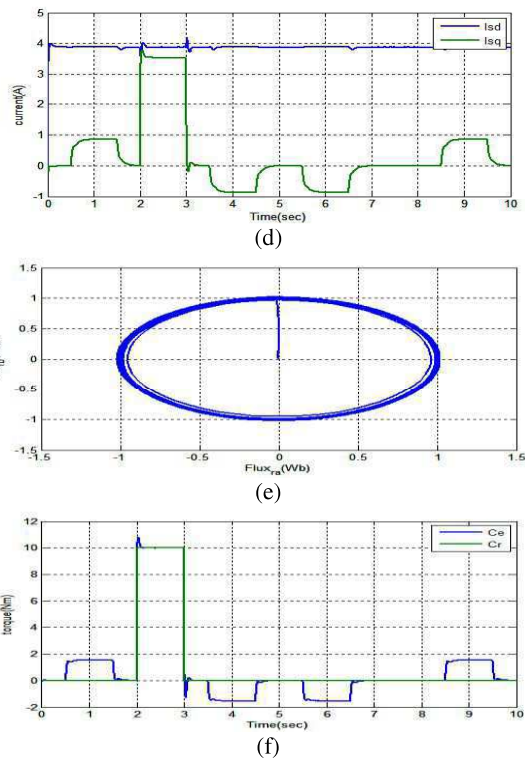
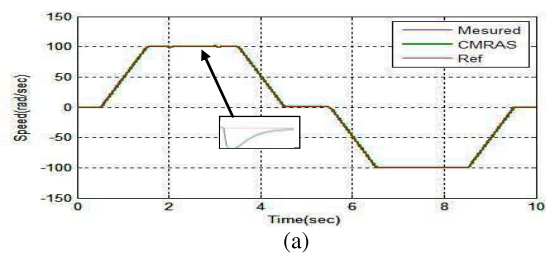
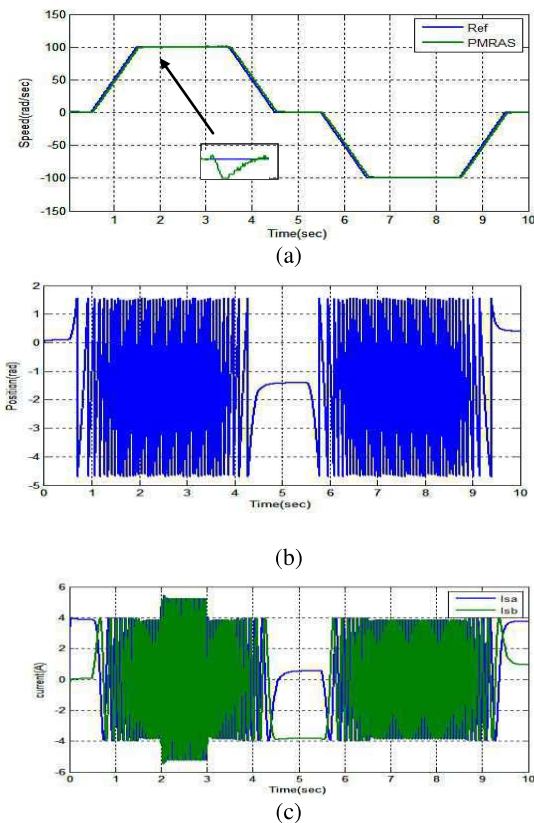


Fig. 6 simulation results of sensorless performance of induction motor drive with PMRAS observer (a) rotor speed, (b) rotor position (c) phase current, (d) d & q axis stator currents, (e) alpha & beta axis rotor fluxes, (f) torque

In figure 8, illustrates the sensorless performance of induction motor drive with impact of rotor and stator resistances change, the rotor speed observer of CMRAS and reference depicted in (a,e), the rotor speed observer of PMRAS depicted in (b,f), speed error of CMRAS depicted in (c,i), speed error of PMRAS depicted in (d,j).

For these significant results, the PMRAS show again à better quality and performance, also high robustness against the rotor and stator resistances change. Figures (a, b) show the rotor speed of both observers work perfect. In figures (c,d) show the PMRAS give a high robustness and more stability against the rotor resistance change. Figure (e,f) show again the PMRAS a better robustness against the stator resistance change with steady and less oscillations then the CMRAS



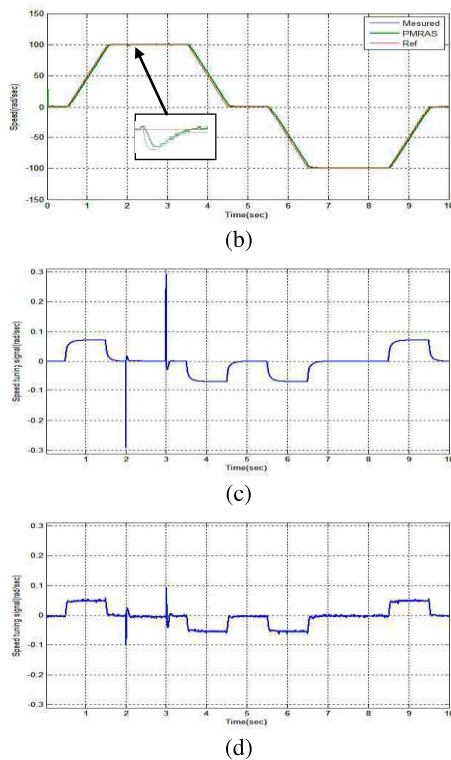


Fig.7 simulation results of comparative sensorless performance of induction motor drive between CMRAS and PMRAS observers (a) rotor speed CMRAS, (b) rotor speed PMRAS, (c) speed error CMRAS, (d) speed error PMRAS.

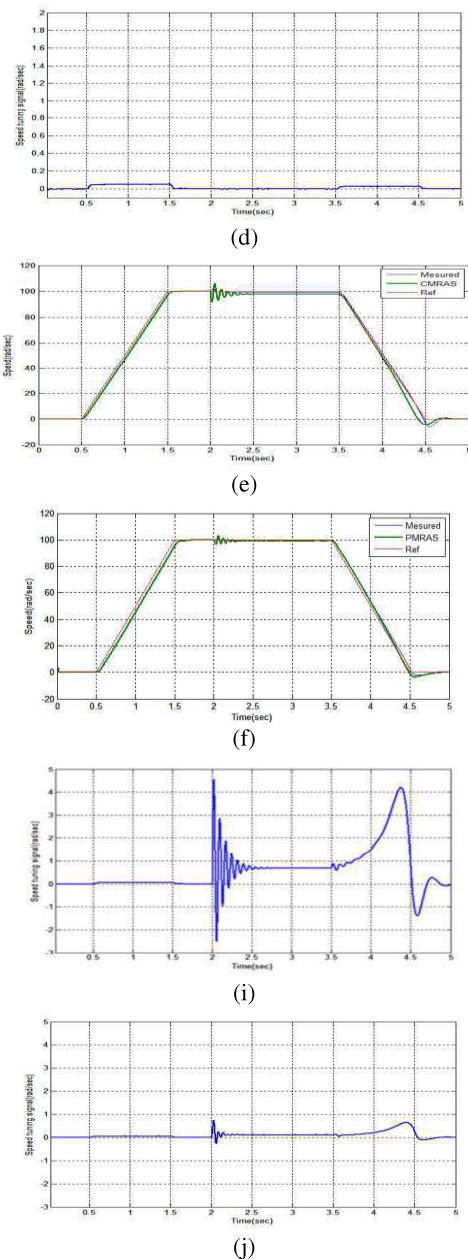
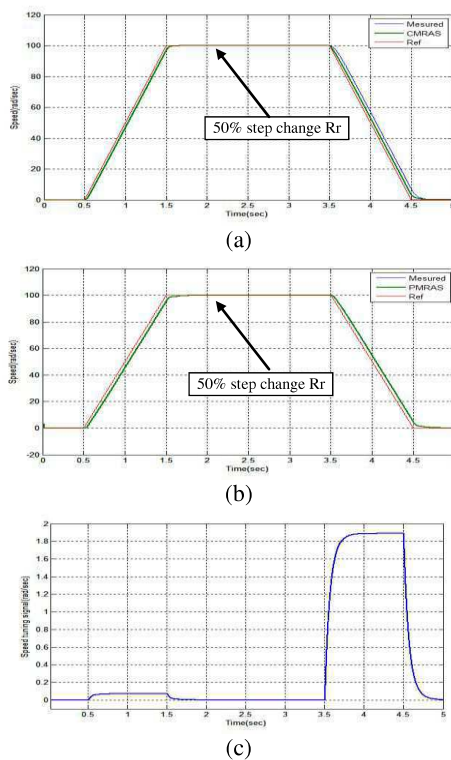


Fig. 8 simulation results of sensorless performance of induction motor drive with impact of rotor and stator resistances change. (a,e) rotor speed CMRAS, (b,f) rotor speed PMRAS, (c,i) speed error CMRAS, (d,j) speed error PMRAS.

VI. CONCLUSIONS

In this paper, a predictive model reference adaptive system (PMRAS) rotor speed observer for sensorless induction motor drives has been presented. These models create from the classical MRAS rotor flux observer and the finite control set model predictive control (FCS-MPC). The success of this combination proved with the satisfactory simulation results, show clearly excellent observation and robustness against external disturbances and motor parameter variation under different operating conditions, especially at zero speeds.

REFERENCES

- [1] P. Vas, *Sensorless Vector and Direct Torque Control*. London, U.K.: Oxford Univ. Press, 1998.
- [2] Bose. B. K, *Modern Power Electronics and AC Drives*. New Delhi, India: Prentice-Hall, 2006, ch. 8, pp. 333–435.
- [3] Ghlib Imane, Messlem Youcef, Gouichiche Abdelmadjid, Chedjara Zakaria, “Neural Adaptive Kalman Filter for Sensorless Vector Control of Induction Motor“ *International Journal of Power Electronics and Drive System (IJPEDS)*, vol. 8 (2017), no 4.
- [4] A. alalei, A.hazzab, Ali nesba “ Self-Tuning Fuzzy Based PI Controller for DFIM Powered by Two Matrix Converters“ *International Journal of Power Electronics and Drive System (IJPEDS)*, vol. 7 (2016), no 3
- [5] A. Omari, I. K. Bousserhane, A. Hazzab, B. Bouchiba, “dSPACE DS1104 Based Real Time Implementation of Sliding Mode Control of Induction Motor“ *International Journal of Power Electronics and Drive System (IJPEDS)*, vol. 9 (2018), no 2.
- [6] S. Huang, Y. Wang, J. Gao, J. Lu, and S. Qiu “The vector control based on MRAS speed sensorless induction motor drive,” in *Proc. World Congr. Intell. Control Automat.* 2004, vol. 5, pp. 4550–4553.
- [7] M. Montanari, S. Peresada, A. Tilli, A. Tonielli, “Speed sensorless control of induction motor based on indirect field-orientation,” in *Proc. Ind. Appl. Conf.*, 2000, vol. 3, pp. 1858–1865.
- [8] C. Schauder, “Adaptive speed identification for vector control of induction motors without rotational transducers,” *IEEE Trans. Ind. Appl.*, vol. 28, no. 5, pp. 1054–1061, Sep./Oct. 1992.
- [9] Hechelef Mohammed, Abdelkader Meroufel, “ Contribution to the Artificial Neural Network Speed Estimator in a Degraded Mode for Sensor-Less Fuzzy Direct Control of Torque Application Using Dual Stars Induction Machine“*International Journal of Power Electronics and Drive System (IJPEDS)*, vol. 5 (2015), no 4.
- [10] Mohamed Horch, Abdelmadjid Boumediene, Lotfi Baghli, “MRAS-based Sensorless Speed Integral Backstepping Control for Induction Machine, using a Flux Backstepping Observer “*International Journal of Power Electronics and Drive System (IJPEDS)*, vol. 8 (2017), no 4.
- [11] P. L. Jansen and R. D. Lorenz, “A physically insightful approach to the design and accuracy assessment of flux observers for field oriented induction machine drives,” *IEEE Trans. Ind. Appl.*, vol. 30, no. 1, pp. 101–110, Jan./Feb. 1994.
- [12] S. Saeidi and R. Kennel, “A novel algorithm for model predictive control of AC electrical drives,” in *Proc. 2nd Int. Elect. Drives Prod. Conf. (EDPC)*, 2012, pp. 78–84.
- [13] S. Alireza Davari, D. A. Khaburi, and R. Kennel, “An improved FCSMPC algorithm for an induction motor with an imposed optimized weighting factor,” *IEEE Trans. Power Electron.*, vol. 27, no. 3, pp. 1540–1551, Mar. 2012.
- [14] Yaman B. Zbede, Shady M. Gadoue, and David J. Atkinson” Model Predictive MRAS Estimator for Sensorless Induction Motor Drives” *IEEE Trans. Ind. Electron.*, vol. 63, no. 6, pp. 3511–3521, June 2016.

Extraction of Zn (II) in acetate medium by 8- Hydroxyquinoline.

Fatiha.Zaoui ^{#1,2} , Mohamed Amine .Didi ^{*2} , Didier Villemin ^{*3}

1. University of Saïda, Faculty of Sciences, Department of Chemistry, PB 139, 20000, Saïda, Algeria

2. University of Tlemcen, Faculty of Sciences, Department of Chemistry, Laboratory of Separation and Purification Technology, PB 119, 13000, Tlemcen, Algeria

¹zaouifatih@yahoo.fr

3. University of Caen, ENSICAEN, Laboratory of Molecular and Thio-organic Chemistry (LCMT), UMR CNRS 6507, INC3M, FR 3038, Labex EMC3, 14050 Caen, France

Abstract –The objective of this work is the liquid-liquid extraction of Zn (II) in an acetate medium by the 8-hydroxyquinoline quinoline compound known by these chelating properties, with respect to heavy divalent metals, as well as these important biological and pharmacological properties. Various parameters have been optimized such as contact time, concentration of aqueous phase, mass of extractant, pH effect and salt effect. The thermodynamic study showed that the extraction process is spontaneous ($\Delta G < 0$) and exothermic ($\Delta H < 0$). On the other hand, the extractant forms a yellow solid complex of structure $M(C_9H_7NO)_2$ confirmed by IR analysis.

Keyword-The 8-Hydrox quinoléine, Environnement, Zinc, Extraction liquid – liquid

1. INTRODUCTION

8-Hydroxyquinoline (8HQ), a derivative of the original quinoline, has been used as an agricultural fungicide and a preservative in the textile, wood and paper industries, 8HQ is a powerful chelant that can restore balance of metals and be useful for the treatment of metal-related diseases[1-7].

8-Hydroxyquinoline (1-8-HQ) (or quinolinol) is a non-specific ligand chelating a large variety of metal ions[8-9]. 8-Hydroxyquinoline is able to chelate essential metallic ions for metabolism of bacteria and fungi, so 8-HQ derivatives are used as antibacterial and antifungal. 8-HQ complexes of Zn or Mn can be also used for such applications[10-14].

Metal complexes of 8-hydroxyquinolines were used in supramolecular chemistry as luminescent or fluorescent solids [4].

The objective principles of this work fall within this framework. We propose to study the liquid-liquid extraction of zinc (II) in an acetate medium

by 8'-hydroxyquinoline and to determine the optimum conditions for extraction.

II. MATERIALS AND METHODS

All commercial reagents were purchased from Prolabo or Aldrich, and were used as received without further purification.

Spectro201plusUV-VISIBLE spectrophotometer and a consort C831 PH meter with combined glass electrode were used for concentration and Ph measurement

The FTIR spectrum was recorded on a Bruker Vector 22 spectrophotometer

Processing of extraction

8-HQ, which is soluble in ethyl acetate and chloroforme, was taken as the organic solvent throughout this study. Equal volumes of organic and aqueous phases (5 mL) were agitated for 30 min (enough for equilibrium) at 22°C under the desired experimental conditions. The two phases were then separated by decantation and assayed by taking known aliquots from the aqueous phases. The zinc concentrations in the aqueous phase were determined, before and after extraction spectrophotometrically.

III. RESULTS AND DISCUSSION

A. *The contact time determined by a kinetic extraction study of Zn (II)*

The contact time is 30 minutes for chloroform and 45 minutes for ethyl acetate.

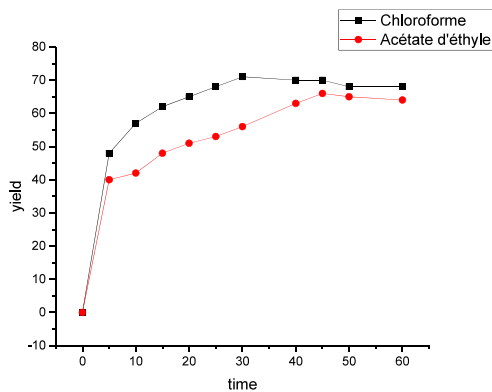


Figure 1: Kinetic of extraction of Zn (II) $pH_i = 4,5$ $T^\circ = 20C$
 $[Zn(II)] = 10^{-2}M$ $[8HQ] = 10^{-2}M$

B. Volume ratio

The ratio Q between the volume of the organic phase and the volume of the aqueous phase is very important in a liquid-liquid extraction

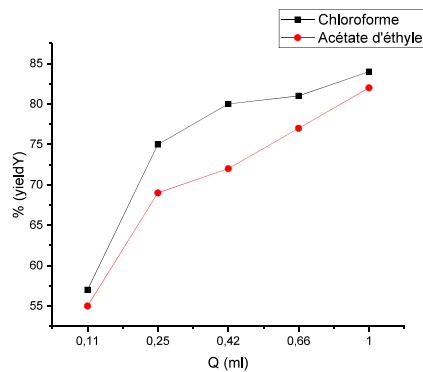


Figure 2: Effect of volume ratio $pH_i = 4,5$ $T^\circ = 20C$ $[Zn(II)] = 10^{-2}M$ $[8HQ] = 10^{-2}M$ $Q=1$

The results for the two solvents show that the best yield is obtained from a volume ratio equal to 1, so to carry out this extraction it is necessary to take the same volume of the organic and aqueous phase

C. Effect of the initial Zn (II) concentration of the aqueous phase

The effect of the concentration of the aqueous phase on the extraction yield was examined in the following concentration range: $[Zn^{2+}] = 10^{-3}$ to $0.005M$

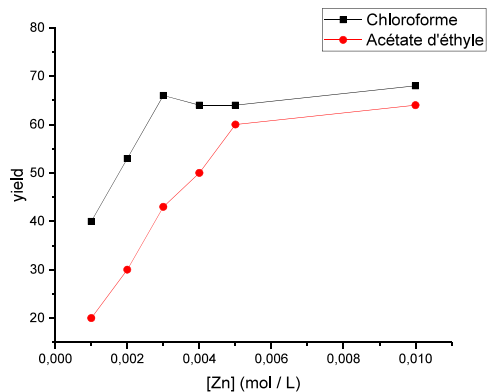


Figure 3: Effect of the concentration initiale of Zn (II) extraction yield of Zn(II) $pH_i = 4 - 5$ $T^\circ = 20C$ $[Zn(II)] = 10^{-2}M$ $[8HQ] = 10^{-2}M$

According to this result the optimal concentration of the feed phase will be taken equal $10^{-2}M$.

D. Effect of the initial pH of the aqueous phase

The study of the influence of the initial pH of the aqueous phase on the extraction yield was examined by adding suitable quantities of hydrochloric acid

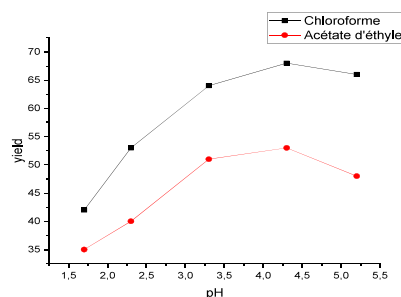


Figure 4: Effect of pH_i on extraction yield of Zn(II) $[Zn(II)] = 10^{-2}M$ $T^\circ = 20^\circ C$ $V_{aq}/V_{org} = 1$ $[8HQ] = 10^{-2}M$

From the figure it can be seen that the extraction efficiency decreases with the increase in the acidity of the medium, this result shows that the extraction of metal is carried out by proton exchange with the aqueous phase. The progress of the extraction reaction increasingly enriches the aqueous phase with H^+ . Therefore, in order to carry out the extraction in good yield, it must work in the less acidic medium possible, in order to avoid the formation of precipitates $Zn(OH)_2$, $Zn(OH)_4^{2-}$

E. Effect of the extractant mass on the extraction of Zn (II)

We conclude from the optimal mass of the extractant is of the order 0.2 g for the two solvents

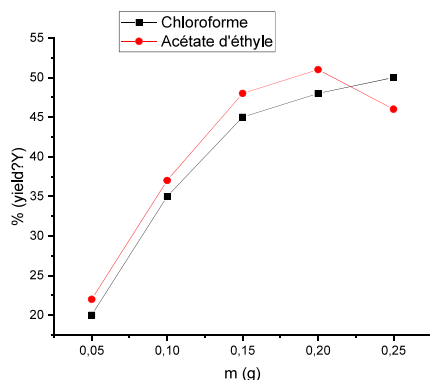


Figure 5: yield of extraction on fonction weight of extractant
 $pH_i = 4,5$ $T^\circ = 20C$ $[Zn(II)] = 10^{-2}M$

F. Effect of salt

We tried in this study to see the effect of addition of CH_3COONa salt at different concentrations on Zinc (II) extraction yields.

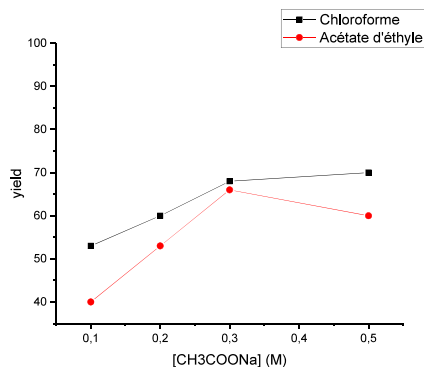


Fig.6: Effect of the addition of Sodium Acetate on the extraction yield of Zn(II)

According to the figure in note the increase yield is due to the increase in ionic strength and then decreases due to the competition of Sodium with the Zinc during the extraction which makes the zinc more accessible to the interface of the extractant.

G. Effect of temperature:

The effect of temperature on Zinc extraction has been studied at different temperatures from 22 ° C (295K) to 60 ° C (333K) by heating in a water bath.

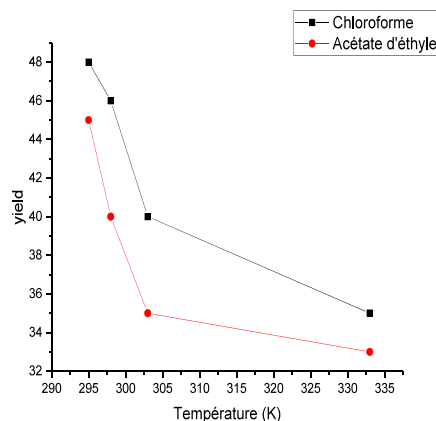


Figure7: Effect of temperature on the yield of extraction $pH_i = 4,5$ $T^\circ = 20C$ $[Zn(II)] = 10^{-2}M$ $[8HQ] = 10^{-2}M$

According to the figure, a temperature increase of the extraction in the range (295a3330k) decreases the extraction yield.

H. Study of thermodynamic parameters

The study of the temperature effect also made it possible to determine the thermodynamic parameters of the extraction, in our operating conditions, such that free enthalpy (ΔH), entropy (ΔS) and free enthalpy (variation in the Gibbs function) (ΔG). These thermodynamic parameters are calculated using the following equations:

$$\Delta G^\circ = -RT \ln K$$

$$\Delta G^\circ = \Delta H - T \Delta S$$

From these two equations we derive the following equation, which will allow us to calculate ΔH and ΔS by plotting the curve which gives the evolution of the constant K as a function of the temperature.

$$\ln K = \frac{-\Delta H}{RT} + \frac{\Delta S}{R}$$

K, T and R are respectively: the partition coefficient of Zn (II) between the two equilibrium phases, the temperature and the perfect gas constant ($R = 8.314 \text{ J. mol}^{-1} \text{ K}^{-1}$).

The partition coefficient is defined by the following expression:

$$K = \frac{[Zn(II)]_{arg}}{[Zn(II)]_{aq}}$$

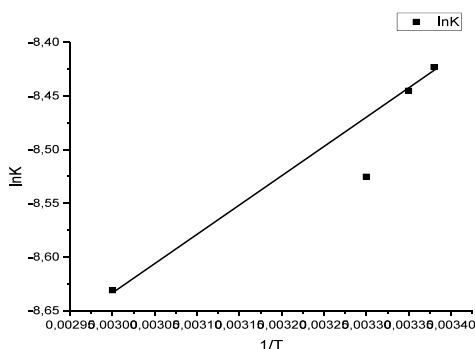


Figure 8: Variation of $\ln K$ in function of $1/T$

The calculated values of ΔH , ΔS and ΔG are summarized in the following table1:

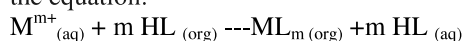
Table 1: Evolution of thermodynamic parameters as a function of temperature

T en K	ΔG (KJ/mol)
295	-3,44
298	-3,41
303	-3,37
333	-3.1

The calculation of ΔH shows that: - The extraction process is exothermic ($\Delta H < 0$). The extraction process is spontaneous ($\Delta G < 0$).

I. Extraction mechanism:

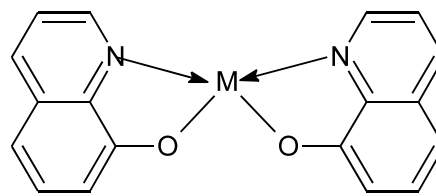
The complexing character of 8HQ is explained by the fact that it creates coordination with O-OH of OH in the formation of water-insoluble complex theoretically the complex formed is of the form $M [C_9H_6ON]_n$ or n the number of charge of the metal in our case $n = 2$ Thus, extraction is carried out by simple proton exchange of the extraction against the divalent cation of the aqueous phase to form a yellow-colored organosoluble complex according to the equation:



J. Spectral study:

In order to confirm the complexation of our metal, we performed ligand IR spectroscopy analysis before and after extraction. The complex is a yellow solid, water-insoluble and soluble in chloroform. The characteristic infrared bands for the 8-hydroxyquinoline ligand (Oxine) and the complex form are shown in fig.10-11 and in table 2 .

The band located at 3236.3cm^{-1} characterizing the OH group. The band 1504 cm^{-1} characterizing the CN bond. The band 1629 cm^{-1} characterizing the CH of the aromatic ring. The band 2856.4 cm^{-1} characterized OH group around two aromatic rings. Then, in the spectrum fig.11 which corresponds to the complex 8HQ-Zn one observes the displacement and disappearance of certain bands and the appearance of new bands, for example the appearance of the characteristic band Zn-N and Zn-O, namely $505.3 - 644.2\text{ cm}^{-1}$. By virtue of these results it is concluded that 8HQ contains two electron donor sites located at the nitrogen atom of the aromatic ring and the atom of oxygen of the second aromatic ring. And the structure of the 8HQ-Zn complex takes the following form:



M= Zn

Figure 9: Structure of complex M-8HQ

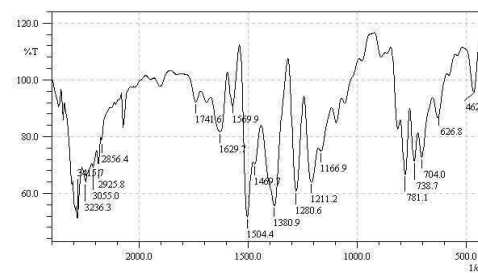


Figure 10: Infrared spectrum of the 8-HQ

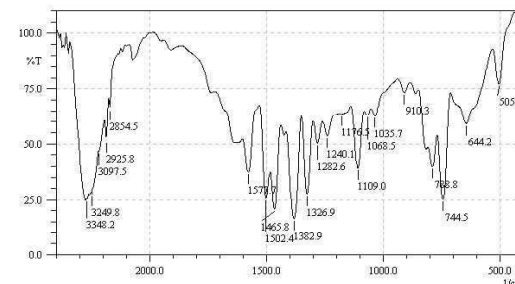


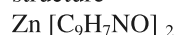
Figure 11: Infrared spectrum of the complex [Zn (8-HQ)]

Table 02:

Compound	ν (CH)	ν (OH)	ν (C-N)	ν (C-O)	ν (Zn-N)	ν (Zn-O)
Oxine (8HQ)	1629	3236.3 2856.4	1504	1280	----- ----	----- --
Zn (oxine)₂	1577	3348	1465.8	1326.9	505.3	644.2

IV. CONCLUSION

The 8-hydroxyquinoline obtained exhibited high efficiency for the uptake and removal of zinc in water and the recovery is quantitative ($\approx 100\%$). The best performance is achieved from a molar ratio equal to 1.. The extraction yield (99.4%) was found to be higher at slightly acid pH. At equilibrium, the extraction yield with chloroform solvent was higher than with ethyl acetate . the thermodynamic parameters showed that the extraction process is exothermic ($\Delta H < 0$) and spontaneous ($\Delta G < 0$). IR spectroscopy confirms the complexation of Zn (II) 8HQ \rightarrow 8HQ forms a stable solid complex of yellow color, and of following structure



REFERENCES

- [1]. Albrecht M, Fiege M, Osetka O. 8-Hydroxyquinoléines dans la chimie metallosupramoléculaire. *Coord Chem Rev.* 2008; 252 (8-9): 812-824.
- [2] a) M. Albrecht, O. Blau. Synthesis of Ethylene-Bridged Bis(8-hydroxyquinoline) Derivatives: New Building Blocks for Metallo Supramolecular Chemistry. *Synthesis.* 1997, 28, 213-216. b) M. Albrecht, K. Witt, R. Fröhlich, O. Kataeva; Inter- and intramolecular hydrogen bonding in amid- and arene-substituted 8-hydroxyquinoline derivatives. *Tetrahedron.* 2002, 58, 561-567.
- [3] B. Erdem, A. Özcan, A. Safa Özcan. Adsorption and solid phase extraction of 8-hydroxyquinoline from aqueous solutions by using natural bentonite. *Applied Surface Sci.* 2010, 256, 5422-5427
- [4] I. Garcia-Santos, J. Sanmartin, A. M. Garcia-Deibe, M. Fondo, E. Gomez. Structural and photophysical studies on a linear trinuclear zinc complex of 2-[(2-hydroxyethylimino) methyl] quinolin-8-ol. *Polyhedron.* 2009, 28, 3055-3059.
- [5] L. E. Sarmiento, M. Rodriguez, L. Echevarria, V. Lubes. Speciation of the Vanadium (III) Complexes with 1, 10-phenanthroline, 2,2'-bipyridine, and 8-hydroxyquinoline. *J. Sol. Chem.* 2010, 39, 1484-1491.
- [6] S. Rubbo, A. Albert, M. Gibson. The influence of chemical constitution on anti-bacterial activity. 5. The anti-bacterial action of 8-hydroxyquinoline. *Br. J. Exp. Pathol.* 1950, 31, 425-441.
- [7] National Toxicology Program (NTP) Technical report on the toxicology and carcinogenesis studies of 8-hydroxyquinoline in F344/N rats and B6C3F1 mice, NTP TR 276, US. 1985 Department of Health and Human Services.
- [8] S. Madonna, C. Beclin et al. Structure-activity relationship and mechanism of action of antitumor bis 8-hydroxyquinoline substituted benzylamines *European J. Med. Chem.* 2010, 45, 2, 623-638..
- [9] a) Q. Zhang, D. Wu, B. Bao. Synergistic extraction of praseodymium with 2-ethylhexyl phosphonic acid mono-2-ethylhexyl ester and 8-Hydroxyquinoline. *J. Shanghai Univ (Engl Ed)* 2009, 13 (1) 72-75, b) C. Wang, Dean; Martin. Cloud-point extraction of chromium(III) ion with 8-hydroxyquinoline derivatives *J. Environmental Sci. and health. Part A, Environmental science and engineering.* 1999, 34 705 - 719. c) T. Moeller. Extraction and Colorimetric Estimation of Certain Metals as Derivatives of 8-Hydroxyquinoline. *Ind. Eng. Chem. Anal. Ed.*, 1943, 15 (5), 346-349.
- [10] a) B. Himmi, Banacer, J. P. Joly, F. Hlimi, M. Soufiaoui, S. Kitane, A. Bahloul, A. Eddaif, A. Sebban. Synthesis of novel 5, 7-substituted 8-hydroxyquinoline. *J. Heterocycl. Chem.* 2008, 45, 4, 1023-1026. b) B. Himmi, B. Messnaoui, S. Kitane, A. Eddaif, A. Bouklouz, M. Soufiaoui Study of Zn (II) extraction by 5-azidomethyl-8-hydroxyquinoline: Experiment and modelling. *Hydrometallurgy.* 2008, 93, 39-44.
- [11] K. Gloe, H. Stephan, T. Krüger, A. Möckel, N. Woller, G. Subklew, M. J. Schwuger, Neumann, E. Weber. Solvent extraction of toxic heavy metal ions with 8-hydroxyquinoline extractants from effluents. *Progress. Colloid. Polym. Sci.* 1996, 10, 145-148.
- [12] L. Li, B. Xu, Synthesis and characterization of 5-substituted 8-hydroxyquinoline derivatives and

their metal complexes *.Tetrahedron*. **2008**, 64, 10986-10995.

[13] D. Wu, Q. Zhang, B. Bao, Solvent extraction of Pr and Nd(III) from chloride-acetate medium by 8-hydroxyquinoline with and without 2-ethylhexyl phosphoric acid mono-2-ethylhexyl ester as an added synergist in heptanes diluent *.Hydrometallurgy* **2007**, 88, 210-215.

[14] F. Zaoui • M.A. Didi • D. Villemin Investigation of 7-((dioctylamino)methyl)quinoline-8-ol for uptake and removal of uranyl ions. *J Radioanal Nucl Chem* (**2013**) 295:419-424. DOI 10.1007/s10967-012-1789-8

Fuzzy Direct Power Control of Voltage Source Rectifier (VSR)

CHAKAR Abdeselem¹, ABDELKHALEK Othmane², TEDJINI Hamza³, GASBAOUI Brahim⁴, HAFSI Ossama⁵, SOUMEUR Mohammed amine⁶

*Dep of Electrical Engineering, University of Tahri Mohammed
Smart Grids & Renewable Energies Laboratory
Rue de l'indépendance B.P 714-08000.Bechar, Algeria*

¹abdeselemchakar@gmail.com

²othmane_elec@yahoo.fr

³tedjini_h@yahoo.fr

⁴gasbaoui_2009@yahoo.com

⁵oussama5bm@gmail.com

⁶amirehamo@gmail.com

Abstract—The main idea of direct power control Depend primarily on, direct control of active and reactive power without any internal control loop and any PWM modulator. The switching states at the rectifier are selected from the switching table where the instantaneous error between the estimation and the reference active and reactive power of choosing the states. Today, almost every intelligent machine has fuzzy logic technology inside it. It presents several advantages, especially its strength. This paper presents a direct power control with integration of FLC for more stability and reduction of harmonics current distortion.

Key words—PWM rectifier, DPC, Fuzzy logic control, harmonic pollution, PI controller

I. INTRODUCTION

In recent decades, the multiplication of the use nonlinear loads during these last decades induces severe problems. The problem lies in the distortion of current and voltage waveforms. Several harmonic pollutions cancellation methods were proposed; the typical one was the connection along the AC side of shunt passive Filters. All the same, they are large and Expensive. Recently, active filtering and PWM Conversion is used in industrial plants [1].

Direct Power Control is a novel technology of control based on the instantaneous Active and reactive power control loops [2].

Noguchi proposes the DPC technical and it's similar to DTC technical for induction motors. In lieu of controlling torque and flux, we control the instantaneous active and reactive powers. For a unity power factor operation The Controlled reactive power Suppose it nil [3]. The Strength point of this technique, there are no internal current control loops and no PWM modulator block, And With that in DPC implementation requires the correct and the instant estimation of the active and reactive line power [2].

The beginning, introduced of the Fuzzy logic is Lofti A Zadeh in 1965in his paper "Fuzzy Sets". Then broke it with a group of scientists because some of the underlying mathematics had not hitherto been explored, this idea of the fuzzy sets and fuzzy logic were not taken well within academic universities. The applications of fuzzy logic were

slow to germinate because of this, except in the Japan. In Japan, specific fuzzy logic was fully taken over and used in products simply because fuzzy logic worked, regardless of whether mathematicians agreed or disagreed. A revival the fuzzy logic in the US in the late 80s See to the success of many fuzzy logic products in Japan. Since that time, America has been playing Catch up with the Japan in the area of fuzzy logic [4]. In this paper, two different Ways of Direct Power Control for rectifier converter have been presented. The first way DPC uses typical PI controllers. The second way DPC introduces an FLC [5].

II. PWM RECTIFIER

A power circuit of the three-phase VSR is shown in Fig.1 [6]. L is the inductance between the grid and the PWM rectifier. Its main function is to filter harmonics and boost DC voltage; in this case, we consider AC current is sinusoidal. C is the capacitance, which stabilize DC voltage and store energy in the DC side [7].

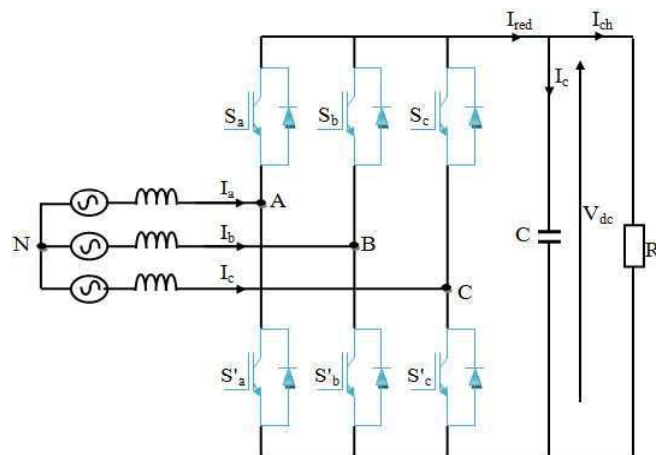


Fig. 1 Three-phase PWM Rectifier.

III. DIRECT POWER CONTROL

This technique depends primarily on the estimation of the instantaneous power p and q [8]. And is characterized by other

techniques in the absence the internal current control loops and PWM modulator block, the switching table is the responsibility for selecting the rectifier switching states, it's based on the sector of voltage line and the instantaneous errors between the reference and estimated values of P and Q. Therefore, the most important thing of the direct power control application is to give the correct and fast estimated value of the active and reactive grid power [2] [8].

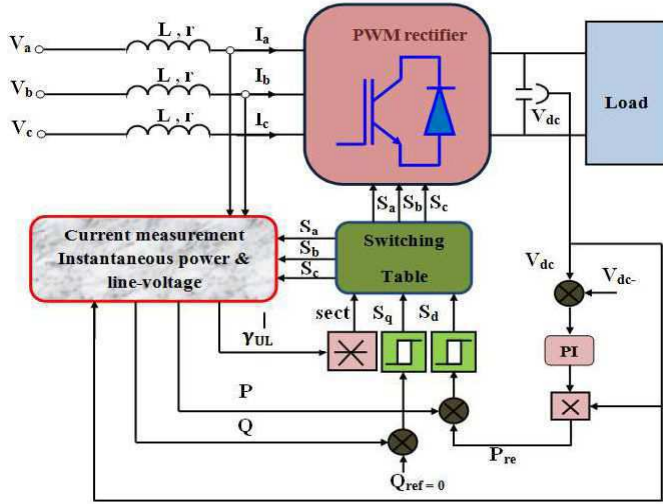


Fig. 2 Direct power control configuration.

A. Active and Reactive Power Estimator

The instantaneous active and the reactive power defines by:

$$p = v_{(abc)} \cdot i_{(abc)} = v_a i_a + v_b i_b + v_c i_c \quad (1)$$

$$q = v_{(abc)} \wedge i_{(abc)} = v'_a i'_a + v'_b i'_b + v'_c i'_c \quad (2)$$

The active and reactive powers values are estimated by the equations (3), (4). In this equation I_a ; I_b ; I_c are the ac-line, S_a ; S_b ; S_c are the switching state of the rectifier.

To compute p and q value from equations (1), (2), require knowing line inductance L [9].

$$\hat{p} = L \left(\frac{di_a}{dt} i_a + \frac{di_b}{dt} i_b + \frac{di_c}{dt} i_c \right) + v_{dc} (s_a i_a + s_b i_b + s_c i_c) \quad (3)$$

$$\hat{q} = \frac{1}{\sqrt{3}} [3L \left(\frac{di_a}{dt} i_c - \frac{di_c}{dt} i_a \right) + v_{dc} (s_a (i_b - i_c) + s_b (i_c - i_a) + s_c (i_a - i_b))] \quad (4)$$

B. Voltage estimator

The expressions of the P and Q can be Expression as follow

$$\hat{p} = v_{(abc)} \cdot i_{(abc)} = v_\alpha i_\alpha + v_\beta i_\beta \quad (5)$$

$$\hat{q} = v_{(abc)} \wedge i_{(abc)} = v_\alpha \cdot i_\beta - v_\beta \cdot i_\alpha \quad (6)$$

By measuring AC-line current and computing active and reactive power by equations (3), (4), the line voltage can be Extracted from the equation (7) [9] [10].

$$\begin{bmatrix} \hat{v}_\alpha \\ \hat{v}_\beta \end{bmatrix} = \frac{1}{i_\alpha^2 + i_\beta^2} \begin{bmatrix} i_\alpha & -i_\beta \\ i_\beta & i_\alpha \end{bmatrix} \begin{bmatrix} \hat{p} \\ \hat{q} \end{bmatrix} \quad (7)$$

C. Detection of sector

The region of the estimated voltage vector is divided into twelve sectors [10].

$$(n-2) \frac{\pi}{6} < \text{sect } t_n < (n-1) \frac{\pi}{6} \dots n = 1, 2, \dots, 12 \quad (8)$$

IV. DC VOLTAGE REGULATION

A. PI regulator

In this proposed functional schema of the DPC, the fundamental input currents is delivered by outer proportional-integral (PI) controller of dc-bus voltage and multiplied the output by the dc voltage for given the reference value of the instantaneous active power, show Fig. 3 [1].

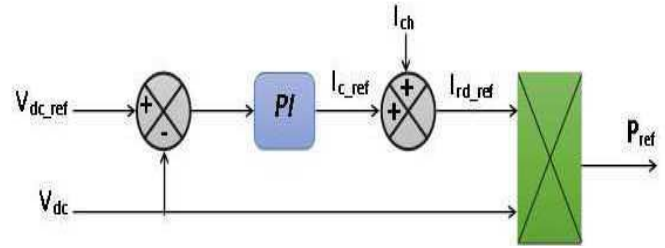


Fig. 3 DC voltage PI control.

B. Fuzzy Controller

Fig. 4 gives the main scheme of the presented FLC. The dc bus voltage V_{dc} is sensed and compared with a reference value V_{dcref} for obtain the error [3].

$$err(k) = v_{dcref}(k) - v_{dc}(k) \quad (9)$$

and its incremental variation

$$derr(k) = err(k) - err(k-1) \quad (10)$$

The k^{th} sampling instant is used as inputs for fuzzy controller. So that we have in the output the instantaneous active P_{ref} . The V_{dc} is controlled by regulating the active power using fuzzy controller [3]. To have a good result in the V_{dc} control. The inference system FLC Depends on IF-THEN rules. The example of fuzzy base rules is shown in Table I [2].

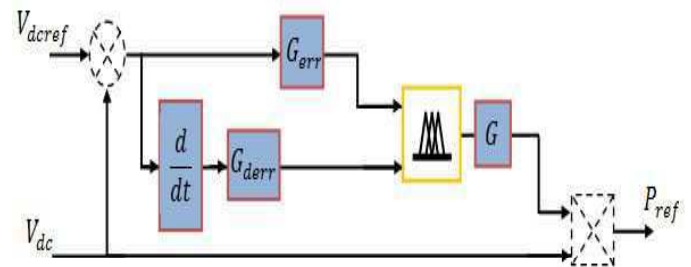


Fig. 4 DC voltage fuzzy control.

The Fuzzy logic Rules system, Determines a set of behaviors and transactions that relate to inputs for obtaining a good result in outputs. So, the fuzzy system approximates at the mathematical function of cause and his effect [11].

Table I: Fuzzy Base Rule

derr \ err	N	Z	P
N	GN	N	N
Z	N	Z	P
P	Z	P	GP

V. SIMULATION

To study the operation of the fuzzy DPC system, the PWM rectifier with the whole control scheme has been simulated using MATLAB Simulink software.

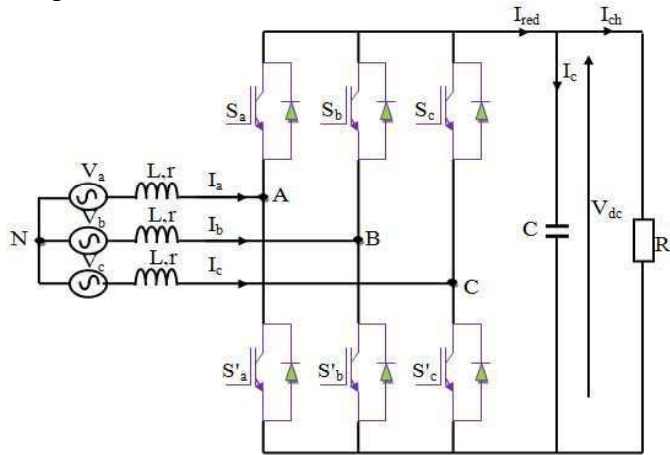


Fig. 5 Studied system

The main electrical parameters of the power circuit given in Table II:

Table 2. Fuzzy Base Rule

Resistance of reactors (R)	0.25[Ω]
Inductance of reactors (L)	10[mH]
DC-link capacitor	0.005[F]
Load resistance (RL)	100[Ω]
Phase voltage (V)	220 * √2 [V]
Source voltage frequency	50[Hz]
DC-link voltage	600[V]

We can observe a comparison between the two kind of control conventional on left and fuzzy logic on right, Fig.6 and 7 shows the line current and voltage

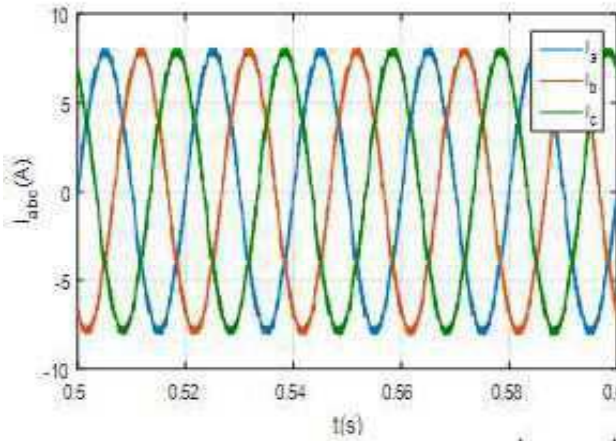


Fig. 6 Line current

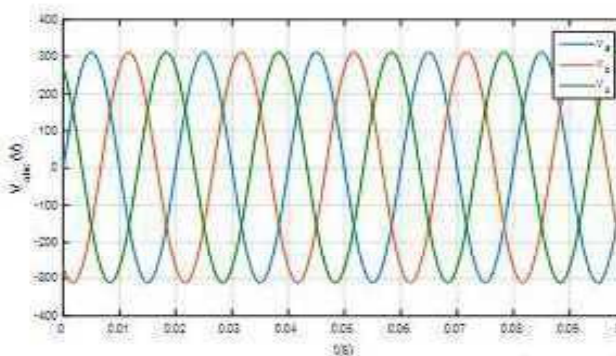
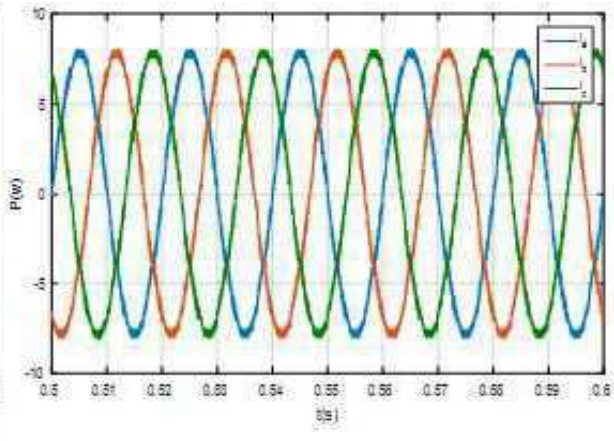


Fig. 7 Line voltage

The control of DC link voltage is presented in fig. 8, fig. 9 we can observe the load current form.

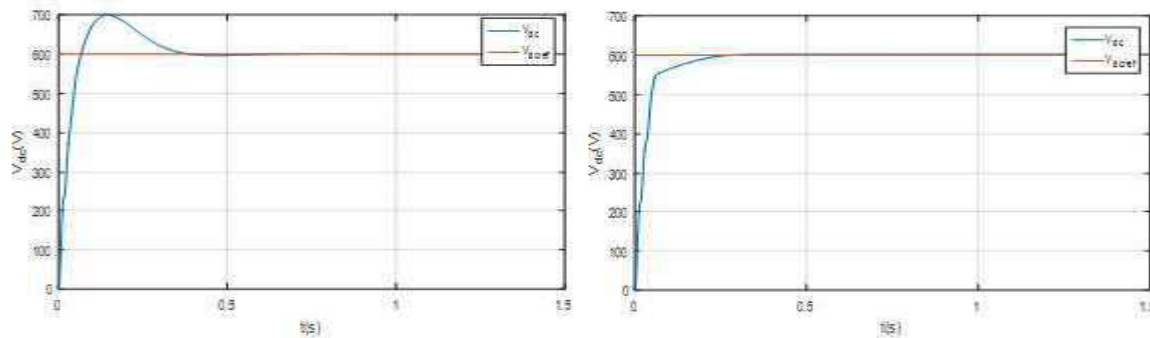


Fig. 8 Control of DC voltage

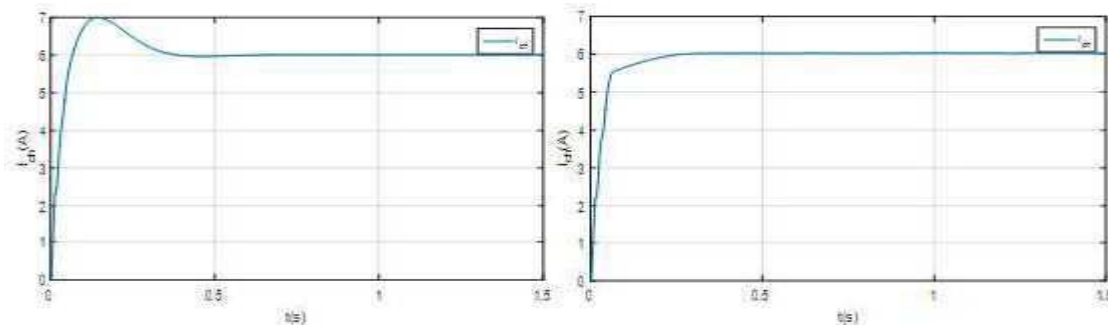


Fig. 9 Load current

In figs.10, 11 we present the estimated active and reactive power, and in, fig.12 Line current and voltage of the first phase.

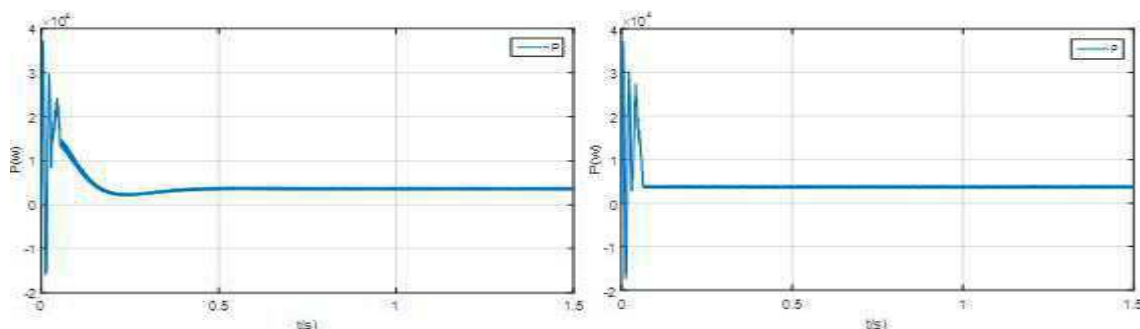


Fig. 10 Estimated active power

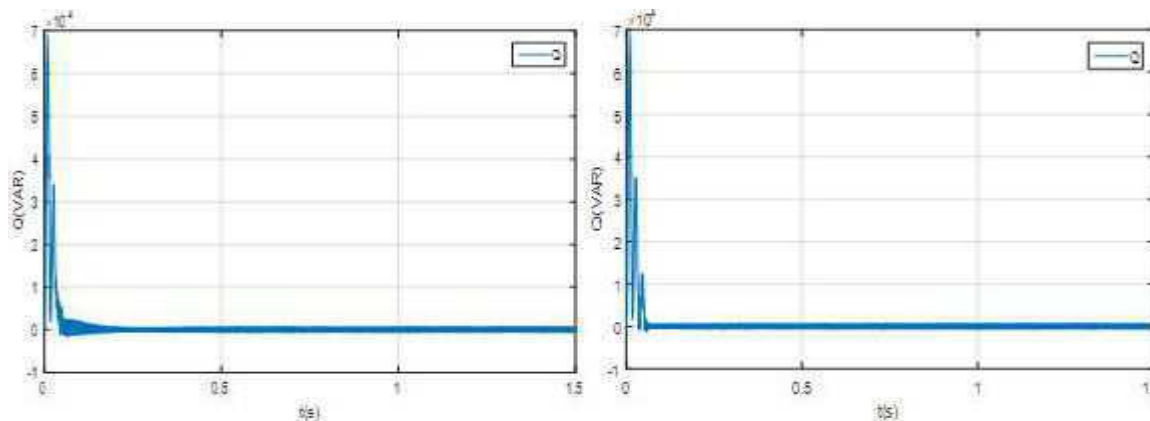


Fig. 11 Estimated reactive power

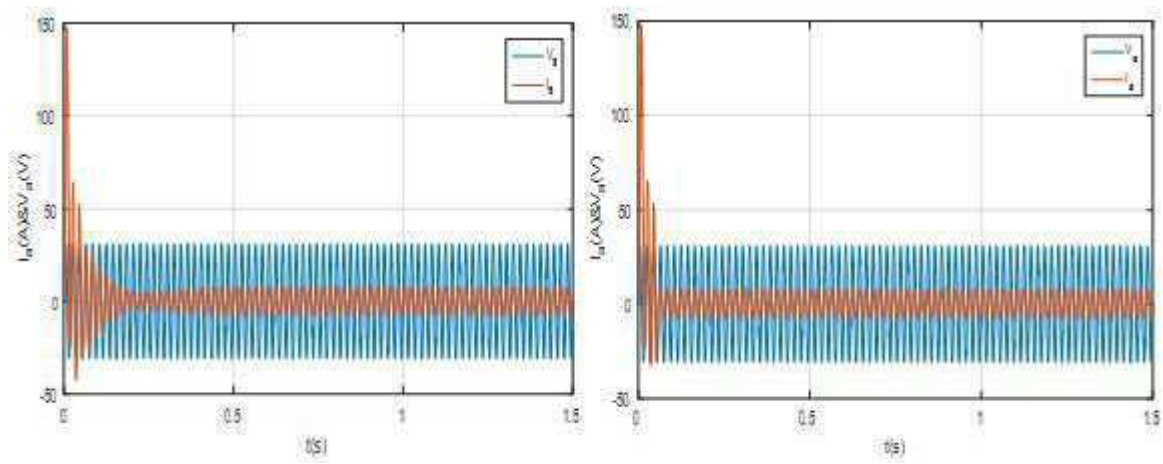


Fig. 12 Line current and voltage of the first phase

Alpha beta trajectory of networks voltage is presented in fig.13, and finally we obtain the spectral analysis of networks current.

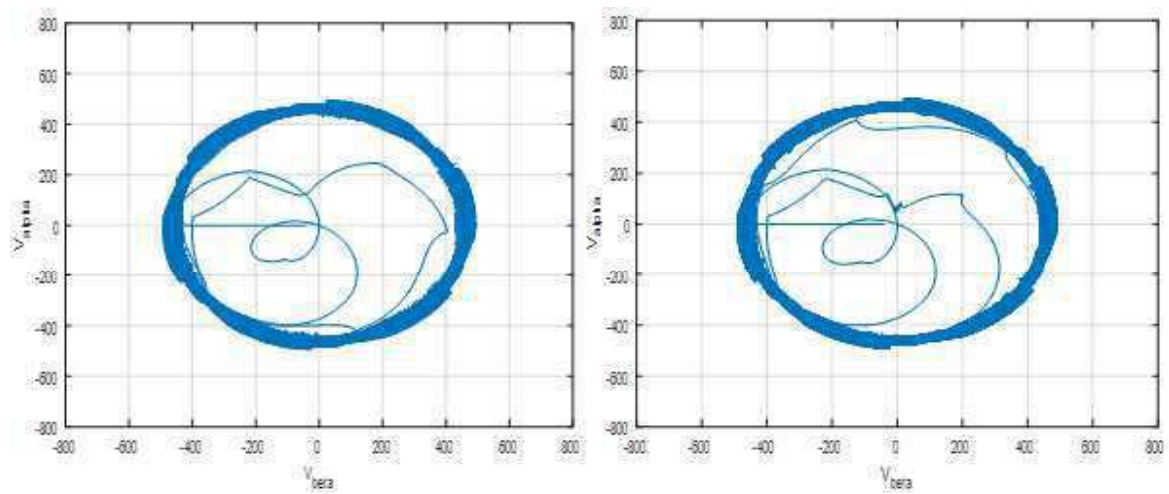


Fig. 13 Alpha beta trajectory of networks voltage

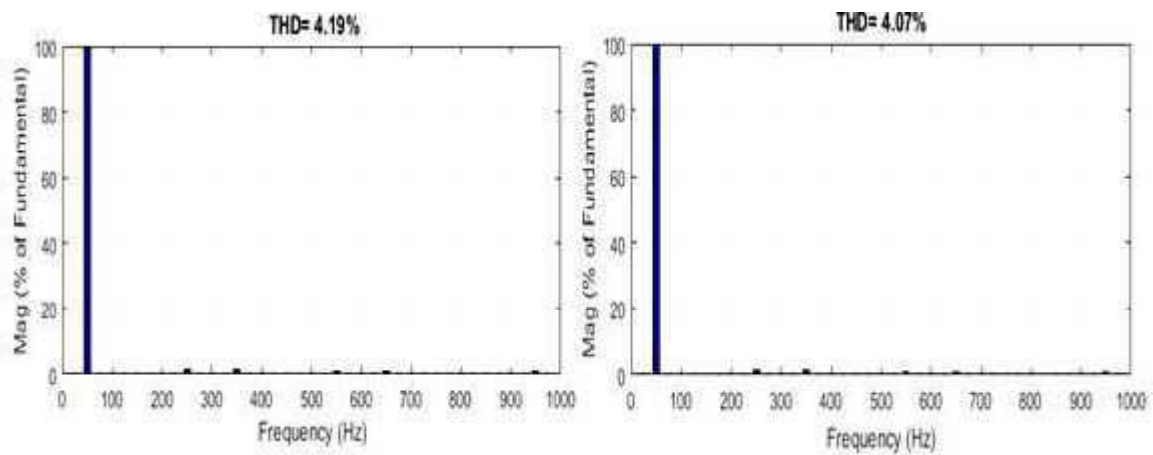


Fig. 14 THD of line current

We can't notice much deference regarding the voltage and the current of networks, The control of DC link voltage with classical control present an overshoot of 100V, the uses of fuzzy controller eliminates this disadvantage with a reduced Response time, we not the same thing for load current, fuzzy logic have good performance in the case of power settings. In Fig.12, the voltage and the current are in phase, which is translated by a unit power factor.

Finally, the spectral analysis shows some improvement when using fuzzy logic; the two THD values are accepted in international standards that impose a THD less than 5%.

VI. CONCLUSION

This paper, proposed a new technique of control for a PWM AC-DC converter with a constant switching frequency. It concerns the use of the direct power control principle via an FLC system on the DC side. DPC technical allows reducing the number of sensors used. In order to obtain a stable exchange of the active power owe between the rectifier and the electrical network, a fuzzy logic regulator using for the DC voltage control. The results of Simulation showed that the direct power control technique with a fuzzy logic for dc voltage control improves the performance system. These improvements concern the performances of the system response on the DC side (overshoot and response time), as well as the power-factor and the THD of the line current [3]. However the conventional regulator has a simple shape, easy to make, and cheaper than the fuzzy regulator.

VII. REFERENCES

- [1] Lamterkati, J, Khafallah, M., Ouboubker, L: A New DPC for Three-phase PWM rectifier with unity power factor operation, IJAREEIE Journal Vol. 3, 2014, pp. 8273-8285.
- [2] Skandari, R, Rahmati, A, Abrishamifar, A, Abiri, E: A fuzzy logic controller for direct power control of PWM rectifiers with SVM, IEEE PEDES, 2006, pp. 1-5.
- [3] Denoun, H, Fekik, A, Benamrouche, N, Benyahia, N, Zaouia, M, Badji, A: Direct Power Control with Space Vector Modulation and Fuzzy DC Voltage Control- PWM rectifier, IJCE LATAGE, Vol. 1, 2016, pp. 78-82.
- [4] Dorf, Richard. C, Bishop, Robert. H. Modern Control Systems. 9th ed. Upper Saddle River, NJ: Prentice Hall, 2001.
- [5] Antoniewicz, P, Kazmierkowski, M. P, Jasinski, M: Comparative study of two Direct Power Control algorithms for AC/DC converters, IEEE SIBIRCON, 2008, pp. 159-163.
- [6] Lamterkati, J, Khafallah, M, Ouboubker, L, El Afia, A: Study of new three phase Voltage source PWM rectifier, via Fuzzy and IP controller for output voltage regulation, IEEE ICMCS, 2016, pp. 576-582.
- [7] Zheng, Z, Wang, C, Jing, X. P: Comparison of two control strategy for three-phase voltage source PWM rectifier, IEEE CCTAE Vol. 1, 2010, pp. 101-104.
- [8] Malinowski, M, Jasinski, M, Kazmierkowski, M. P: Simple direct power control of three-phase PWM rectifier using space-vector modulation (DPC-SVM), IEEE TIE Vol. 51 no. 2, 2004, pp. 447-454.
- [9] H.Azizi, A.Vahedi: Performance Analysis of Direct Power Controlled PWM Rectifier under Disturbed AC Line Voltage, RE&PQJ, Vol. 1 no 3, 2005, pp. 153-158.
- [10] Toshihiko, N, Hiroaki, T, Seiji, K, Isao, T: Direct Power Control of PWM Converter without Power Source Voltage Sensors, IEEE Journal, 1992, pp. 941-946.
- [11] Garrido, A: A Brief History of Fuzzy Logic, Broad Research in Artificial Intelligence and Neuroscience BRAIN, Vol 3 no 1, 2012, pp. 71-77.

Analysis and Evolution of Solid and Leachates Residues at the Level of the Gas Complex

REZIG Walid ^{#1}. BESSAIAH Ibtissem ^{*2}. BAGHDAD Amina ^{#3}. HADJEL Mohammed ^{#4}

^{#1} *Laboratoire des Sciences Technologie et Génie des Procédés LSTGP . Département de Génie Chimique . Faculté de Chimie. Université des Sciences et de la Technologie d'Oran Mohamed Boudiaf USTO-MB . BP 1505 El M'anouer Bir El Djir 31016 Oran Algérie.*

^{2,3,4} *Laboratoire des Sciences Technologie et Génie des Procédés LSTGP . Département de Chimie Industrielle . Faculté de Chimie. Université des Sciences et de la Technologie d'Oran Mohamed Boudiaf USTO-MB . BP 1505 El M'anouer Bir El Djir 31016 Oran Algérie.*

E-mail^{#1} : walidrzg@gmail.com / walid.rezig@univ-usto.dz

Abstract— The purpose of this work was to identify and recover sludge from the Wastewater treatment plant WWTP and sludge from the CPS. Sampling is one of the most important operations in monitoring the proper functioning of a Wastewater Treatment Plant WWTP and Corrugated Plate Separators CPS. This is because the representativeness of the sample is the most important parameter because it makes it possible to make the necessary adjustments for the proper operation of the equipment. Sampling, however, requires means adapted to the types of pollutant and difficulties that the site or facility offers. This problem is not solved at GL1Z, because the sampling is carried out according to archaic techniques using This point is considered as priorities which must be supported by the GL1 / Z. The conservation of the samples must itself meet standards and criteria, and requires means. This aspect of the problem is not properly taken into account by the GL1/Z, it is necessary to operate a directive to respect in terms of taking and conservation of the samples. The various analysis that we have carried out, respecting the instructions of the manufacturer are: BOD5, COD, total phosphorus, dissolved oxygen, oils and fats, Suspended Matter SM, heavy metals, pH and Temperature. This forces the GL1/Z complex to rehabilitate these two sanitary : water treatment plants and oily water of corrugated plate separators of CPS, the problem that arises and that has always been how to do with these sludge and how to reduce their volumes, and their impacts on the aquatic environment. Long considered, as a subsidiary operation of water treatment, the treatment of sludge can not obviously be more lightly defined. To be able to properly and rationally solve a sludge problem, it is absolutely essential to know how to characterize the "Waste" product and choose a treatment system depending on the type of sludge and the final destination possible. And for this we chose to study the establishment of drying beds at the GL1/Z complex. Drying is used for very different products such as granular materials, liquid products, pasty materials, etc. The purpose of this work was to identify and recover sludge from the WWTP and sludge from the CPS. This is why it was recommended to set up the drying beds and a sludge treatment unit. It can be said that the requirement of the quality and the reliability of the treatment of the water has a direct impact on the management, sludge which is particularly expensive and needs to be optimized, taking into account, in particular, the

possible final destinations for sludge. Oily water deposits do not have to be dried in drying beds because the weight of the sludge after drying is negligible in front of the water eliminates either by evaporation or sand filtration; and since it has an oily sludge it can be used for incineration. This sludge can not be used in agriculture because of the very high amount of heavy metals that are very toxic to humans and are environment it can be used in a dead land or landfill.

Keywords — Sludge . WWTP . CPS . environnement . drying.

I. INTRODUCTION

The activity of certain chemical and petrochemical industries, considered as being responsible for the degradation of the environment, appears as an undesirable parasitic activity. In this context, it is not only the image of the company or its competitiveness in some markets that are at stake [1], but its own survival in general. Inevitably, almost all purification processes applied to effluents from industrial sectors, whether biological or physico-chemical, result in the concentration of pollutants in the form of aqueous suspension or sludge. For some years, sludge treatment has been a real environmental, economic and social issue. Urban sludge is characterized by a high water content and a potentially harmful composition for the environment (heavy metals, pathogenic micro-organisms) and poses a real management problem for the farmers. The sludge disposal channels are moreover in addition regulated. Incineration is relatively flexible (little storage, few intermediates) but remains very expensive (transport, operation, maintenance, disposal of slag, treatment of fumes) and demanding quality of sludge (prior drying of sludge to have sufficient dryness). And finally the agricultural valorization (spreading or composting); This treatment process is based on the input of nutrients to the cultivated soil contained in the sludge. However, this sector is very controversial by the public opinion. Our study falls

within this framework; and in agreement with the technical services of GL1/Z. we have been proposed to identify pollution in general. to focus on the treatment of sludge and to propose solutions [2-7].

II. IDENTIFICATION OF AQUEOUS POLLUTION AT GL1/Z [8]

Contamination of water with foreign bodies such as microorganisms. chemicals. industrial waste or other degrade the quality of water and make it unsuitable for the desired uses. Regarding the complex GL1/Z . water contamination has been identified in different areas: the utility zone. the process zone. the sanitary water treatment plant (WWTP) and the Corrugated Plate Separators (CPS).

A. *Traitement of Effluents*

From domestic water treatment plant (WWTP) The treatment of sanitary water is provided by a purification plant operating by aeration (activated sludge system), by means of air diffusers. it is designed to treat a daily volume of 177m³ / d, to obtain a final effluent that will be discharged into the sea in accordance with the quality standard of 40mg / l BOD (biological oxygen demand) and 30 mg / l of solid in suspension. Finally a disinfection is made before the discharge to the sea, the effluent is treated with chlorine. A residual chlorine content of 0.5 mg / l is maintained [9].

The different treatment phases are :

- Collection of sanitary water in a network and then return to a lifting station located in the zone of train 400.
- Transfer of the effluent by one of the two pumps to the sanitary water treatment plant.
- Screening - grinding
- Ventilation.
- Clarification.
- Chlorination.
- Rejection to the sea.

Principle of operation

For the treatment to work successfully, it is necessary to understand how the system works.

There are two basic components of the system, a ventilation chamber and a settling tank.

In the aeration chamber the wastewater is aerated in order to obtain the ideal conditions for growth of aerobic organisms. In the settling tank, these organisms can settle and are collected and proportionally recycled to the aeration chamber and the holding tank. These organisms represent the means for which the purification of wastewater is accomplished [10].

a) Grinder

The pumped effluent from the general lifting station is oriented towards the entrance of the grinder / grate with a receiving box.

This grinder decreases large particles to facilitate the activated sludge treatment operation and to ensure the non-clogging of the pipe by these particles as shown in fig.1.

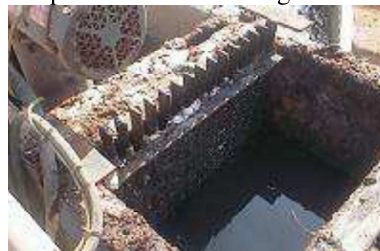


Fig.1 : photo of screen / grinder

b) Aeration chamber

Leaving the mill-sprayer, the flow of wastewater enters the aeration chamber.

The wastewater solution is aerated by means of 40 diffusers equipped with air regulating valves, and the air is supplied by two blowers, each having a capacity of 546 m³ / hr.

Once the growth conditions combined, we notice the gradual appearance of a brown flocculated sludge and generally the purification of wastewater is completely completed only when this sludge is present in sufficient quantity.

The organisms have time to exhaust their food sources and self-destruction occurs resulting in reduced growth rate and hence minimal sludge production as shown in fig.2.



Fig.2 : photo of aeration chamber

d) Chlorination tank

The protection of the environment is an important activity in the development of petrochemical plants. In this sense. the GL1/Z complex has set to this policy and proceeded to the rehabilitation of the units and systems installed for the protection of the environment. For this purpose. during the project renovation of the facilities of the complex. two (02) new stations were installed. one for the treatment of oily water and the other for the treatment of sanitary water as shown in fig.3.



Fig. 3 : Disinfection basin

B. Oily Water Treatment System

The treatment of contaminated water, consisting of oily water and runoff water, is provided by a battery of 4 separators called CPS separators which are inclined, corrugated and alternating plates to separate the oils and suspended solids from the water by gravity and using the principle of coalescence in order to obtain oily effluent levels towards the seawater discharge channel of less than 15 mg/l, given that the allowable limit of discharges of industrial effluents is 20 mg / l of water for oils and fats.

III. PROBLEMATIC

The treatment of sludge is a difficult phase of the fight against pollution, a puzzle for the scrubber, for multiple reasons: scarcity of land available for spreading and disposal, necessities and requirements of the environment and public hygiene, etc. The GL1/Z complex has been certified since 2006 with 3 types of certifications: ISO 14001 (environmental management), ISO 9001 (Quality Management System), OHSAS 18001 (British Standard Occupational Health and Safety Assessment Series). And so the complex GL1 / Z is committed to ensuring the implementation of the Quality Health Safety Environment QHSE policy that leads to manage all types of liquid discharge, solid and even This obliges the GL1/Z complex to rehabilitate these two sanitary water treatment plants of WWTP and CPS oily water the problem which arises and which has always been:

- What to do with the sludge issues?
- How to reduce their volumes?
- Are they harmful?

And for that we chose to study the establishment of drying beds at the GL1 / Z complex. Drying is a unitary operation which consists in eliminating totally or partially a liquid impregnating a material by supply of thermal energy. It considerably reduces the mass and volume of products which facilitates their transport, storage and handling.

IV. MATERIAL AND EXPERIMENTAL METHODS

A. Sampling

The taking of samples is one of the most important operations in monitoring the proper functioning of a WWTP and the CPS or a structure intended for the protection of the environment. Indeed, the representativeness of the sample is the most important parameter because it makes the necessary adjustments for the proper operation of equipment. Sampling however requires means adapted to the types of pollutant and to the difficulties of the site or the installation. This problem is not solved in GL1/Z, in fact the sampling is carried out according to archaic techniques using weak This point is considered as a priority to be taken care of by the GL1/Z. The conservation of the samples must itself meet standards and criteria, and requires means. Table 1 gives the conservation rules in force. This aspect of the problem is not properly taken into consideration by GL1/Z, it is necessary to introduce a directive to be observed in terms of taking and storing samples [11-17]. The various analysis that we have carried out, in following the manufacturer's guidelines are: phosphate, dissolved oxygen, oils and fats, suspended matter SM, heavy metals, pH and temperature. Sampling points are represented In fig.3, fig.4, table 1 and table 2.



Fig.3. : Levy of sanitary water deposits

Table 1: Measurement of global parameters of the pollution of the depots of sanitary water deposits

pH	T (°C)	SM (mg/l)	Phosphates (mg/l)	Total phosphorus (mg/l)	Oils and fats (mg/l)
8.3	21.3	147.05	36.184	11.799	< 0.1

Table 2 : Heavy metals analysis of sanitary water deposits

Cu (mg/l)	Pb (mg/l)	Zn (mg/l)	Cd (mg/l)	Fe (mg/l)	Ni (mg/l)
<0.001	< 0.001	0.063	0.031	0.139	0.001



Fig.4. Sanitary water deposits Dépôt des eaux sanitaires

The physico-chemical characteristics as well as the analysis of the heavy metals of the depots of sanitary water are represented in the tables (1 and 2).

V. RESULTS AND DISCUSSIONS

A. Preparation of drying beds

Total phosphorus : The phosphate content of the water is related to the decomposition of the organic matter. The analyzes carried out on the deposits of the health waters of the GL1 / Z complex give a value of 11.79 mg / l of phosphorus, which proves that phosphorus is used as a nutrient during the biological treatment is also its presence in the kitchen waters (detergents). **Oils and fats:** the analysis of oils and fats gives a value < 0.1 mg / l which depends on the rejected materials during the day. **For heavy metals** traces of copper and lead have been found; and a slightly high value of iron is tantamount to the contamination of the deposition of sanitary water by the corrosion of the walls of the installations. For our

experiment we chose 03 uniform bins of the same volume as shown in Figure 3; Height = 15 cm; Width = 25 cm; Length = 35 cm as shown in figures (5-7).

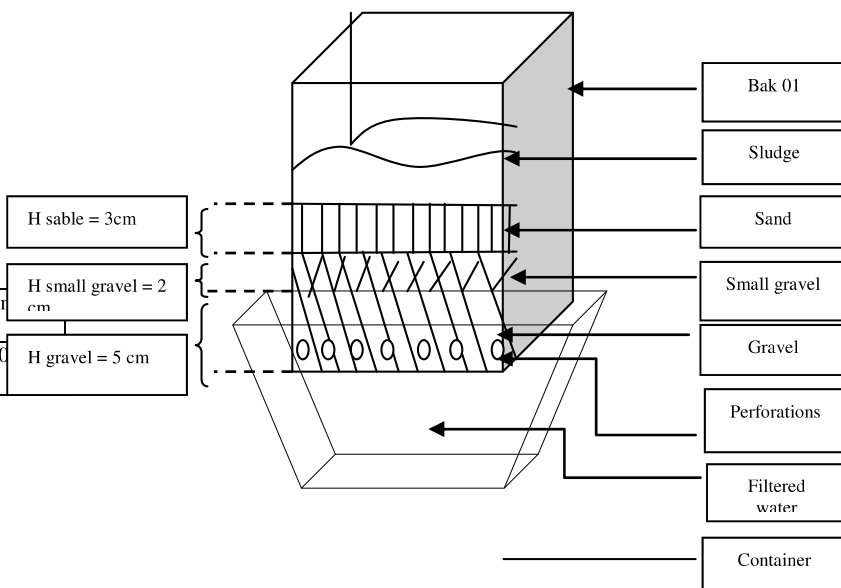


Fig.5 : Representative diagram of pilot A



Fig.6 : Preparation of drying pilots



Fig.7 : Set up of pilot A

**B. Characterization of the filtered water on sand of the pilot
 A sludge**

V.4.1 characterization of sanitary water deposits

The physicochemical characteristics as well as the analysis of heavy metals from the sanitary water deposits are shown in the tables (3-4) :

Table 3 : Measurement of global parameters of sand filtered water pollution

pH	T (°C)	SM (mg/l)	Phosphates (mg/l)	Total Phosphorus (mg/l)	Oils and fats (mg/l)
8.1	20.2	0.2	7.114	2.320	< 0.1

Table 4: Heavy metals analysis of filtered water from sanitary sludge

Cu (mg/l)	Pb (mg/l)	Zn (mg/l)	Cd (mg/l)	Fe (mg/l)	Ni (mg/l)
<0.001	<0.001	<0.001	0.012	<0.001	<0.001

C. Drying of sanitary water deposits

Drying of sanitary water deposits was carried out in a period of six days in the open air; the drying results are shown in Table 5 and figures (6-11) :

Table 5: Drying of sanitary water deposits

Time of drying (h)	Weight of sludge after drying (g)	Quantity of water removed after drying (%)
144h15 min	141.13	92.94



Fig.6. : Sludge



Fig.7. : Drying of sludge ue

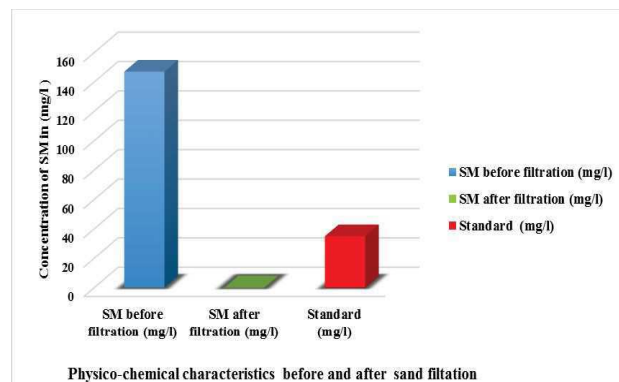


Fig. 8 : Concentration of SM before and after sand filtration

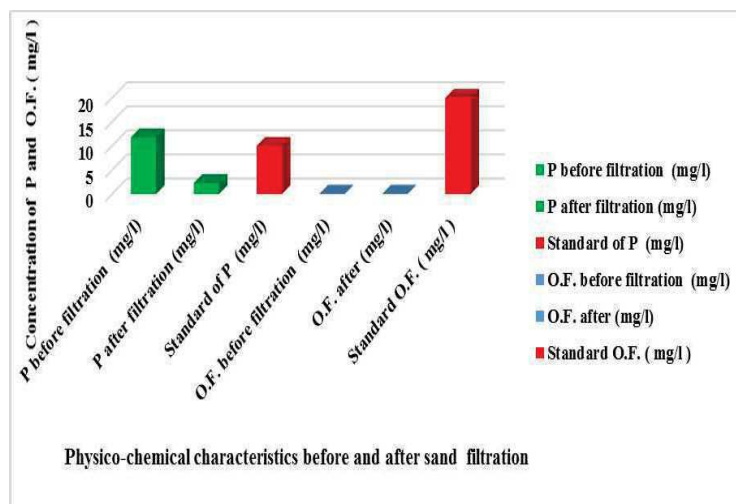


Fig. 9 : Total phosphorus analyses, and Oils and fats before and after sand filtration

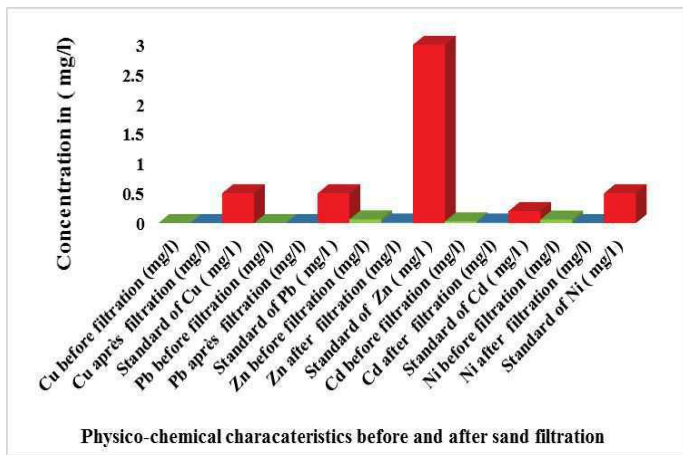


Fig.10 : Analysis of heavy metals before and after sand filtration

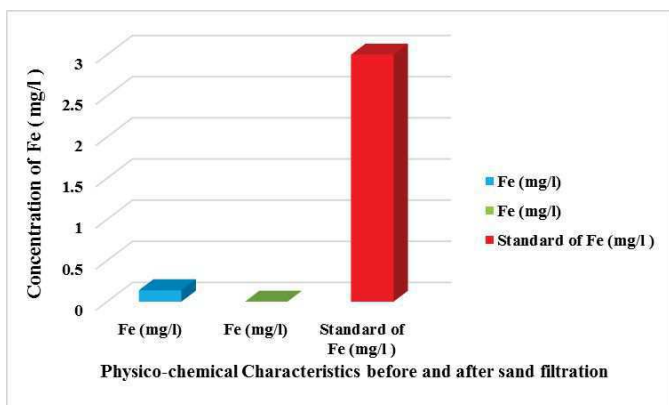


Fig. 11 : Analysis of Fe before and after sand filtration

D. Analysis result of oily and sanitary sludge

The different results of the various analyses and tests are summarized in the tables below

a) Determining the rate of waste oils

Calculation of the oil concentration in the sludge with:
Equation N° 1

The mass of the 1.22 g filter paper is already tare on the scale when measuring sludge as shown in tables (7-8).

Sanitary sludge :

$$\text{Oil content (\%)} = ((5-4.82) \div 5) \times 100 = 3.6\%$$

Oily sludge :

$$\text{Oil content (\%)} = ((5-3.65) \div 5) \times 100 = 27\%$$

Table 6 : Change in oil content in sludge

	Sanitary sludge	Oily sludge
Oil rate (%)	3.6 %	27 %

b) Hydrocarbon content

Table 7 : Change in hydrocarbon content in sludge

Hydrocarbon content (mg / l)	Sanitary sludge	Oily sludge
	< 0.1 mg / l	21.75 mg / l

Our oily sludge of CPS contains a quarter of its mass in used oil and a large quantity of hydrocarbons which are important sources of pollution since the used oil and the hydrocarbons are toxic and carcinogenic products on the one hand, and on the other hand a mine of energy due to their great calorific value.

c) Phosphorus and total nitrogen content

Table 8 : Variation of phosphorus content and total nitrogen in sludge

Type of sludge	Sanitary sludge	Oily sludge
Phosphorus content (mg / l)	21.73 mg / l	3.108 mg / l
Total nitrogen content (mg / l)	28.95 mg / l	2.31 mg / l

The sanitary sludge is very rich in phosphorus and nitrogen nutrients which are essential for the development of the flora which favors its valorisation in agriculture.

d) Determination of metallic elements

The heavy metal masses in the oily and sanitary sludge are summarized in the following table of results in mg / l as shown in tables (9-11) :

Table 9 : Quantification of metallic elements in oily and sanitary sludge in mg / l

Elements	Cu	Zn	Fe	Ni	Pb	Cd
Sanitary sludge of WWTP (mg/l)	0.8545	0.672	2,8312	0.2367	0.1362	0.00161
Oily sludge of CPS (mg/L)	1.214	1.30	4.04	0.5367	0.3565	0.00931

In Algeria there are no regulations that set the limit values for sludge parameters from wastewater treatment plants, the only regulation that exists is the AFNOR U44041 standard, developed for France in application of the European directive n ° 86-278 of June 12, 1986 anyway it is a norm which concerns the inputs of sludge intended for the spreading and in practice, it constitutes the only reference for sludge ;

The values given by the atomic absorption spectrophotometry of the laboratory GL1 / Z are expressed in mg / l) the norm AFNOR gives us values in mg / kg of dry matter DM that is why we must convert them in mg / kg of dry matter DM of the following way:

To prepare the treated water we dissolved 1 g of sludge in 100 ml of final solution in 1 liter of dry matter solution and we calculate the amount of these elements in 1kg of dry sludge with the following formula:

EQUATION N °2 :

$$\text{Value in mg / kg of DM} = X * 100/1000$$

Table 10 : Quantification of metallic elements in sanitary sludge in mg / kg

Elements	Cu	Zn	Fe	Ni	Pb	Cd
Sanitary sludge of WWTP (mg/kg)	85.45	67.2	283.12	23.67	13.62	0.161
Norm in agriculture in (mg / kg)	1 000	3 000	/	200	800	20

Table 11: Quantification of metallic elements in oily sludge in mg / kg

Elements	Cu	Zn	Fe	Ni	Pb	Cd
Oily sludge of CPS (mg/kg)	121.4	130	404	53.76	35.65	0.931
Norm in agriculture in (mg / kg)	1 000	3 000	/	200	800	20

The chemical analysis of traces of heavy metals in the oil sludge of CPS and the sanitary sludge of WWTP, shows us well The predominance of three metallic elements with elevation of concentration are: copper (Cu), iron (Fe) as well as zinc (Zn) succeed by low concentration of nickel (Ni) and lead (Pb) and finally the presence of cadmium (Cd) in the form of a trace; but the concentration of these metal elements remain below the AFNOR standard which concerns the valuation of sludge in agriculture.

e) Thermal treatment of CPS oily sludge

The energetic recovery of oily mud is accompanied by a production of heat recovered in the form of steam or electricity and the residues of the incineration called "ash" which becomes another source of pollution if it is not eliminated c that is why we have suggested that it be valued as an addition in the manufacture of building materials.

f) Calcination of the oily sludge at 500 ° C

At the level of the RA1 / Z refinery laboratory, the oily CPS sludge was calcined in an oven at 500 ° C for 2 hours in figures (12-17).



Fig.12 : Put the oily sludge of CPS



Fig.13: Oily mud of CPS in the oven calcined at 500 ° C

Then, using a worm mortar the ash was crushed to prepare it in the various analyzes (see Photo IV.27) this operation makes it possible to homogenize the material taken.



Fig.14 : Ash of oily mud

□ The ash powder will be used for:

- Chemical composition of oily sludge
- X-rays diffraction analysis (XRD);
- Fourier transform Infrared (FTIR) analysis;
- Analysis of scanning electron microscopy (SEM).
- Determination of heavy metals by the atomic absorption spectrophotometry method.

E. Analysis result of the oily sludge (GL1 / Z) dries at 500 ° C

a) Determining the rate of waste oils

Calculation of oil concentration in sludge with in figures (15-17) :

Equation N° 2 :

The mass of the 1.22 g filter paper is already tare on the scale when measuring sludge.

$$\text{Oil content (\%)} = ((5-4.8) \div 5) \times 100 = 4\%$$

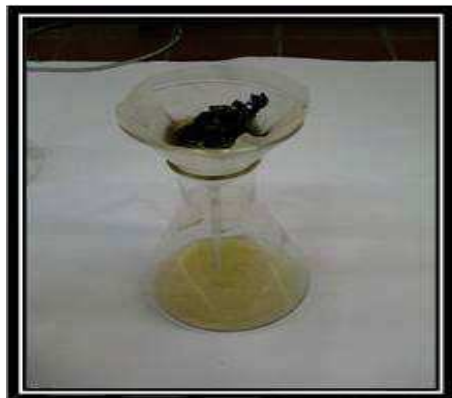


Fig.15 : Used oil level in oily mud



Fig.16 : Oil content of CPS oily sludge



Fig.17 : Oil content of WWTP sanitary sludge

F. Techniques and characterization of sludge

a) Chemical composition of drying oily sludge (XRF)

The importance of this analysis is to determine the nature of the oily mud, the results obtained are described in the following in table 12 and fig.18:

Table 12 : The chemical composition of oily sludge

Chemical composition	Percentage %
Fat	30,6
Ashes	15,2
Humidity	6,9
Hydrocarbons	17,3
Heat output	7000 Kcal/kg

The chemical composition of the oily sludge produced at the EL FETH laboratory level shows us that, in addition to containing used oils, it also contains a high level of fat and hydrocarbons from the refining of oil hence its high calorific value, and a source of pollution for the soil that is why the refinery of Arzew can neither the landfill nor the used in the Agriculture.

b) X-rays diffraction (XRD)

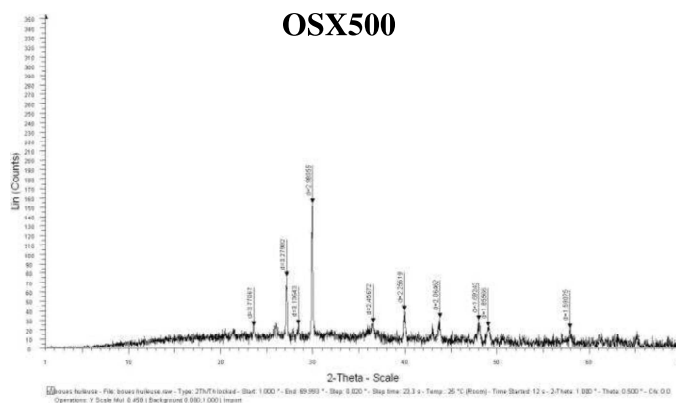


Fig.18 : Diffractogram of oily sludge dries at 500 ° C

- The peak at $2\theta = 23.2^\circ$ with the interarticular distance $d = 3.77$ corresponds to the opal-A ($\text{SiO}_2 \cdot n\text{H}_2\text{O}$) [18].

- The peak at $2\theta = 27^\circ$ With the interarticular distance $d = 3.27$ corresponds to quartz (SiO_2) [19].
- the peak at $2\theta = 27^\circ$ With the interarticular distance $d = 3.27$ corresponds for lepidocrocite ($\gamma\text{-FeOOH}$) [20].
- The peak at $2\theta = 28.5^\circ$ With the interarticular distance $d = 3.13$ corresponds to the diopside ($\text{CaMgSi}_2\text{O}_6$) [18]. [18] B.Y. Imaz, M,Ediz ,the use of raw and calcined diatomite in cement & concrete composites 30,202-21 ,2008.
- the peak at $2\theta = 28.5^\circ$ with the interarticular distane $d = 2.98$ corresponds to opal-A ($\text{SiO}_2\cdot n\text{H}_2\text{O}$) [18].
- the peak at $2\theta = 30^\circ$ with the interarticular distance $d = 2.98$ corresponds to calcite (CaCO_3) [18,19].
- the peak at $2\theta = 36.5^\circ$ With the interarticular distance $d = 2.45$ corresponds for Kaolinite ($\text{Al}_2\text{Si}_2\text{O}_5(\text{OH})_4$) (ASTM N°=5-490) .
- the peak at $2\theta = 40^\circ$ With the interarticular distance $d = 2.25$ corresponds to For hematite ($\alpha\text{-Fe}_2\text{O}_3$) (ASTM N°=8-98) .
- the peak at $2\theta = 40^\circ$ with the interarticular distance $d = 2.25$ corresponds to quartz (SiO_2) [19].
- the peak at $2\theta = 43.5^\circ$ with the interarticular distance $d = 2.06$ corresponds to the opal-A ($\text{SiO}_2\cdot n\text{H}_2\text{O}$) [19].
- the peak at $2\theta = 48^\circ$ with the interarticular distance $d = 1.89$ corresponds to quartz (SiO_2) [19].
- the peak at $2\theta = 49^\circ$ with the interarticular distance $d = 1.85$ corresponds to quartz (SiO_2) [19].
- the peak at $2\theta = 58^\circ$ with the interarticular distance $d = 1.59$ corresponds to quartz (SiO_2) [19].

According to the diffractogram of oily sludge dried at 500°C . The phase identification has shown that there are two dominant phases of crystalline structure, calcium carbonate (CaCO_3) and silicon oxide (SiO_2).

c) Fourier transform infrared spectroscopy (FTIR)

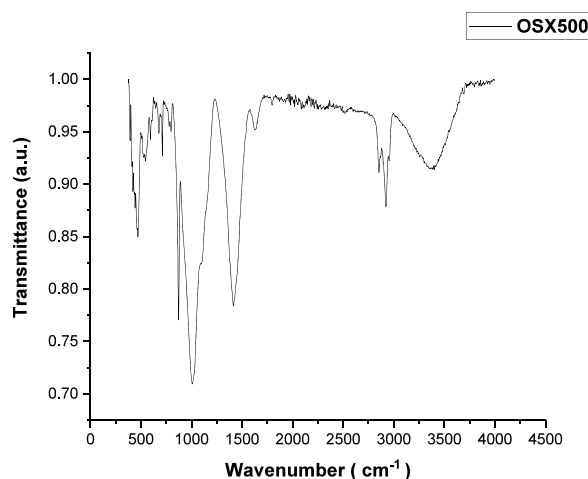


Fig.19 : spectrum of oily sludge dried at 500°C

According to the spectrum we have different bands to explain in fig.19 :

The two absorption bands at 200 cm^{-1} and 1350 cm^{-1} in particular represent the families Halides (C-I, C-Br, C-Cl, C-F) (ASTM N°=5-490).

- The 469.84 cm^{-1} absorption plug corresponds to C-F vibrations (ASTM N°=5-490).
- The 543.87 cm^{-1} absorption plug corresponds to C-I vibrations (ASTM N°=5-490).
- The two absorption drains at 711.81 cm^{-1} and 676.88 cm^{-1} correspond to the C-Cl and C-Br vibrations (ASTM N°=5-490).
- The 797.46 cm^{-1} absorption plug corresponds to C-Cl vibrations (ASTM N°=5-490) .
- The 1007.15 cm^{-1} absorption plug corresponds to the C-C and C-F vibrations . (ASTM N°=11-654).
- The two absorption bands at 1370 cm^{-1} and 3000 cm^{-1} correspond to alkanes and alkenes (ASTM N°=11-654) .
- The absorption bung at 1415.63 cm^{-1} corresponds to C-H vibrations (ASTM N°=11-654).
- The absorption bung at 1627.80 cm^{-1} corresponds to the vibrations C=C and C=N and N-H.
- The 1797.33 cm^{-1} absorption plug corresponds to C=O covalent carbonate vibrations (ASTM N°=11-654)..
- The 2852.51 cm^{-1} absorption plug corresponds to the C-H vibrations (ASTM N°=11-654).
- The 2922.09 cm^{-1} absorption plug corresponds to C-H vibrations (ASTM N°=11-654)..

Generally it is hydrocarbons of long carbon chain from C_{11} to C_{30} (ASTM N°=11-654).

The two broad absorption bands at 2500 cm^{-1} and 3300 cm^{-1} correspond to the carboxylic acids (ASTM N°=11-654) .

- The absorption plug at 3355.06 cm^{-1} corresponds to the O-H vibrations of the carboxylic acid R-COOH (ASTM N°=11-654).

According to the spectrum of dry oily sludge at 500°C indicates the presence of halides which are probably the

additives that go into the production of finished oils, the persistence of heavy hydrocarbons and the formation at low amounts (traces) of acids carboxylic because of the different chemicals use.

d) Scanning electron microscopy

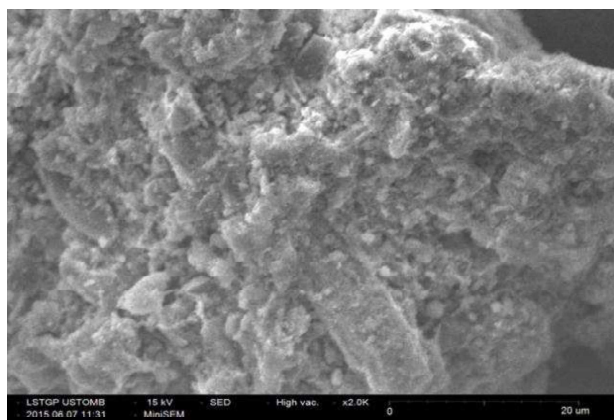


Fig.20.: SEM observation of the sludge of the WWTP at T = 500 ° C

The fig.20 represents the scanning electron microscopy (SEM) observation of the CPS oil sludge at temperature T = 500 ° C. we note that the sludge structure of CPS at T = 500 ° C is homogeneous and in the form of fibers as shown in fig.20.

e) Determination of metallic elements

The heavy metal masses in the oily sludge dried at 500 ° C are summarized in the following table 13:

Table 13 : Quantification of metallic elements in dry oily sludge at 500 ° C

Elements	Cu	Zn	Fe	Ni	Pb	Cd
Oily sludge dries at 500 ° C in mg / l	1.2237	1.06	4	0.564	0.349	0.0065
Dry oily mud at 500 ° C in mg / kg	122.37	106	400	56.4	34.9	0.65
Norm in agriculture in mg / kg	1 000	3 000	/	200	800	20

The chemical analysis of traces of heavy metals of dry oily Sludge at 500 ° C, shows us that it contains in majority of its composition the following metals: copper, iron and zinc which have not disappeared under the effect of the heat but which remain inferior to the norm AFNOR which concerns the valuation of the sludge in agricultures.

VI. CONCLUSION

From our experiments on the three drying pilots containing three different materials selected on the basis of their large adsorption capacities which are respectively: sand, sawdust, and molecular sieve. Sand has been found to be the most suitable material for drying and filtration of GL1 / Z complex sanitary water deposits which are characterized by their overly liquid structure. And sand has also been found, gravel and gravel not only retain organic matter but also heavy metals, and the total phosphorus. Or the filtered water of the sludge needs to be recycled because we could not carry out all the analyzes concerning the parameters of pollution like the ammonium ion for lack of materials.

Our study is part of a sustainable development, recyclable materials and protection of natural receiving environments in order to minimize or eliminate waste such as treated solid urban effluents (sludge) from the wastewater treatment plant, de-oilers (CPS) of the GL1 / Z complex with a view to an agronomic valorisation for the sanitary and energetic sludge for the oily sludge.

In a first step we characterized the residual sludge of the GL1 / Z complex; the results of the analyses showed that the sanitary sludge contains the essential nutrients for the soil as part of the overall crop fertilization program. The important nutrients in the sanitary sludge are nitrogen, phosphorus and potassium; other macro and micronutrients may also be present.

The concentrations of heavy metals cadmium (Cd), chromium (Cr), copper (Cu), nickel (Ni), lead (Pb) and zinc (Zn) are below the required standards.

The oily sludge according to the results obtained, contains a very high rate of used oils contributing to its valorization as a substitute fuel in the furnaces of cement plants or blast furnaces foundries, the principle is to promote the energetic power of the material, organic dried sludge because its calorific value is very high, ready that of methane. The use of alternative fuels makes it possible to diversify energy resources and reduce costs.

On the one hand In the ovens, the organic components will be exposed to a heat of 2000 ° C and will be burned integrally, while the mineral components will undergo a chemical

transformation which will integrate with the clinker without altering the excellent quality of this one.

The use of sludge ash as an additive to cement clinker in order to minimize the increasing amount of waste in coordination with existing industries in the national territory using the least expensive processes.

Finally, we can say that our sludge recovery study completely eliminates this waste in an ecologically and economically exemplary industrial process. It is the most environmentally and economically the tightest way to address the problem of sludge and ash disposal.

ANNEXE

Table 14 : Limit values for industrial liquid effluent discharges Joradp. April 2006

N°		UNITE	VALEUR S LIMITES	TOLERANCES AUX VALEURS LIMITES ANCIENNES INSTALLATIONS
1	Température	°C	30	30
2	pH	-	6.5 - 8.5	6.5 - 8.5
3	MES	mg/l	35	40
4	Azote Kjeldahl	"	30	40
5	Phosphore total	"	10	15
6	DCO	"	120	130
7	DBO5	"	35	40
8	Aluminium	"	3	5
9	Substances toxiques	"	0.005	0.01
10	Cyanures	"	0.1	0.15
11	Fluor et	"	15	20
12	Indice de phénols	"	0.3	0.5
13	Hydrocarbures	"	10	15
14	Huiles et graisses	"	20	30
15	Cadmium	"	0.2	0.25
16	Cuivre total	"	0.5	1
17	Mercuré total	"	0.01	0.05
18	Plomb total	"	0.5	0.75
19	Chrome Total	"	0.5	0.75
20	Etain total	"	2	2.5
21	Manganèse	"	1	1.5
22	Nickel total	"	0.5	0.75
23	Zinc total	"	3	5
24	Fer	"	3	5
25	Composés organiques	"	5	7

REFERENCES

[1] H. Zeddami ; «Mémoire d'induction au (GLI/Z) » ; (Bethioua).2003.

[2] Michael, I., Rizzo, L., Mcardell, C.S., Manaia, C.M., Merlin, C., Schwartz, T., Dagot, C.,

Fatta-Kassinou, D., 2013. Urban wastewater treatment plants as hotspots for the release of antibiotics in the environment: a review. *Water Res.* 47 (3), 957–995.

[3] Gao, J., Huang, J., Chen, W., Wang, B., Wang, Y., Deng, S., Yu, G., 2016. Fate and removal of typical pharmaceutical and personal care products in a wastewater treatment plant from Beijing: a mass balance study. *Front. Environ. Sci. Eng.* 10 (3), 491–501.

[4]Sadeghpour, M., Hosseini, B., Najafpour, G.D., 2009. Assessment of wastewater treatment plant's performance in Amol Industrial Park. *Am. Eur. J. Agric. Environ. Sci.* 5 (5),707–711.

[5]Yuan, Z.W., Ling, Z., Bi, J., 2010. Which is more cost-effective? A comparison of two wastewater treatment models in China-Singapore Suzhou Industrial Park, China. *J.Clean. Prod.* 18 (13), 1270–1275.

[6] Dong, X., Zhang, X., Zeng, S., 2017. Measuring and explaining eco-efficiencies of wastewater treatment plants in China: an uncertainty analysis perspective. *Water Res.* 112, 195–207.

[7]Lorenzo-Toja, Y., Vázquez-Rowe, I., Amores, M.J., Termes-Rifà, M., Marañón-Na varro,D., Moreira, M.T., Feijoo, G., 2016. Benchmarking wastewater treatment plants under an eco-efficiency perspective. *Sci. Total Environ.* (566–567), 468–479.

[8] Anonyme. « présentation du complexe GLI/Z » *Document interne. (Bethioua)* .1978.

[9] Anonyme, « Séminaire : système de traitement des rejets liquides », document interne (Bethioua 1999).

[10] Anonyme, « Manuel de constructeur de STEP (METITO) », document interne ; (Bethioua). (1978)

[11] O. Belmiloud et S. Zazou . « évaluation de la pollution des eaux au GLI/Z en vue de l'application de la norme ISO 14001 » , Mémoire de fin d'étude 2006. département de chimie ; (USTO) :2006.

[12] M. Elskens , Analyse des eaux résiduaires –mesure de la pollution , Techniques de l'ingénieur , p 4200,2010.

[13] M. Benmecherane, K.Attatba , Etude de la performance d'une station des eaux sanitaires Au GLI/Z , Mémoire de fin d'étude d'ingénieur , Département de chimie industrielle , USTO-MB. 2003.

[14] E. Guibelin , Lutte contre la pollution des eaux-traitement des boues d'épuration , TIG,1450,1999.

[15] J.C.Boeglin, Traitement et destinations finales des bioues résiduaires , Techniques de l'ingénieur,TIJ3944,2000.

[16] A.Meledjem, Mémoire de fin de la période d'induction . «Etude et analyse environnementale de la boue industrielle au niveau du GLI/Z,2010.

[17] Mc.Graw-Hill , Wastewater Engineering Treatment Disposal Reuse Hardcover, 920 pages , 2nd Edition , December , 1978.

[18] B.Y. Imaz, M,Ediz ,the use of raw and calcined diatomite in cement & concrete composites 30,202-21 ,2008.

[19] M.Karlik ,B.Jouffrey , Étude des métaux par microscopie électronique en transmission (MET), Formation des images , Réf : M4135 v1, 10 Septembre, 2008.

[20] S.Mukamel, « Multidimensional Diffractometry_the_rayons_x_DRX _
Annual Review of Physical Chemistry. Vol. 51:691-729, (Volume publication
date October , DOI: 10.1146/annurev.physchem.51.1.691., 2000.

[21] A.P. Scott Carney , Characteristic infrared group frequencies ,
reproduced through country, laboratory , American Cyanamid and the editor of
the journal of the optical society of America), OSA Publishing , 1st April,
2017 .

The controlling of the DFIG Based Wind Energy Conversion System modeling and simulation

HADDAR Mabrouk^{#*1}, ALLAOUA Boumediene^{#*2}

[#] Department of Electrical Engineering , Bechar University, Algeria

¹mabrouk.haddar@gmail.com

²ballaoua@univ-bechar.dz

^{*}Smart Grids & Renewable Energies Lab Bechar, Algeria

Abstract— This paper presents a general modeling and control of the Doubly Fed Induction Generator (DFIG) based Wind Energy Conversion System (WECS). Firstly, We start by modeling the wind turbine. Then, an maximum power point tracking (MPPT) control algorithms is detailed. Thereafter, we given DFIG's mathematic model in the d-q coordinates. Both Grid Side Converter (GSC) and Rotor Side Converter RSC control strategy are presented theoretically based on vector control. Finally, The validity of this control algorithm has been verified by the simulation of the 2-MW DFIG wind turbine system.

Keywords— DFIG, WECS, MPPT, RSC, GSC.

I. INTRODUCTION

Over the last recent years, Wind Energy Conversion System (WECS) became the center of attention for intensive research, and a number of studies have been done by different groups of researchers. It can be classified into two groups : fixed-speed and variable-speed turbines.

The typical configuration of variable-speed WECS using DFIG considered in this paper is illustrated in figure 1. It can be divided into two principal parts which will be modeled separately: the DFIG whose stator is connected directly to a grid, whereas its rotor is connected to the grid through two static converters bidirectional and a DC-link in a configuration called Back to Back converter (BTB), The back-to-back converter consists of two voltage source converters, one called as the Rotor Side Converter (RSC) and the other called as the Grid Side Converter (GSC) [1,2].

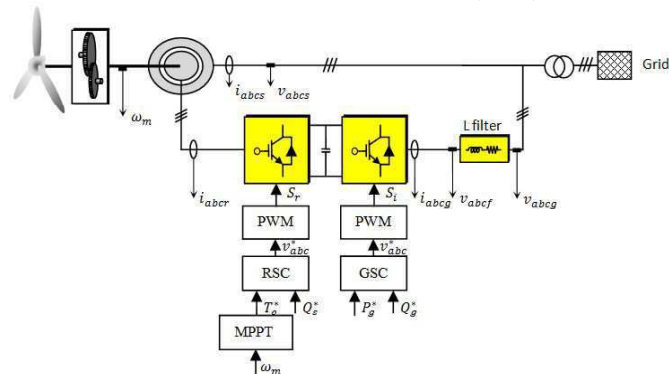


Figure 1. wind energy conversion configuration of DFIG system

II. AERODYNAMIC TURBINE MODEL

A. Characterizations of wind turbines:

To classify wind turbines, two terms are commonly used: the tip speed ratio and the power factor [3]:

- The tip speed ratio is given by the following expression

$$\lambda = \frac{\Omega_T R_T}{v_w} \quad (1)$$

where Ω_T is the angular velocity of the wind turbine shaft measured in mechanical radians per second, R_T is the radius of the wind turbine (length of blade) in m, v_w is the wind speed in m/s.

- The power coefficient of the wind turbine is defined by the following relation [2]:

$$\left\{ \begin{array}{l} \frac{1}{\lambda_i} = \frac{1}{\lambda + 0.02\beta} - \frac{0.003}{\beta^3 + 1} \\ C_p = C_p(\lambda, \beta) = 0.46 \left(\frac{151}{\lambda_i} - 0.58\beta - 0.002\beta^{2.14} - 13.2 \right) e^{-18.4/\lambda_i} \end{array} \right. \quad (2)$$

Figure 2 shows the function in Equation 2 plotted for several values of β .

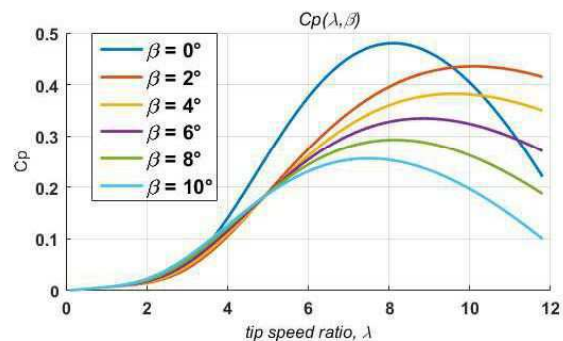


Figure 2. Tip-speed ratio versus power coefficient

B. Mechanical power of turbine

The kinetic power of the wind is given by the following relation [3-5]:

$$P_w = \frac{1}{2} \rho A_T v_w^3, A_T = \pi R_T^2 \quad (3)$$

Where ρ is air density (kg/m^3), A_T is the rotor swept area (m^2),

According to the theory of German scientist *Albert Betz*, the mechanical power extracted from the wind kinetic power is given by:

$$P_T = P_w \times C_P = \frac{1}{2} \rho A_T v_w^3 C_P \quad (4)$$

C. Torque of the turbine:

the torque of the turbine is expressed according to the angular speed of the rotor and the mechanical power of the turbine by the following relation:

$$T_T = \frac{P_T}{\Omega_T} = \frac{1}{2} \rho A_T v_w^2 C_t, C_P = C_t \lambda \quad (5)$$

Where C_t is torque coefficient.

III. DYNAMIC TURBINE MODEL

A. Turbine Gearbox

The Turbine Gearbox aims at the adaptation between the shaft velocity of the turbine (Low speed shaft) and that of the generator (High speed shaft). In the case of an ideal gearbox, the gear ratio can be modeled mathematically by [3-5]:

$$N = \frac{\Omega_m}{\Omega_T} = \frac{T_T}{T_m} \quad (6)$$

where N is the gear ratio, T_T and T_m are torque of the turbine on Low and high speed shaft respectively, Ω_T and Ω_m velocity of the turbine on Low and high speed shaft respectively.

B. Equation dynamic of wind Turbine

The fundamental equation of the dynamics which makes it possible to determine the evolution mechanical speed from the torque exerted on the shaft of the rotor of the wind turbine T_T and the electromagnetic torque T_{em} [3-5]:

$$J \frac{d\Omega_m}{dt} = T_m - T_{em} - D\Omega_m \quad (7)$$

where D is the damping coefficient of turbine.

The diagram of the dynamic model of the wind-based turbine is given in

The diagram of the dynamic model of the wind-based turbine is given in figure 3.

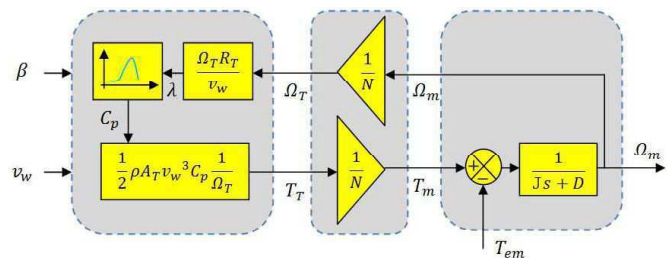


Figure 3. Dynamic model of the wind turbine

IV. MAXIMUM POWER POINT TRACKING (MPPT)

The strategy of this control consists in controlling the electromagnetic couple in order to regulate mechanical speed to maximize the generated electric output [2,4,5].

From the dynamic equation of the turbine, we have:

In permanent mode, one can write (by neglecting the effect of the couple of viscous frictions):

$$T_m = T_{em} \quad (8)$$

The electromagnetic couple of adjustment is given starting from an estimate of the wind couple:

When the turbine functions with the maximum power point, then: $\lambda = \lambda^{op}$ and $C_P = C_P^{op}$.

The electromagnetic couple of reference must be regulated with the following value:

$$T_{em}^* = \frac{T_T}{N} \quad (9)$$

Consequently:

$$T_{em}^* = k^{op} \Omega_m^2 \quad (10)$$

Where

$$k^{op} = \frac{1}{2} \rho A_T R_T^3 \frac{C_P^{op}}{\lambda^{op} N^3} \quad (11)$$

The expression of the couple of reference then becomes proportional to the square of generator speed.

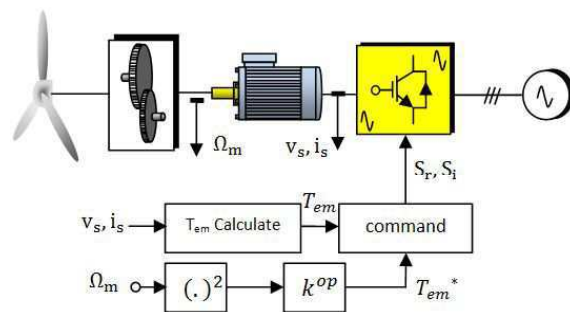


Figure 4. MPPT based on Optimal torque control

V. MODEL OF DFIG

The mathematical model is expressed, in the reference frame (d-q) turning at the speed of the stator field, by the relations given below[2,5,6]:

A. The dq voltage equations

$$\begin{cases} v_{ds} = R_s i_{ds} + \frac{d}{dt} \psi_{ds} - \omega_s \psi_{qs} \\ v_{qs} = R_s i_{qs} + \frac{d}{dt} \psi_{qs} + \omega_s \psi_{ds} \\ v_{dr} = R_r i_{dr} + \frac{d}{dt} \psi_{dr} - \omega_r \psi_{qr} \\ v_{qr} = R_r i_{qr} + \frac{d}{dt} \psi_{qr} + \omega_r \psi_{dr} \end{cases} \quad (12)$$

B. The dq flux equations

$$\begin{cases} \psi_{ds} = L_s i_{ds} + L_m i_{dr} \\ \psi_{qs} = L_s i_{qs} + L_m i_{qr} \\ \psi_{dr} = L_m i_{ds} + L_r i_{dr} \\ \psi_{qr} = L_m i_{qs} + L_r i_{qr} \end{cases} \quad (13)$$

Where R_s, R_r, L_s, L_r are respectively the resistances and inductances of the stator and rotor windings, and L_m is the mutual inductance.

C. Dynamic Power Expressions

The active and reactive stator and rotor powers are expressed by:

$$\begin{aligned} P_s &= \frac{3}{2} \text{Re} \{ v_s i_s^* \} = \frac{3}{2} (v_{ds} i_{ds} + v_{qs} i_{qs}) \\ P_r &= \frac{3}{2} \text{Re} \{ v_r i_r^* \} = \frac{3}{2} (v_{dr} i_{dr} + v_{qr} i_{qr}) \\ Q_s &= \frac{3}{2} \text{Im} \{ v_s i_s^* \} = \frac{3}{2} (v_{qs} i_{ds} - v_{ds} i_{qs}) \\ Q_r &= \frac{3}{2} \text{Im} \{ v_r i_r^* \} = \frac{3}{2} (v_{qr} i_{dr} - v_{dr} i_{qr}) \end{aligned} \quad (14)$$

D. Electromagnetic Torque Equation

$$T_{em} = \frac{3}{2} p \frac{L_m}{L_s} (\psi_{qs} i_{dr} - \psi_{ds} i_{qr}) \quad (15)$$

E. Mechanical Equation

$$\begin{aligned} J \frac{d\Omega_m}{dt} &= T_{em} - T_{load} \\ \frac{d\omega_m}{dt} &= \frac{p}{J} (T_{em} - T_{load}) \end{aligned} \quad (16)$$

Where: J is the inertia on the shaft, ω_m is rotor angular velocity ($\omega_m = p\Omega_m$), T_{load} is the torque on the shaft originating from mechanical means, p is the number of pole pairs.

VI. BACK-TO-BACK CONVERTER MODELLING

The back to back converter can be associates into two[5,6]:

- A first rectifier part.
- An inverter second part.

The storage of the energy on the continuous side is done via a capacitor C of tension V_{dc}

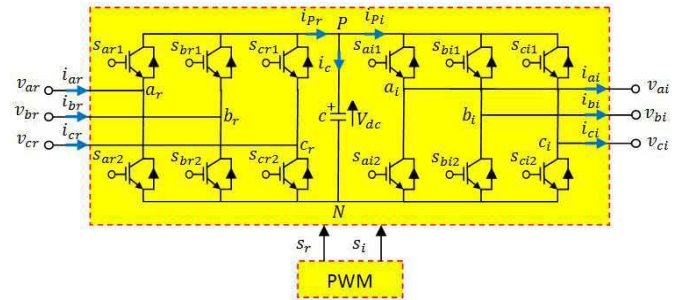


Figure 5. Power circuit of Back-to-back converter

The output voltage of rectifier and inverter of the back to back converter are calculated by using the following relation:

$$\begin{pmatrix} v_{ar} \\ v_{br} \\ v_{cr} \end{pmatrix} = V_{bus} \begin{pmatrix} S_{ar1} \\ S_{br2} \\ S_{cr3} \end{pmatrix}, \begin{pmatrix} v_{ai} \\ v_{bi} \\ v_{ci} \end{pmatrix} = V_{bus} \begin{pmatrix} S_{ai1} \\ S_{bi2} \\ S_{ci3} \end{pmatrix} \quad (17)$$

The current i_c that flows DC-link is given by the following relation:

$$i_c = i_{pr} - i_{pi} = (S_{ar1} i_{ar} - S_{br1} i_{br} - S_{cr1} i_{cr}) - (S_{ai1} i_{ai} - S_{bi1} i_{bi} - S_{ci1} i_{ci}) \quad (18)$$

VII. VECTOR CONTROL OF THE DFIG

A. Rotor-side Converter (RSC) control

Vector control is one of the most widely used control schemes for the DFIG based Wind Turbine Systems. Alignment to the stator flux simply means that the d-axis of the reference frame is chosen to coincide with the stator flux vector. This causes the q-axis component to be zero in the equations [6-10]. We can write:

$$\begin{cases} \psi_{ds} = \psi_s \\ \psi_{qs} = 0 \end{cases} \quad (19)$$

The rotor voltage dynamics are derived by aligning the rotor voltage equation to the stator flux. we have:

DFIG is rated at 2 MW, and the main system parameters used in the simulation are listed in Table 1.

TABLE I THE MAIN SYSTEM PARAMETERS

System	Parameter
DFIG	Rated power : 2 MW,
	Rated stator voltage : 690 V _{rms}
	Rated stator current : 1760 A _{rms}
	Rated torque : 12.7 k.Nm,
	Pair of poles : 2,
	Rated rotor voltage :2070 V _{rms}
	$R_s = 2.6 \text{ m}\Omega$, $L_{\sigma s} = 87 \text{ mH}$,
	$L_m = 2.5 \text{ mH}$, $L_{\sigma r} = 783 \text{ mH}$,
	$R_r = 2.9 \text{ m}\Omega$, $L_{\sigma r} = 87 \text{ }\mu\text{H}$,
	$L_s = L_m + L_{\sigma s} = 2.587 \text{ mH}$,
$L_r = L_m + L_{\sigma r} = 2.587 \text{ mH}$	
Multiplier	$N = 100$
DC BUS	$C_{bus} = 80 \text{ mF}$, $V_{dc} = 1150 \text{ V}$
L Filter	$R_f = 20 \text{ }\mu\Omega$, $L_f = 40 \text{ mH}$
Turbine	$J = 127 \text{ kg.m}^2$, $R = 42 \text{ m}$
GRID	$V_s = 690 \text{ V}$, $f = 50 \text{ Hz}$

The switching frequency of the power switches of the GSC and RSC is set to 4 kHz, and the frequency of the AC grid was 50 Hz.

To maximum value of the power coefficient corresponding, we choose a null pitch angle ($\beta = 0 \text{ rad}$).

The grid-side converter controller is examined under the following condition; The reference of the DC bus voltage V_{dc}^* is set at 1150 V, and the reactive power reference value Q_g^* is set to zero for unity power factor operation of the converter.

The rotor-side converter controller is examined under the following condition; The reference torque T_{em}^* is calculated according to OT MPPT strategy, and The reference stator reactive power value Q_s^* is set to zero for unity power factor.

Figure 8 shows the wind speed profile varies as a step function with wind speed of 8, 10, and 12 m/sec

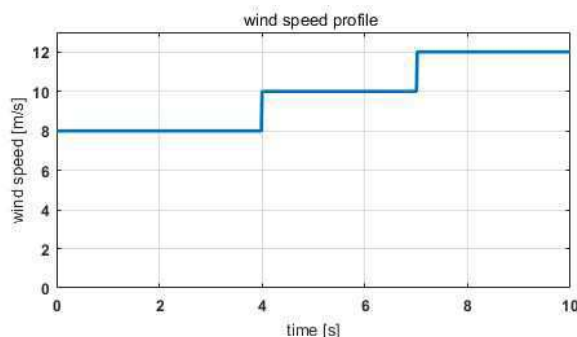


Figure 8. wind speed profile

Figure 9 shows the electromagnetic torque corresponds to a MPPT strategy and the generator electromagnetic torque.

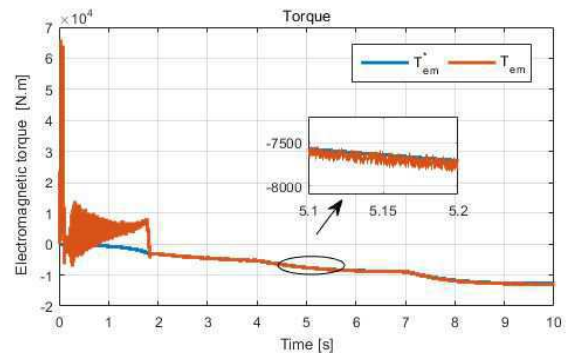


Figure 9. Electromagnetic torque

Figure 10 shows the stator reactive power.

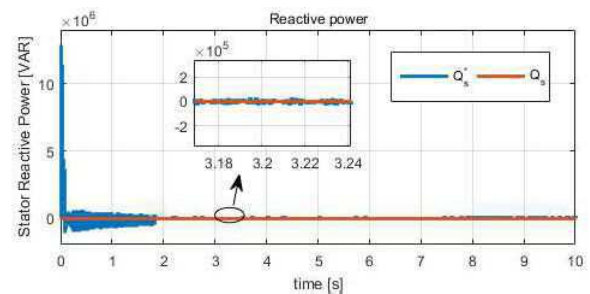


Figure 10. Stator reactive power

The evolution of the DC bus voltage can be seen in Figure 11

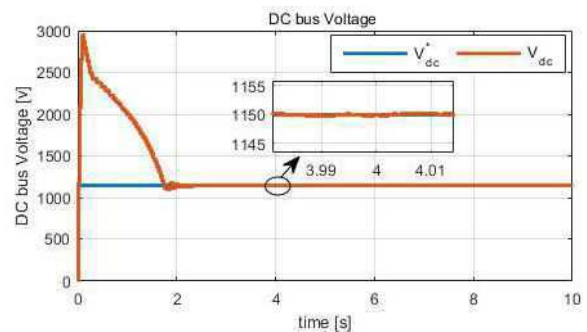


Figure 11. DC bus voltage

Figure 12 shows the phase shift between the stator current and the stator voltage is 180°. This means that the stator active power is deliver to the grid.

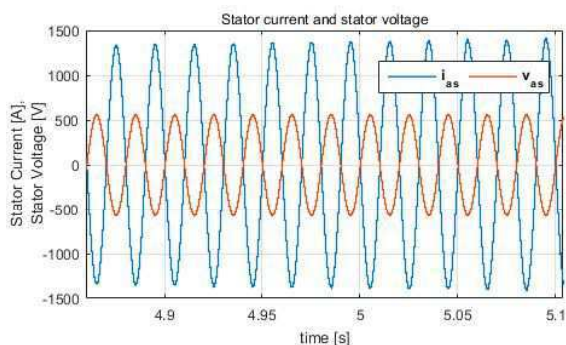


Figure 12. the stator current and the stator voltage

IX. CONCLUSIONS

In this paper, the modeling of the DFIG based on Wind Energy Conversion System (WECS) have been considered and clearly explained. Control strategies and fundamental mathematical equations of the RSC, GSC and MPPT have been presented in detail. The simulation results of DFIG controlled by RSC control and GSC control showed when the wind speed changed for given profile.

The obtained result using MATLAB®/Simulink® allows verify confidently working principle of the DFIG based on WECS.

X. REFERENCES

- [1] MOURAD LOUCIF. Synthèse de lois de commande non-linéaires pour le contrôle d'une machine asynchrone à double alimentation dédiée à un système aérogénérateur, Université de Tlemcen, Phd thesis, 2016.
- [2] G. Abad, L. Marroyo, G. Iwanski et al, Doubly Fed Induction Machine: Modeling and Control for wind energy generation. Wiley-IEEE Press, 2011.
- [3] Marc, Rapin et Jean-Marc, Noël. *ÉNERGIE ÉOLIENNE Principes • Études de cas*, Dunod, 2009.
- [4] Rekioua, D. "Wind Power Electric Systems." Green Energy and Technology, London Springer., 2014.
- [5] Yaramasu, V. et B. Wu, Model predictive control of wind energy conversion systems, John Wiley & Sons, 2016.
- [6] ABAD GONZALO, Power Electronics and Electric Drives for Traction Applications, John Wiley & Sons, 2017
- [7] Abdoulaye mamadie sylla, modélisation d'un émulateur éolien à base de machine asynchrone à double alimentation, université du québec, . Phd thesis, 2013.
- [8] Belmokhtar, K., et al. Modélisation et commande d'un système éolien à base de machine asynchrone à double alimentation pour la fourniture de puissances au réseau électrique. Quatrième Conférence Internationale sur le Génie Electrique CIGE. (2010).
- [9] Abu-Rub, H., et al. Power electronics for renewable energy systems, transportation and industrial applications, John Wiley & Sons. (2014).
- [10] Ghofrani, M., et al. Modeling and simulation of a DFIG-based wind-power system for stability analysis. Power and Energy Society General Meeting, IEEE. (2012).

Power loss reduction in power system using optimal location of STATCOM

F.Z.Messaoud^{#1}, H.Tédjini^{#2}, M. Boudiaf^{*3}

[#]Smart Grids & Renewable Energies (SGRE), University Tahri Mohammed
Bechar, Algeria

¹fz.messaoud45@gmail.com

²tedjini_h@yahoo.fr

^{*}Laadi Laboratory, University Ziane Achour
Djelfa, Algeria

³Boudhiaf_mohamed@yahoo.fr

Abstract— In this paper, we studied the integration of shunt Static Synchronous Compensator (STATCOM) in the electrical networks for a main objective is the reduction of total active power losses of the network 5-bus, we relied on the algorithm of Newton-Raphson (N-R) for load flow and to find optimal sizing and allocation of STATCOM, the simulation results obtained clearly show the beneficial effect of the optimum location of STATCOM on the performance of the power system reliability and feasibility by minimize the voltage deviations such for minimum power loss, voltages of the all buses are found in the allowable margin ($\pm 10\%$) by injecting reactive power at the point where it is implanted, the power flow and power loss before and after placing the STATCOM have been compared the effect of the STATCOM on the power flow remains moderate. Proposed algorithm is implemented in MATLAB.

Keywords— STATCOM; Optimal location; Newton-Raphson; Power flow; Power loss.

I. INTRODUCTION

Currently and in the decades to come, public utilities will be forced to operate the system close to its thermal and stability limits due to major obstacles such as, the dominance of environmental law and over all the problems of cost. The cost of the lines and the power losses, as well as the difficulties encountered in the construction of new transmission lines, would often limit the available transport capacity, there are many cases where economic energy or reserve sharing is limited by transmission capacity, and the situation does not improve[1], [2]. Moreover, in a liberalized electricity service environment, an efficient power grid is essential to the competitive environment of reliable electricity service, in the present days, and with the deregulation of the electricity market, the traditional power system practices have completely changed. Better use of existing power system resources with economic cost has become essential[3]. FACTS devices (Flexible AC Transmission Systems) could be a way to carry out this function without the disadvantages of electromechanical devices such as slowness, the increased

intent for these devices is largely due to the recent development of high power electronics, combined with the deregulation of the energy sector, which has made the use of FACTS cost-effective in power transmission business. In addition, for economic reasons[4], [5], the installation of FACTS devices in all nodes or branches of the power network is impossible and is not necessary therefore the placement of FACTS devices in a network is necessary. In this work, the approach taken for calculating power flow and solving the optimal placement problem of STATCOM relies on Newton Raphson algorithm, we tried to put the STATCOM in three nodes to find the optimal location and its size in a power system 02 machines 5-bus, it will be shown that power losses is greatly affected by presence of a STATCOM in transmission system has been presented to increase the transfer capability and it will be concluded that the voltage profile can be improved effectively, so STATCOM is one of the most effectiveness custom power devices (CPDs) [6] is applied to improve the power system operation.

II. PRINCIPLE OF STATCOM

The STATCOM is the SVC version consisting of a high-tech semiconductor-based voltage converter associated with a capacitor as a DC voltage source and the set connected in parallel to the system network as shown in the Fig.1, The STATCOM is connected through a filter circuit to the grid at the point of common coupling (PCC).[7]

Power S_f at the output of STATCOM can be expressed by the following expression:

$$S_f = P_f + jQ_f \quad (1)$$

The expressions of the active and reactive powers in the reference of Park are given by:

$$P_f = V_d i_{cd} \quad (2)$$

$$Q_f = -V_d i_{cq} \quad (3)$$

Such as:

V_d : Voltage of the point common coupling (PCC) in the reference of Park.

i_{cd}, i_{cq} : Direct and quadratic current of STATCOM.

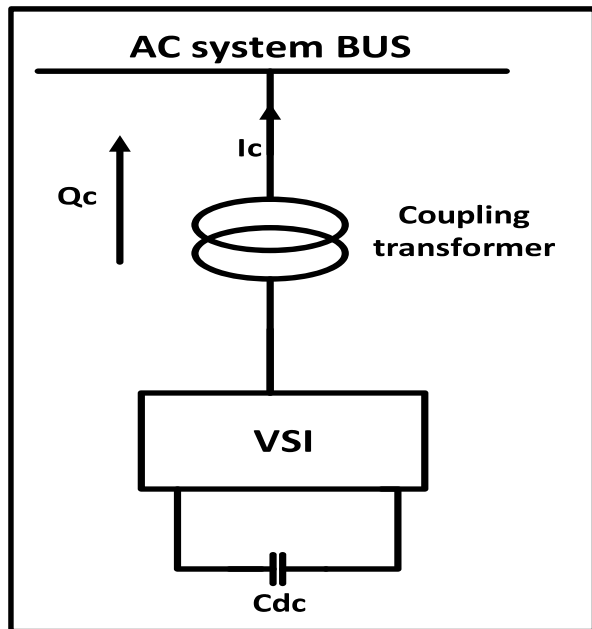


Fig. 1 STATCOM diagram.

We then notice that the component i_{cq} allows to control the reactive power and the component i_{cd} to control the active power. If the current is late, as shown in the Fig. 2 the sign of the quadratic component of the current is negative so the result is positive reactive power means the STATCOM absorbs reactive power (inductive mode)[7]

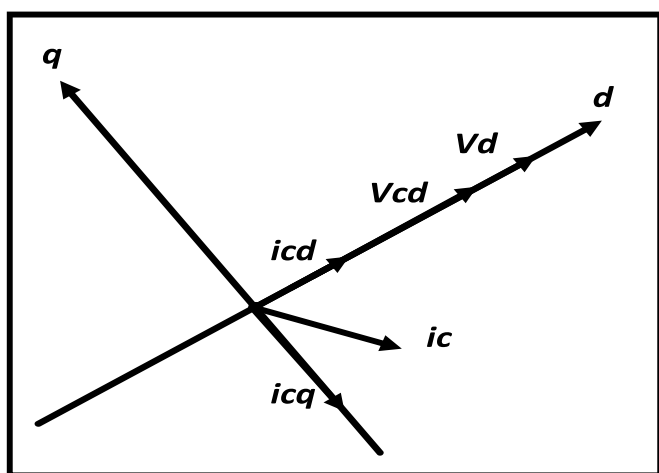


Fig. 2 Operation in inductive mode.

When the sign of the quadratic component of the current is positive, the current is in advance, as shown in Fig. 3, the result is a negative reactive power[8], which means the STATCOM provides reactive power to the network (capacitive mode)

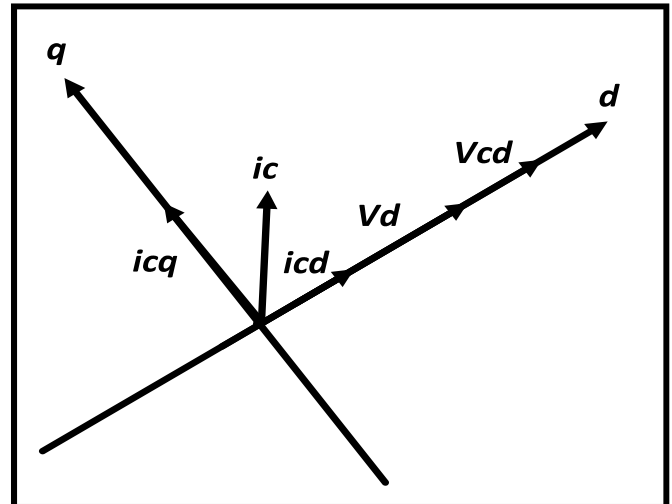


Fig. 3 Operation in capacitive mode.

III. BASIC CONCEPTS OF NEWTON – RAPHSON

The search for the optimal configuration of STATCOM, to be installed on a power network, requires the call of a program, one of these programs, the load-flow calculation program. The calculation of the load flow of a given power network consists in calculating the nodal voltages, the powers passing through the lines[9], as well as the reactive powers generated by the different generators. In this work the Newton-Raphson load flow calculation program is performed on the MATLAB platform, simulations are applied on a network 2 machines 5 bus which is presented in the fig. 5.

The main parts of the load flow calculation program (LF) are:

- Reading the network database.
- Constitution of the admittance matrix Ybus.
- Program launch calculates nodal voltages.
- Calculation of the energy flow P and Q in the lines and the total losses.
- Display of results.

A .constitution of the admittance matrix

The nodal admittance matrix Y, is a square matrix of order n describing the power system consisting of n buses[10], it presents the nodal matrix of the buses of the power systems, and each bus in a real power system is usually connected only to a few other buses through the transmission lines. Matrix Y is also one of the data needed to formulate a power flow study.

Form of the admittance matrix presented in system of equation (4):

$$Y_{bus} = \begin{bmatrix} Y_{11} & Y_{12} & \dots & Y_{1n} \\ Y_{21} & Y_{22} & \dots & Y_{2n} \\ \dots & \dots & \dots & \dots \\ Y_{n1} & Y_{n2} & \dots & Y_{nn} \end{bmatrix} \quad (4)$$

The shunt or series admittances are calculated by the formula:

$$Y_{ij} = \begin{cases} y_{ii} + \sum_{i \neq j} y_{ij} & , Si i = j \\ -y_{ij} & , Si i \neq j \end{cases} \quad (5)$$

B. Newton-Raphson method for load-flow calculation

Newton Raphson's method is the most important method for solving the power flow problem. It's the most important method for solving the power flow problem. Among the important steps of this method is the formation of the Jacobian matrix.[1] So the method of Newton Raphson consists in calculating the voltages (module and phase) of the nodes of a given network. These nodes belong to three types, (PV, PQ, slack bus). The node PQ has two unknowns (modulus and phase of the voltage), while a node PV has a single unknown which is the phase of the voltage. The reference node or the slack bus has no unknowns.

The formation of the Jacobian matrix requires the computation of partial derivatives:

$$\frac{\partial f_1(x)}{\partial \theta_j}, \frac{\partial f_1(x)}{\partial v_j}, \frac{\partial f_2(x)}{\partial \theta_j}, \frac{\partial f_2(x)}{\partial v_j} \quad (6)$$

$$\begin{cases} \frac{\partial f_1(x)}{\partial \theta_i} = \sum_{k=1}^n |V_i| |V_k| (-G_{ik} \sin \theta_{ik} + B_{ik} \cos \theta_{ik}) \\ \frac{\partial f_1(x)}{\partial v_i} = \sum_{k=1}^n |V_k| (G_{ik} \cos \theta_{ik} + B_{ik} \sin \theta_{ik}) \\ \frac{\partial f_2(x)}{\partial \theta_i} = \sum_{k=1}^n |V_i| |V_k| (-G_{ik} \sin \theta_{ik} + B_{ik} \cos \theta_{ik}) \\ \frac{\partial f_2(x)}{\partial v_i} = \sum_{k=1}^n |V_k| (G_{ik} \cos \theta_{ik} + B_{ik} \sin \theta_{ik}) \end{cases} \quad (7)$$

IV. THE APPLIED ALGORITHM

The Newton Raphson (N-R) algorithm is an iterative numerical method that tries to find a solution to the nonlinear equation system, by an iterative solution in fig. 4:

```

Beginning
Reading the database
Constitution of the admittance matrix
Constitution of the Jacobian matrix
iter = 0
i = 0
While stop criterion = 0
iter = iter + 1
Calculate voltage V and angle θ
calculate P, Q
if condition stops < tol or iter = iter_max
stop criterion = 1
end if
end while
if stop criterion = 1 then
calculate the load flow of the lines
display of results
if not
solution does not converge
end if
end
    
```

Fig. 4 different steps of the algorithm used.

V. TEST NETWORK AND LOAD FLOW SIMULATION

A model of the network used for 5 of its buses have 2 generators, as shown in Fig.5. Firstly without the integration of STATCOM we extract the voltage and the nodal angles, the active and reactive power of the lines also the total active power losses, by using the load flow program of the fig. 4

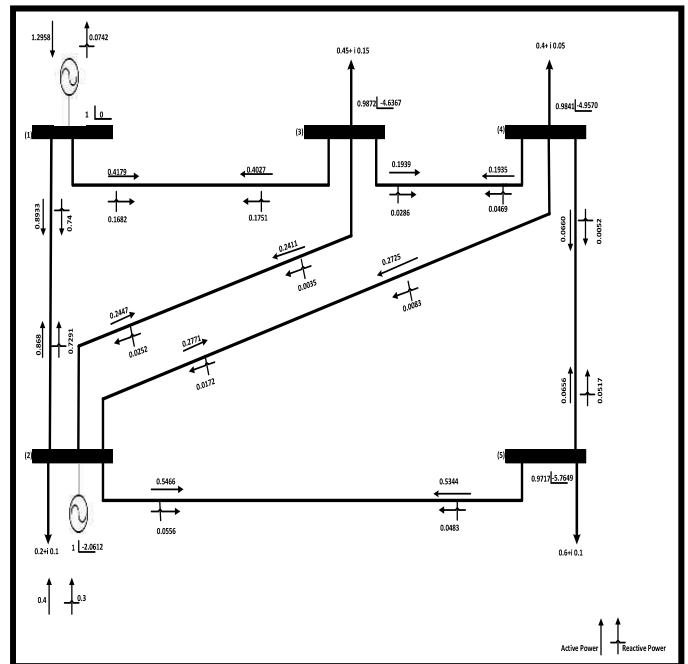


Fig. 5 Network 02 machines 05 buses without STATCOM.

Program result also gave us the total active losses without the integration of STATCOM:

Such as:
 $P_{loss} = 0.0612$ Pu.
 Maximum iteration number = 100.

TABLE I
 EXTRACTS DATA OF LINES OF THE 5-BUS TEST NETWORK

Line	From bus	To bus	R(Pu)	X (pu)	B(pu)
1	1	2	0.02	0.06	0.06
2	1	3	0.08	0.24	0.05
3	2	3	0.06	0.18	0.04
4	2	4	0.06	0.18	0.04
5	2	5	0.04	0.12	0.03
6	3	4	0.01	0.03	0.02
7	4	5	0.08	0.24	0.05

VI. METHODOLOGY FOR PROPOSED WORK

- Step 01: Network data must be collected for 02 machines 05 bus
- Step02: Apply Newton-Raphson method for load flow in MATLAB program is carried out from which nodal voltages, nodal angles, active and reactive power and determine the total active losses without STATCOM.
- Step03: The network comprises five nodes, on the three load nodes we successively place the STATCOM, at each installation we extract the curve of the active power loss according to the reactive power injecting or absorbing between: $[-0.5 \text{ Pu}, +0.5 \text{ Pu}]$.
- Step04: Then, we locate the exact STATCOM location relative to the minimum active power loss according to a single value of the reactive power between: $[-0.5 \text{ Pu}, +0.5 \text{ Pu}]$.
- Step05: For the value of the reactive power injecting or absorbing which gave us a minimum of power losses and about which, we will be able to determine if this value will give us the voltage of all the three nodes in the allowable margin.
- Step06: Finally, the impact of STATCOM upon load flow, before and after optimal localization

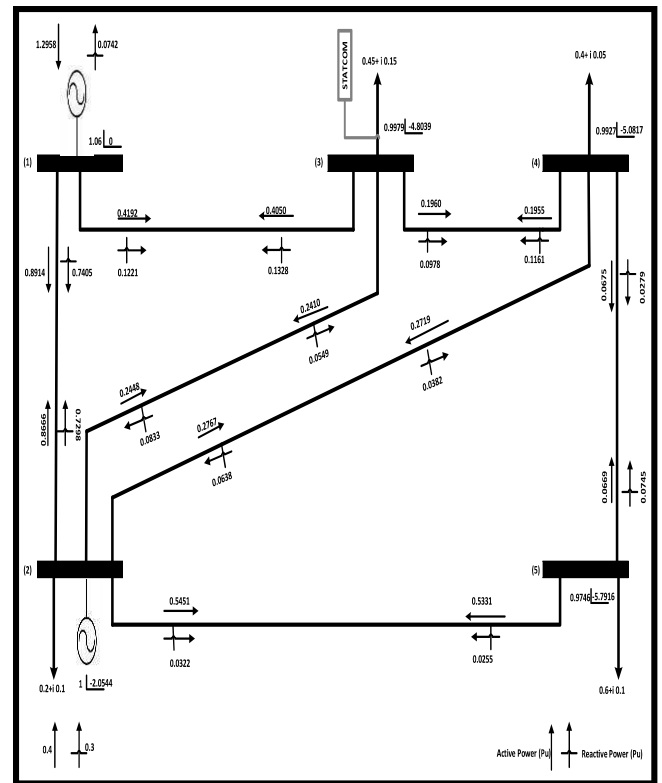


Fig. 7 Network with STATCOM in Bus N°3

The result of the program of total active losses with the integration of STATCOM is:
 $P_{loss} = 0.0605 \text{ Pu}$.

VII. SIMULATION RESULTS

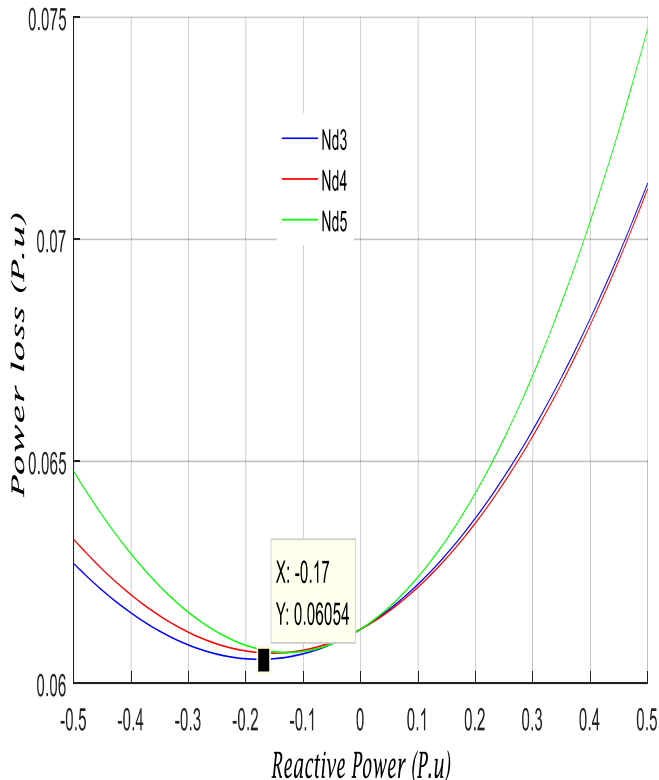


Fig. 6 Power Losses according to Reactive Power (injecting and absorbing)

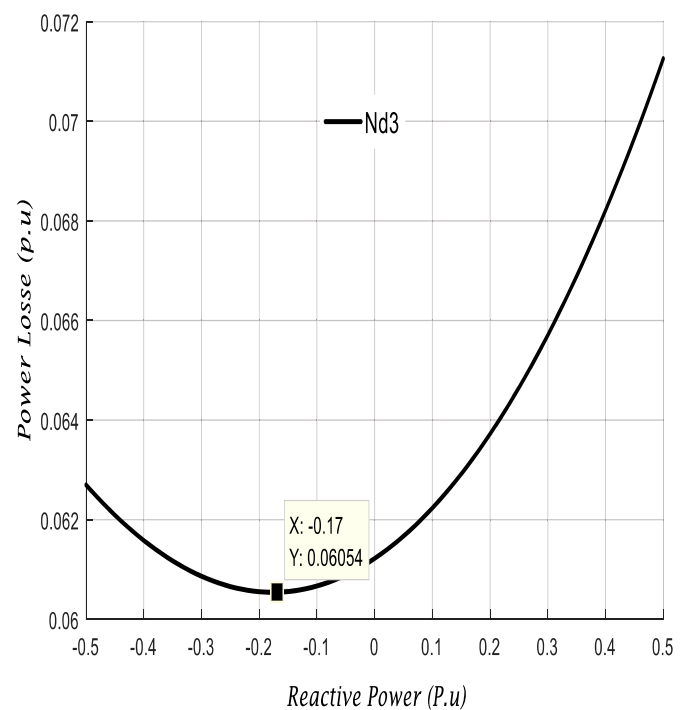


Fig. 8 Power Losses according to Reactive Power (injecting and absorbing), STATCOM in Bus N°3

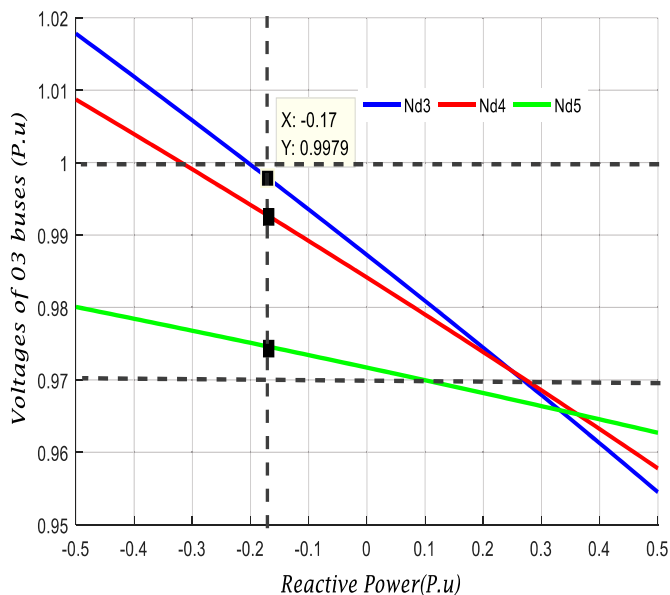


Fig. 9 Voltages of the three Buses: 03,04,05, STATCOM in Bus N°3

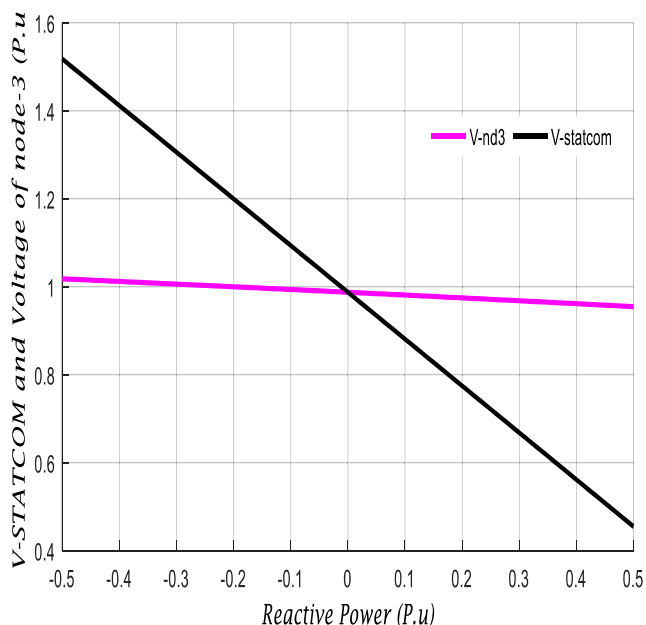


Fig.10 STATCOM and Point Common Connection (PCC) voltages.

In the beginning, we started the simulation without STATCOM results of the power flow shows in fig.5, in this case the total power losses is: $P_{loss} = 0.0612$ Pu.

To improve network power losses, the STATCOM is installed in the three load nodes are: “03”, “04” and “05”, in fig.6 it is noted that the placement of STATCOM in the bus 03 gives the best result compared to the other buses, such that for a minimum of power losses the reactive power delivered to the network is: $Q_C = -0.17$ Pu.

In Fig.8, it seems very clear that the optimal location to get the minimum power losses: $P_{loss} = 0.0605$ Pu for a single value of reactive power injected is $Q_C = -0.17$ Pu is to place the STATCOM in the load node “03”.

Fig. 9 proves the effectiveness of the optimal location of the synchronous static compensator to maintain the voltages of the all buses in the allowable margin ($\pm 10\%$)

In “Fig.10”, it is noted that the voltage of STATCOM is greater than the voltage of the point common of coupling (v-nd3) between $[-0.5\text{pu}, 0\text{pu}]$, therefore STATCOM operated in capacitive mode and provides the reactive power to the network, and between $[0\text{Pu}, 0.5\text{Pu}]$ the voltage of STATCOM is smaller than the voltage of the point common of coupling (v-nd3) therefore STATCOM operated in inductive mode and absorbs the reactive power from the system.

Fig.5 and fig.7 shows the power flow before and after placing the STATCOM so the effect of the STATCOM on the power flow remains moderate.

VII. CONCLUSION

Power demands will keep increasing more and more, consequently the power system network is become less secure, it is concluded from many research that by placing FACTS controllers the power system security is improved, This work mainly helps in understanding the principles of STATCOM and also the basics of reactive power compensation using STATCOM, we have used MATLAB coding for Newton-Raphson load flow method to calculate the active power losses before and after STATCOM’S allocation, From above obtained results, it is clearly understood that STATCOM can providing appropriate amount of reactive power for reducing the power losses and maintaining voltage in allowable margin.

REFERENCES

- [1] E. Acha et B. Kazemtabrizi, “A New STATCOM Model for Power Flows Using the Newton–Raphson Method”, IEEE Trans. Power Syst., vol. 28, no 3, p. 2455-2465, août 2013.
- [2] A. R. Gupta et A. Kumar, “Impact of various load models on D-STATCOM allocation in DNO operated distribution network”, Procedia Comput. Sci., vol. 125, p. 862-870, 2018.
- [3] S. Raj et B. Bhattacharyya, “Optimal placement of TCSC and SVC for reactive power planning using Whale optimization algorithm”, Swarm Evol. Comput., vol. 40, p. 131-143, juin 2018.
- [4] P. Arboleya, C. Gonzalez-Moran, et M. Coto, “Modeling FACTS for power flow purposes: A common framework”, Int. J. Electr. Power Energy Syst., vol. 63, p. 293-301, déc. 2014.
- [5] A. Bagherinasab et N. A. Azli, “Optimal Placement of D-STATCOM Using Hybrid Genetic and Ant Colony Algorithm to Losses Reduction”, vol. 2, no 2, p. 8, 2013.
- [6] O. P. Mahela et A. G. Shaik, “A review of distribution static compensator”, Renew. Sustain. Energy Rev., vol. 50, p. 531-546, oct. 2015.
- [7] F. H. Gandoman et al., “Review of FACTS technologies and applications for power quality in smart grids with renewable energy systems”, Renew. Sustain. Energy Rev., vol. 82, p. 502-514, févr. 2018.
- [8] T. DEB et A. S. SIDDIQUI, “Optimal Placement Of Statcom Using Gravitational Search Algorithm For Enhanced Voltage Stability”, vol. 11, p. 5, 2016.
- [9] S. S. Chandrakanth et A. Ramulu, “Optimal Location of Statcom for Power Flow Control”, vol. 3, no 4, p. 5, 2013.
- [10] M. Simeon et W. S. Tita, “Minimization of Active Transmission Loss in Power Systems using Static Var Compensator”, vol. 13, no 7, p. 9, 2018.

Valorization Of Sand Dune Of Taghit (South-Western Algeria) In The Construction: Technical And Eco-Environmental Aspect

A. Makani^{#1}, F.Z. Rennani^{*2}, A. Tafraoui^{#3}, F. Benmeriou^{#4}, S. Zaoia^{#5}

[#] Civil Engineering Department, TAHRI Mohamed- Bechar University
LFGM (Laboratoire de Fiabilité du Génie Mécanique), BP 417 Bechar (08000), Algeria

¹makaniabdelkadir@yahoo.fr

³ahmedtafraoui@yahoo.fr

⁴faridbba37@yahoo.com

⁵zawiamin@yahoo.com

^{*} Civil Engineering Department, TAHRI Mohamed- Bechar University
FIMAS (Laboratoire de Fiabilité des Matériaux et Structures), BP 417 Bechar (08000), Algeria

²rennaifatimazahra@gmail.com

Abstract— Currently, it is necessary to replace Portland cement with environmentally friendly materials. The cement production process is associated with a high consumption of energy, resources and of course a large amount of carbon dioxide emissions. This research work deals with the valorization of dune sand of Taghit (south-western Algeria) in construction and more particularly the new concretes namely self-compacting concretes (SCC) and high performance concretes (HPC). The results obtained on the different materials studied show that the use of Taghit sand dune as a partial replacement of cement considerably improves both their rheological properties and their mechanical performance.

Keywords— Dune sand, New materials, rheological characterization, mechanical performance, Eco-environmental study

I. INTRODUCTION

Sand Dune has many uses around the world. The granulometry, the uniformity, the chemical purity and the nature of the dune sand make it a unique resource. Demand for this resource is increasing due to an increase in the number of products using dune sand and because other new uses have been developed [1]. The main use of dune sand is in the construction of materials [2-4]. Sand is used to make molds and cores. Molds are used to form new materials. Core sand fills spaces and voids. Silica sand (quartz) is also used in the manufacture of glass. Railroads use large amounts of sand to improve traction on wet or slippery rails. Sand is used in sanding. The floors of some large open hearth furnaces are covered with siliceous sand. Sand is an excellent filter for removing sediment and bacteria from water. Finally, one area of increased use of sand is in fiberglass manufacturing [1].

Sand is a unique raw material for the construction industry at present. Not only is it used for glass but more so for making concrete, filling roads, reclamations and building

sites [2]. Each has its own requirements in respect of the quality of the sand [5-6].

The main objective of this research work is to develop the Taghit dune sand (south-western Algeria) in the construction and more particularly the new concretes namely self-compacting concrete (SCC) and high performance concrete (HPC).

II. TECHNICAL CHARACTERIZATION OF BASIC MATERIALS

A. Physical properties

The cement used is Portland cement resistance real 425 bars. The dune sand coming from crushing sand dune which is on the level of Taghit, wilaya of Bechar (Algeria), the maximum coarse aggregate of crushed dune sand does not exceed 80 μ m. Table 1 present a Physical properties of Portland cement and dune sand.

TABLE I
PHYSICAL PROPERTIES OF PORTLAND CEMENT AND DUNE SAND [7]

Items	Portland Cement	Dune Sand	Regulatory
Absolute density	3.05	2.8	NF P 18-558
specific surface (cm ² /g)	3200	3000	EN 196-6
Unit weight (kg/m ³)	1120	1300	NF P 18-554

B. Mineralogical and chemical properties

The results of DRX analysis carried out on the dune sand of Taghit and Portland cement are presented graphically on Fig 1. It was noticed a peak of approximately 100 % of silica with dune sand and calcite for cement which translated the predominance of SiO₂ and CaCO₃, the others revealed elements present at small percentages.

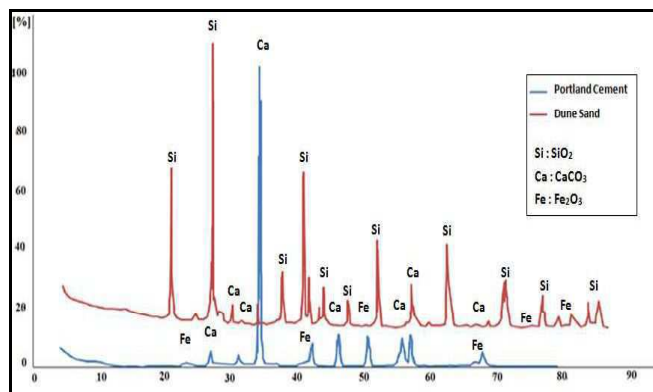


Fig. 1 XRD analyze of Portland cement and dune sand

From the fig 2, it was observed that the shape of Portland cement particle is angular, dappled, broken or round forms observed for dune sand.

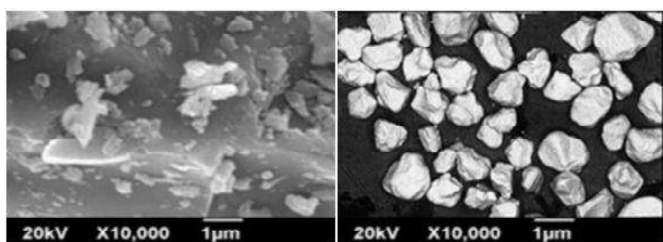


Fig. 2 SEM photographs of: (a) Portland cement; (b) Dune sand

The chemical compositions of Portland cement and dune sand are presented in table 2.

TABLE 2
 CHEMICAL PROPERTIES OF PORTLAND CEMENT AND DUNE SAND [8]

Elements (%)	Cement	Dune sand
SiO ₂	17.49	97.15
Al ₂ O ₃	4.51	0.79
Fe ₂ O ₃	3.02	0.21
CaO	62.78	0.11
MgO	2.15	0.05
SO ₃	2.38	0.14
Na ₂ O	0.05	0.18
TiO ₂	0.64	0.05
Others	0.02	< 0,02
Loss of ignition	8.10	0.58

III. VALORIZATION OF DUNE SAND IN NEW MATERIALS

A. Self-compacting concrete

The SCC must satisfy many tests, we chose three that are recommended by AFGC. [3] that allow to characterize the principal properties of SCC in the fresh state (fluidity , static and dynamic stability, free and confined environment) spreading Abrams cone flow box L and stability through a sieve. The test slump flow (fig.3-a) is carried with the

Abrams cone consists of measuring the diameter of concrete spread on two perpendicular lines and takes the mean. The test L-box (fig 3-b) is used to check the mobility of confined concrete and verify the implementation of concrete will not be thwarted by blocking phenomena. The test of stability (fig. 3-c) by sieve can qualify compacting concrete to the risk of segregation and indicates the degree of segregation of SCC.



Fig. 3 Qualification test of self-compacting concrete: a-Slump flow, b- L-Box and c-Stability in sieve

According to Table 3, all self-compacting concrete (SCC) must meet the recommended criteria for testing [AFGC, 2008].

TABLE 3
 RHEOLOGICAL PROPERTIES OF SELF- COMPACTING MIXES

SCC mixes	Rheological properties		
	Slump flow (cm)	L-box	Segregation index (%)
Limited values according to AFGC. [9]	60 - 75	≥ 0.80	≤ 15

B. High performance concrete

The Compressive strength is an indicative characteristic of concrete that allows us to envisage other properties. Generally, enhanced durability properties can be obtained with concretes of higher compressive strength. The fig 4 presents the compressive strength of various HPC mixes determined at different ages. As expected, the compressive strength of HPC increased with age. As can be observed, the compressive strength slightly increased with increase of amount of dune sand. This is due to the physical nature of better packing, as addition of dune sand governs the compressive strength due to the denser matrix and the better dispersion of cement grains [6]. Fineness of the dune sand also affects the strength as it filled up the micro pores within the concrete matrix and densified the concrete [7]. The dune sand have improved the properties of HPC such as porosity reduced and better bonding in inter transition zone [6].

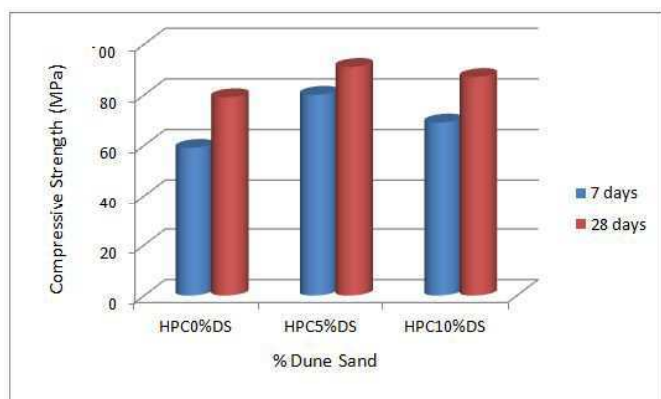


Fig. 4 Mechanical properties of high performance concrete mixes

IV. CONCLUSIONS

In light of the results obtained during this research work, this study allowed us to extract the following conclusions:

- It is possible to manufacture a new concrete (SCC and HPC) based on dune sand with better rheological and mechanical performances;
- The incorporation of dune sand slightly improves the mechanical resistance of concretes. The addition of dune sand can help increase the compactness of concrete by forming a more compact granular skeleton;
- The use of sand dune of Taghit in the construction is very interesting economically and ecologically on the one hand through the partial replacement of cements, and on the other hand, it contributes to the improvement of physical and mechanical properties of concretes.

Finally, we can say that the development of sand dune can provide a solution for some work in the desert regions of our country.

ACKNOWLEDGMENT

We would like to thank all LFGM, FIMAS and TAHRI Mohamed-Bechar University technical staff for their cooperation and assistance throughout our experimental work.

REFERENCES

- [1] J. Lewis, "Sand and sand mining part I" Michigan Geological Survey Division Circular (#11), 1975 website. [Online]. Available: <http://geo.msu.edu/extra/geogmich/dunes.html>
- [2] R. Mahendran, K. Godwin, T. Gnana Selvan and M. Murugan "Experimental study on concrete using sea sand as fine aggregate" International Journal of Scientific & Engineering Research, Volume 7, Issue 5, May-2016.
- [3] S. Zaoiai, A. Makani, A. Taфраoui, F. Benmerioul "Optimization and mechanical characterization of self-compacting concrete incorporating rubber aggregates" Asian Journal of Civil Engineering, BHRC, Volume 17, Issue 6 pp. 817-829, Octobre 2016.
- [4] Z. Damene, M.S. Goual and I. Saiti "Valorisation of Dune Sand and Waste Brick Filler in Elaboration of Cellular Concrete: Mechanical and Thermal Properties" European Journal of Science and Technology Special Issue, pp. 52-56, January 2018.
- [5] [S. Zaoiai, A. Makani and A. Taфраoui "Amélioration des Caractéristiques Mécaniques des Bétons Auto-Plaçants à Base des Granulats Caoutchouc par l'Ajout des Fines Siliceuses" 2eme Séminaire International de Génie Civil SIGCB'2015, Béchar, 27 et 28 octobre 2015.
- [6] F. Benmerioul, A. Taфраoui, A. Makani and S. Zaoiai "A study on mechanical properties of self-compacting concrete made utilizing ground dune sand" Romanian Journal of Materials (RJM), Volume 47, Issue 3, September 2017.
- [7] F. Benmerioul, A. Makani, A. Taфраoui and S. Zaoiai "Valorization of the crushed dune sand in the formulation of self-compacting-concrete" Procedia Engineering, Volume 171, 672 – 678, Janvier 2017.
- [8] F. Benmerioul, A. Makani, A. Taфраoui and S. Zaoiai "Incorporation of dune sand in the formulation of self-compacting concrete: optimization and characterization" International Conference on Civil and Environmental Engineering, Cappadocia, Turkey, 20-23 Mai 2015.
- [9] AFGC. "Recommandations pour l'emploi des bétons autoplaçants" Documents scientifiques et techniques Association Française de Génie Civil. Paris. France. 2008..

THE FP-LAPW CALCULATIONS OF STRUCTURAL, ELECTRONIC AND THERMODYNAMIC PROPERTIES OF OF ALKALINE EARTH OXIDES CaO, SrO AND THEIR ALLOYS.

M. Slimani, N. Chouit, H. Meradji and S. Ghemid

Laboratoire LPR, Département de Physique, Faculté des Sciences, Université d'Annaba, Algeria
e-mail: menoubas@yahoo.fr

Abstract— The structural, electronic, and thermodynamic properties of $\text{Ca}_{1-x}\text{Sr}_x\text{O}$ ternary alloys in NaCl structures at various Sr concentrations are presented. The calculations were performed using the full potential linearized augmented plane wave (FP-LAPW) method within the density functional theory (DFT) in the local density approximation (LDA) and two developed refinements, namely the generalized gradient approximation (GGA) of Perdew *et al* (1996 *Phys. Rev. Lett.* **77** 3865) for the structural properties and Engel and Vosko (1993 *Phys. Rev. B* **47** 13164) for the band structure calculations. Deviation of the lattice constants from Vegard's law and the bulk modulus from the linear concentration dependence (LCD) were observed for the alloys. The microscopic origins of the gap bowing were explained by using the approach of Bernard and Zunger (1986 *Phys. Rev. Lett.* **34** 5982). In addition, the thermodynamic stability of the alloys was investigated by calculating the critical temperatures of alloys.

Keywords— *DFT, Alloys, FP-LAPW, Band gap, semiconductor*

INTRODUCTION

Semiconductor alloys, which are solid solutions of two or more semiconducting elements, have important technological applications, especially in the manufacture of electronic and electro-optical devices. One of the easiest ways to change artificially the electronic and optical properties of semiconductors is by forming their alloys; it is then interesting to combine two different compounds

with different optical band gaps and different rigidities in order to obtain a new material with intermediate properties. Hence, the major goal in materials engineering is the stability to tune the band gap independently in order to obtain the desired properties. The alkaline earth chalcogenides (AX: A = Be, Ca, Mg, Sr, Ba; X = O, S, Se, Te) form a very important closed shell ionic system crystallizing in NaCl-type structure at room conditions except for the MgTe and the beryllium chalcogenides. These compounds are technologically important materials having many applications ranging from catalysis to microelectronics. They have also application in the area of luminescent devices [1-3]. In fact, one of the easiest ways to change artificially the electronic and optical properties of semiconductors is by forming their alloys; it is then interesting to combine two different compounds with different optical band gaps and different rigidities in order to obtain a new material with intermediate properties. Therefore, a great deal of progress has made in the last few decades in understanding the effects of disorder in random alloys. Zunger and co-workers [4] have introduced an approach that greatly reduces the size of the supercell required to obtain a realistic description of a random alloy by using so-called 'special quasirandom structures (SQSs)'. In this paper, we model $\text{Ca}_{1-x}\text{Sr}_x\text{O}$ ternary alloys at some selected compositions with ordered structures described in terms of periodically repeated supercells (SQSs). In order to carry out our calculations, we have applied the full potential-linearized augmented plane wave (FP-LAPW) method. On one hand we focused our efforts on the

physical origins and variation of the optical band gap within the alloy fraction; on the other hand we address the more fundamental issue of the phase stability of these alloys.

METHOD OF CALCULATION

The calculations presented in this work were performed using the FP-LAPW method. By this method no shape approximation on the potential or on the electronic charge density is made. Inside atomic spheres, a linear combination of radial functions times spherical harmonics is used, while in the interstitial region a plane wave expansion is used. The method is implemented in WIEN2K code [5], which allows the inclusion of local orbitals in the basis in order to improve the linearization and make possible a consistent treatment of semicore and valence states in an energy window. We used both local density approximation (LDA) and generalized gradient approximation (GGA). The exchange-correlation potential for the structural properties was calculated by GGA based on the Perdew *et al* [6] form, while for the optical and electronic properties, the exchange-correlation functional of Engel and Vosko (EV-GGA) [7] was applied. In the calculation, the convergence parameter RKmax, which controls the size of the basis sets in these calculations, was set as 8.0. The cut-off energy, which defines the separation between the core and valence states, was set as -6.0 Ry. For the sphere radii, we have adopted the values of 2.3, 2.2 and 2.1 au for Ca, Sr and O, respectively. A mesh of 47 special k -points for binary compounds and 125 special k -points for the alloy were taken in the irreducible wedge of the Brillouin zone. The lattice structures of the alloys under investigation have been modeled at selected compositions as detailed in our previous work [8].

RESULTS AND DISCUSSION

A. Structural properties

In this section, we have analyze the structural properties of CaO and SrO compounds in the rocksalt structure using the GGA scheme. The alloys have been modeled at some selected compositions ($x = 0.25, 0.5, 0.75$) following the SQS approach. For the considered structures, we

perform the structural optimization by minimizing the total energy with respect to the cell parameters and also the atomics positions.

The total energy calculated as a function of unit cell volume where fitted to the murnaghan's equation of state [9]. The equilibrium lattice constants and bulk modulus both for binary compounds and their alloys are given in table 1 and 2. Considering the general trend that GGA usually overestimates the lattice parameters [10], our results of binary compounds are in reasonable agreement with the experimental and other calculated values.

Table 1. Calculated lattice parameter of CaO and SrO compounds and their alloys at equilibrium volume.

		Lattice constant $a(\text{Å})$			
x		This work		Exp.	other calculation
		GGA	LDA		
Ca _{1-x} Sr _x O	1	5.198	5.068	5.16[18]	5.197[16], 5.223[17]
	0.75	5.125	4.994		
	0.5	5.043	4.912		
	0.25	4.947	4.821		
	0	4.837	4.719	4.81[19]	4.86[17], 4.84 [16]

Table 2. Calculated bulk modulus B of of CaO and SrO compounds and their alloys at equilibrium volume

		Bulk modulus B (GPa)			
x		Nos calculs		Exp.	Autres
		GGA	LDA		
Ca _{1-x} Sr _x O	1	83.248	104.491	91 [18]	86 [16]
	0.75	90.067	108.308		
	0.5	94.401	113.747		
	0.25	98.295	120.478		
	0	102.070	128.9602	110[19]	117 [17]

Usually, in the treatment of alloys, it is assumed that the atoms are located at the ideal lattice sites and the lattice constant varies linearly with according to the so-called Vegard's law [11]. However, violation in this linear law has been reported in semi-conductor alloys both experimentally [12, 13] and theoretically [14, 15]. As an example the results obtained for the composition dependence of the calculated equilibrium lattice parameter for Ca_{1-x}Sr_xO alloys, respectively are shown in Fig 1.

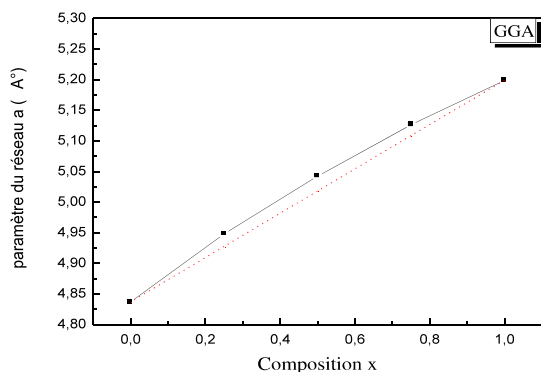


Fig 1. Calculated equilibrium lattice constants of the $\text{Ca}_{1-x}\text{Sr}_x\text{O}$ alloy for different concentrations using GGA.

A small deviation from Vegard's law (a linear variation of the lattice constant of alloys versus composition x) is clearly visible with an upward bowing parameter equal to -0.099 \AA for $\text{Ca}_{1-x}\text{Sr}_x\text{O}$ alloy obtained by fitting the calculated values with a polynomial function. Fig. 2 shows the bulk modulus as a function of x for the $\text{Ca}_{1-x}\text{Sr}_x\text{O}$ alloy respectively. A Similar behavior was observed for the composition dependence of the bulk modulus for the alloy. Deviations of the bulk modulus from the linear concentration dependence (LCD) with downward bowing equal to 7.459 GPa for this alloy, was observed. This deviation is mainly due to the large mismatch of the bulk modulus of SrO and CaO binary compounds

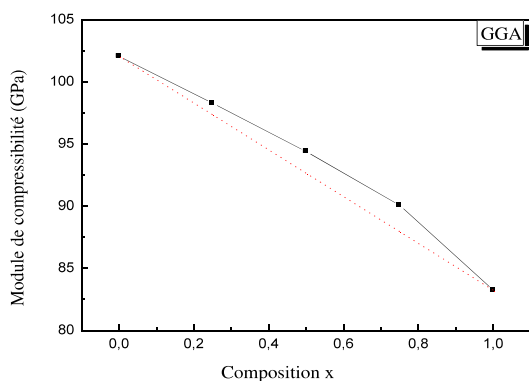


Fig.2. Composition dependence of the calculated bulk modulus (solid squares) of $\text{Ca}_{1-x}\text{Sr}_x\text{O}$ alloy compared with LCD prediction (dashed line).

B. Electronic properties

To compute the band gaps for binary compounds and their alloys self-consistently, the LDA, GGA and EVGGA are used within the DFT. The band gap results for the different concentrations are given in Table 3. The band gap values given by the EVGGA formalism are reasonably in agreement with experiment; the LDA and GGA gives a lower value. In fact, it is well known that the GGA usually underestimates the experimental energy band gap [20, 21].

Table 3. The gap energy E_g of the $\text{Ca}_{1-x}\text{Sr}_x\text{O}$ ternary alloy at equilibrium volume (all the values are in eV).

x	$\text{Ca}_{1-x}\text{Sr}_x\text{O}$		E_g (eV)	
	Our work GGA	EVGGA	Exp.	Other work
1	3.327	4.032	5.272 [22]	3.01 [11], 3.2 [23]
0.75	3.353	4.025		
0.5	3.379	4.006		
0.25	3.423	4.048		
0	3.671	4.271	4.1 [24]	2.097 [25]

In fact, the energy gaps are systematically underestimated in ab initio calculations, and this is an intrinsic feature of the density functional theory (DFT), DFT being a ground-state theory is not suitable for describing excited-state properties, such as the energy gap. However, it is widely accepted that GGA (LDA) electronic band structures are qualitatively in good agreement with the experiments as regards the ordering of the energy levels and the shape of the bands. Engel and Vosko [26], by considering the underestimation of the energy gap, constructed a new functional form of the GGA which is able to reproduce better the exchange potential at the expense of less agreement in the exchange energy. This approach (EVGGA) yields a better band splitting. However, in this method, the quantities that depend on an accurate description of exchange energy E_x , such as equilibrium volumes, are in poor agreement with experiment. Fig. 3 shows the composition dependence of the calculated band gaps using the GGA and EVGGA schemes. It is clearly seen that the calculated band gap decrease with the composition for the $\text{Ca}_{1-x}\text{Sr}_x\text{O}$ alloy.

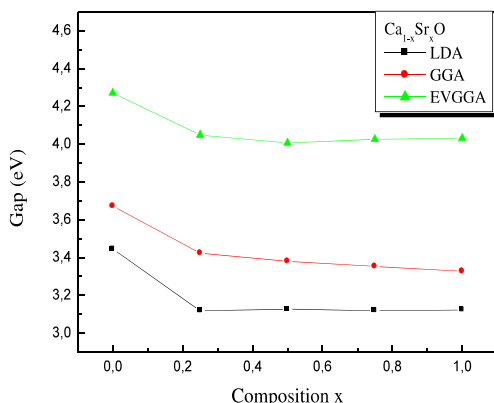


Fig 3. Composition dependence of the calculated band gap for $\text{Ca}_{1-x}\text{Sr}_x\text{O}$ alloy.

C. Thermodynamic properties

In order to study the phase stability of the $\text{Ca}_{1-x}\text{Sr}_x\text{O}$ alloy, we calculated the phase diagram based on the regular-solution model [27-29]. For alloys, the Gibbs free energy of mixing ΔG_m is expressed as: $\Delta G_m = \Delta H_m - T\Delta S_m$, where, $\Delta H_m = x(1-x)$, $\Delta S_m = -R [x \ln x + (1-x) \ln (1-x)]$, ΔH_m and ΔS_m are the enthalpy and entropy of mixing, respectively; is the interaction parameter and depends on the material; R is the gas constant and T the absolute temperature. The mixing enthalpy of alloys can be obtained from the calculated total energies as $\Delta H_m = E_{\text{ABxC1-x}} - x E_{\text{AB}} - (1-x)E_{\text{AC}}$, where $E_{\text{ABxC1-x}}$, E_{AB} and E_{AC} are the respective energies of the $\text{A}_{1-x}\text{B}_x\text{C}$ alloy and the binary compounds AB and AC. We then calculated ΔH_m to obtain as a function of concentration. The interaction parameter increases almost linearly with increasing x . From a linear fit. First we calculate ΔG_m using the equations above, and then we use the Gibbs free energy at different concentrations to calculate the $T-x$ phase diagram, which shows the stable metastable and unstable mixing regions of the alloy. At a temperature lower than the critical temperature T_c , the two binodal points are determined as those points at which the common tangent line touches the ΔG_m curves. The two spinodal points are determined as those points at which the second derivative of ΔG_m is zero; $\partial^2(\Delta G_m)/\partial x^2 = 0$. Figure 4 shows the calculated phase diagram including the spinodal and binodal curves of the alloy of interest. We observed a critical temperature $T_c = 596$ K for the $\text{Ca}_{1-x}\text{Sr}_x\text{O}$

alloy. Hence, our results indicate that the alloy $\text{Ca}_{1-x}\text{Sr}_x\text{O}$ is stable at low temperature.

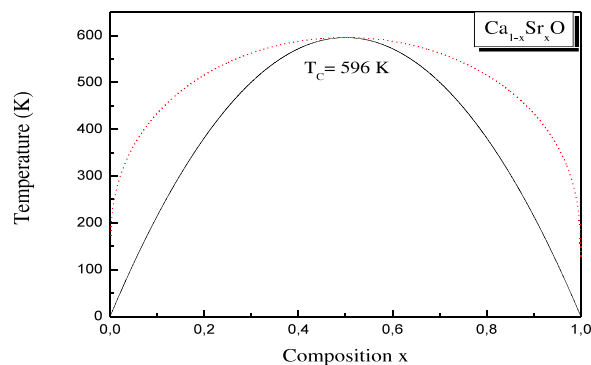


Fig 4. $T-x$ phase diagram of the $\text{Ca}_{1-x}\text{Sr}_x\text{O}$ alloy.

CONCLUSION

We have used the FP-LAPW method to study the structural, electronic and thermodynamic properties of the $\text{Ca}_{1-x}\text{Sr}_x\text{O}$ alloy. The composition dependence of the lattice constants, bulk modulus and band gap has been studied. The calculated band structure shows a transition from indirect to direct band gap. Like the lattice constant, the band gap exhibits nonlinear behavior or bowing effect with the change of concentration. We observed a critical temperature $T_c = 596$ K, which means that the $\text{Ca}_{1-x}\text{Sr}_x\text{O}$ alloy is stable at low temperature. These data may be useful for mechanical, chemical and electronic industries where the performance of a device is affected by its thermodynamic properties.

REFERENCES

- [1] Pandey R, Sivaraman S 1991 *J. Phys. Chem. Solids* **52** 211.
- [2] Asano S, Yamashita N, Nakao Y 1978 *Phys. Status. Solidi* **89** 663.
- [3] Nakanishi, Ito T, Hatanaka Y, Shimaoka G 1992 *Appl. Surf. Sci* **66** 515.
- [4] Zunger A, Wei S H, Ferreira L G and Bernard J E 1990 *Phys. Rev. Lett* **65** 353.
- [5] Blaha P, Schwarz K, Madsen G K H, Kvasnicka D and Luitz J 2001 *Phys. Rev. B* **64** 195134.
- [6] Perdew J P, Burke S and Ernzerhof M 1996 *Phys. Rev. Lett.* **77** 3865.
- [7] Engel E and Vosko S H 1993 *Phys. Rev. B* **47** 13164.
- [8] El Haj Hassan F, Breidi A, Ghemid S, Amrani B, Meradji H and Pagès O 2010 *J Alloys Compd.* **499** 80.

- [9] Murnaghan F D 1944 Proc. Natl Acad. Sci. USA **30** 244.
- [10] Chrifi Z, Baaziz H, El Haj Hassan and Bouarissa N (2005) J. Phys. Condens. Matter **17** 4083.
- [11] Vegard L 1921 Z. Phys. **5** 17.
- [12] Jobst B, Hommel D, Lunz U, Gerhard T and Landwehr G 1996 *Appl. Phys. Lett.* **69** 97.
- [13] Dismukes J P, Ekstrom L and Poff R J 1964 *J. Phys. Chem.* **68** 3021.
- [14] El Haj Hassan F and Akdarzadeh H 2005 *Mater. Sci. Eng. B* **121** 170.
- [15] El Haj Hassan F 2005 *Phys. Status Solidi b* **242** 909.
- [16] T. Tsuchiya, K. Kawamura, J. Chem. Phys. 114 (22) (2001) 10086.
- [17] F. Marenelli, A. Lichanot, Chem. Phys. Lett. 367 (2003) 430.
- [18] Y. Fei, Am. Mineral. 84 (1999) 272.
- [19] P. Pichet, H. K. Mao, P.M.Bell, J. Geophys. Res. 93 (1988) 15279.
- [20] P. Dufek, P. Blaha, and K. Schwarz, Phys. Rev. B 50, 7279 (1994).
- [21] G. B. Bachelet and N. E. Christensen, Phys. Rev. B 31, 879 (1995).
- [22] R. Pandey, J.E. Jaffe. A. B. Kunz, Phys. Rev. B 43 (1991) 9228.
- [23] G. Kalpana, B. Palanivel, M. Rajagopalan, Phys. Rev. B 52 (1995) 4.
- [24] Y.-D.Guo, X.-L. Chen, L.-P. Zhou, Z.-J, Liu, X.-D? Yang, Physica B 373 (2006) 334.
- [25] W. Gu, S.Y. Wang, M. Xu, Y.R. Chen, L.Y. Chen, Y. Jia, Opt. Commun. 48 (2008).
- [26] E. Engel and S. H. Vosko, Phys. Rev. B 47, 13164 (1993).
- [27] Swalin R A 1961 *Thermodynamics of Solids* (New York: Wiley).
- [28] Ferreira L G, Wei S H, Bernard J E and Zunger A 1999 *Phys. Rev. B* **40** 3197.
- [29] Teles L K, Furthmuller J, Scolfaro L M R, Leite J R and Bechstedt F 2000 *Phys. Rev B* **62** 2475.

Determination of The T_g , T_d and the Refractive Index (n) of the Poly (PEA) Network as a Function of the Degree of Crosslinking.

N. Benmessaoud^{1,2}, T. Bouchaour¹, U. Maschke²

¹Laboratoire de Recherche sur les Macromolécules, Faculté des Sciences, Université Abou Bakr Belkaid, 13000 Tlemcen, Algeria

^{1,2} nouarab87@gmail.com

¹ bouchaour@yahoo.fr

²Laboratoire de Chimie Macromoléculaire (UMR CNRS N° 8009), Bâtiment C6, Université des Sciences et Technologies de Lille, 59655 Villeneuve d'Ascq Cedex, France

² ulrich.maschke@univ-lille1.fr

Abstract— In this work, we present a characterization of the physical properties of a crosslinked network of poly (2 phenoxy ethyl acrylate) (poly (PEA)) prepared by UV photopolymerization. Glass transition temperature (T_g), thermal degradation temperature (T_d) and refractive index (n) of poly (PEA) networks are determined experimentally. The study of behavior of variation of these parameters as a function of the degree of crosslinking was made. Empirical models of Askadskii et al are also used to calculate these physical parameters. The estimated parameters have been compared with the available experimental values.

Keywords— crosslinked network, UV photopolymerization, Glass transition temperature, thermal degradation temperature, refractive index.

I. INTRODUCTION

Poly (2-Phenoxyethyl acrylate) networks are chemically synthesized by UV radiation. This method has proven effective with acrylates, particularly because of its advantages. UV radiation polymerization is a method that shows its reliability compared to other methods of synthesis and considered the cleanest method since it does not require additives that can alter the properties of the polymer so it usually occurs at ambient temperatures [1].

The study of the physical properties of materials, whether natural or artificial, and their relationship with the environment, is very important in the field of application and industrial. As a result, many methods are developed as well as many academic studies are conducted to study the relationships between physical properties and the extraction of the laws that connect them.

On the other hand, several theoretical models have been developed to predict these properties. There are models based on the chemical structure of the repeating unit. The approaches that derive the best predictions from these properties are those of: van Krevelen [2], Bicerano [3], [4] and Askadskii - Matveev [5] – [10]. These three models are different in the treatment method but have given good results compared to the experimental ones for the case of linear polymers and copolymers. However, polymer networks are

much more processed by Askadskii et al. They have succeeded in presenting empirical models for calculating the physical properties of polymer networks by taking into account the presence of the crosslinking point as well as its functionality.

In this work we will study the variation of vitreous transition temperatures and those of thermal degradation as well as the variation of the refractive index as a function of the degree of crosslinking experimentally using different techniques; An attempt has also been made to compare the experimental results with those obtained by calculations based on the Askadskii's model.

II- MATERIALS AND METHODS

1- Materials

The acrylic monomers used for this study is 2-Phenoxy Ethyl Acrylate (PEA) (from Aldrich). The cross-linking agent is: 1.6-Hexane Diol Diacrylate (HDDA) (supplied by Cray Valley, France). The photo-polymerization agent used is: 2-hydroxy-2-methyl-1-phenyl-propane-1 (Darocur 1173, from Ciba Geigy). The chemical structures of the different components are given in Figure 1.

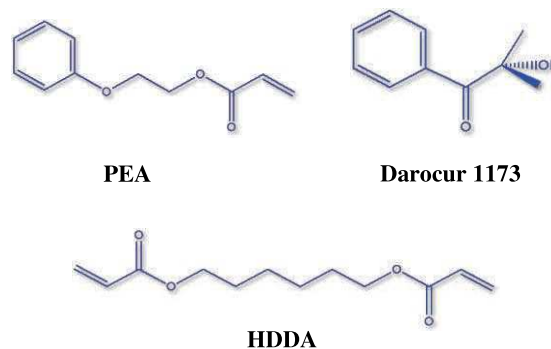


Fig 1: Chemical structure of the components of the initial mixtures.

The kinetics of polymerization were carried out using a Fourier Transform Infrared Spectrometer (FT-IR "Perkin Elmer").

2- Polymer networks synthesis:

Blends of PEA/HDDA/Darocur1173, were prepared in different weight fractions by varying the quantity of HDDA and keeping the amount of the photo initiator constant (PEA/HDDA/Darocur1173=99/0.5/0.5wt.%,...), These initial mixtures were stirred mechanically for some hours before they were cast in small flat sample holders, exhibiting a single homogeneous phase. The samples were exposed to UV radiation under nitrogen atmosphere, using Philips TL08 UV lamps exhibiting a wavelength $\lambda=365$ nm and an intensity $I=1.5$ mW/cm². The exposure time was fixed at 20 minutes to achieve complete conversion of all monomers in the precursor system. The samples obtained are optically transparent cross-linked polymer networks.

A characterization by the infrared spectroscopy technique (FT-IR) before and after polymerization showed the total disappearance of the characteristic strip of the acrylates (C=C) at 1635 cm⁻¹, indicating that the conversion is very important (see Figure 2).

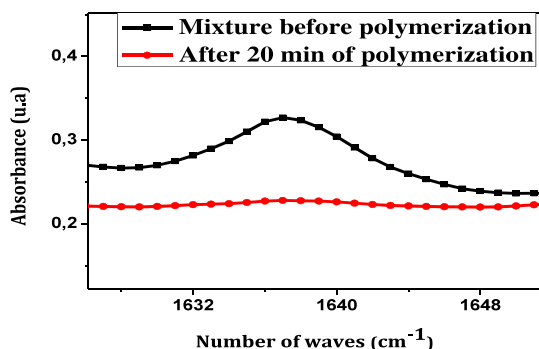


Fig 2: Illustration of the disappearance of the characteristic band C=C (1637cm⁻¹).

III- EXPERIMENTAL PART

A. Determination of glass temperature:

Analysis of transition temperatures and enthalpies of polymers networks were performed on a Pyris Diamond DSC apparatus (Perkin-Elmer model 8000).

Figure 3 shows the characteristic thermograms for Poly(PEA) / HDDA polymer networks.

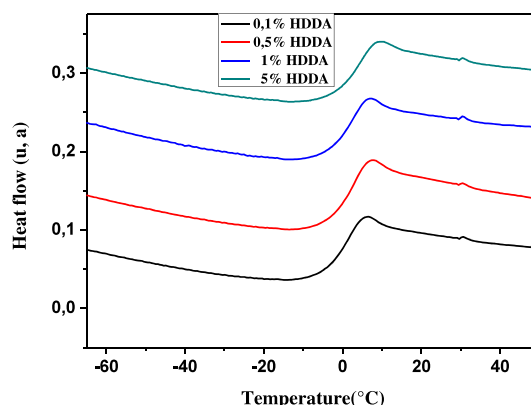


Fig 3: Influence of the degree of crosslinking (% HDDA) on the thermograms of isotropic networks of poly 2-Phenoxy-Ethyl-Acrylate (Poly (PEA)).

To visualize the influence of the increase of the glass transition temperature T_g , we have traced (Figure 4) the evolution of the glass transition temperature as a function of the degree of crosslinking of the Poly (PEA) networks. On this graph, it is clear that the T_g increases following the increase in the degree of crosslinking. We also note that this increase to a parabolic form.

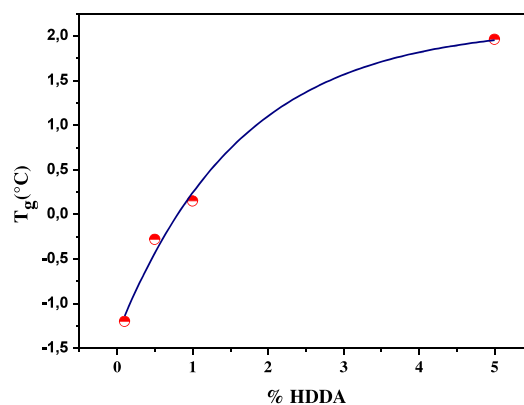


Fig 4: Influence of the degree of crosslinking (% HDDA) on the glass transition temperature of Poly (PEA) networks.

The increase of the glass transition temperature of a polymer matrix following the increase in crosslinking is a phenomenon that has already been observed in the literature [11] – [12]. This effect is not surprising and can be explained in terms of the internal mobility of the system. Indeed, the presence of crosslinking points (ie chemical bridging) between the polymer chains reduces the overall mobility of the system. Therefore, a reduction in the mobility of the molecules leads to an increase in the T_g because it requires more thermal energy to cause the movements of the polymer chains.

B. Determination of the temperature of thermal degradation:

Thermogravimetric analyzes were performed using a TGA apparatus Pyris 1 from Perkin Elmer.

The weight loss curves were recorded over the 20-700 °C temperature range at a rate of 10 ° C / min in a nitrogen atmosphere and are shown in Figure 5.

The network Poly (PEA) cross-linked at 0.1% HDDA has a thermal stability in the range 20- 100 ° C (Figure 5), and then the network manifests a more significant loss of mass from the temperature 320 ° C to 95% decomposition to 430 °. The presence of a second domain for total decomposition may be due to an oxidation reaction due to the presence of oxygen.

Noting in this study that the rate of crosslinking has no more influence on the system behavior and its temperature of degradation of fate that one marks the same value of T_d whatever the degree of crosslinking.

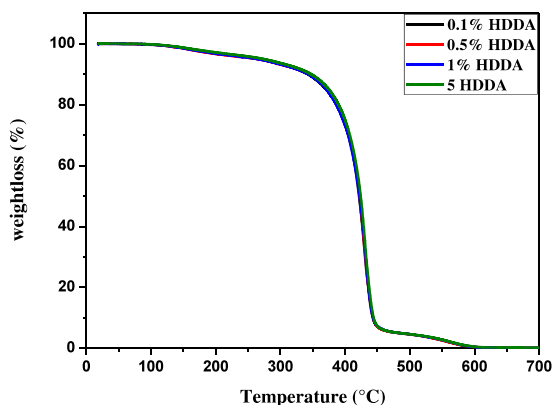


Fig 5: Thermogravimetric curves of system (Poly (PEA) / HDDDA)

C. Determination of the refractive index:

The refractive index (n) is an important optical property of polymers and is widely used in materials science. As it is characteristic for each material, it can be used for identification purposes or for the prediction of other properties. For example, the refractive index undergoes a second order transition at the glass transition temperature and can therefore be used to determine its value.

The refractive index is defined as the speed of light in vacuum relative to the velocity in the polymer. It is directly related to polarizability and depends on the wavelength of light.

Most polymers are amorphous and are, therefore, isotropic. Their refractive indices are the same for all the senses that the path of light can take through the solid. Several methods for determining the refractive indices of amorphous polymers have been carefully described in the literature.

To measure the refractive index of our polymer networks, we adopted a simple method that gives more precise results invented by M. Gharbia at al. [13].

The principle of the optical experimental technique consists of measuring the deflection by reflection of a laser beam ($\lambda = 633 \text{ nm}$) at normal incidence (Figure 6).

To measure the refractive index, we illuminate a vacuum prism that gives a first rectangular point. The same prism containing the polymer network thin film gives a second rectangular deflection point. The laws of Descartes make it possible to measure the index of refraction.

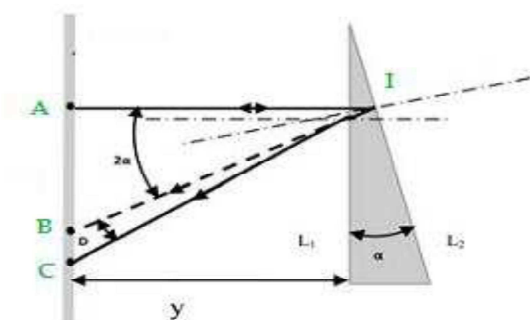


Fig 6: picture of typical spots of light by reflection through the vacuum prism and the isotropic prismatic sample centered on the reflected laser beam [13]

According to the law of Snell-Descarte we have:

$$n = \frac{\sin(2\alpha + D)}{\sin(2\alpha)}$$

the variation of the refractive index as a function of the degree of crosslinking is illustrated in figure 7. it is observed that the refractive index increases in the denser networks. As a beam of light enters a medium, it causes a disruption of the electron density, slowing down the electromagnetic wave. Dense materials slow down the wave, increasing the refractive index (n). the appearance of the variation of (n) is similar to that of the variation of the glass transition temperature (T_g); a growing parable.

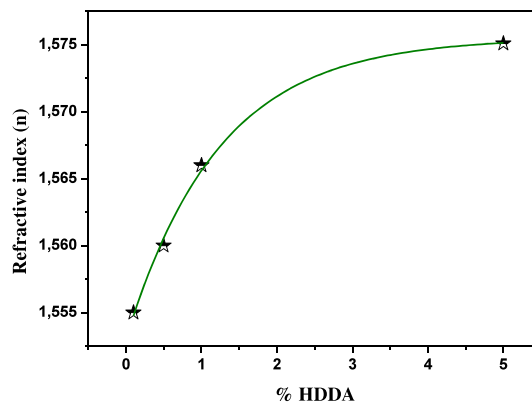


Fig 7: variation of the refractive index as a function of the degree of crosslinking (% HDDDA)

IV- CALCULATION PART

A. Calculation of the glass transition temperature of Poly (PEA) polymer networks:

It has been determined experimentally that the glass transition temperature, as well as many other properties of the network systems, depends on the number of repeating units between the cross-linked points 'm', in other words the degree of crosslinking.

Askadskii at al's approach to calculating the glass transition temperature is based on considering the unit as a set of anharmonic oscillators, connected by different types of intermolecular bonds. The magnitudes of the increments, put into the calculation, have a definite physical meaning and are energetically characterized both as weakly dispersive interactions and as strongly intermolecular interactions (dipole-dipole interaction, H bonds, etc.).

The general formula used to calculate the glass transition temperature of polymer networks is as follows:

$$T_g = \frac{\left(\sum_i \Delta V_i \right)_{f.r.}}{\left(\sum_i a_i \Delta V_i + \sum_j b_j \right)_{l.ch.} + \left(\sum_i K_i \Delta V_i \right)_{crl.p}}$$

Where:

$\sum \Delta V_i$ is the van der Waals volume of the repeated fragment in the network.

$(\sum a_i \Delta V_i + b_j)_{l.ch.}$ is a selection of constants for linear strings participating in the repetitive fragment of the network such as:

- a_i is a selection of constants, which characterizes the energy of a weak dispersion interaction as the average contribution of each atom in this interaction.
- b_j is a selection of constants that characterizes the energy of a strong specific intermolecular interaction (dipole-dipole, hydrogen bonds, etc.).

$(\sum K_i \Delta V_i)_{crl.p}$ is a selection of constants for the network link point.

We will apply this equation to our poly (PEA) network. This network displays the structure (Figure 8). He owns.

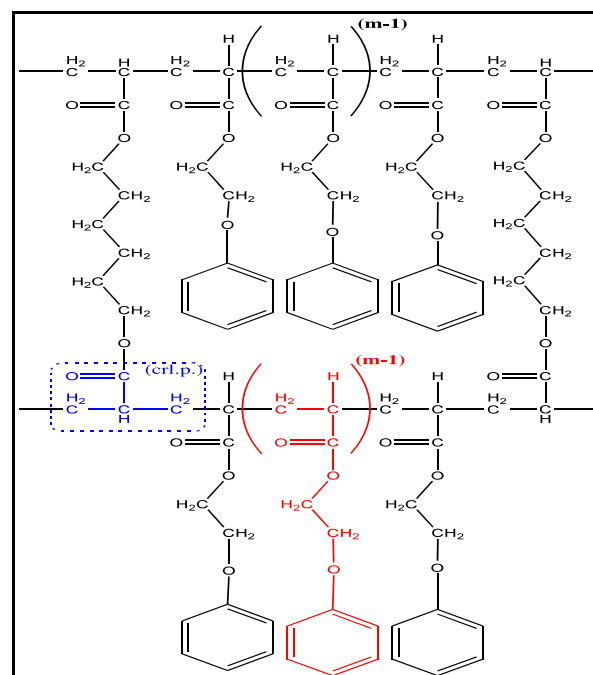


Fig 8: representation of the poly (PEA) polymer network structure.

The general formula of the glass transition temperature T_g obtained is as follows:

$$T_g = \frac{181 * m + 107.6}{677.42 * m + 317.08} \cdot 10^3 (K)$$

B. Calculates thermal degradation temperature T_d for Poly (PEA) networks:

The approach for calculating the temperature of the thermal degradation T_d is the same as for the estimation of the glass transition temperature T_g . But in this case, the energy of the chemical bonds, but not that of the intermolecular interaction, is taken into account in the calculations, although the latter also has a significant influence on the dissociation energy of the chemical bonds.

The form that describes the degradation process is as follows:

$$T_d = \frac{\sum_i \Delta V_i}{\sum_i K_i \Delta V_i}$$

Or

- T_d : is the 'Onset' temperature of thermal degradation.
- K_i : are contributions of the individual atoms to the initial degradation.

using the same structure of Figure 8 to perform the calculations. we thus obtain the equation which describes the variation of T_d as a function of the number of monomers between two crosslinking points as follows:

$$T_d = \frac{181 * m + 107.6}{249.21 * m + 164.12} \cdot 10^3 (K)$$

C. Calculates the refractive index 'n':

The refractive index is the most important optical property of polymers. The index of refraction n is determined from the following relation which is derived from the famous Lorentz-Lorentz formula:

$$\frac{n^2 - 1}{n^2 + 2} = \frac{k_{av} \sum_i R_i}{N_A \sum_i \Delta V_i}$$

Where:

- N_A : is the number of Avogadro;
- K_{av} : is the average molecular packing coefficient (for voluminous monolithic bodies, $K_{av} = 0.681$ and for films, $K_{av} = 0.695$);
- $\sum R_i$: is the molecular refraction which includes the refractions relative to each atom and the type of bond (double, triple, etc.).

the application of this formula on the structure shown in figure 8 gives us the following expression:

$$\frac{n^2 - 1}{n^2 + 2} = \frac{0.695(50.494 * m + 28.262)}{0.6023(181 * m + 107.6)}$$

D. Result and discussion:

the table below shows a comparison between the experimental results and those calculated by the empirical models of Askadskii.

knowing that the values of m corresponding to those of % HDDA are calculated from the following equation [14]:

$$m = \frac{\overline{M_c}}{M_r}$$

- $\overline{M_c}$ is the number average molecular weight between crosslinks.
- M_r is the molecular weight of the PEA repeating unit.

we also note that the values of a_i , b_j , ΔV_i and K_i of individual atoms in the repeating unit of the polymer are obtained from the reference [5].

TABLE I: ESTIMATED AND AVAILABLE VALUES OF PHYSICAL PARAMETERS OF POLY (PEA) NETWORK

Parameter	% HDDA	Estimated value	Experimental value
Glass-Transition Temperature (T_g)	0.1	-6	-1.2
	0.5	-5.6	-0.28
	1	-5.5	0.15
	5	-4.3	1.96
Temperature of Initial Degradation (T_d)	0.1	450°C	430°C
	0.5	450°C	430°C
	1	450°C	430°C
	5	450°C	430°C
Refractive Index (n)	0.1	1.557	1.555
	0.5	1.556	1.56
	1	1.556	1.566
	5	1.556	1.575

V- CONCLUSIONS

determination of different physical parameters of poly (2-phenoxyethyl acrylate) networks was obtained using different techniques. the study of the variation of these parameters as a function of the degree of crosslinking shows that the latter has an influence on the glass transition temperature and on the refractive index. the variation behavior of these two parameters is similar and shows increasing parabolic speeds. This observation leads us to think that there is a relationship between the two properties. but more work is needed to confirm this remark. the degree of crosslinking has no influence on the temperature of thermal degradation. the calculated calculations based on the empirical models of Askadskii are in good agreement with what has been obtained experimentally for the case of glass transition temperatures and thermal degradation, while the calculation of the refractive index shows that the latter is not affected by the degree of crosslinking which is not the case in the experimental. Overall, the comparison between the theoretical results and the applied results is acceptable, even the difference between the results is in the standards.

ACKNOWLEDGMENT

REFERENCES

- [1] C. Decker, Kinetic Study and New Applications of UV Radiation Curing, *J Macromol Rapid Commun*, Vol. 23, pp.1067–1093, (2002).
- [2] D.W. van Krevelen, and K. Nijenhuis, *Properties of Polymers*, Amsterdam: Elsevier, 2009.
- [3] D.W. van Krevelen, *Properties of Polymers*, Amsterdam: Elsevier, 1997.
- [4] Bicerano, J., *Prediction of Polymer Properties*, New York: Marcel Dekker, 1993.
- [5] A. A. Askadskii, *Computational Materials Science of Polymers*, Cambridge: Cambridge Int., 2003.
- [6] A. A. Askadskii, *Physical Properties of Polymers: Prediction and Control*, Amsterdam: Gordon and Breach, 1996.
- [7] A. A. Askadskii, *Analysis of the Structure and Properties of High_Crosslinked Polymer Networks*, London, Paris, New York, Melbourne: Harwood, 1992.
- [8] A. A. Askadskii, influence of crosslinking density on the α properties of polymer networks, *Polymer Science U.S.S.R.* Vol. 32, pp. 2061-2069, 1990
- [9] A. A. Askadskii, Methods for Calculating the Physical Properties of Polymers. *Review Journal of Chemistry*, Vol. 5, pp. 83–142, (2015)
- [10] A. A. Askadskii, T. A. Matseevich, and V. A. Markov, Determination of Glass-Transition Temperatures of Polymers: A Modified Computational Scheme, *Polymer Science, Series A*, Vol. 58, pp. 506–516, (2016).
- [11] R. Vera-Graziano, F. Hernandez-Sanchez, *J. Appl. Polym. Sci.*, Vol. 55, pp. 1317-1327, (1995)
- [12] M. Richard Vendamme, PhD thesis of the University of Science and Technology of Lille (2004).
- [13] I.Loubiri, S. Fadhel and M. Gharbia, " Refractive index and dispersion measurements in prismatic thin film of phasidic columnar liquid crystals" *Molecular Crystals and Liquid Crystals*, Vol. 648, pp. 22-28, (2017).
- [14] C. T. Reinhart and N. A. Peppas, solute diffusion in swollen membranes. Part ii. Influence of crosslinking on diffusive properties, *Journal of Membrane Science*, Vol. 18, pp. 227-239, (1984).

A Green Catalyst “Maghnite Na⁺” For Synthesis and Anionic Polymerization of Methacrylamide

Samira Derkaoui*¹, Mohammed Belbachir¹ and Fatima Zohra Zeggai²

¹Laboratory of Polymer Chemistry, Department of Chemistry, Faculty of Science, University of Oran1 Ahmed Benbella. BPN°1524El'Menouer,31000 Oran, Algeria.

derkaoui.samira@gmail.com

legenial@gmail.com

²Center of scientific and technical research in physicochemical analyzes (CRAPC) BP 384, Siège ex-Pasna Zone Industrielle, Bou-Ismaïl CP 42004, Tipaza, Algeria
zeggai.fatimazohra@gmail.com

Abstract—The novelty of this work is to study the anionic polymerization of methacrylamide using an environmentally friendly catalyst Maghnite Na⁺, a proton exchanged montmorillonite clay, in an ice bath. We have synthesized the monomer methacrylamide (MAM) by the condensation of Ammonia with methacrylic anhydride in bulk (without solvent) at 0°C for 1 hour and its polymer was synthesized using a green catalyst “maghnite Na⁺” in tetrahydrofurane THF at 0°C. The Poly methacrylamide structure is characterized and confirmed by Infrared Spectroscopy (FTIR), ¹H nuclear magnetic resonance (NMR) spectroscopy and Thermal properties of the polymers were determined using thermogravimetric analysis (TGA).

Keywords— Anionic polymerization; Maghnite-Na⁺; Methacrylamide; Montmorillonite; Green catalyst.

I. INTRODUCTION

Heterogeneous catalysis is of vital importance to the world's economy, allowing us to convert raw materials into valuable chemicals and fuels in an economical, efficient, and environmentally benign manner. For example, heterogeneous catalysts have numerous industrial applications in the chemical, food, pharmaceutical, automobile and petrochemical industries [1]. They are preferred due to their robustness and lower operational cost, in particular through easier recovery/separation from the products. [2].

The wide range of industrial applications of PMAM is due to their high water solubility. The most important uses for the polymers are as flocculating agents for minerals, coal, industrial waste, and additives in paper manufacturing [3].

The methacrylamide monomer is polymerized by both radical and anionic route [4]. The radical polymerization of methacrylamide is described in previous works; in various solvents and initiators by R. Anbarasan et al in water at 75°C using potassium persulfate as initiator [5] and by Muserref Onal and Meltem Celik in water at 85°C using benzoyl peroxide as initiator [6] and their copolymerization was studied by M. Sadeghi et al onto pectin in water at 70°C using ammonium persulfate as initiator [7], and with methylmethacrylate in absolute ethanol using

Azobisisobutyronitrile (AIBN) as initiator by N. Grassie et al [8].

The novelty of this work is to study the anionic polymerization of methacrylamide initiated directly by a montmorillonite clay, “Maghnite-Na⁺” a new nontoxic and recyclable catalyst. Initially, we have synthesized the monomer methacrylamide by the condensation of ammonia with methacrylic anhydride in bulk (without solvent) at 0°C for 1 hour; and subsequently the polymerization of monomer was carried out under suitable conditions in THF at (0°C) for 24 hours initiated by anionic catalyst “maghnite Na⁺”.

The monomer and polymer are characterized and confirmed by Infrared Spectroscopy (FTIR), ¹H nuclear magnetic resonance (NMR) spectroscopy and Thermal properties of the polymers are determined using thermogravimetric analysis (TGA).

II. EXPERIMENTAL

1. Preparation of Catalyst “Maghnite-Na⁺”

“Maghnite-Na⁺” was prepared as described by Belbachir and collaborators [9, 10]. Raw-Maghnite (20 g) was crushed for 20 min using a prolabo ceramic balls grinder. It was then dried for 2 h at 105 °C. The Maghnite was placed in an Erlenmeyer flask together with 500 ml of 1 M NaCl solution. The Maghnite/water mixture was stirred using a magnetic stirrer until saturation was achieved over 24 h at room temperature, the mineral was then washed with distilled water to become chloride free and then filtered and dried at 105 °C.

• XRD analysis of Catalyst

The X-ray diffractogram of sodic montmorillonite shows an offset of the angle 2θ from 6.8 to 12°, thus indicating the increase in the interlayer distance of 12.52 Å for raw maghnite and 12.34 Å for sodic clay, confirming the intercalation of Na⁺ ions in the space initially occupied by H⁺ ions.

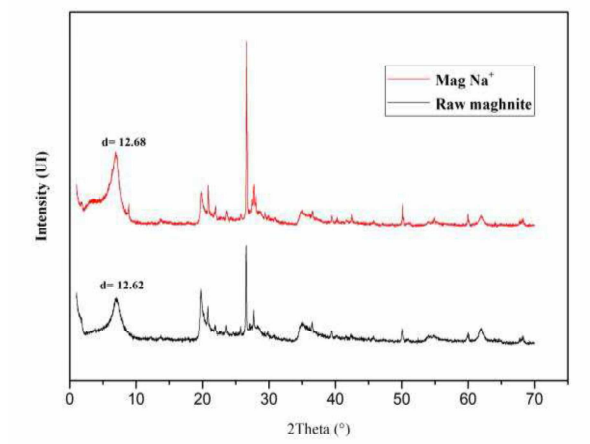


Fig 1. XRD spectra of Raw-Maghnite and Maghnite- Na⁺.

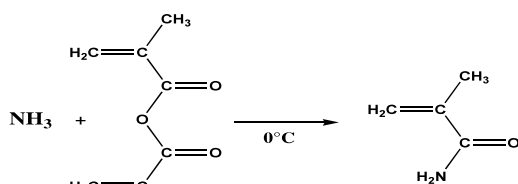
2. Syntheses

2.1. Synthesis of methacrylamide monomer (MAM)

Synthesis of monomer was carried out by mixing 0.1mole (10ml) of ammonia with 0.1mole (15ml) of Methacrylic anhydride in bulk (without solvent); the reaction mixture was cooled to 0-5°C using an ice bath during 1h.

After that, we filtered the solution recover the product. The product obtained was a white powder which when recrystallized in a methanol-diethylether mixture.

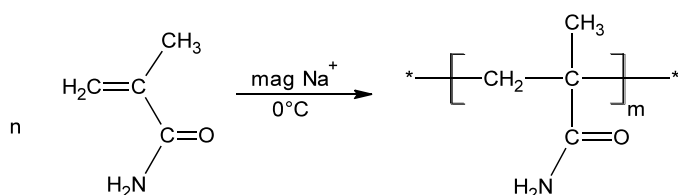
➤ Yield=85%



Scheme1. Schematic representation of the synthesis of methacrylamide (MAM)

2.2. polymerization of MAM

The anionic polymerization of MAM was carried out in sealed tubes. Each tube contains a mixture of 1 g of MAM, 10ml of tetrahydrofurane THF and (0.15g) 15% of maghnite-Na⁺. The mixtures were kept in an ice bath at 0°C and stirred with a magnetic stirrer under dry nitrogen for 24 hours. The resulting polymer was precipitated in methanol, washed for several times, dried at 40°C in vacuum and weighed.



Scheme 2. Schematic representation of the synthesis of Poly (methacrylamide) (PMAM) catalyzed by Maghnite Na⁺.

3. RESULTS AND DISCUSSION

3.1 Characterization of the monomer (MAM)

The structures of monomer are characterized and confirmed by Infrared Spectroscopy (FTIR), ¹H and ¹³C nuclear magnetic resonance (NMR) spectroscopy.

The IR (cm⁻¹) spectrum of (MAM): ν_{NH} primary amine 3374.45, 3179.85, 607, ν_{CH₂,CH₃} 2930.75, 2984, ν_{C=Oamide} 1671.64, ν_{C=C} 1600, ν_{C-N} 1401.49.

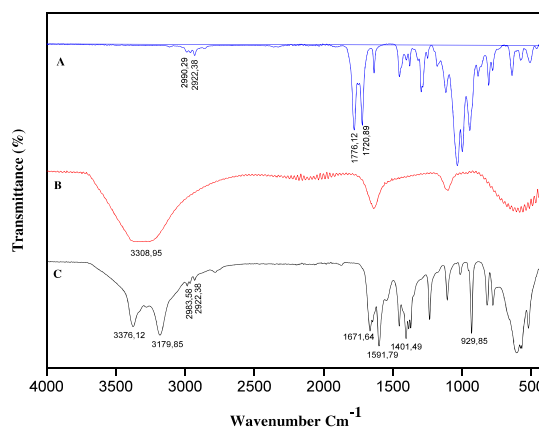


Fig 2. FTIR spectra for the starting products (A) Methacrylic anhydride; (B) Ammonia and product synthesis (C) methacrylamide (MAM)

The ¹H NMR in (CDCl₃) shows: (δ ppm) 1.951(s, 3H of -CH₃), 5.39-5.76 (d, 2H of =CH₂), 6.027- 6.488 (2s, 2H of -NH₂).

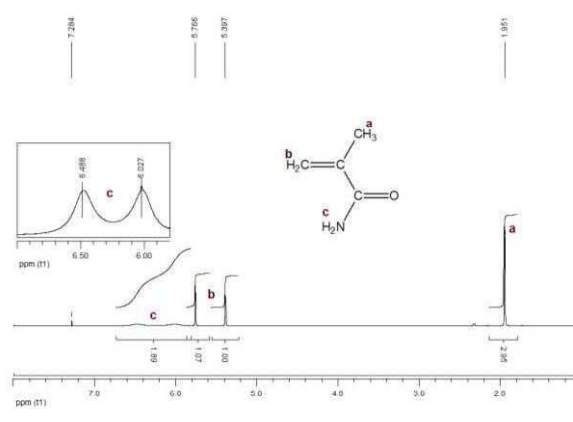


Fig 3. H NMR spectrum (CDCl₃) of Methacrylamide (MAM) obtained.

The ¹³C NMR in (CDCl₃) shows: (δ ppm) 18.63(-CH₃); 120.88 (=CH₂), 139.123(C=C), 170.95(C=O)_{amide}.

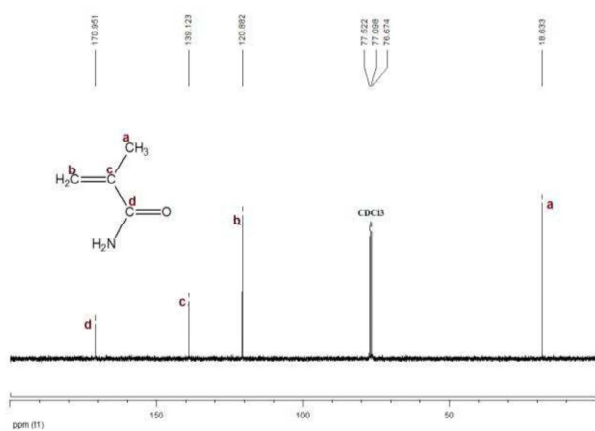


Fig 4. ^{13}C NMR spectrum (CDCl_3) of Methacrylamide (MAM).

3.2. Characterization of Poly (methacrylamide)

The IR spectrum of poly (MAM) is identical for the monomer excepting that we observe the increase of the intensity of the bands. Two large and intense bands at 3314.93cm^{-1} corresponding to N-H stretching and large bands between 2836 and 2990cm^{-1} were attributed to C-H symmetrical and asymmetrical stretching on CH_2 and CH_3 groups, respectively. The absorptions at 1653cm^{-1} are assignable to amide carbonyl (C=O) stretching.

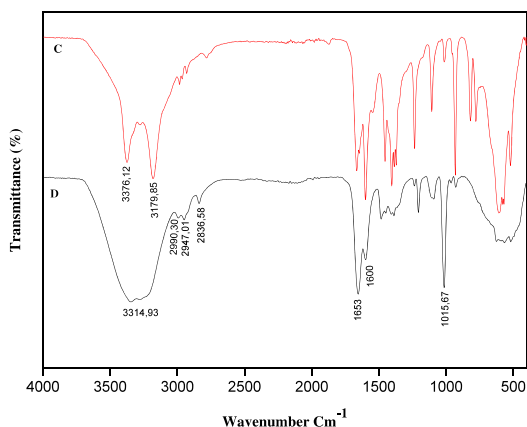


Fig 5. FTIR spectra for the methacrylamide (MAM) monomer (A) and polymer methacrylamide (PMAM) (B)

The ^1H NMR spectrum in figure 7 confirms the structure of the polymer obtained in this study. Two broad peaks observed between 1.058 and 1.68 ppm are assigned to methylene and methyl protons of the polymer repeating unit and second broad peak between 6.80 and 7.55 ppm corresponding to the protons of amine group ($-\text{NH}_2$). The small peak at 1.82ppm

and at 3.23ppm are attributed to the methyl protons groups ($-\text{CH}_3$) at the end of the polymer chain; as well as a doublet at $5.39\text{-}5.76$ ppm are assigned to the vinylic hydrogens (b) ($=\text{CH}$). The strongest and sharp peak centered at 4.70 ppm corresponds to water deuterated solvent (D_2O) respectively.

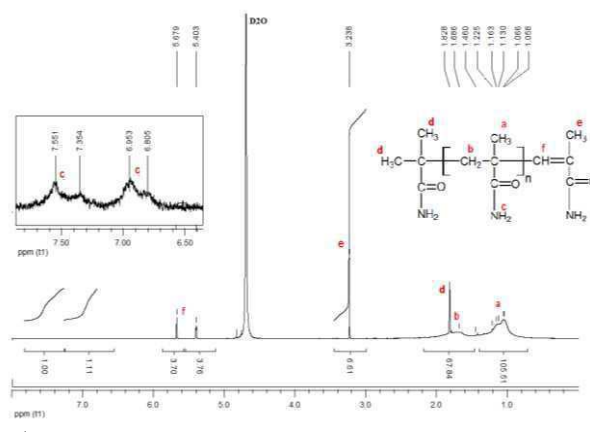


Fig 6. ^1H NMR spectrum (D_2O) of Poly(methacrylamide) (PMAM) obtained.

3.3. Thermal studies

The thermal stability of the polymer is studied by thermogravimetric analysis in air from room temperature. The TGA a curve of PMA is shown in the Figure 7 clearly indicates that the polymers undergo one stages of degradation. The degradation is varying from $196\text{ }^\circ\text{C}$ to $238\text{ }^\circ\text{C}$, which depends on the PMAM decomposition due to the sensitive and the weakest the methyl group from the PMAM chain correspond to 99.38% weight loss indicating that the polymer exhibits low thermostability. The PMAM have flexible aliphatic main chains exhibit much lower thermal stability and degrade rapidly at low temperature.

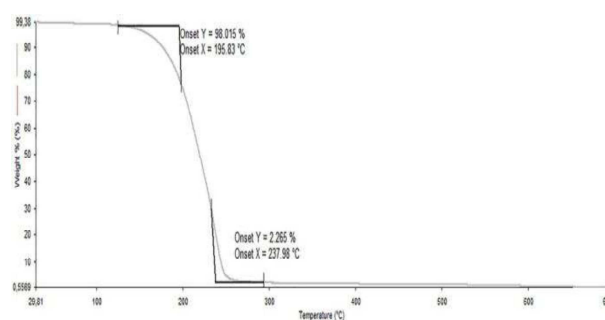
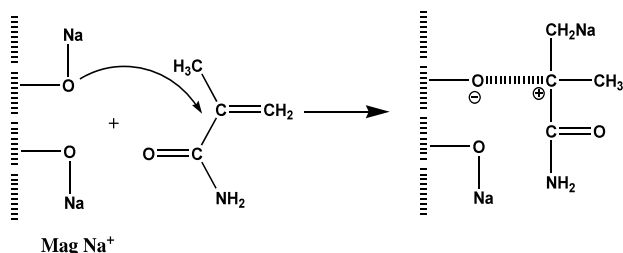
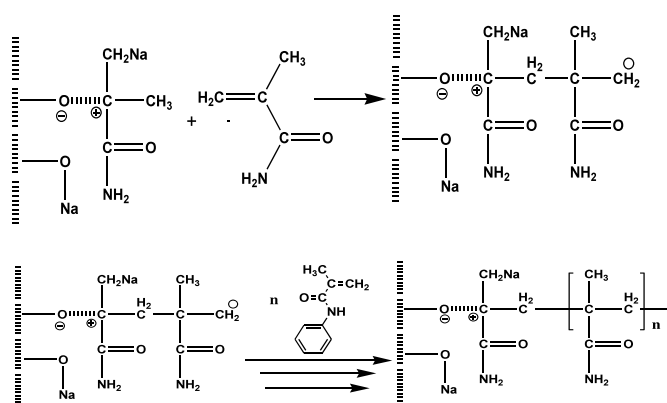


Fig 7. TGA a curve of the Poly(methacrylamide) PMAM in air.

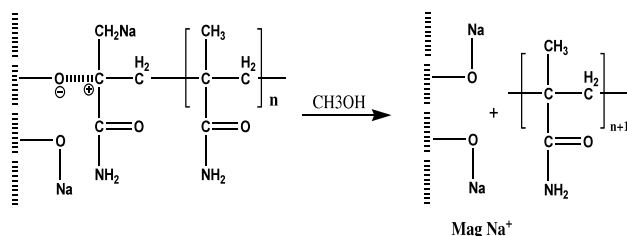
An anionic mechanism for the reaction was proposed. From the mechanism studies, it was showed that monomer was inserted into the growing chains.



Scheme 1. Initiation



Scheme 2. Propagation



Scheme 3. Termination

III. CONCLUSION

This paper has described a novel method to synthesis and polymerization of methacrylamide initiated by solid and non-toxic Maghnite-Na⁺ clay at room temperature in the conditions that respect the principles of green chemistry. The synthesis of the monomer is carried out by reaction of ammonia with a single reactant methacrylic anhydride in bulk (without solvent)

and at 0 °C for 1 hour, obtaining a better yield and selectivity to the product 100% and the structure of monomer and polymer are confirmed by Infrared Spectroscopy (FTIR), ¹H and ¹³C nuclear magnetic resonance (NMR) spectroscopy. The result of thermogravimetry indicated that the polymer exhibits low thermostability.

Finally, The simplicity of the method, good properties catalytic of the support catalyst solid (Maghnite-Na⁺) make it an attractive method for the synthesis and polymerization of methacrylamide.

Acknowledgment(s)

The authors wishes to thank Mr. A.Addou (Laboratory of Polymer Chemistry LCP, University of Oran 1) for the FTIR analysis, The authors are also thankful to the department head, Mrs. H. Hidour (Applied Organic Synthesis Laboratory, University of Es-sénia Oran) for the NMR analysis.

REFERENCES

- [1] JA Dumesic, Huber GW and Boudart M (2008) Principles of Heterogeneous Catalysis. In *Handbook of Heterogeneous Catalysis*. WILEY-VCH, pp.1-15. doi.org/10.1002/9783527610044.hetcat0001
- [2] T-C Ong, R Verel, C Coperet, *Encyclopedia of Spectroscopy and Spectrometry*, 3rd ed. 121-127, 2017. doi.org/10.1016/B978-0-12-409547-2.12130-4.
- [3] Marcel Dekker, *Hand book of polymers synthesis*, 2nd ed. 2005.
- [4] G.Odian, *Principale of Polymerization*,. 4th ed. College of Staten Island, City University of NewYork. Wily, 2004
- [5] R. Anbarasan, P. Arvind and V. Dhanalakshmi, "Synthesis and characterization of Polymethacrylamide-Clay Nanocomposites". *J Applied Polym Scien*, 121, 563-573, 2011.
- [6] Muserref Onal and Meltem Celik, "Polymethacrylamide/Na-montmorillonite nanocomposites synthesized by free-radical polymerization", *Materials Letters*. 60, 48-52, 2006. DOI: 10.1016/j.matlet.2005.07.069.
- [7] Mohammed Sadegui, Soudeh Sarari, Hadis Shahsavari, Hossein Sadegui and Faemeh Soleimani, "Graft Copolymerization Methacrylamide onto Pectin in homogeneous solution" *Asian j. chem*. 8, 4615-4618, 2013.
- [8] N. Grassie, I. C. McNeill and J. N. R. Samson, "The Thermal Degradation of Polymethacrylamide and Copolymers of Methacrylamide and Methyl Methacrylate" *European Polym J*. 14931-937, 1978.
- [9] M. Belbachir and A.Bensaoula "Composition and method for catalysis using bentonite". U.S. Patent.6,274,527. B1 2001.
- [10] M. Belbachir and A.Bensaoula "Composition and method for catalysis using bentonite". U.S. Patent.7,094,823. B2 2006.

Wind turbine generator based on PMSG connected to DC microgrid system

Hafsi Oussama^{#1}, Abdelkhalek Othmane^{#2}, Chakar Abdeselem^{#3}, Hartani Mohammed Amine^{*4}

*#Dep of Electrical Engineering. University of Tahri Mohammed
Smart Grids & Renewable Energies Laboratory
Bechar, Algeria*

¹oussama5bm@gmail.com

²othmane_elec@yahoo.fr

³abdeselemchakar@gmail.com

**Dept of Electrical Engineering. University of Ahmed Draya Energy,
Environment and Information System Laboratory
Adrar, Algeria*

⁴aminedcgrid17@gmail.com

Abstract— In this paper, the presentation of DC microgrid and wind turbine generator based on PMSG (permanent magnet synchronous generator) is presented. The system contains a permanent magnet synchronous generator based WECS (wind energy conversion system) connected with DC-microgrid through an AC/DC converter and DC/DC converter type boost converter to fed a DC load under 400 VDC. Wind turbine model has been utilized for generation a 10 KW, and the MPPT technique has been utilized here for more efficiency. The modelling and the simulation of WECS under Matlab environment has been effectuated and the result are obtained.

Keywords— DC microgrid, WECS, PMSG, DC-DC converter, MPPT

I. INTRODUCTION

Now day, the world ongoing to the renewable energies because it's free, clean and environment friendly to decreasing fossil fuel consummation and CO₂ emission.

Renewable energies as wind energy conversion (WEC) and solar photovoltaic (PV) systems and geothermal, are now well developed, cost effective and are being widely used, while some others like fuel cells (FC) and biomass are in their advanced developmental stage [1]. Wind energy is the fastest growing energy technology in terms of percentage of yearly growth of installed capacity per technology source [1].

There are two main types of wind energy conversion systems: fixed speed and variable speed WECS. The variable-speed WECS uses power maximization method and algorithms to extract as much power as possible from the wind [2].

PMSG is direct drive, can be used without gearbox, has high efficiency and low maintenance, and it's the prefer for standalone system [3][4].

MPPT technique can be used to capture the maximum power from available wind, by mechanical way (pitch angel control) or electrical method (electronics converter).

Various techniques of MPPT have been considered in WECS like hill climbing search HCS, tip speed ratio control TSR, optimal torque control OTC, perturb and observe P&O, fuzzy logic controller and many evolutionary technique [4][5].

P&O algorithm is well known MPPT method due to its simplicity and effectiveness [4], which requires no information about the turbine characteristics, need only voltage and current measurements.

A microgrid system integrates the several types of renewable energy sources, such as solar system (PV), wind turbine, fuel cell, to the household and industrial load [7].it can be classified to AC microgrid and DC microgrid.

DC microgrid is Aggregation of renewable energy sources such as PV, wind energy and FC, storage devise such as batteries, super capacitor and fly wheel, DC loads such as dc machines and plug-in electric vehicles.

Today's many of consumer loads are DC supplied. Electronic based office and home appliances, such as computers, laptops, tablets, phones, printers, TVs, microwave ovens and lighting, consume electricity in DC form [6].

This paper proposes a modelling and control of PMSG based on wind turbine generator as a part from DC microgrid.

II. PROPOSED SYSTEM

The figure 1 shows a DC microgrid model, the last includes 2 renewable sources and their converters, a battery for storage with bidirectional converter for charging and discharging and 2 kinds of loads.

The study in this paper is about WECS, modelling and simulation. And the benefits of this clean source on DC microgrid operation.

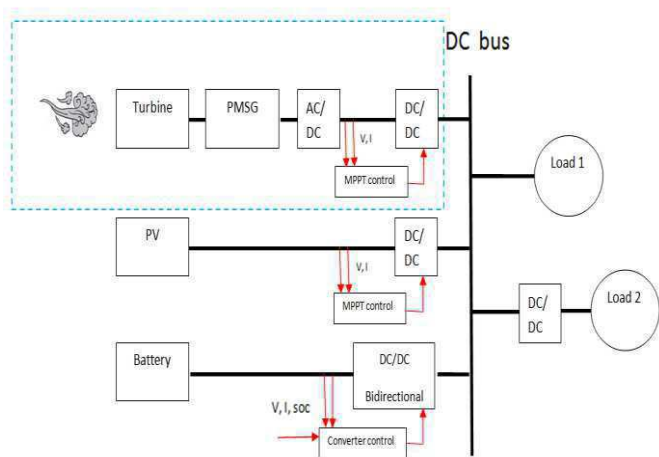


Fig.1 standalone DC microgrid PV/wind/battery.

III. MODELLING OF WECS

A. Modelling of wind turbine

The wind turbine is used for the conversion of wind kinetic energy to mechanical work.

The mechanical power P_m captured by wind turbine rotor blades [1,2,3]

$$P_m = \frac{1}{2} \rho \pi R^2 V^3 C_p(\beta, \lambda) \quad (1)$$

Where,

ρ is the air density (kg/m^3).

R is radius of wind turbine blade (m).

V is wind speed (m/s).

$C(\lambda, \beta)$ is the power coefficient, which expresses the relationship between the tip speed ratio λ and the pitch angle β .

The power coefficient is the ratio between obtained power and the available power. C_p can have a max of 0.59 (Betz limit), and we can calculate it as:

To eliminate the mechanical control of pitch angel, we take $\beta = 0$.

The power coefficient is as

$$C_p(\lambda) = 0.5176 \left(\frac{116}{\lambda} - 9.06 \right) e^{-\frac{21}{\lambda} + 0.735} + 0.0068\lambda \quad (2)$$

And tip-speed ratio given by:

$$\lambda = \frac{R \cdot \omega}{V} \quad (3)$$

Where ω is the blades angular velocity.

B. Modeling of permanent magnet synchronous generator

To simplify the study of the PMSG, it is convenient to transform the equations from the stationary stator frame into

the d-q axis using Park transformations. The mathematical model of PMSG can be described in the d-q reference system as follows [7]

The equations for d-axis and q-axis currents are defined in [3,4] as:

$$\frac{di_{sd}}{dt} = -\frac{R_{sa}}{L_{sd}} i_{sd} + \omega_s \frac{L_{sq}}{L_{sd}} i_{sq} + \frac{1}{L_{sd}} u_{sd} \quad (4)$$

$$\frac{di_{sq}}{dt} = -\frac{R_{sa}}{L_{sq}} i_{sq} - \omega_s \left(\frac{L_{sd}}{L_{sq}} i_{sd} + \frac{1}{L_{sq}} \psi_p \right) + \frac{1}{L_{sq}} u_{sq} \quad (5)$$

The electromagnetic torque obtained from the rotor of PMSG is given by:

$$T_e = 1.5 \frac{P}{2} [\psi_p i_{sq} + i_{sd} i_{sq} (L_{sd} - L_{sq})] \quad (6)$$

Here,

i_{sd} , i_{sq} , u_{sd} and u_{dq} are the current and voltage of d and q axis respectively. ω_s is the angular frequency of the generator. L_{sd} and L_{sq} are the inductance of the generator. ψ_p is the permanent flux. R_{sa} is the resistance of the stator and P is the number of poles.

IV. MPPT AND BOOST CONVERTER

To reduce of cost energy must be use an effective technique for truck and capture the maximum power from wind turbine that is called the maximum power point tracking MPPT [8].

Perturb and observe P&O is the algorithm widely used to extract MPP because it is simple and easy to implement [9].

The boost converter is electronic intermediate to implement the MPPT in the system by reducing the duty cycle. (fig 2) and (fig 3) show the MPPT flow chart of P&O algorithm and boost scheme respectively.

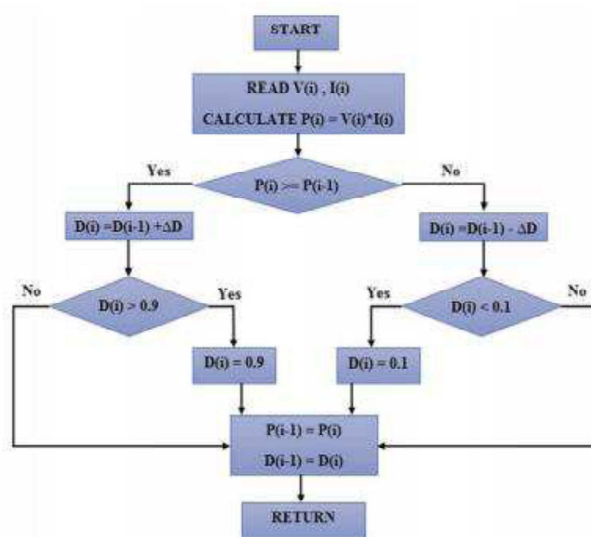


Fig. 2 P&O algorithm Flow chart [10]

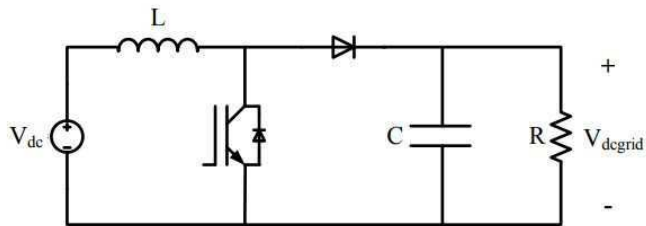


Fig. 3 boost converter scheme

V. SIMULATION AND RESULT

The proposed WECS is simulated by Matlab/Simulink fixed wind speed for rated speed of wind 11m/s.

In rated wind speed, the system extracts 10 KW, and DC bus has 400V.

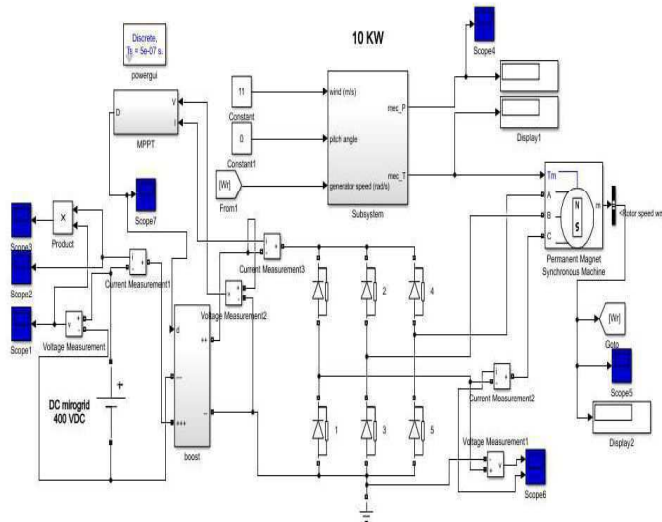


Fig. 4 simulation scheme of the system

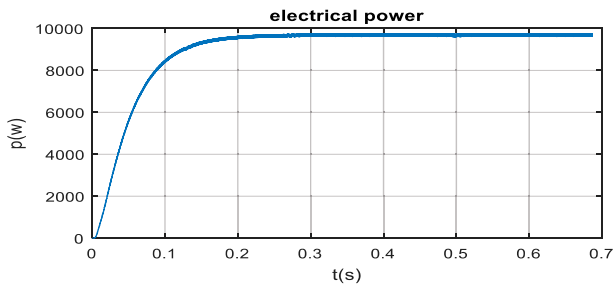


Fig. 5 curve shows load power

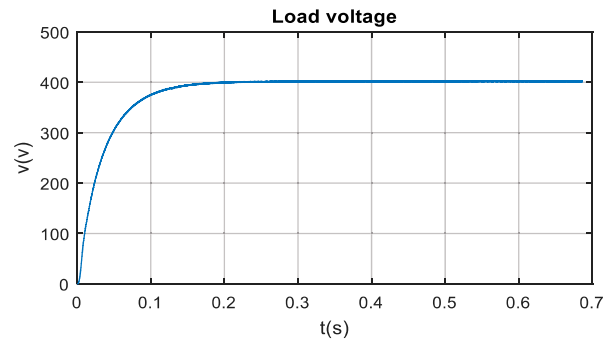


Fig. 6 curve shows dc load voltage

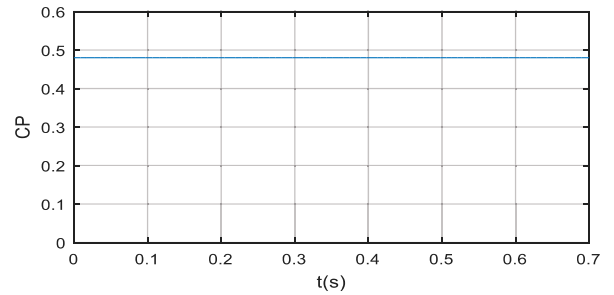


fig. 7 curve illustrates cp value in fixed speed

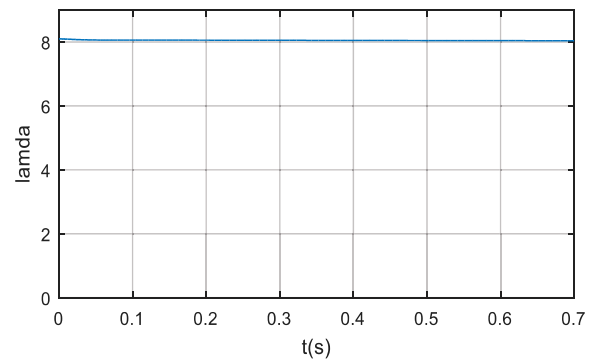


Fig. 8 Curve illustrates lambda value when beta=0

In DC microgrid system there is only one condition for the connection, this condition is $V_{wind} = V_{DC_microgrid}$, for that we can achieve $V_{load}=400v$ at all time on the simulation.

VI. CONCLUSION

This paper presented a modelling and simulation of WECS based on PMSG in DC microgrid system.

the proposed MPPT algorithm based on P&O control the boost converter by varying the duty cycle.

In the simulation section, we implemented the global system and got the results in the case of fixed speed generator.

REFERENCES

- [1] Nabil A. Ahmed, A.K. Al-Othman, M.R. AlRashidi, "Development of an efficient utility interactive combined wind/photovoltaic/fuel cell power system with MPPT and DC bus voltage regulation," *Electric Power Systems Research*, vol. 81, pp. 1096-1106, 2011.
- [2] Janardan Gupta, Ashwani Kumar, "Fixed Pitch Wind Turbine-Based Permanent Magnet Synchronous Machine Model for Wind Energy Conversion Systems," *Journal of Engineering and Technology*, vol.2, pp. 52-62, 2012.
- [3] Chia-Nan Wang, Wen-Chang Lin, and Xuan-Khoa Le, "Modelling of a PMSG Wind Turbine with Autonomous Control," *Mathematical Problems in Engineering*, pp. 1-9, 2014.
- [4] Ramji Tiwari, Ramesh Babu. N, "fuzzy logic based mppt for permanent magnet synchronous generator in wind energy conversion system," *IFAC*, vol. 49, pp. 462-467, 2016.
- [5] A.Suyampulingam, V. Subbiah, "pmsg based wind turbine system connected to dc micro-grid with mppt control," *International Journal of Pure and Applied Mathematics*, vol.118, pp.99-105, 2018.
- [6] Ahmed T. Elsayed, Ahmed A. Mohamed, Osama A. Mohammed, "DC microgrids and distribution systems: An overview," *Electric Power Systems Research*, vol. 119, pp. 407-417, 2015.
- [7] Ekhas Hossain, Jakir Hossain , Nazmus Sakib , Ramazan Bayindir, "Modelling and Simulation of Permanent Magnet Synchronous Generator Wind Turbine: A Step to Microgrid Technology," *international journal of renewable energy research*, vol.7, pp. 443-450, 2017.
- [8] Ratna Ika Putri and all, "fuzzy mppt controller for small scale stand alone pmsg wind turbine , " *ARNP Journal of Engineering and Applied Sciences*, vol. 2, pp. 188-193, 2017.
- [9] Daniel Zammit, Cyril Spiteri Staines, Alexander Micallef, Maurice Apap, "MPPT with Current Control for a PMSG Small Wind Turbine in a Grid-Connected DC Microgrid," *TurbWind 2017 (Research and Innovation on Wind Energy Exploitation in Urban Environment) Colloquium*, Riva del Garda, Italy, 15-16 June 2017.
- [10] Sahin.P, Resmi.R, V. Vanitha, "PMSG Based Standalone Wind Electric Conversion System with MPPT" *IEEE, International Conference on Emerging Technological Trends (ICETT)*, India, 2016.

Development of the renewable electricity generation in Algeria: Impact of oil Price using a Vector Error Correction Model (VECM)

Widad Berriche^{#1}, Meriam Bougueroua^{*2}

Higher National School of Statistics and Applied Economics,

University of Kolea, Tipaza, 42003 Algeria

1wberriche08@gmail.com

**University of Mostaganem, Department of Economics,*

BP 188/227 Mostaganem, 27000 Algeria

2mbougueroua@gmail.com

Abstract— The purpose of this article is to investigate the relationship between renewable electricity generation, oil price and economic growth in Algeria using the cointegration approach and Vector Error Correction Model (VECM). We examine simultaneously short-term and long-term impacts between the studies variables: renewable electricity generation, oil price and economic growth during the period 1990–2016. We propose also to forecast the renewable electricity generation to 2025 under different scenarios. The main results of the analysis show that the oil price influenced positively, in the short and long term, the renewable energy generation in Algeria. It implies that higher oil price allows more investment in the renewable energy. This result further confirms the strong dependence of Algerian economy on oil revenues and raises several questions about looking for new sources of financing to develop renewable energies and achieve the sustainable development.

Keywords — Electricity generation, Renewable energy, Oil price, Economic growth, VECM.

I. INTRODUCTION

Algeria, a producer and exporter of hydrocarbons, is exploiting its natural wealth in order to provide the resources needed for its economic development through the expanding of the energy sector. Therefore, its economy is strongly dependent on fossil fuels exportation revenue, which account for about 30% of the country's Gross Domestic Product (GDP). However, the level of socio-demographic, economic and climatic changing requires a thinkable energy policy that takes into account the challenges of the future, including the decline of fossil resources, the volatility of oil price and the environmental issues. Indeed, the integration of renewable energies (RE) into the national energy-mix is a major challenge in terms of preserving the availability of the fossil resources, responding to the growing domestic energy demand and

contributing to the sustainable development. In fact, the use of renewable sources aims not only to decrease the harmful environmental effects of using fossil fuels, but it can also delay the depletion of our hydrocarbon reserves. Furthermore, Algeria has a great potential for developing its share of RE as conditions especially for solar and wind energy are of outstanding quality [1]. Aware of these advantages, the Algerian authority adopted in 2011 its national renewable energy target. The RE program had an experimental phase devoted to testing the various available technologies and conducting pilot project. It included: Hybrid power plant (Gas-Solar) of Hassi R'Mel (150MW that includes 25 MWh of solar power capacity), operational since 2011, and the photovoltaic power station of Ghardaïa (1,1 MW) with the wind farm of Adrar (10 MW) operational since July 2014 [2]. The encouraging results of this phase, added to the significant technological progress (especially in photovoltaic and wind technologies) and the sharp decline of their costs [3], led the policy-makers to update and enlarge the program in May 2015. It envisions the installation of 22 GW of RE by 2030, which is almost double than what was set as a target before (12 GW), providing a share of 37% in the total installed capacity and 27% in the electricity generation. Of these 22 GW, about 4.5 GW are supposed to be installed by 2020 [4]. The RE program will be conducted in two phases:

First phase 2015 - 2020: The installation of 4000 MW shared between photovoltaic and wind power capacity, as well as 500 MW, between biomass, cogeneration and geothermal energy.

Second phase 2021 - 2030: The development of the electrical interconnection between the North and the Sahara (Adrar), which will allow the installation of large RE plants in the regions of In Salah, Adrar, Timimoun

and Bechar and their integration in the national energy system.

The targets per technology are set according two phases as outlined in the table below:

Table 1 Phases of the Algerian renewable energy program [4]

Unit : MW	1 st phase 2015-2020	2 nd phase 2021-2030	Total
Photovoltaic	3 000	10 575	13 575
Wind	1 010	4 000	5 010
CSP	-	2 000	2 000
Cogeneration	150	250	400
Biomass	360	640	1 000
Geothermal	05	10	15
Total	4 525	17 475	22 000

Furthermore, to support investments in this sector, the authority implemented a Renewable Energy National Fund (RENF) in 2009, merged later with the National Energy Efficiency Fund (NEEF) in 2014, to provide financing through a 1% levy on oil tax revenues [4]. Other forms of State's assistance and incentive are carried out through a guaranteed purchase price mechanism (feed-in tariffs), for the projects connected to the network, over a period of 20 years for solar and wind and 15 years for cogeneration [4].

Even if policymakers keep on providing the necessary policies and subsidies, the RE program is slow to materialize [5] (only 3.19% of RE in the energy balance in 2016) (see Fig.2). According to the above and knowing the importance of fossil's revenue in the Algerian economy, we can think that the oil price is a determining factor, among others, in the development of the RE program. Thus, this paper attempts to examine empirically the nexus between these variables using an advanced econometric model.

Among the studies conducted in the developed economies, Chul-Yong and Sung-Yoon [6] listed many studies exploring the relationship between oil prices and renewable energy diffusion and most perform panel data analysis. These investigations present contrasting results (substitutive/complementary effect, or non-existent), and the authors suggest that an analysis of their relationship in each market is necessary.

In the case of Algeria, there have been no academic studies focusing on this in our best knowledge. Mostly, despite their rarity, the existing researches have dealt either with nexus of electricity consumption (renewable non-renewable) and the economic growth, or with renewable electricity consumption and the environmental degradation. Among the recent one, we can mention

Belaïd and Abderrahmani [7] examined the causal relationship between economic growth, petroleum price, and electricity consumption using the 1971–2010 period. The results of the cointegration and causality tests confirm the presence of a bidirectional causal relationship between electricity use and economic growth. The authors indicate also the absence of causality across energy consumption and petroleum price.

Belaïd and Youssef [8] explored the dynamic causal relationship between CO2 emissions, renewable and non-renewable electricity consumption and economic growth in Algeria over the period 1980–2012. The Cointegration approach revealed the existence of a long-run relationship among the variables. However, in the short-run, results proved unidirectional causality relationship running from GDP to non-renewable electricity consumption. Furthermore, results attest that renewable electricity generation has not a significant contribution to energy-based carbon dioxide emissions reduction target.

Amri [9] analysed the relationship between economic growth and energy consumption (renewable and non-renewable) in Algeria between 1980 and 2012. The cointegration tests show the existence of long-run link between real gross domestic product, real capital and the two categories of energy consumption i.e. renewable energy per capita and non-renewable energy. Also, the estimations with long-run and the short-run autoregressive distributed lag (ARDL) indicate that only the non-renewable energy sort and capital can contribute to enhancing economic growth whereas renewable energy does not show any significant effect.

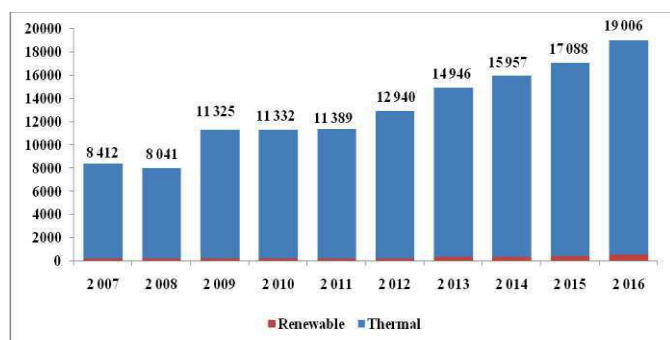
In addition to these studies, the nexus between energy and economic growth in Algeria has been also examined in other papers referred to several countries. Among these: Ziramba [10] investigated the relationship between economic growth and hydroelectricity consumption using series data from Egypt, Algeria, and South Africa over the period 1980-2009. The multivariate framework's results provide support for the neutrality hypothesis for Egypt. The feedback hypothesis is confirmed in Algeria while the conservation hypothesis is supported in South Africa. Sahbi and Shahbaz [11] explored the causal relationship between renewable and non-renewable electricity consumption, economic growth and CO2 emissions for 10 Middle East and North Africa (MENA) countries over the period of 1980–2009. Their short-run dynamics reveal the unidirectional causality running from renewable and non-renewable electricity consumption and economic growth to CO2 emissions. In the long-run, the results confirmed a bidirectional causality between electricity consumption (renewable and non-renewable) and CO2 emissions.

II. ALGERIA'S ELECTRICITY GENERATION

To make electricity available to all, both for the benefit of the economy and citizens, Algeria provided a great means (financial and material) to develop its electricity network and improve its capacity.

Therefore, Algeria has a successful electrification rate of more than 99%, with 9 million customers connected to electricity network in 2016 [12].

As illustrated in the Fig.1 below, the Installed capacity has steadily increased over the past decade to reach 19,006 MW in 2016. Electricity from renewable sources represented only a tiny fraction, representing 606 MW of the installed capacity in this year.



Note: Renewable includes hydro, solar, wind and others sources; thermal includes diesel, combined cycle, gas and steam.

Fig. 1. Installed Capacity of Generation in Algeria (MW) [13]

Algeria's electricity generation is mainly based on non-renewable sources. Out of the 19,006 MW worth of installed capacity registered in 2016, natural gas accounted for an astounding 95%, which by itself amounts to more than 18 GW. The RE (Hydroelectric, solar, wind) and the Diesel represent respectively 3% and 2% of the installed capacity.

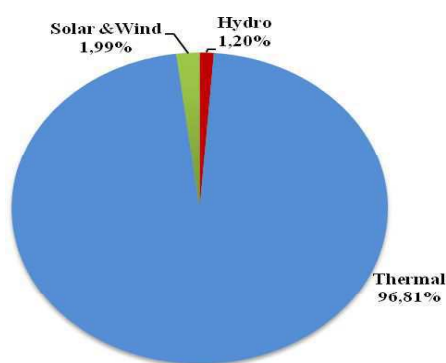


Fig. 2. Algeria Installed Energy Capacity (2016) [13]

In 2016, electricity consumption reached 54,149 GWh compared to 30,320 GWh in 2007.

In parallel, electricity generation rose from 36,474 GWh to 65,686 GWh between 2007 and 2016.

Both electricity generation and consumption have increased by an average of 7% per annum during this period.

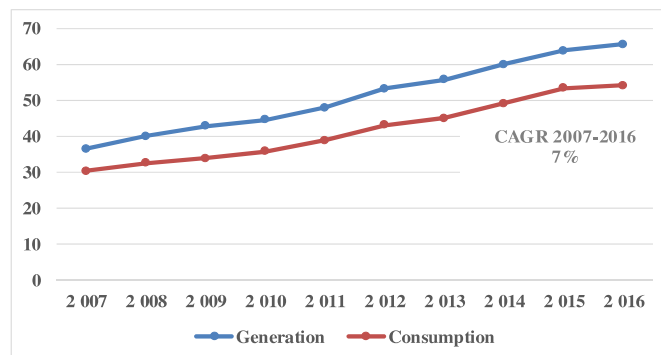


Fig. 3 Growth in electricity generation and consumption in Algeria (TWh) [14]

III. DATA AND METHODS

A. Data

The aim of this contribution is to estimate the impact of oil price and economic growth on the renewable electricity generation in Algeria. Using the cointegration tests and vector error correction model (VECM), we will examine simultaneously short run and long run impacts between the renewable electricity generation, oil price and economic growth.

The choice of the variables was not an easy task to model the impact of economic conditions upon the development of the renewable energy in Algerian case. Some data are quite incomplete and are only available at limited period. For this reason, we have limited our empirical study at a sample of 27 years, covering the period 1990 -2016. The considered variables are renewable electricity generation (RELEC), oil price (OILP), economic growth (GDP) and the non-renewable electricity generation (NRELEC). There are collected from World Development Indicators (WDI-2017) and BP Statistical Review of World Energy (2018).

Fig.4 presents the general evolution of the economic growth (%), oil price (\$/Baril), renewable and non-renewable electricity generation (GWh).

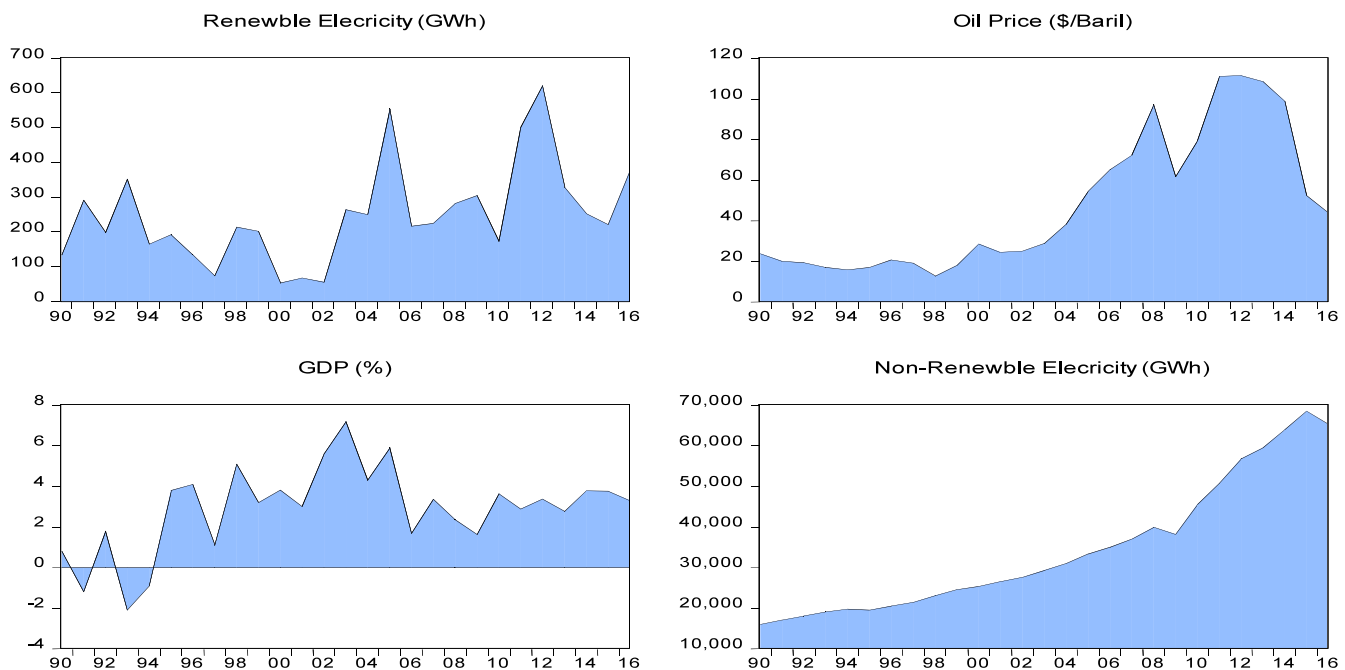


Fig. 4 Renewable and non-renewable electricity generation, oil price and economic growth, in Algeria (1990-2016)

B. Methods

1) Stationarity Test (Unit root tests):

Most macroeconomic time series are trended and therefore in most cases are non-stationary. Therefore, the standard ordinary least squares (OLS) regression procedures can easily lead to spurious regression. In some cases, the results of the OLS regression show a very large value of R^2 and very large values of t-ratios, whereas the variables used in the analysis have no real interrelations [15]. Therefore, the stationarity test of the series is very important. If a series is stationary without any difference, it is designated I (0). On the other hand, a series that has stationary first differences is designated I (1), or integrated of order one. To test stationarity of our series, the Augmented Dickey-Fuller test has been used.

Augmented Dickey and Fuller tests (ADF) (1979, 1981) determine the presence of a unit root (the series can be considered as non-stationary) or not (the series is stationary) [16-17]. Moreover, if the series (RELEC, NRELEC, OILP and GDP) present the same order of integration, we can conclude that there is a risk of cointegration between our variables.

2) Johansen's Test for Cointegration

The Johansen's Test for cointegration uses two tests to determine the number of cointegration vectors: The Maximum Eigenvalue Test and the Trace Test. In some case, Maximum Eigenvalue and Trace test may yield different

results, according to Alexander (2001); the results of Trace test should be preferred [18].

Knowing that, if we have more than two variables in the model, then there is a possibility of having more than one co-integrating vector (the variables in the model might form several equilibrium relationships). In general, for k-number of variables, we can have only up to k-1 co-integrating vectors. To find out how many cointegrating relationships exist among k variables requires the use of Johansen's methodology [19].

After testing the order of integration of all variables, the Johansen's methodology require the selection of the optimum lags (p) of the vector autoregressive (VAR) models, which are determined with the Likelihood Ratio (LR), Final Prediction Error Criterion (FPE), Akaike Information Criterion (AIC), Schwarz information Criterion (SC) and Hannan-Quinn information criterion (HQ). Then, the lag length (p) was selected through the estimation of an unconditional VAR model. It is a crucial input for the cointegration test, which makes the estimation of long run relationships possible.

The identification of some long-run relationships between the studies variables (RELEC, NRELEC, OILP and GDP) leads to estimate a VECM by using the Johansen estimation techniques [19-20].

3) Vector Error Correction Model (VECM)

After finding a cointegration relationship between the examined variables, we can estimate a VECM.

VECMs are a category of multiple time series models to model simultaneously short run and long run impacts. The VECM separates the short-run and long-run relationship among the variables. It is recommending when the times series variables are cointegrated [21]. Otherwise, VECM is no longer required and we directly precede to Granger causality tests to establish causal links between series. The estimation of our model is based on the following equations:

$$RELEC_t = \alpha_0 + \sum_{i=1}^p \alpha_{1i} OILP_{t-i} + \sum_{j=1}^p \alpha_{2j} GDP_{t-j} + \sum_{n=1}^p \alpha_{3n} NRELEC_{t-n} + \sum_{m=1}^p \alpha_{4m} RELEC_{t-m} + \varepsilon_{1t} \dots (1)$$

$$OILP_t = \beta_0 + \sum_{i=1}^p \beta_{1i} RELEC_{t-i} + \sum_{j=1}^p \beta_{2j} GDP_{t-j} + \sum_{n=1}^p \beta_{3n} NRELEC_{t-n} + \sum_{m=1}^p \beta_{4m} OILP_{t-m} + \varepsilon_{2t} \dots (2)$$

$$GDP_t = \gamma_0 + \sum_{i=1}^p \gamma_{1i} OILP_{t-i} + \sum_{j=1}^p \gamma_{2j} GDP_{t-j} + \sum_{n=1}^p \gamma_{3n} NRELEC_{t-n} + \sum_{m=1}^p \gamma_{4m} RELEC_{t-m} + \varepsilon_{3t} \dots (3)$$

$$NRELEC_t = \theta_0 + \sum_{i=1}^p \theta_{1i} OILP_{t-i} + \sum_{j=1}^p \theta_{2j} GDP_{t-j} + \sum_{n=1}^p \theta_{3n} RELEC_{t-n} + \sum_{m=1}^p \theta_{4m} NRELEC_{t-m} + \varepsilon_{4t} \dots (4)$$

The VECM presents not only the long-run relationship of the variables, but it has an additional significant advantage: forecasting [22]. Thus, we apply dynamic forecasts to assess how far the estimated model has approximated the real-historical values and to see if long-term forecasts are close to the targets set in terms of renewable electricity production.

IV. RESULTS

Table 2 indicates that the null hypothesis of no unit roots for the three series (RELEC, OILP and GDP) are rejected at their first differences, because the ADF statistical values are

less than the critical values at a 5% significant level¹. All variables become stationary after first difference. They are then integrated of order one I (1).

Table 2 The Augmented Dickey Fuller (ADF) test results

Variable	t-statistic	
	At level	At 1 st difference
RELEC	-1.1647	-6.9079*
NRELEC	1.7300	2.9907*
OILP	-0.5272	-4.4596*
GDP	-0.6767	-8.5440*

Lag lengths are selected automatically according to Akaike Info Criterion.

*: Test statistics are significant at 1 % level of significance.

To know the number of cointegration vectors by using Johansen approach, the length of VAR model must be determined by considering the different lag selection criterions (previously cited). Table 2 shows that the optimal lag order is one (p = 1) for three of information criterion.

Table 3 Lag order selection criterion

Lags	Log L	LR	FPE	AIC	SC	HQ
0	-543.39	NA	5.52e+15	47.59	47.79	47.64
1	-477.36	103.35*	7.33e+13*	43.24	44.23*	43.49
2	-466.86	12.77	1.37e+14	43.72	45.50	44.17
3	-454.22	10.99	2.81e+14	44.01	46.58	44.66
4	-413.69	21.14	9.74e+13	41.88*	45.24	42.73*

* indicates lag order selected by the criterion

The results of Johansen's test for cointegration with a lag of order one are presented in table 3 (the model with constant, no trend is chosen). The Trace statistic indicates that RELEC, NRELEC, OILP and GDP are cointegrated. The null hypothesis of at most one cointegration relation is not rejected at 5% level (10.59 < 15.49). In other words, the number of cointegrated vectors with one lag is equal to one.

Table 4 Results of Cointegration tests

Unrestricted Cointegration Rank Test (Trace)				
Hypothesized	Trace	0.05		
No. of CE(s)	Eigenvalue	Statistic	Critical Value	Prob.**
None *	0.59	48.21	47.85	0.046
At most 1	0.48	25.36	29.79	0.148
At most 2	0.24	8.78	15.49	0.385
At most 3	0.06	1.78	3.84	0.181

No intercept no trend Trace test indicates 1 cointegrating equation at the 5% level of significance.

* denotes rejection of the hypothesis at the 5% level.

**MacKinnon-Haug-Michelis (1999) p-values

¹ The critical values of test statistics are tabulated in Fuller (1976) and MacKinnon (1996).

1) Short and long-run relationships:

The presence of cointegration relationship between the variables requires the estimation of the VECM. The log run relationship between the RELEC, NRELEC, OILP and GDP for one cointegrating vector is given in the table 5.

Table 5 Long-run relationship

Dependant variable Δ RELEC	Coefficient	Std Error	t-statistic
OILP	3.828	2.258	1.695
GDP	43.169	15.763	2.738
NRELC	-0.014	0.007	- 2.079
Constant	65.75	/	

In the long term, all the coefficients are significant at 5% of significance. Based on these results, we can say that the impact of OILP and GDP on RELEC are positive and significant. It implies that a higher oil price and more economic growth permit a more investment in the renewable energy. Besides, the impact of NRELEC is negative, due to a substitution effect between the shares of the two sources of generation electricity.

In the short run, table 6 indicates that only the variable oil price has a significant and positive effect at 5% level of significance. The effect of the economic growth on renewable electricity generation is statistically insignificant in the short term.

Table 6 Short-run relationship

	Coefficient	Std. Error	t-Statistic	Prob.
ECT	-0.78	0.24	-3.17	0.004
D(RELEC ₋₁)	0.09	0.22	0.41	0.685
D(OILP ₋₁)	5.96	2.34	2.54	0.019
D(GDP ₋₁)	14.69	12.01	1.22	0.236
D(NRELEC ₋₁)	0.005	0.01	0.38	0.701
Constant	-17.07	39.30	-0.43	0.668
R-squared	0.46	F-statistic		3.29
Adjusted R-squared	0.32	Prob(F-statistic)		0.026
		Durbin-Watson stat		1.87

2) Parameter stability

To test the parameter stability, we have use the cumulative sum of recursive residuals CUSUM and the cumulative sum of recursive residuals of squares CUSUM² tests. Figs 6 and 7 show that both diagrams are situated inside

the critical bounds, which reflect the stability of model's parameters.

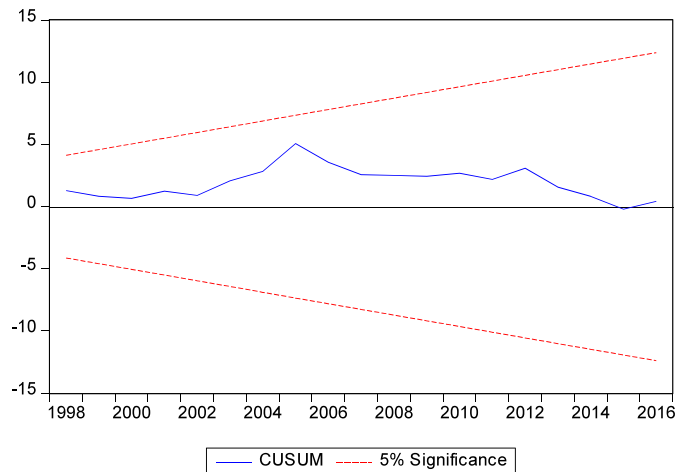


Fig. 5 Plot of cumulative sum of recursive residuals

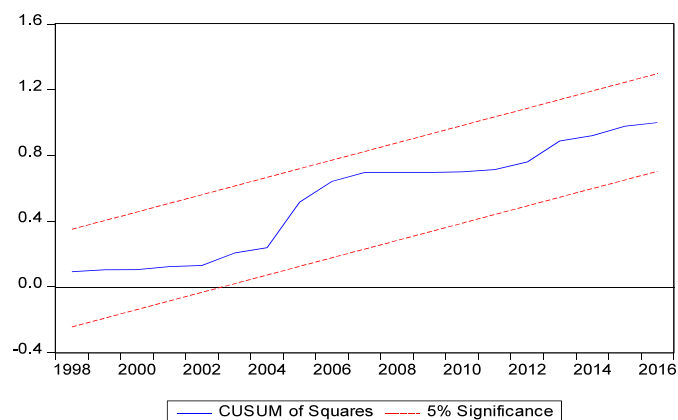


Fig.6. Plot of cumulative sum of recursive residuals of squares

3) Forecasting using alternative scenarios

According to the Annual Energy Outlook (2018), the price of Brent crude, in 2017 dollars, reaches \$125 per barrel by 2020 and \$170 per barrel by 2025, in the assumption of Higher Oil Price case, compared with \$35 per barrel by 2020 and \$40 per barrel by 2025 in the Low Oil Price case.

We use these projections of oil prices to determine the different scenarios for the renewable electricity generation in Algeria by 2025.

Fig.7 represents the forecasting output of our VECM model, which correspond to the three scenarios of oil price:

In the Reference case² (Base Line scenario), the renewable electricity generation will progress by 5% to reach 584 GWh by 2025.

In the High Oil Price case, the Renewable electricity generation will almost tripled by 2025, where it will rise to 1058 GWh, reflecting good financial conditions.

Finally, in the case of low oil prices, renewable electricity production is expected to decrease by 7% by 2025.

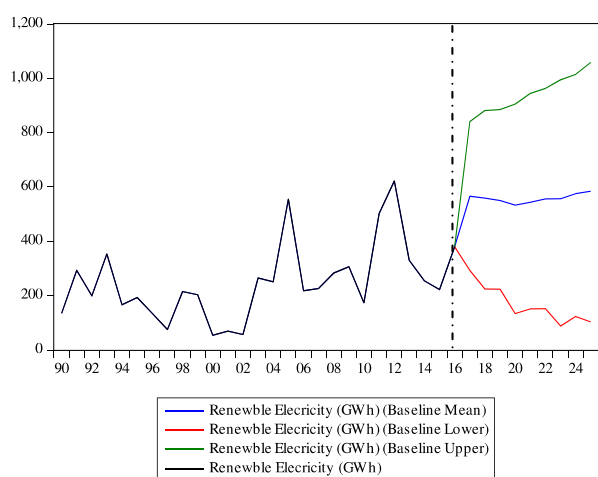


Fig. 7 Scenarios of Renewable Electricity Generation by 2025

V. DISCUSSION AND CONCLUSIONS

The goal of this paper was to set out the nexus between renewable electricity generation, economic growth and oil price in Algeria from 1990 to 2016. We reached this objective by using the cointegration approach and vector error correction model (VECM). The main results of the analysis show that the oil price influenced positively the renewable energy generation in Algeria (*ceteris paribus*) in the short and long term. It implies that higher oil price allows more investment in the renewable energy. In fact, in our forecast analysis, the high oil price case almost tripled renewable electricity generation. This result further confirms that public investment based on oil revenues has shown its limits especially in a context of low prices, and raises several questions about looking for new sources of financing to develop renewable energies and achieve the sustainable development. Currently, Algeria produces about 96% of its electricity from thermal technologies. However, considering the depletion of hydrocarbons with high greenhouse gas emissions, renewable electricity has become a major alternative to fossil fuels to cope with the runaway domestic demand and to honor the environmental commitments. In the regulatory framework, Algeria has ambitious quantitative

² Notice that the Reference case projection assumes trend improvement in the actual conditions of the renewable electricity generation in Algeria.

targets to generate almost 40% electricity from RE by 2030, with financial incentives, but its implementation comes slowly.

So far, Algeria has relied on its hydrocarbon revenues to diversify its economy and deploy its renewable energy plan. This strategy has shown its limits given the volatility of oil prices.

The Algerian authorities have recently recognized the need to find new sources of financing for renewable energies and the public-private partnership seems to be a chosen option as a new scheme of financing. Indeed, on the inauguration of the 9th edition of the International Exhibition of Renewable Energies (ERA 2018), hold in Oran in October 2018, the Algerian Minister of Energy, launched messages to the national partner, public or private as well as the foreign partners to convince them to invest in Algeria where there is "good business, win-win partnerships". He also invited, during a press briefing, all present, foreign and national partners, to attend a meeting on 22 October 2018 in Algiers to discuss and prepare the tender notices of the renewable energy. The Minister explained: "We want to involve you in discussing the specifications, we changed the way we do things ... and now, we are open, and we want to welcome investors". This is a new era for the development of renewable energies in Algeria, which we hope will be more reactive and more efficient, to see green energy becomes a reality in Algeria.

References

- [1] Hadji L., «How 100% Renewable Energy possible for Algeria by 2030?», GENI Global Energy Network Institute, 2016.
- [2] Abdeladim K., et al., «Renewable Energies in Algeria: Current situation and perspectives», *Conference Paper of 29th European Photovoltaic Solar Energy Conference and Exhibition*, 2014.
- [3] IEA International Energy Agency & NEA Nuclear Energy Agency, «Projected Cost of Generating Electricity», 2015.
- [4] Algerian Ministry of Energy and Mines, «Programme National des Energies Nouvelles et Renouvelables», [En ligne]. Available: <http://www.energy.gov.dz>. [Accès 2018].
- [5] Haddoum S., and al., «Algerian Energy Policy: Perspectives, Barriers, and Missed Opportunities», *Global Challenges* 2, 1700134, 2018.
- [6] H.-Y. L.Chul-Yong, «Forecasting the diffusion of renewable electricity considering the impact», *Applied Energy*, p. 31, 2017.
- [7] A. F. Belaid F., «Electricity consumption and economic growth in Algeria: a multivariate causality analysis in the presence of structural change», *Energy Policy* 55:286–95, 2013.
- [8] Y. M. Belaïd F., «Environmental degradation, renewable and non-renewable electricity consumption, and economic growth: Assessing the evidence from Algeria», *Energy Policy* 102 :277–287, 2017.
- [9] A. F., «The relationship amongst energy consumption (renewable and nonrenewable)», *Renewable and Sustainable Energy Reviews* 76: 62–71, 2017.
- [10] Z. E., «Hydroelectricity and economic growth nexus: time series experience of three African countries», *ESJ* 9:84–96, 2013.
- [11] S. M. Sahbi F., «What role of renewable and non-renewable electricity consumption and output is needed to initially mitigate CO2 emissions in MENA region?», 21 09 2014. [En ligne]. Available: http://mpira.uni.muenchen.de/57461/MPRA_Paper_No.57461.

- [12] Algerian Ministry of Energy and Mines, «La Revue algérienne de l'Energie.» Juillet-Août 2018. [En ligne]. Available: <http://www.energy.gov.dz>.
- [13] Arab Union of Electricity, «Statistical Bulletins.» [En ligne]. Available: <http://www.auptde.org/>. [Accès le 2018].
- [14] CREG Commission de Régulation de l'Electricité et du Gaz, «Programme indicatif d'approvisionnement du marché national en gaz naturel 2019 - 2028.» 2018.
- [15] Granger, C. W., & Newbold, P., «Spurious regressions in econometrics.» *Journal of econometrics*, 2(2), 111-120, 1974.
- [16] Dickey, David A., and Wayne A. Fuller. «Distribution of the estimators for autoregressive time series with a unit root.» *Journal of the American statistical association* 74.366a: 427-431, 1979.
- [17] Dickey, D. A., & Fuller, W. A., «Likelihood ratio statistics for autoregressive time series with a unit root.» *Econometrica: Journal of the Econometric Society*, 1057-1072, 1981.
- [18] Alexander, Carol., «Market models: A guide to financial data analysis.» *John Wiley & Sons*, 2001.
- [19] Johansen. S., «Statistical analysis of cointegration vectors.» *Journal of Economic Dynamics and control*, 12(2), 231-254, 1988.
- [20] Johansen S., «Estimation and hypothesis testing of cointegration vectors in Gaussian vector autoregressive models.» *Econometrica*, 59, pp. 1551-1580, 1991.
- [21] Engle, R.F., Granger, C.W.J., «Cointegration and error correction: representation, estimation and testing», *Econometrica*, 55, pp. 277-304, 1987.
- [22] Anderson, R.G., Hoffman, D.L., Rasche, R.H.), «A vector-error correction forecasting model of the US economy.» *Journal of Macroeconomics*, 23, pp. 569-598 , 2002.

Study of the Evolution of Mechanical Properties of Laminated Composites

Mansouri Lilla^{#1}, Djebbar Arezki^{#2}, Samir Khatir ^{*3} and Magd Abdel Wahab ^{*4}

[#]Laboratory of Structural Mechanics and Energetics (LMSE), Mouloud Mammeri University BP17RP, Tizi- Ouzou, Algeria

¹mansouri_lila@yahoo.fr

²ar.djebbar@yahoo.fr

^{*}Soete Laboratory, Faculty of Engineering and Architecture, Ghent University, Technologiepark Zwijnaarde 903, B-9052 Zwijnaarde, Belgium

³Khatir_samir@hotmail.fr

⁴magd.abdelwahab@ugent.be

Abstract— In this paper, experimental mechanical characterization of two laminated composite materials with woven fiberglass reinforcement and thermosetting unsaturated polyester resin is carried out. Our laminates consist of 04 folds of fabrics (Mat 450g / m², Taffetas 800g / m²) and are implemented by contact molding in the form of plates. The main objective of this study is to determine the mechanical characteristics (ultimate stress, elastic limit, flexural modulus) and to follow their evolution as a function of the distance between supports, taking into account the effect of shear stress. The variations of the force-displacement curves during the three-point bending will be presented and discussed in this conference.

Keywords— Composite Laminates, Reinforcement Woven three-point bending, slenderness, Behavior.

I. INTRODUCTION

The composite materials have been the first choice in the aerospace industry since they are flexible in the design process to be adapted for specific applications. Fatigue properties of composites are vary significantly due to the difference in the properties between the fibers and matrix of the composite and the composition. Failure mechanisms of composite materials can be categorized into four major groups, fiber/matrix shear-out, fiber breakage, matrix cracking, and delamination. Philippidis and Vassilopoulos [1] used modified of Tsai–Hill criterion as well to develop a deterministic fatigue life model based on the static failure criteria to cyclic loading. Reifsnider and Gao [2] Presented a model of fatigue life model based on the microstructural level. The objective is to determine the failure of the composites by considering the interactions between the fibers and the matrix, as well as the interfacial bonding in the micromechanical analysis. Fawaz and Ellyin [3] presented a new model to predict the S-N Curve of unidirectional laminates with arbitrary ply orientation based on S-N Curve of laminates with fibers aligned in one orientation. The development of composites based on the mechanical and geometric properties

have evolved over the years to avoid damage and to provide a good working condition. The effect of environment on the fatigue of bonded composite joints according to the fatigue threshold prediction, also the diffusion of moisture in adhesively bonded joints presented by Wahab et al. [4, 5]. The damage of composite structure playing very attractive in the mechanical application. Different application in the static and dynamic are presented in recent years. Khatir et al.[6] presented a damage identification of composite based on experimental analysis using model reduction, optimization techniques, and modal analysis. Capozucca and Magagnini [7] presented a static and dynamic of damaged composited using experimental and numerical analysis. Pascal, F., et al. [8] was presented FEM of the 5-harness satin woven composite material based on the semi-continuous approach. The bundles are modeled with rod elements and a specific damageable shell element is used to stabilize this truss structure. This proposed approach is validated by a comparison with three-point bending tests and low-velocity impact tests. The calculated load-displacement curves and the damage extent correlate well with experimental results. Mansouri, Lilla, et al. [9] presented the effect of hygrothermal aging in different media on the mechanical behavior of mixed short fiber/woven composite laminates of 4 plies of fiberglass fabrics (Mat 300 g/m², Mat 450 g/m², Taffetas 800 g/m²) and unsaturated polyester resins, which are realised by contact moulding. Lampani, L., et al. [10] analyzed the damage in composite laminates with embedded piezoelectric patches subjected to bending action. Meng, Maozhou, et al. [11] investigated the effect of moisture ingress on the bending fatigue of laminated composites. The authors, developed of accelerated testing to investigate the correlation between composite fatigue and moisture diffusion effects. Zhang, Diantang, et al.[12] the influence of the off-axis angles on the flexure behaviors of three-dimensional (3D) woven carbon/epoxy composites is presented with different angles, 0 degree, 30 degree, 45 degree, and 90 degrees, are

experimentally tested via three-point bending method. Al-Hajaj, Zainab, et al [13] presented the impact of properties of a new hybrid composite material made from woven carbon fibers plus flax fibers in an epoxy matrix. The Failure of woven composites under combined tension-bending loading was presented by Khoshtakht, M., et al. [14]. Aboshio et al. [15] presented an experimental investigation of the mechanical properties of neoprene coated nylon woven reinforced composites.

This study has application for of the evolution of mechanical properties bending of laminate composites according to the distance between supports for wider applications in other fields of engineering. The remaining parts of the article are organized as follows. Initially, The material study is presented in Section 2. Then, Section 3 experimental condition. In the Section 4 , Results and discussion. Finally, the concluding remarks are given in Section 6.

II. MATERIAL STUDY PRESENTATION

In this study, we used two different laminates consisting of 04 folds of type E glass fiber in the form of mats and fabrics (Mat 450g / m², Taffeta 800g / m²) see Table 1 and Fig 1, and an unsaturated polyester thermosetting resin.



Fig. 1 Different reinforcements used in this study.

TABLE I
 STRATIFICATION USED

Material	reinforcement	Empilement
1	Glass mat 450 g / m ²	4 layers
2	Taffeta glass 800 g / m ²	4 layers

In this case, the laminate plates used to cut the specimens are obtained by the same manufacturing process as that used for fishing vessels, namely, contact molding. The process is manual as presented in Fig 2.



Fig. 2 Contact molding

III. EXPERIMENTAL CONDITIONS

The three-point bending tests are carried out according to the recommendations of French standards NFT57-105. The tests are made on a universal machine model IBERTEST, instrumented with a load capacity of 100KN with speeds ranging from 10 to 500 mm / min. The central failure of radius 5 mm as well as lateral supports of spokes of 2.5 mm. the geometry of the test is given in Fig 3. The static test provides access to the resistance formulas of the following materials:

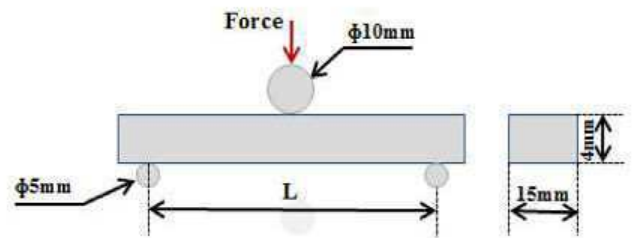


Fig. 3 Geometry in the Bending test.

$$\sigma = \frac{3 PL}{2bh^2} \quad (1)$$

$$\epsilon = \frac{6 Yh}{L^2} \quad (2)$$

$$E_{app} = \frac{L^3}{4 bh^3} \frac{\Delta P}{\Delta Y} \quad (3)$$

$$\tau_{max} = \frac{3P}{4 bh} \quad (4)$$

Where :

σ : The normal stress; ϵ : The relative deformation.

During the bending stress, the stress field is not homogeneous, and the applied force generates not only

normal tensile stresses - compression (1) but also shear stresses (4). In practice, for a sufficiently large value L/h the effects of shear can be neglected. The values of the arrow for different ranges (L) are (40, 50, 64, 80 and 100 mm).

The plates used are textured fibers, we have determined the mechanical properties of the two types of materials in two directions as presented in the Fig 4.

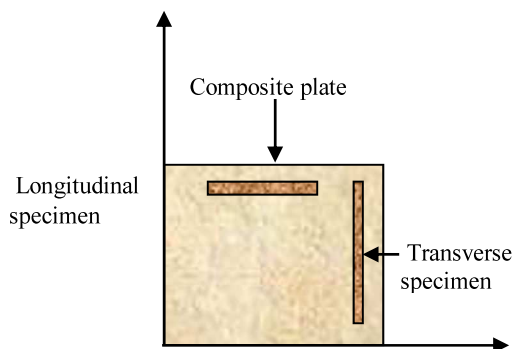


Fig.4 Cutting direction of the specimens

IV. RESULTS AND DISCUSSION

We presented the results of the various experimental tests carried out as part of our study.

A. Bending results in two directions

The results obtained according to the direction of solicitations are summarized in Table 2.

TABLE 2
 MECHANICAL PROPERTIES IN TWO DIRECTION FOR BOTH MATERIALS

Material		E_{app} [Gpa]	σ_e [MPa]	σ_r [Mpa]	ϵ_e [%]	ϵ_r [%]
1	Longitudinal	4.33 (0.4)	123.91 (9.24)	142.37 (9.7)	0.028 (0.04)	0.038 (0.002)
	Transverse	4.05 (0.51)	107.54 (12.19)	120.85 (7.34)	0.026 (0.001)	0.032 (0.001)
2	Longitudinal	15.53 (0.59)	251.65 (20,01)	271.68 (0.4)	0.016 (0.001)	0.018 (0.001)
	Transverse	13.89 (0.99)	261.61 (7,68)	309.42 (60.95)	0.018 (0.001)	0.028 (0.007)

Fig 5 shows the evolution of the stresses as a function of the direction of stress for the laminate and the fabric reinforcement laminate, respectively. We can say that in both materials the laminate does not have the same behavior. First of all, we find for elastic modulus and deformation is insensitive to the direction of stress. On the other hand, the deformation at break is influenced by the direction of stress and type of reinforcement.

B. Influence of the distance between supports

The evolutions of the mechanical properties obtained as a function of the slenderness are summarized in the Tables (3, 4) and represented by the curves of Figs 6 and 7.

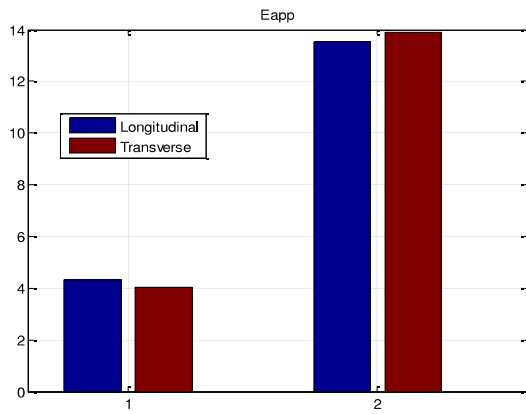
According to the results obtained, we noticed that all the specimens exhibit a similar behavior for the same material with a dispersion of the mechanical characteristics. The overall mechanism of rupture of our test pieces differs according to the type of the fold.

TABLE 3
 MECHANICAL CHARACTERISTICS OF MATERIAL 1.

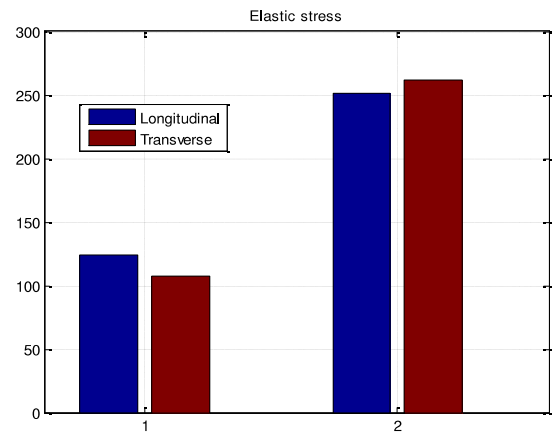
Pinch [mm]	E_{app} [Gpa]	σ_e [MPa]	σ_r [Mpa]	ϵ_e [%]	ϵ_r [%]	τ_{max} [MPa]
40	4.63 (0.45)	80.53 (24.16)	148.91 (6.16)	0.018 (0.007)	0.041 (0.001)	8.21 (0.37)
50	5.51 (1.77)	142.59 (21.86)	179.40 (37.36)	0.027 (0.006)	0.036 (0.005)	7.13 (0.57)
64	5.83 (2.23)	138.15 (33.32)	171.74 (29.74)	0.025 (0.003)	0.036 (0.005)	5.34 (0.57)
80	2.87 (1.77)	108.52 (3.29)	133.11 (10.18)	0.028 (0.001)	0.039 (0.001)	3.67 (0.15)
100	4.11 (0.16)	100.76 (2.56)	127.78 (2.52)	0.024 (0.002)	0.038 (0.002)	2.79 (0.09)

TABLE 4
 MECHANICAL CHARACTERISTICS OF MATERIAL 2.

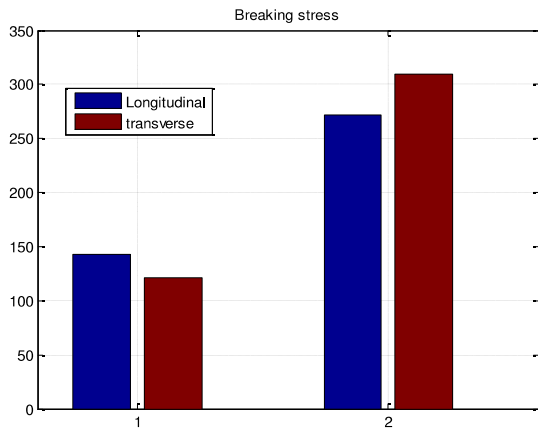
Pinch [mm]	E _{app} [Gpa]	σ _e [MPa]	σ _r [Mpa]	ε _e [%]	ε _r [%]	τ _{max} [MPa]
40	9.55 (0.72)	210.14 (43.62)	223.06 (49.65)	0.022 (0.003)	0.032 (0.015)	9.47 (2.12)
50	12.09 (0.46)	216.23 (30.88)	249.02 (4.11)	0.018 (0.002)	0.03 (0.007)	8.47 (0.23)
64	11.71 (0.51)	90.33 (34.13)	249.98 (42.08)	0.016 (0.003)	0.032 (0.007)	6.55 (1.16)
80	11.09 (0.43)	207.29 (33.51)	236.43 (27.71)	0.018 (0.002)	0.034 (0.001)	4.85 (0.6)
100	13.18 (0.54)	209.85 (19.74)	238.44 (16.82)	0.016 (0.001)	0.026 (0.005)	3.91 (0.24)



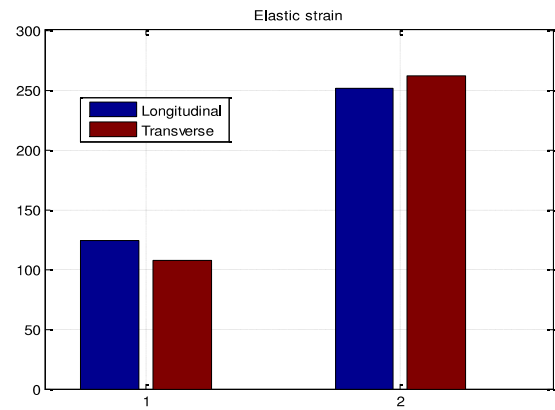
(a)



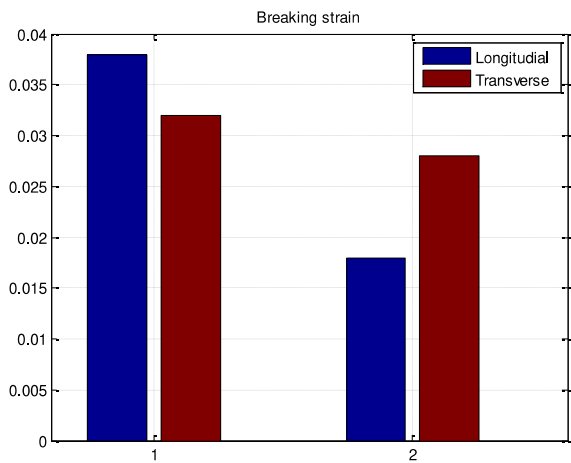
(c)



(b)



(d)



(e)

Fig.5 Evolution of the Mechanical characteristics versus sens of two materials.

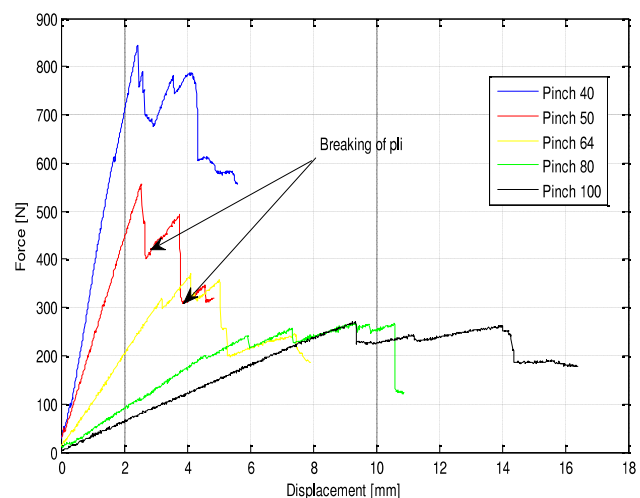


Fig. 7 Force versus deflection Curve in material 2

According to the results presented in the Figs 6 and 7 (force / displacement) it can be seen that the behavior of the material 1 is semi-fragile.

For material 2 (see Fig 7), we noticed a nonlinear zone associated with the appearance of plastic deformation and the beginning of the damage where we heard cracks, which correspond first to the delamination inter folds. In order to characterize the effect of the distance between supports and the type of folds effect. A comparative study of the properties of use is conducted.

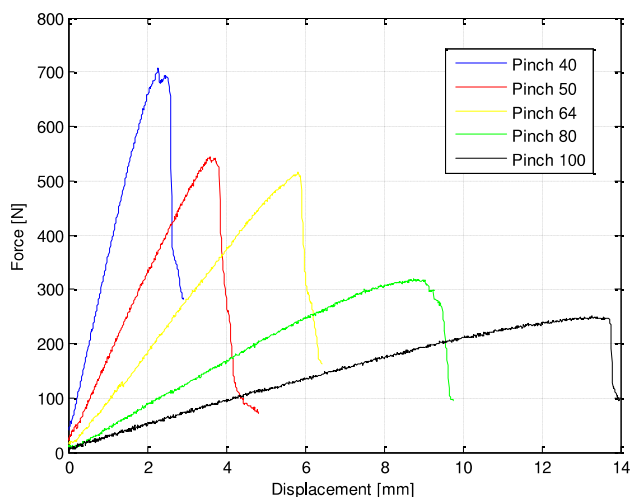


Fig. 6 Force versus deflection Curve in material 1

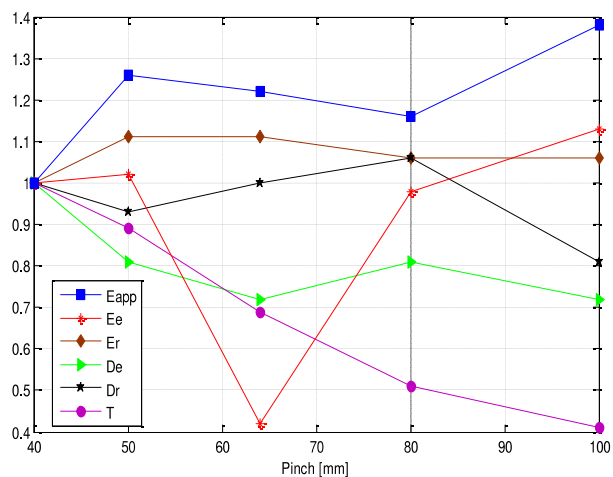


Fig.8 Evolution of the Mechanical characteristics versus pinch of material 1

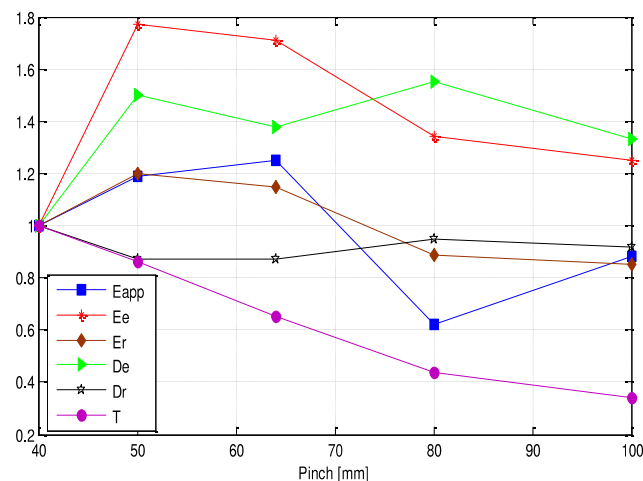


Fig. 9 Evolution of the Mechanical characteristics versus pinch of material

Figs 8 and 9 show the dimensionless evolution of mechanical properties as a function of slenderness. It is noted that all the mechanical properties are influenced by the variation of the slenderness. We note for both materials a sudden decrease in the shear stress with the variation of the slenderness which shows that the shear is inversely proportional to the distance between supports. For sufficiently large values of L / h the effects of shear can be neglected.

C. Influence of type of folds

In Figs 10 and 11 show a comparison of mechanical properties as a function of slenderness. The first remarks to extract from these figures that the behavior between the two materials is different and the stresses of the specimens of the laminate 2 are significantly higher than those of the specimens of the laminate 1.

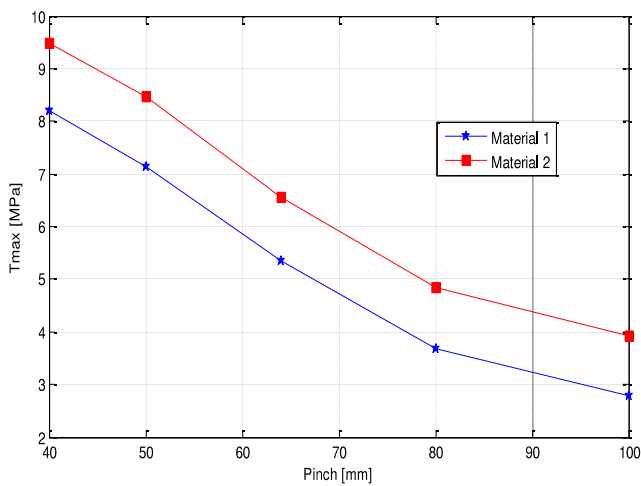
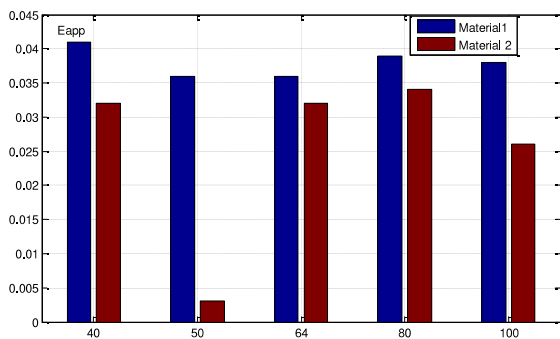
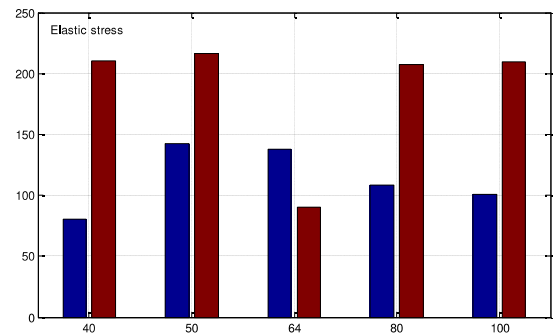


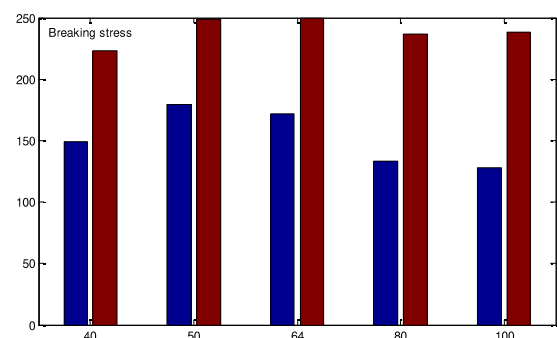
Fig.10 Evolution of the shear stress versus pinch of two materials.



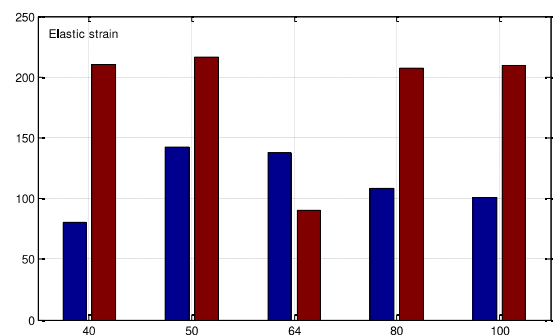
(a)



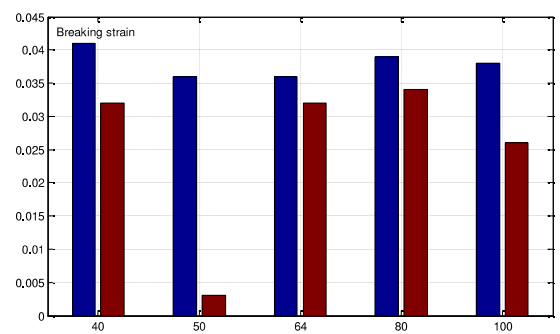
(b)



(c)



(d)



(e)

Fig.11 Evolution of the Mechanical characteristics versus pinch of two materials.

In the Fig 11, we found that the modulus and stress of the specimens of the laminate 2 are higher than those of the specimens of the laminate 1. This difference can be explained by the fiber content. Material 1 contains 31.15% fiber and the other 63.16%.

In the applied loading a matrix increases the mechanical strength of the material, an increase in the volume fraction of the fibers increases the modulus of elasticity according to the law of the mixtures and the modulus of young. Nevertheless, the opposite is to be noted concerning the breaking strain and the elastic stress for $L = 64\text{mm}$.

V. CONCLUSIONS

In this study, a strong interest was focused on the type effect of the stack and the distance between supports on the mechanical properties of the composite material and their evolutions. The analysis of all the results obtained shows that the influence of the distance between supports on these characteristics is difficult and depending on the efforts to be made, the designer is potentially free to steer the reinforcing fibers as he wishes.

The performance of stratified composite materials in service depends on several structural parameters such as, fiber geometry (mats, fabrics), rate, quality of the matrix/reinforcement interface, etc., as well as the matrix that can modify the properties mechanically.

REFERENCES

1. Philippidis, T. and A. Vassilopoulos, *Fatigue strength prediction under multiaxial stress*. Journal of Composite Materials, 1999. **33**(17): p. 1578-1599.
2. Reifsnider, K. and Z. Gao, *A micromechanics model for composites under fatigue loading*. International Journal of Fatigue, 1991. **13**(2): p. 149-156.
3. Fawaz, Z. and F. Ellyin, *Fatigue failure model for fibre-reinforced materials under general loading conditions*. Journal of Composite Materials, 1994. **28**(15): p. 1432-1451.
4. Wahab, M.A., et al., *The effect of environment on the fatigue of bonded composite joints. Part 2: fatigue threshold prediction*. Composites Part A: Applied Science and Manufacturing, 2001. **32**(1): p. 59-69.
5. Wahab, M.A., et al., *Diffusion of moisture in adhesively bonded joints*. The Journal of Adhesion, 2001. **77**(1): p. 43-80.
6. Samir, K., et al., *Damage detection in CFRP composite beams based on vibration analysis using proper orthogonal decomposition method with radial basis functions and cuckoo search algorithm*. Composite Structures, 2018. **187**: p. 344-353.
7. Capozucca, R. and E. Magagnini, *Experimental vibration response of homogeneous beam models damaged by notches and strengthened by CFRP lamina*. Composite Structures, 2018. **206**: p. 563-577.
8. Pascal, F., et al., *Impact damage prediction in thin woven composite laminates—Part I: Modeling strategy and validation*. Composite Structures, 2018. **190**: p. 32-42.
9. Mansouri, L., et al., *Effect of hygrothermal aging in distilled and saline water on the mechanical behaviour of mixed short fibre/woven composites*. Composite Structures, 2019. **207**: p. 816-825.
10. Lampani, L., et al., *Analysis of damage in composite laminates with embedded piezoelectric patches subjected to bending action*. Composite Structures, 2018.
11. Meng, M., et al., *Moisture effects on the bending fatigue of laminated composites*. Composite Structures, 2016. **154**: p. 49-60.
12. Zhang, D., et al., *Off-axis bending behaviors and failure characterization of 3D woven composites*. Composite Structures, 2019. **208**: p. 45-55.
13. Al-Hajaj, Z., et al., *Impact properties of a new hybrid composite material made from woven carbon fibres plus flax fibres in an epoxy matrix*. Composite Structures, 2019. **208**: p. 346-356.
14. Khoshbakht, M., et al., *Failure of woven composites under combined tension-bending loading*. Composite Structures, 2009. **90**(3): p. 279-286.
15. Aboshio, A., S. Green, and J. Ye, *Experimental investigation of the mechanical properties of neoprene coated nylon woven reinforced composites*. Composite Structures, 2015. **120**: p. 386-393.

Application of sand dunes in the machining of molds of composite materials

A. CHAOUFI, A. TAFRAOUI, M. ZAOUI, S. TAFRAOUI, M. DAHMANI

Département Génie Mécanique

Laboratoire de Fiabilité du Génie Mécanique

University of TAHRI Mohamed

BP 417 route de Kenadsa 08000 Bechar Algeria

Email: chaoufi_a@yahoo.fr

ahmedtafraoui@yahoo.fr

miloud_zaoui@yahoo.fr

tafraouisalima@yahoo.fr

dahmani.mohamed-sktm@sktm.dz@yahoo.fr

Abstract — The composite materials are largely used (aeronautical, railway, automobile, etc....) because of their advantageous mechanical properties (weight ratio/resistance). Because of the complexity of the phenomena present in the zone of cut, current knowledge on their machining is limited and prevents their optimal use. Of share their constitution, these materials pose many problems during their machining. The objective of this study is to ultra seek the parameters of cut during the composite machining of materials Concrete High efficiency (HPC) and Concrete Fiber Ultra High efficiency (HPCF) is proposed for the manufacturing of the moulds to carry out parts out of composite materials, or the materials used for the manufacturing of the moulds of the composite material parts like polyester, silicone and resin epoxy etc. , do not resist high temperatures, and also to analyze the behavior of the composite concrete during machining. Allowing to avoid the appearance of the defects (heating and wear of the cutting tool). An experimental design of machining of some tests was defined for the research of the parameters of cut (cutting speed V_c , depth of cut ap and advances by turn f). The variation of the parameters of cut for each test showed that machining after treatment to cause problems in particular on the level as of cutting tools and the appearance of the quoted defects.

Keywords: machining, HPC, HPCF, mould, composite materials, parameters of cuts, surface quality.

I. INTRODUCTION

The current challenge of the industrialists is based more and more on the profit of time and the reduction in the manufacturing costs while respecting the environment. Among these industries, machining occupies a very important place in the technical family of manufacturing of machine elements. The principle of machining is to remove matter so as to give to the blank the wanted form, using a machine tool. By this

technique, parts of a high degree of accuracy are obtained. During the machining of a part, the removal of matter is carried out by the conjugation of two relative movements between the part and the tool: the movement of cut (cutting speed) and the movement in advance (speed in advance). There exist two manners of generating required surface: by work of form or work of envelope. In the case of the work of form, it is the shape of the sharp edge of the tool which conditions surface obtained. In the case of the work of envelope, it is the conjunction of the movements of cut and in advance which defines final surface. Nowadays, machine tools of digital control, i.e. brought under control by a computer system, make it possible to automate partially or completely the procedure. At the time of the cut, the matter in interference with the trajectory of the tool is detached by plastic deformation moreover of the part and is transformed into chips. The characteristics of surface depend on the couple tool-matter, i.e. parameters concerned during the cut (cutting speed, speed in advance, depth of cut,...). In machining, there exist several configurations usable according to the process of cut (turning, milling, drilling,...). In the context of our study, we will be interested more precisely in the first two techniques the most used namely:

- Plane correction, application on a concrete HPC part;
- Milling, application on a material concrete HPC and HPCF. This work in two parts was shared:

II. OPERATION OF SURFACING WITH A STRAWBERRY

Part A: Machining of the new Concrete with cutting tool mills out of metal carbide The machining of Concrete HPC where HPCF with for goal to manufacture a mould for composite material part, or to give simple form or to complicate, or to correct the surface quality during use of the Concrete mould several times. To be done from there, it is necessary to know the parameters of cuts of the Concrete. The preliminary test of the machining of the Concrete and surfacing as shown in the figure



Tool mills two metal carbide Sizes

machining one notes that the tool crushes material it does not have their cut. In short: Even however the cutting speed and speed decreases by it in advance; this nuance of the matter of tool is not appropriate for the machining of concrete HPC where HPCF. With another test one takes the same tool with a speed of 40 tr/min the mini value on the machine, and even speed in advance one notes that stop them cutting changed color as of the first master key and the same stop them cutting are to damage, so takes some of other passes one notices that the tool will damage all stop them cuts because the material Concrete with machined east constitutes of sand of dune which contains silica grain which explains the hardness of this concrete and the black zone in figure 3.

Figure 1: surfacing with tool out of metal carbide

According to the formula $N = 1000V_c / \pi * D$ one finds a value of 630tr/min and

$V_f = 770\text{mm/min}$, as of the first master key appears a flame in a zone of the part as indicates it the following figure:



Figure 2: problem of machining

What it will explain for this zone; that is to say the material is very hard that the tool or the parameters of cuts is male selected.

The parameters of cut one will know:

To keep the speed of the pin.

Vary speed in advance.

Or conversely.

One notes:

For a speed of 112tr/min and speed in advance of 215mm/min; it is noticed that this material is very hard and this kind of work of surfacing with a tool mills two metal carbide Sizes is not appropriate; because the tool with heated and has to change its state and even carries it tool to roasted; during

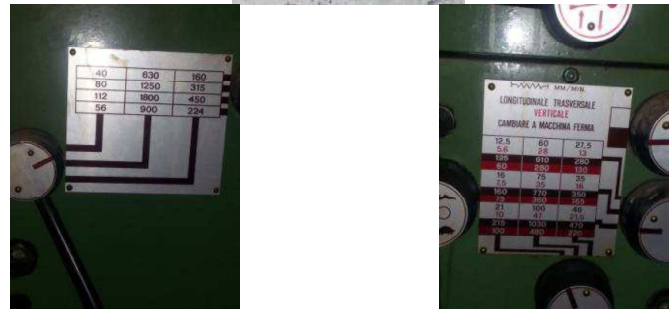


Figure 3: problem of machining and variation of the parameters of cuts

For the test of following surfacing one used a strawberry two Sizes diameter 80mm to brought back plate SANDVIK with a rotational frequency 630tr/min and advance a value of 125mm/min; during machining in the first does not pass from remark; for the second master key at the end of the operation of surfacing it appears a flame, this flame and due to the temperature due to friction tool part, one stopped the machine for bomb disposal expert the rotational frequency of 630tr/min to the value 315tr/min it there is always problem of machining, there thus one has to decrease speed until 160tr/min and the flame is disappeared.



Figure 4: strawberry 2 T with plate brought back nine.

For a test of surfacing on another concrete HPCF part one raised two points essential 1st it is that if one takes the same cutting speed with a depth of cut equal or lower than 1mm, one notes that it there is no problem of machining but for the 2nd point if the depth of cut is increased one notices the appearance of a flame there one intervened for decree the machine, to decrease the number of revolutions until 160tr/min, the following figures explains the phenomenon.



Figure 5: Before reducing speed.



Figure 9: After the reduction speed.

The operation of surfacing on a Concrete part HPCF (Concrete fibre ultra high efficiency) with milling showed that machining without use of lubrication was one can difficult because the part is very hard, to maintain the form of stop cuts it is necessary to use lubrication; after use of the last one has vary the number of revolutions of 630tr/min until the speed of 160tr/min for the 1st speed one notices the light-back even with the use of lubrication as indicates the figure so below but the 2nd disappearance of the flame; thus even with the use of lubrication one notices the appearance of the flame. One can calculate the advance F of the formula:

$$vf = N * f \quad d'ou: f = \frac{vf}{N} = \frac{125}{160} = 0.78125mm$$



Problem of machining



No Problem of machining

Lubrication

Figure 6: appearance of a flame Figure 7: disappearance of the flame until has speed 630 and 315tr/min speed 160tr/min.

III. COMPLETION WITH CUTTING TOOL

The finishing operation with a cutting tool then remains the last operation for obtaining a quite polished surface quality; for that one makes a control of surface quality by one installs roughness.

The measurement of roughness with installs roughness shows that the machining of Concrete (HPC and HPCF) without or with lubrication does not give a good performance for was of surface according to the measurement of several points in the two parts. For the other Concrete part (HPCF) Concrete fiber ultra high efficiency after surfacing with lubrication one recorded for three points of surface roughness as shown in the figure herewith a reduction of the value of roughness what wants to say that tends some towards a good performance of surface quality.

Graph of roughness Ra (µm) according to number of revolutions (tr/min) :

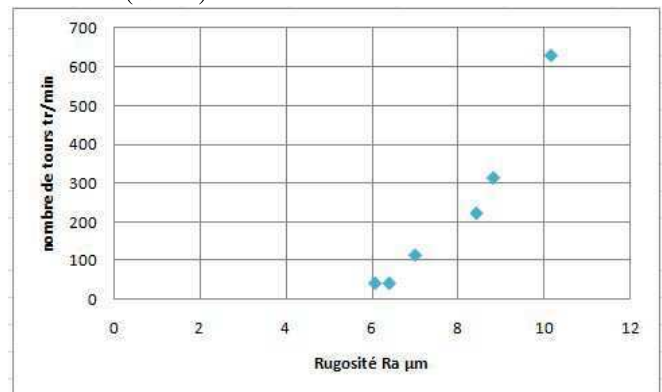


Figure 8: Graph of roughness Ra (µm) according to number of revolutions (tr/min)

one notices that the surface quality to be increased it becomes more polished by decreasing the number of revolutions, but remains insufficient in front of roughness by measuring the last 6.08µm. The following tables illustrate the tests of two materials HPC and HPCF.

IV. CONCLUSION

In this work we have to treat a general information on the machining of composite materials concrete and given the parameters of cuts for each kind of machining (milling, plane correction, drilling...), the defect of machining of composite materials; but for the composite kind of material Concrete HPC where HPCF it should be machined has the fresh state without treatment to form the model of the mould i.e. in the 1st day of the release from the mould, then to make a heat treatment after machining can about it use it to increase the characteristics of material to mould the composite material parts. The operation of surfacing of a mould out of Concrete (HPC) or (HPCF) treaty with the drying oven because several problems in particular on the level of the cutting tool out of metal carbide even by using lubrication; for a strawberry with plate brought back SANDWIK, one has manages to determine the parameters of cuts of material HPC and HPCF. The results obtained helps us to fix these parameters for the machining of this material, a number of revolutions of 160tr/min and a speed in advance of 125mm/min and a depth of cut de1mm are sufficient for the machining of these materials. For obtaining a roughness of value of 6.08µm one

takes a number of revolutions 40tr/min and speed in advance 240mm/min. The machining of the mould out of Concrete (HPC) or (HPCF) after thermal treatment the drying oven to cause problems of machining. Machining before treatment does not cause any problem with the same cutting conditions.

[Zitoune, 2010] Zitoune R, Krishnaraj V, and Collombet F, "Study of drilling of composite material and aluminium stack," Composite Structures, vol. 92, pp. 1246-1255, 2010.

some bibliographical reference

[Abele, 2007] Abele E., Weigold M., Rothenbucher S., Modeling and identification of an industrial robot for machining applications, CIRP Annals – Manufacturing Technology 56 (2007) 387 390

[Bouziane, 2016] Bouziane A., BOULANOUAR L., AZIZI M.W., KEBLOUTI O; Étude de l'effet de la vitesse de coupe sur l'usure des outils de coupe en carbure métallique revêtu et non revêtu icemaep2016

[Chibane, 2013] Chibane H. Contribution à l'optimisation multi objectif des paramètres de coupe en usinage et apport de l'analyse vibratoire Application aux matériaux métalliques et composites. Thèse avril 2013.

[Kress, 2011] Kress G. Mechanics of composites materials. Rapport technique, Centre of structure technologies, ETH Zurich, ETH Zurich, 2011.

[Masashi, 2012] Masashi Yoritaka, Yukio Yamamoto, Yasuaki Hasegawa, Tomio Hokari, « Automotive Application of Advanced Superalloys », 2012.

[Rawat, 2009] Rawat, S. et Attia, H. Characterization of the dry high speed drilling process of woven composites using Machinability Maps approach. CIRP Annals - Manufacturing Technology, 58(1) :105-108, 2009.

[Shyha, 2010] Shyha I. Soo S. L. Aspinwall D. K, Bradley S, Dawson S, and Pretorius C. J, "Drilling of Titanium/CFRP/Aluminium Stacks," Key Engineering Materials, vol. 447-448, pp. 624-633, Sep. 2010.

[TAFRAOUI.A, 2009] TAFRAOUI A. Contribution à la valorisation du sable de dune de l'erg occidental (Algérie).Application aux nouveaux bétons. Thèse doctorat de l'université de toulouse.2009.

[TAFRAOUI.A, 2012] TAFRAOUI A. Valorisation du sable de l'erg occidental (Algérie): Application aux nouveaux bétons. Editions Universitaire Européennes. Pp 233.2012

[Waris, 2012] Marc WARIS, la mise en œuvre, l'instrumentation, la validation et la modélisation d'un système d'injection RTM pour la fabrication de structures composites de hautes performances. École nationale supérieure des mines de Saint-Etienne, 2012.

Modelling and simulation of a gypsum decomposition process by carbon monoxide

Hasna Soli^{#1}, Bassem Jamoussi^{*2}

[#] *Department of Geology, Faculty of Mathematical, Physical and Natural Sciences of Tunis, Tunisia*¹
*The Higher Institute of Education and Lifelong Learning "ISEFC", Tunisia*²

¹hasna.soli@gmail.com

²bassem.jamoussi@gmail.com

Abstract— Gypsum is produced as a waste product by various industries. Tunisian chemical industries, which are specialized in manufacturing aluminum fluoride AlF_3 from fluorspar, produce in big quantities synthetic gypsum $CaSO_4$ as a by-product. Only a small quantity of this waste is directed to industrial or commercial use. The challenge of this study is to model a complete process of gypsum (waste) decomposition by carbon monoxide. The simulated process allows to recover sulfur from the solid waste by integrating it into the production cycle as a raw material of sulfuric acid manufacture. In this study a comprehensive assessment is developed using Aspen HYSYS V8.8 software for process modelling.

Keywords— gypsum, sulfur, carbon monoxide, simulation, HYSYS.

I. INTRODUCTION

The “Industries Chimiques du Fluor” (ICF) is one of the largest producers of aluminum fluoride in the world with a capacity of 42,000 MT per year destined wholly for the commercialization to the aluminium smelters in the world. ICF proceeded during the year 2009 with the construction of an Anhydrite production unit. The annual production is about 100,000 MT[1]. Such a quantity will be interesting to be valorized at the economical and environmental side. In an environmental protection policy context which addresses current issues such as acidification and degradation of air and soil quality, and being aware of the problems posed by different types of medium- and long-term releases behind ecosystem, ICF has been continuously deploying for years efforts in the order to improve the quality of the environment in different units of production.

The key idea of the project is to develop a process to recover sulfur from $CaSO_4$. Thus to introduce it into the sulfuric acid production cycle. A valorization of the gypsum will be carried out.

Besides, the performances of gypsum’s valorization, as an industrial waste, are generally very good. In fact, $CaSO_4$ can be easily valorized. Additionally, it has an interesting economic value to be employed particularly concerning its becoming and use.[2]

The choice of the valorization process depends primarily on the company’s needs. This study proposed a process of gypsum decomposition by carbon monoxide. Firstly two out of three stages of this process are already industrially mastered. The proposed process is more profitable thanks to the production of NH_3 , in parallel with the production of CaO and SO_2 , through the revalorization of H_2 . It generates high profits just in one year. Moreover, it allows the recovery of sulfur in the form of SO_2 . The generated SO_2 will be used to produce sulfuric acid which will be reintroduced into the production cycle [3]. Through the use of Aspen HYSYS V8.8 software to make simulations, we studied the gypsum’s decomposition in order to produce the sulfur dioxide. The first part of this paper focused on the presentation of the simulated process. In the second part we discuss the whole simulation results

II. MATERIAL AND METHODS

Simulation software is a very good tool for the process industry, according to the level of conceptual design and also during the entire lifecycle of the equipment, were it can be very useful for performance, debottlenecking and process studies. [4]

The present process model of gypsum decomposition by CO is efficient and profitable. This process which produces valuable quantities of CaO and SO_2 would be economically reliable once the CO is produced in site. This requires not only the installation of a reactor to decompose the gypsum, but also the installation of a CO production process. The processing plant will likely include a synthesis gas production step and then a gypsum decomposition step using CO which is present in the synthesis gas. Hence, this will enable us to reduce expenses since the costs to obtain CO through this process are cheaper than buying CO as a raw material. Also, the sale or the use of the formed products, NH_3 , SO_2 and CaO , would make this process profitable. Thus, a new source of incomes is created.

A. Process simulation:

Commercial software ASPEN HYSYS® program version 8.8 was used to model the gypsum

decomposition by CO .HYSYS is an oriented-object design simulator. Any specified changes on an element are reflected throughout the model. [5] .This software is characterized by, the Integrated Engineering Environment: All necessary applications are used in a common simulation environment, the possibility of modeling in a stable or stationary state and in dynamic model. Also, it contains an Internal Macro Engine that supports the same syntax as Microsoft Visual Basic. You can also automate different tasks in HYSYS without another program need.

The methodology of process modelling includes selecting chemical components from database, choosing proper unit system, defining stream conditions (temperature, pressure, flow rate and individual composition of each chemical component) and lastly selecting the proper thermodynamic model.[6]. A set of representative chemical composition is extracted and obtained from the literature reports. Chemical components are available in the Aspen library. For the thermodynamic model, the Peng-Robinson equation was defined. The process that will be simulated includes two stages. The first stage is the production of synthesis gas followed by CO production. The second stage is the decomposition of gypsum by CO. Process models are built and established by connecting energy and material streams to unit operation blocks such as, reactors, separator, and cyclone. There are two main steps in this simulation process: The first one is the setup, in which the Fluid package, reaction sets, and components are selected. The list of reaction components includes CH₄, H₂O, CO, CO₂, H₂, N₂, and O₂.The second step is the simulation that contains the following equipment, a reformer which is a conversion reactor in which the major part of methane reacts with the steam to produce dihydrogen, carbon monoxide, and carbon dioxide, a combustor which is a second conversion reactor which holds the reformer product, the air stream, and the steam stream of the combustor as the reactor feeds, a series of three equilibrium reactors in which the water-gas-shift reaction takes place, a separator ,a Gibbs reactor and finally a cyclone.

B. Process flow diagram (PFD)-A conceptual design of gypsum decomposition by carbon dioxide:

All main unit operations are illustrated in a simplified process flow diagram in Fig. 1.

The process that will be simulated includes two stages. The first stage is the production of synthesis gas followed by CO production. The second stage is the decomposition of gypsum by CO.

Gas production is an important stage in this process. It allows to synthesize ammonia. In a typical synthesis process of synthesis gas four reactors are required. In this model, we need five reactors since the conversion and the equilibrium reactions do not trigger the same modelling settings and thus cannot be placed in the same reactor. The combustor is separated into a conversion reactor and an equilibrium reactor. Desulfurized natural gas is the source of hydrogen in this model. It is reformed in a conversion reactor (reformer) when

combined with steam. As the temperature of the steam is successively lowered, the water-gas shift equilibrium reaction takes place in the last two reactors.[7]

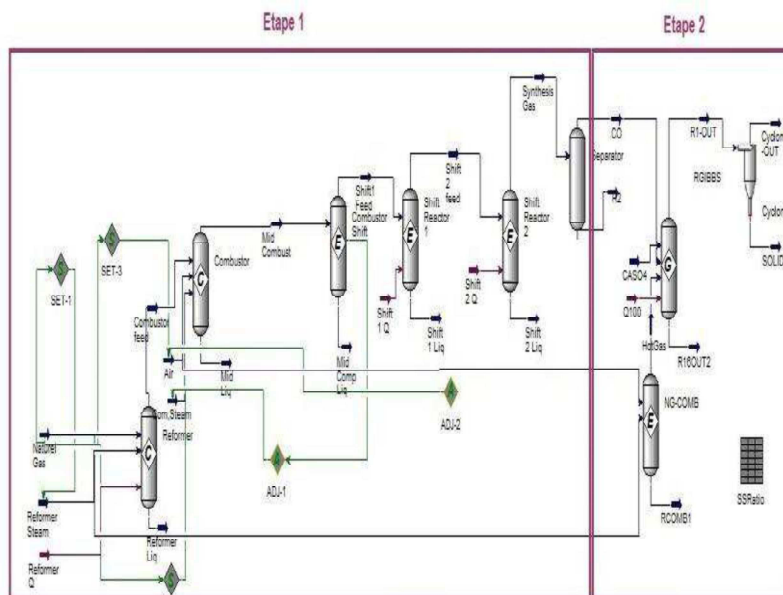


Fig. 1 Process flow diagram simulated on HYSYS

1) Production of carbon monoxide Production of carbon monoxide

The steam reforming (SMR) is the most widespread process on an industrial scale and the best controlled for the production of hydrogen in synthesis gas.[8]

It is one of the important processes in the production of hydrogen and syngas.[9]

It is a classic technology for the synthesis gas production, carbon monoxide and oxo gas (hydrogen / carbon monoxide mixture). [10]

Several technologies produce syngas from natural gas. The steam reforming is the most used one. Methane (CH₄) and water vapour are converted to H₂ and CO in a catalyst presence nickel [11]. This reaction is endothermic. The reaction illustrated by equation (3) optimizes H₂ production by converting the CO produced by the reforming reaction. This technique is targeted in the production of hydrogen to manufacture NH₃.

Steam reforming:



CO₂ reforming:



"Water-gas shift":



The CO required to decompose gypsum can be produced from the steam reforming of methane (CH₄) from natural gas. Other methods are possible, such as the biomass gasification. However, methane reforming was chosen, because it is a known and controlled process on an industrial scale. Examples of industries which employ such process to produce syngas include Sasol in South Africa, Exxon in the United States, and Shell in Netherlands.

In fact, the price of natural gas is currently stable. Natural gas is not expensive particularly due to the growing exploitation of shale gas. The production of CO is simulated on HYSYS as the first step process. Methane steam reforming process is simulated by a reformer which is a conversion reactor in which most of the methane reacts with the steam to produce dihydrogen, carbon monoxide, and carbon dioxide, a combustor which is a conversion reactor which holds the product of the reformer, air stream, and the combustor steam stream, and a series of three equilibrium reactors in which the water-gas-shift reaction takes place. The CO stream is connected to step 2 (Gypsum decomposition). Hydrogen (H₂) will be connected to a step of ammonia production. Other gases are released with the flue gases through step 2 and ammonia production's step.

Figure 2 shows the methane steam reforming diagram used on HYSYS.

CH₄ and water are mixed at 371.1 ° C and 34473.9 hPa psia and heated to 926.6 ° C.

Finally, this step requires 1455.5 kg / h of CH₄ and 4249.25 kg / h of water in order to get enough CO to decompose 3605.6 kg / h of gypsum.

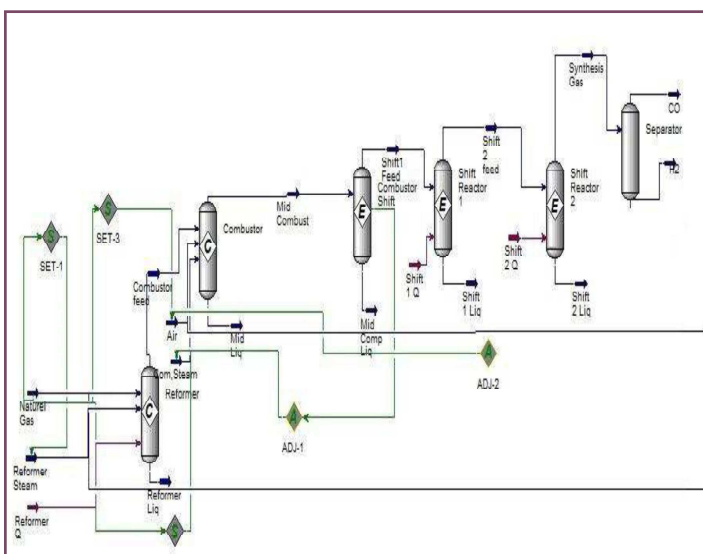


Fig. 2. Methane steam reforming diagram used on HYSYS.

1) Gypsum decomposition:

The second step of the simulation on HYSYS is the decomposition of gypsum at equilibrium (in Figure 3). It is composed of a Gibbs reactor: at 1100 C ° and 101353.3 hPa. Another reactor appears on the process diagram, but indeed it is included in the Gibbs reactor. Since the decomposition reactions are endothermic, this reactor serves to bring the heat of reaction by combustion of natural gas.

The combustor requires 1455.5 kg / h of natural gas and 1455.5 kg / h of oxygen to heat the Gibbs reactor at 1100 ° C. It is followed by a cyclone which separates the solid phase from gases.

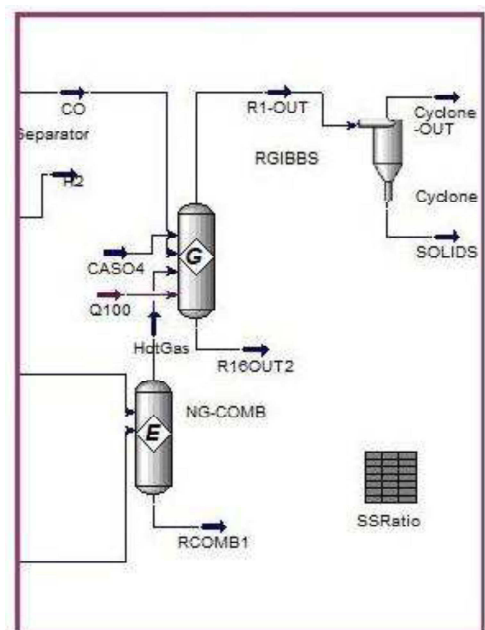


Fig.3. Gypsum decomposition at equilibrium on HYSYS

Several tests were carried out on the parameters of reactors to determine the optimal conditions of the operation. The main objective is to obtain maximum values of SO₂ and CaO quantity.

Firstly, it was necessary to determine the required incoming quantities knowing that those for gypsum (with a small humidity percentage) were fixed at 3605.6 kg / h by optimizing the quantities of SO₂ and CaO.

Besides, it is important to determine the temperature of the Gibbs reactor, because it is also a parameter which determines the conversion rates for the different involved reactions.

C. Results and discussion:

After several performed tests by simulation modifying the CO quantity produced in step 1, it was noted that an amount of moles of CO equivalent to that of CaSO₄ is required to convert all the input quantity of CaSO₄. Around 1254.18 kg /

h of CO are produced by the reaction between 1455.5 kg / h of CH₄ and 4249.25 kg / h of water vapor.

In order to determine the optimum temperature of CaSO₄ decomposition, the conversion rate was calculated for temperatures between 900 ° C and 1600 ° C. It is interesting to obtain the highest possible conversion's rate while

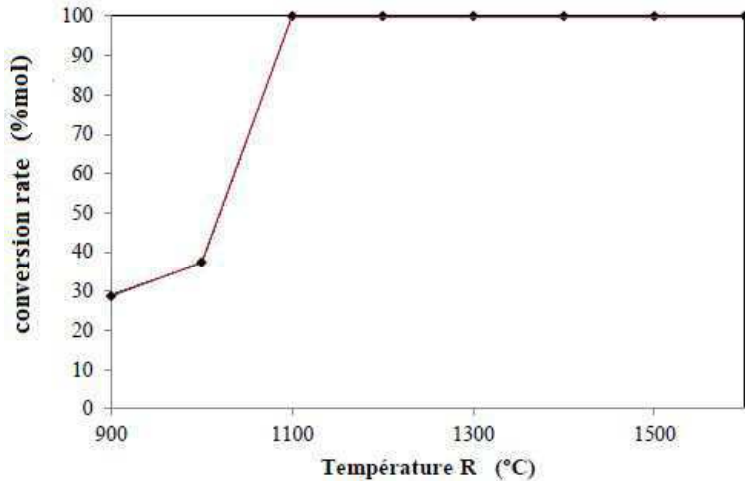


Fig. 4. CaSO₄ conversion rate as a function of the Gibbs reactor temperature on HYSYS

These results show that a Gibbs reactor operating at 1100°C would be sufficient to decompose CaSO₄ and the conversion is maximum.

The chemical yields of SO₂, CaO, and CaSO₄ were calculated for different Gibbs reactor's temperatures between 900 ° C and 1400 ° C. As illustrated in Figure 5, when the reactor's temperature is above 1100 ° C, the chemical yields of CaO and SO₂ are maximum; about 55% of CaO and 45% of SO₂, and CaSO₄ is absent.

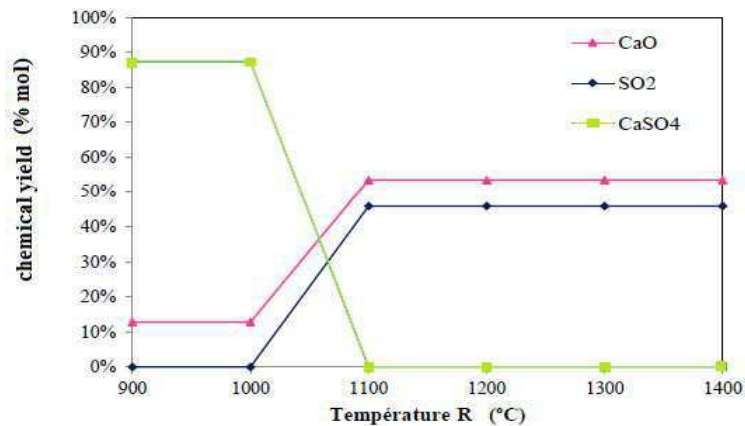


Fig 5. Chemical performances of the different components according to Gibbs's temperature on HYSYS

minimizing the operating temperature. In fact, high temperature requires more resistant and more expensive materials.

Figure 4 shows that CaSO₄ is converted to 100% from 1100 ° C.

An experimental validation of the simulation was made by comparison between simulation's results and gypsum decomposition experiments on fixed bed reactor.

In her studies, Sandrine Marty made several experiments on phosphogypsum to determinate phosphogypsum behavior in an oxidizing reducing atmosphere. The goal of this series of experiments is to find a way to reduce CaS produced quantities and then to maximize CaO and SO₂ production . To analyse the effects of combining a reducing and oxidizing atmosphere on the production of CaS, CaO and SO₂, phosphogypsum was previously decomposed with CO at 1000 ° C. The CO inlet was closed and pure oxygen was injected into the tube. The solid composition, was analyzed then by XPS.

TABLE I
 PHOSPHOGYPSUM COMPOSITION(ANALYZED BY XPS.)

T(°C)	Atmosphere	CaSO ₄ (% mol)	CaO(% mol)	CaS(% mol)	Conversion rates	Chemical yield CaO(%)	Chemical yield CaS(%)
1000	reductive oxidative	56.3	44	0	43.7	19	0

According to the experimental results, the optimal temperature for the CaO and SO₂ production from phosphogypsum decomposition in the presence of CO is 1100 ° C .There is an optimal quantity of CO when the mass ratio CO / PG = 0.2 .Then the reactions should have place in a reactor which combines two phases; in a reductive environment and then with presence of O₂, seems to favor the production of SO₂.

The results of the simulations made with the HYSYS software are thus validated by the experimental results. Indeed, the experiments and the simulations confirmed that the decomposition of the gypsum by CO in CaO and SO₂ is feasible and favored when the reactions are made in a reactor which makes the combination of two phases reductive then oxidizing (Gibbs in HYSYS) fuel at a temperature of 1100 ° C, and the conversion will be maximum.

TABLE II
 COMPOSITION OF THE SOLID OBTAINED FROM THE HYSYS SIMULATION

T(°C)	Atmosphere	CaSO ₄ (% mol)	CaO(% mol)	CaS(% mol)	Conversion rates	Chemical yield CaO(%)	Chemical yield CaS(%)
1100	Reductive oxidative	0	53	0	100	53	0

III. CONCLUSIONS

Through theoretical simulations by HYSYS, the gypsum decomposition was studied in a reducing environment by CO at an operating temperature fixed at 1100°C. This process produces valuable quantities of CaO and SO₂. It would be economically reliable once the CO is produced in site. This requires not only the installation of a reactor to decompose the gypsum, but also the installation of a CO production process. An innovative process was presented in this study including a synthesis gas production step and then a gypsum decomposition step using CO which is present in the synthesis gas. The sale or the use of the formed products, NH₃, SO₂ and CaO, would make this process profitable.

The gypsum decomposition process by CO is efficient and profitable. First, it produces NH₃ from H₂. Thus, a new source of incomes is created. Second, by using the CO generated from the syngas process, we would be able to afford the needed fuel for Gypsum decomposition process. Hence, this will enable us to reduce expenses since the costs to obtain CO through this process are cheaper than buying CO as a raw material.

Acknowledgment

On an industrial scale, it will be important to test the chosen optimization in a continued operation and to rectify it before making a larger investment.

REFERENCES

- [1] ICF, 2012, <http://www.icf.ind.tn>.
- [2] H.Soli,B,Jamoussi, "Valorisation du gypse comme étant un déchet industriel", Proceeding of Engineering and Technologie.2017,vol.30,pp 72.75.
- [3] S.Marty, Production of Calcium Oxide and Sulfur Dioxide from the Decomposition of Phosphogypsum, Polytechnique Montreal, 2014Canada,2014.
- [4] J. Inverno , E. Correia, P. Jiménez-Asenjo ,J. A. Feliu, Two examples of steady state simulation with HYSYS at GALPenergia Sines Refinery, Computer Aided Chemical Engineering,2004,18, 211-216
- [5] A. Djebbari, Simulation of a methanol production unit using Aspen plus-Hysys ", Faculty of Science and Technology, Algeria,2014.
- [6] K. Cheah , S. Yusup , H. Singh , Y.Lam,Process simulation and techno economic analysis of renewable production via catalytic decarboxylation of rubber seed oil e A case study in Malaysia ,journal of Environmental Management,2017,203, 867-1208
- [7] Hyprotech,Tutorial and applications, 2002 <http://www.Hyprotech.com>.
- [8] C. P. Marion, "Production of cleaned and purified synthesis gas and carbon monoxide," éd: Google Patents, 1978.
- [9] U. I. Amran et al .Kinetic Based Simulation of Methane Steam Reforming and Water Gas Shift for Hydrogen Production Using Aspen Plus. Chemical Engineering Transactions.2017
- [10] Production de gaz de synthèse et de gaz oxo via le reformage du méthane à la vapeur (SMR) [en ligne]. France : Air Liquide. Disponible sur : <https://www.engineering-airliquide.com/fr/reformage-du-methane-vapeur-smr-production-gaz-synthese>
- [11] K. Aasberg-Petersen et al.Natural gas to synthesis gas – Catalysts and catalytic processes, 2011,3, 423-459.
- [12] FASCICULE DE BREVET EUROPEEN.EP 2 223 888 B1.2016
- [13] B. C et al. Comment produire de l'hydrogène? 2004. 31-33

Efficient Receiver of Parabolic Trough Collector for Indirect Steam Production Applications

Karima Ghazouani^{#1}, Safa Skouri^{#2}, Salwa Bouadila^{#3}, AmenAllah Guizani^{#4}

[#] *Thermal Processes Laboratory, The Research and Technology Center of Energy
Hammam Lij, B.P. 95, 2050 Tunis, Tunisia*

¹karimaghazouani63@yahoo.com

²skouri_safa@yahoo.fr

³bouadilasalwa@yahoo.fr

⁴amenallah.guizani@crten.rmt.tn

Abstract— The thermal performance of a Parabolic Trough Solar Power Plant (PTSP) is critical to the overall efficiency of the system. The advancement in PTSP technologies has led to the development of steam production and efficient solution that utilizes the sun's energy for thermal power generation. In this work a parabolic trough concentrator with aperture area of 10.8 m² was designed and evaluated in the Research and Technology Center of Energy (CRTE) in Tunisia. This type of concentrating solar power collector is analyzed for indirect steam generating system. Several parameters, as thermal characterization of absorber; thermal efficiency of mixed heat exchangers; thermal efficiency and concentration ratio of PTSP and quantification of steam generation, were considered in order to study their effects on energy efficiency. Experimental results show that the receiver of parabolic trough concentrator extracts 552.73 W of absorbed energy. We found that the thermal energy efficiency varies from 24% to 34% for PTSP system and reach an average concentration factor around 200. As result, parabolic trough concentrator produced 4 kg/h of the steam generated.

Keywords— Concentration ratio, Parabolic Trough Solar Power Plant, Receiver, Steam generating systems, Thermal efficiency

I. INTRODUCTION

Recent studies have proved that the global energy demand is increasing. The massive use of fossil fuels has led to energy shortages and environmental pollution. Therefore, it is increasingly important to find alternative fuels. Renewable energy is the promising solution to this problem such as wind, solar, river, sea waves and nuclear which scientists are trying to benefit from [1], [2], in many sectors, by generating electricity. A study predicts that renewable energies provided electricity in the world by 44% in 2035 [3]. Electricity production solar systems are the common technologies for solar thermal power plants. Solar energy utilization is a promising choice due to its abundance, low carbon emission and wide distribution. Concentrating solar power (CSP) technology is one of solar energy utilization technologies which can be classified into four types based on a system's method of collecting solar energy: linear

Fresnel, parabolic trough, central receiver and parabolic dish. The CSP technology is an attractive option in the renewable energy generation market, an environmental-friendly renewable energy approach that can greatly contribute to environmental protection and energy conservation [4]. The CSP can be used in a great variety of applications such as desalination, solar cooling, industrial heating, refrigeration and electricity production [5], [6]. According to the International Energy Agency (IEA), the installed capacity of CSP will reach 20 GW by 2020 and 800 GW by 2050 [7]. Parabolic Trough Collector (PTC) is one of the mature and widespread solar concentrating technologies [8], [9] and it can be used for large scale power generation very effectively with high dispatchability. The solar parabolic trough systems have many advantages such as high efficiency modularity, high power density, versatility, abundant operational experience, and the ease of coupling with fossil fuels and other renewable energy sources [9]. The performance of this technology is significantly influenced by the distribution of radiant flux around the line focus absorber. In the literature, there are numerous studies on Concentrating Solar Power performance. Ravelli et al.[10] presented a model of direct steam generation in Concentrating Solar Power Plants. They developed a simulation procedure in order to predict the performance of a Concentrating Solar Power Plant with direct steam generation technology. They used three different simulation environments such as TRNSYS, Thermoflex and Octave to predict the performance of a five MWe direct steam generation solar power plant, designed under the INDITEP project. Experimental studies on a Solar Heat Concentrating Steam Generator developed by Qiangqiang et al. [11]. They interested of the steam production rate and the steam production under different solar irradiance. The daily steam production of the system is about 6.174 kg, when the average solar irradiance is about 896 W/m², and the steaming cumulative time is about five hours. Experimental characterisation of a solar parabolic trough collector used in a micro-CHP (micro

cogeneration) system with direct steam generation was developed by Bouvier J.L. et al. [12]. Authors demonstrated that the system produces saturated steam during 8 h with a quality higher than 0.6 for a flow rate of 33 kg/h and the collector performances are suitable for the coupling with the steam engine. Marefati et al. [13] developed an optical and thermal analysis of a parabolic trough solar collector for production of thermal energy in different climates in Iran with comparison between the conventional nanofluids. They evaluated the solar energy potential using PTC in under consideration cities with different climates. Masood et al. [14] presented a simplified design procedure of parabolic trough solar field for industrial heating applications. This study conducted for solar-only system without thermal energy storage which resulted low annual capacity factor. Abboud et al. [15] designed, constructed and tested a parabolic trough solar concentrator system for hot water and moderate temperature steam generation. They designed and operated a three PTC in order to generate hot water and moderate temperature steam. Several parameters were investigated in the performance analysis of the PTC array. They found that the technical feasibility of using PTC for applications requiring thermal energy at temperature up to 150°C. Abdelhady et al. [16] designed and tested a parabolic trough solar collector. They tested the performance of parabolic trough solar collector experimentally and they obtained a thermal efficiency in the range 70% - 65%. Murtuza et al. [17] presented an experimental and simulation studies of PTC design for obtaining solar energy. They tested the newly developed parabolic trough solar collector and characterize its performance. The results of this work allowed the performance of new parabolic trough components such as heat collecting elements and surface materials to be measured when the collector becomes a test-rig in on ongoing solar thermal research program. Bellos and Tzivanidis [18] developed an analytical expression of parabolic trough solar collector performance. They determined the thermal performance of PTC and determined five parameters by this model for the calculation of the thermal efficiency.

II. EXPERIMENTAL SETUP.

Our experimental setup is a Parabolic Trough Collector (PTC) designed and constructed in the Research and Technology Center of Energy (CRTEn) in Tunisia. A Parabolic Trough Collector is described as a long, trough-shaped reflector that has a parabolic cross-section with a slope affected by the rim angle. It focuses the reflected sunlight irradiation along a line running the length of PTC. A cylindrical receiver is located at a linear focus and maintained by two arms in the extremities (Fig.1). The absorber tube is designed to absorb most of the energy focused onto it to heat thermal oil "Transcal N" as Heat Transfer Fluid (HTF) to a higher temperature. Thermal exchange between Transcal N and water will be transferred

to a mixed heat exchanger to achieve the hot temperature for steam production. PTC always has a tracking system, which are usually adjusted with their long axes from north to south.



Fig.1 Real image of Parabolic Trough Collector in CRTEn

III. MATHEMATICAL MODEL FOR PTC:

The useful heat delivered by a Parabolic Trough Concentrator Q_u is the heat flux absorbed by thermal oil as working fluid circulated in the solar heat exchanger and it is also the difference between the solar power absorbed by the absorber Q_a and the heat losses from the receiver to the surroundings Q_p which is defined by :

$$Q_u = \dot{m}_{oil} C_{p-oil} (T_{out-ab}^{Oil} - T_{in-ab}^{Oil}) = Q_a - Q_p \quad (1)$$

\dot{m}_{oil} is the oil mass flow rate, C_{p-oil} is the oil heat capacity and $(T_{out-ab}^{Oil} - T_{in-ab}^{Oil})$ is the difference between the inlet and outlet temperatures of the oil.

The expression of solar power absorbed by the absorber Q_a is:

$$Q_a = \eta_{op} I A_{ap} \quad (2)$$

η_{op} is the optical efficiency its estimated value is taken as 0.85 [19]. I is the direct solar radiation incident on the collector and A_{ap} represents the aperture area of the solar concentrator PTC.

The heat loss (the conductive, convective and radiative losses) Q_p from the receiver of the parabolic trough of the surroundings (as shown in Fig.2) is defined by:

$$Q_p = U_L A_r (T_r - T_a) \quad (3)$$

U_L is the overall heat transfer coefficient, it can be calculated based on the conductive, convective and

radiative heat transfer coefficient proposed by Ref. [20], A_r is the receiver area of PTC and $(T_r - T_a)$ is the difference between the temperature of the absorber and the ambient temperature.

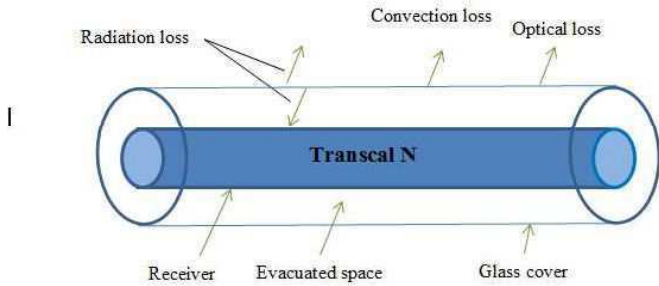


Fig.2 Cylindrical receiver of Parabolic Trough Collector

The thermal efficiency of the PTC is the ratio between the useful energy delivered and the available solar energy [21].

$$\eta_{en} = \frac{Q_u}{Q_a} \quad (4)$$

The mean concentration factor of the system is:

$$C_R = \frac{A_r}{A_{ap}} \eta_{en} \quad (5)$$

A_{ap} represents the aperture area of the PTC

The thermal energy efficiency of the absorber η_{ab} is the ratio between the thermal efficiency of the solar concentrating system and the optical efficiency which is defined by [22].

$$\eta_{ab} = \frac{\eta_{en}}{\eta_{op}} \quad (6)$$

The mass of evaporated water (steam) during the test period m_s defined by the difference between the measured quantity of water m_2 and the quantity of residual water in the water tank m_1

$$m_s = m_2 - m_1 \quad (7)$$

IV. RESULTS AND DISCUSSION

The receiver tube is the main component of Parabolic Trough Collector and plays an important role. Therefore, it is important to study the absorber efficiency of PTC. Fig.3 shows variations of the inlet, outlet temperatures of Transcal N which circulated in the receiver of Parabolic Trough Collector. It is seen from the illustration that the optimum outlet temperatures of the PTC absorbers are

equal to 71°C at noon. It is clearly perceived in Fig 3 that the average difference between the oil inlet and the oil outlet temperatures in the absorber of parabolic trough is equal to 7°C as shown in Fig.3.

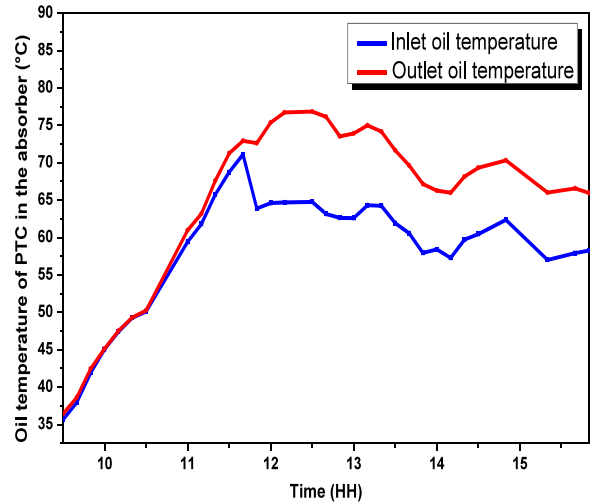


Fig.3 Variations of the receiver inlet and outlet oil temperatures as a function of time.

The figure 4 represents the variation of concentrated solar flux and global solar sunshine as a function of time. It is clearly that the absorbed solar flux reaches an average value around 800 W/m² for global sunshine in the order of 1000 W/m² as shown in Fig.4. So, our PTC presented an acceptable thermal and optical quality.

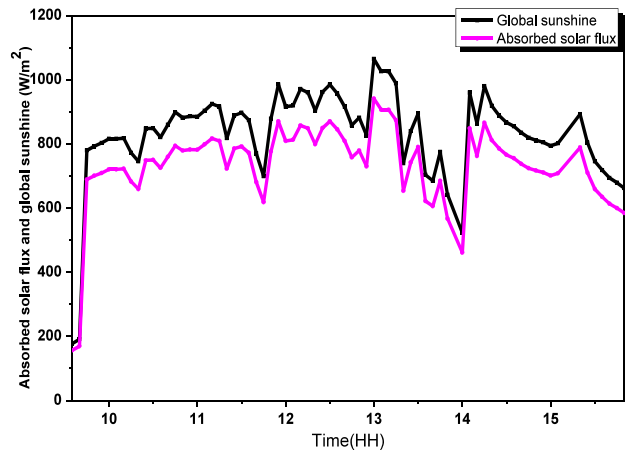


Fig.4 Variation of solar flux absorbed as a function of time.

The thermal efficiency of PTC is influenced by the mechanical parameters, the optical parameters, the sun tracking system and the hydraulic circuit. To evaluate the experimental thermal energy efficiency and the concentration ratio for parabolic trough, analytical expressions Eq. (4) and (5) evaluated and described in Section III. It is observed that the thermal energy efficiency varies from 22 % and 32 %. Eq. (6) shows that the efficiency of the absorber is proportional to the thermal efficiency of PTC as shown in Fig.5.

It is clearly seen that the parabolic trough solar collector reaches an average concentration factor around 200.

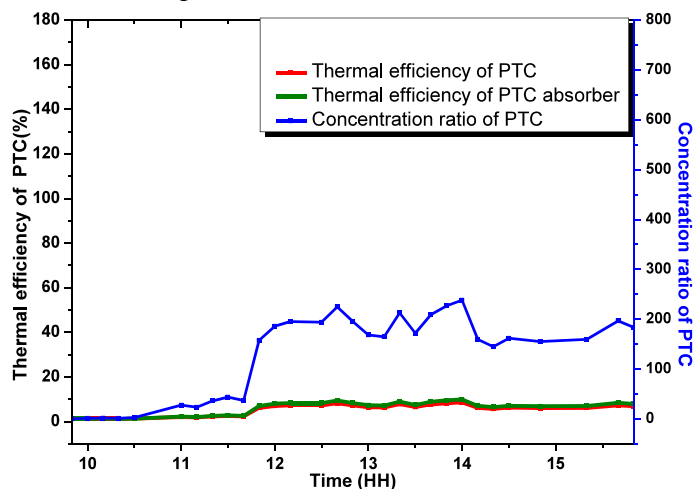


Fig.5 Variations of thermal efficiency and concentration ratio as a function of local time

Figure 6 illustrates the steam mass generating obtained during the test period with different values of pressure. The maximum value of the steam generated is 4 kg/h for PTC system.

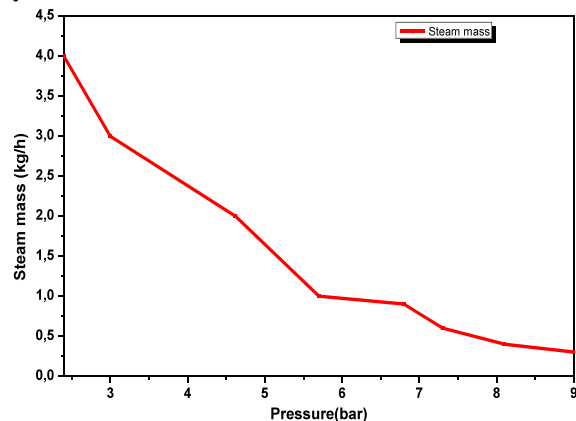


Fig.6 Variations of steam mass as a function of pressure.

Conclusion

A detailed experimental study was presented to determine thermal characterization of PTC absorber installed in the Research and Technology Center of Energy (CRTE) in Tunisia. The receiver tube provides high thermal efficiency with large heat transfer area and transfers it to the mixed heat exchanger to produce indirect steam generation. The PTC thermal energy efficiency varies from 22 % to 32 % and reaches an average concentration factor around 200. As result of this study, the maximum value of the steam generated is 4 kg/h using an efficient PTC receiver.

References

[1] M. Khaled, M. Ramadan, K. Chahine, and A. Assi, "Prototype implementation and experimental analysis of water heating using recovered waste

heat of chimneys," *Case Stud. Therm. Eng.*, vol. 5, pp. 127–133, 2015.

- [2] M. Ramadan, S. Ali, H. Bazzi, and M. Khaled, "New hybrid system combining TEG , condenser hot air and exhaust air fl ow of all-air HVAC systems," *Case Stud. Therm. Eng.*, vol. 10, no. May, pp. 154–160, 2017.
- [3] "WORLD ENERGY OUTLOOK," 2011.
- [4] E. Xu, Z. Wang, G. Wei, and J. Zhuang, "Dynamic simulation of thermal energy storage system of Badaling 1 MW solar power tower plant," *Renew. Energy*, vol. 39, no. 1, pp. 455–462, 2012.
- [5] R. V. Padilla, A. Fontalvo, G. Demirkaya, A. Martinez, and A. G. Quiroga, "Exergy Analysis of Parabolic Trough Solar Receiver," *Appl. Therm. Eng.*, 2014.
- [6] S. E. Ghasemi and A. A. Ranjbar, "Numerical Thermal Study on Effect of Porous Rings on Performance of Solar Parabolic Trough Collector," *Appl. Therm. Eng.*, 2017.
- [7] Q. Yu, Z. Wang, and E. Xu, "Analysis and improvement of solar flux distribution inside a cavity receiver based on multi-focal points of heliostat field," *Appl. Energy*, vol. 136, pp. 417–430, 2014.
- [8] J. Jin, Y. Ling, and Y. Hao, "Similarity analysis of parabolic-trough solar collectors," *Appl. Energy*, pp. 1–8, 2017.
- [9] W. Fuqiang, C. Ziming, T. Jianyu, Y. Yuan, S. Yong, and L. Linhua, "Progress in concentrated solar power technology with parabolic trough collector system : A comprehensive review," *Renew. Sustain. Energy Rev.*, vol. 79, no. May, pp. 1314–1328, 2017.
- [10] S. Ravelli, G. Franchini, A. Perdichizzi, S. Rinaldi, and V. E. Valcarengi, "Modeling of Direct Steam Generation in Concentrating Solar Power Plants," *Energy Procedia*, vol. 101, no. September, pp. 464–471, 2016.
- [11] Q. Xu, X. Ji, J. Han, C. Yang, and M. Li, "Experimental Study on a Solar Heat Concentrating Steam Generator," vol. 12, no. 4, 2018.
- [12] J. Bouvier, G. Michaux, P. Salagnac, F. Nepveu, D. Rochier, and T. Kientz, "Experimental characterisation of a solar parabolic trough collector used in a micro-CHP (micro-cogeneration) system with direct steam generation," *Energy*, vol. 83, pp. 474–485, 2015.
- [13] M. Marefati, M. Mehrpooya, and M. Behshad, "Optical and thermal analysis of a parabolic trough solar collector for production of thermal energy in different climates in Iran with comparison between the conventional nano fl uids," *J. Clean. Prod.*, vol. 175, pp. 294–313, 2018.
- [14] R. Masood, S. Ihtsham, U. Haq, and H. H. Al-kayiem, "A simplified design procedure of parabolic trough solar field for industrial heating

- applications,” *J. Eng. Appl. Sci.*, vol. 11, 2016.
- [15] M. H. Abbood, R. M. Radhi, and A. A. Shaheed, “DESIGN , CONSTRUCTION , AND TESTING OF A PARABOLIC TROUGH SOLAR CONCENTRATOR SYSTEM FOR HOT WATER AND MODERATE TEMPERATURE تنخاسلا هايمل جاتتلا نفاكلا عطقلا ناذ تيسمش تازكرم تموظنم رابتخاو ءانب ، ميمصت ةطسوت م قرارح ةجرد دنع راخبلاو ديهش قازرلا دبع دمحا,” *Kufa J. Eng.*, vol. 9, no. 1, pp. 42–59, 2018.
- [16] S. Abdelhady, M. Shaban, M. Fathy, and A. Ahmed, “Design and Testing Parabolic Trough Solar Collector,” *J. Sci. Eng. Res.*, vol. 4, no. 1, pp. 105–109, 2017.
- [17] S. Ameen, H. V Byregowda, M. Mohsin, H. Ali, and M. Imran, “Experimental and simulation studies of parabolic trough collector design for obtaining solar energy,” *Resour. Technol.*, vol. 3, no. 4, pp. 414–421, 2017.
- [18] E. B. and C. Tzivanidis, “Analytical Expression of Parabolic Trough Solar Collector Performance,” 2018.
- [19] E. Bellos, C. Tzivanidis, K. A. Antonopoulos, and G. Gkinis, “Thermal enhancement of solar parabolic trough collectors by using nano fl uids and converging-diverging absorber tube,” *Renew. Energy*, vol. 94, pp. 213–222, 2016.
- [20] S. A. Kalogirou, “Solar Energy Engineering Processes and Systems,” 2009.
- [21] S. Y. Wu, L. Xiao, Y. Cao, and Y. R. Li, “A parabolic dish/AMTEC solar thermal power system and its performance evaluation,” *Appl. Energy*, vol. 87, no. 2, pp. 452–462, 2010.
- [22] S. A. Kalogirou, “Solar thermal collectors and applications,” *Prog. ENERGY Combust. Sci.*, vol. 30, pp. 231–295, 2004.

A Flexible Active and Reactive Power Control Strategy of a LV Grid Connected PV System

Hamrouni Nejib, Younsi Sami

Analysis and treatment of energetic and electric systems (ATEES)

Science Faculty of Tunis-University of Tunis El Manar

nejib.hamrouni@inrap.rnrt.tn/hamrouni_nejib2003@yahoo.fr

Abstract -The aim of this paper is to present a command approach of a typical double-stage grid-connected PV system functioning under normal conditions and symmetrical grid voltage dips (SGVD). In Normal Operation Mode (NOM), the command developed rises the relatively low solar voltage to a suitable level corresponds to the Maximal Power Point Tracking (MPPT) and regulates, respectively, the dc-link voltage and the output inverter currents. It permits to inject energy into the grid at unity power factor and a current with low harmonic distortion.

Under SGVD, the control strategy approach should ensure a stable connection as long as possible and inject some reactive power to support the grid faults. This command calculates dynamically active and reactive powers that inverter can deliver according to the level of voltage dips and inverter rating currents. Those values are used as reference to control output inverter currents, the dc-link voltage and to deactivate the MPPT command. To validate and to prove the effectiveness of the control strategy, some experimental results are also presented.

Keywords- PVG, Connected PV system, normal operation mode, SGVD, MPPT, balance voltage sag,

I. INTRODUCTION

The high penetration of the Photovoltaic Generators (PVG) in the Low Voltage (LV) parts of the grid raises several concerns and voltage problems in the Point of Common Coupling (PCC). They are generally voltage amplitude drop, frequency deviations and higher harmonic components. The impact of those problems cannot be ignored on the LV-level grid because they affect the grid stability and the safety, as well as the power quality. For this reason, some grid requirements and standards are published to regulate the interaction between the PVG and the grid network and to ride through fault during the disturbance [1-9].

The main problems of the grid connected PV systems are the balance and unbalance voltage sags [10, 11]. Their common cause is principally the short circuits and the connection of large load. The consequence is the disconnection of the PVG from the grid. In [12-16], it is required that the PV generator ceases to energize local loads in the presence of voltage sags and frequency variations. The disconnection of PVG units, with large scale, from the grid at the first time of the fault is not an optimal approach. Moreover, the repeated disconnections might have a negative impact on components life time and disturbance of the grid. For this reason, the inverter should

stay connected to the grid within a short time and injected some reactive power to support the grid when it presents a voltage dips. In that case, the inverter control provides dynamic grid support in terms of Low Voltage-Ride Through (LVVRT) in order to stabilize the grid and to avoid loss of a massive amount of PV power [1,9]. Thus, the stability, the reliability and the safety of the whole system can be improved if the command keeps the PVG connected as long as possible. To maintain a stable connection, many control strategies are developed to handle grid faults for three-phase PV systems. They are principally unity power factor control, positive sequence control, constant active power control and constant reactive power control [17-23]. The control strategy developed in [24], using power factor control, allows the single-stage inverter based three-phase grid connected PV system operations under unbalance grid faults without over current. In addition, it overcomes the high level harmonics and the over current when voltage sag occurs. The control is made on stationary reference frame using Proportional-Resonant current control. In [25], a control of positive and negative sequence components of a large scale grid connected PV system under unbalance voltage grid sags is discussed. The use of filtering techniques to extract dq-components of voltages and currents introduce delays which makes the dynamic response of the system slower. Furthermore, there is a great restriction on choosing suitable parameters for the current and voltage controllers. In [26] a study on double-stage based three-phase grid connected PV systems under several grid faults is presented. It used an external control loop that regulates dc-link voltage and an internal control loop that regulates active and reactive current components of the grid current. It demonstrates that symmetrical faults have a higher impact on PV system performances than asymmetrical faults, both at the PCC and inside the grid connected PV system. All the papers discussed above are focused on controlling the grid connected PV system under balance and unbalance grid voltage sag. They discussed some issues regarding stability and dynamic performance of the connected system but they haven't studied the interaction between the grid fault and the MPPT control. They discussed partially and only the inverter control and omitted the MPPT algorithm.

This paper proposes a flexible active and reactive power control strategy which allows the double-stage grid connected PV system operation under normal conditions and SGVD. This command is made in dq-rotating reference

frame using proportional- Integral (PI) controllers in the current and voltage control loops.

In NOM, The command developed around the first stage will raise the relatively low solar voltage to a suitable level corresponds to the optimal photovoltaic power. Around the second stage a voltage and current loops have been designed to regulate respectively the dc-link voltage and the output inverter current. In the Grid Faulty Operation Mode (FOM), the control approach calculates dynamically the active and reactive power that inverter can deliver when SGVD occurs at the PCC. Those values are used to calculate the reference inverter currents and to deactivate, by an external control loop, the MPPT command according to the level of voltage dips and the inverter rating currents. This proposed strategy overcomes drawbacks such as current harmonics, dangerous dc-link voltage and current peak and ensures a safe connection as long as possible to the grid.

This paper is organized as follows. Section II describes the overall system configuration and control structure in NOM and FOM. Section III presents the simulation results and discussions.

II. CONFIGURATION AND CONTROL DESCRIPTION OF THE SYSTEM

A general diagram of the control strategy of a typical double-stage grid-connected PV system is presented by Figure 1. It includes a dc-dc converter which boosts up the PV voltage within an acceptable range of the PV inverter [12, 14, 16] and makes the system flexible to track the maximum PV power. A dc capacitor that connects the output terminals of boost to the three-phase voltage inverter. The main purpose of the dc-ac converter is to check the active and reactive power which is transferred to the grid. An LCL-filter is used to couple the converter to the ac grid and to limit the high order harmonics coming from the inverter switching behaviour. The monitoring and control unit consists of a voltage sag detection, a power calculation bloc, a current and voltage controllers and a MPPT control.

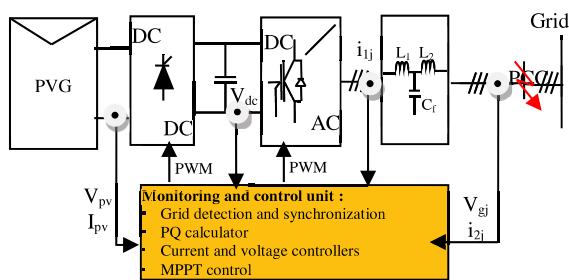


Fig.1. Overall control structure of the grid connected PV system

Two main operation modes for the proposed grid connected PV system are discussed in this paper; the Normal Operation Mode (NOM) and the grid Faulty Operation Mode (FOM). Hence, a fast grid fault detection block should be used. It permits to switch from NOM to FOM once the grid voltage drop exceeds its limits. In the NOM and around the grid side converter, the proposed control can be implemented as the reference profiles by setting the reference powers (active power (P^*) and reactive power

(Q^*)). The active power reference is approximately equal to the maximum PV power and the reactive power reference should be zero in order to have the grid current in phase with the grid voltage (i.e., high power factor). The active power control is achieved through the control of the dc-link voltage.

Due to its simplicity and less costly implementation, a conventional perturbation and observation-MPPT algorithm has been adopted around the first stage to extract the maximum PV power. Once a SGVD is detected at the PCC, the inverter increased instantaneously its output current to keep a balance power between the PVG and the grid. However, the current is limited by the inverter rating current. This situation can disturb the connected PV system. To improve the stability of the overall system without a disconnection, the control should switch from NOM control to the FOM control [27-31]. In this case, the monitoring unit switches to the non-MPPT functioning mode in order to avoid tripping the inverter over-current protection [32, 33]. Simultaneously, the inverter should inject a reactive power varying with the voltage sag level, the inverter rating current and the requirements given in [34, 35]. The power delivered by the PVG should be equal to the inverter output power in order to maintain constant dc-link voltage and to protect the bus capacitor. For this reason, an external control loop is designed which used the inverter output power as reference to deactivate the MPPT control (Figure 5). The flowchart given by Figure 2, presents the conditions allowing the switch between the both operation modes. If the maximum PV power exceeds the inverter output power and the dc-link voltage deviates from its reference; the control strategy switched instantaneously to the FOM and thus the MPPT control has been deactivated and the inverter should inject a reactive power in order to support the grid fault. However, if the two conditions are not satisfied, the FOM should be disabled and the PVG delivers as much energy as possible to the grid with a MPPT control algorithm.

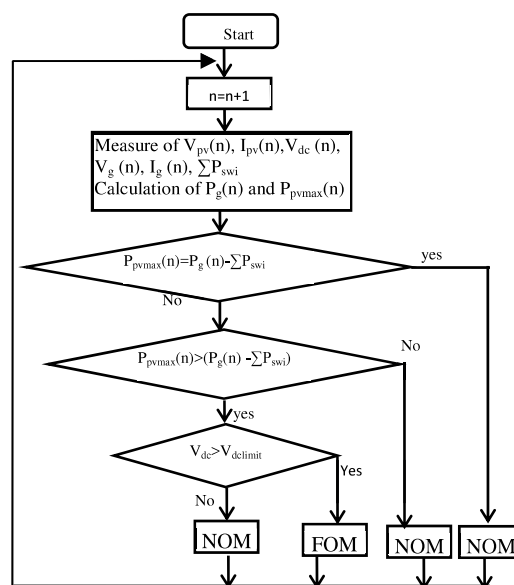


Fig.2. Flowchart of the normal and fault operation modes

A. PV- side power control

The proposed control scheme of the dc-dc converter in various operation modes is given by Figure 3. In NOM, a MPPT algorithm based on Perturbation and Observation (P&O) method (Figure 4) is employed along with the PVG. Its objective is to extract the maximum power from the PVG at any operating conditions based on the irradiation and temperature. The MPPT algorithm should find the adequate reference voltage (V_{pv}^*) imposed by the dc-dc converter to the system. The reference voltage (V_{pv}^*), provided by the MPPT/non-MPPT algorithms, constitutes the input of the voltage and the current controllers. As indicated by Figure 3, voltage and current control loops are used in cascade. The voltage control loop with the PV current compensation provides the reference current (I_1^*), while the current control loop with the PV voltage compensation gives the reference voltage (V_m^*) for PWM, as indicated by equation 1.

The inversion of equations, representing the voltage and current variations, respectively, in the capacitor C_{pv} and the inductance L_{pv} given in [36], provides the optimal control of the PV current and voltage. The controller parameters are chosen to maintain constant the voltage and to reduce the current ripple.

$$\begin{cases} \dot{i}_l^* = R_v(v_{pv}^* - v_{pv}) + i_{pv} \\ \dot{v}_m^* = R_c(i_l^* - i_l) + v_{pv} \end{cases} \quad (1)$$

The boost converter command signal is given, according to [37], by:

$$m_h^* = \frac{v_m^*}{v_{dc}} \quad (2)$$

Where the reference voltage value v_m^* may be described according to the control input and the state variables. According to equation 1, the reference voltage is given by:

$$v_m^* = R_v R_c v_{pv}^* + (1 - R_v R_c) v_{pv} + R_c \dot{v}_{pv} - R_c \dot{i}_l \quad (3)$$

R_v and R_c represent respectively the PV voltage and current regulators. When the boost switch frequency is higher, the time constant is very small and its influence to the whole system may be ignored, so proportional correctors are sufficient. They are parameterized according to the value of the capacitor, the inductance and the dynamic of the regulation loops [38].

Under SGVD, the inverter output current (I_2) should increase to keep the power constant [39], but the current is limited by a maximum rating current ($I_2 < I_{max}$) which avoids inverter to shut-down. Therefore, the inverter can't deliver the PV power to the grid and its output power (P) becomes lower than the maximum PV power (P_{pvmax}). Thus, the difference between the input and the output inverter powers is stored in the dc-link capacitor. Consequently, the dc-link voltage increases and exceeds its limit ($V_{dclimit}$) which makes the plant disconnected from the grid network. In that case, to limit the dc-link voltage and to maintain the connection as long as possible in FOM, it should be limiting the power delivered by the PVG. The control system switches to the non-MPPT operation mode in order to ensure a balance power between the PVG and the grid and to avoid tripping the inverter over current protection. Consequently, the PV current decreases according to the characteristic of the PVG and the control of the dc-link

voltage has been ensured by an external control loop as given by Figure 5.

B. Grid-side power control

The main purpose of the inverter control is to transfer all PV power produced into the grid, to regulate the dc-link voltage and to set a unity power factor for grid currents. The proposed control scheme is two loops based as indicated in Figure 6. The outer loop is the dc-link voltage and the inner one is around inductor currents. The compensation of the reactive energy required by the local load is ensured by the electrical network. Under these conditions, three elementary blocks of command around the inverter appear; the dc-link voltage controller, the current loop and the phase locked loop (PLL). Under SGVD, the inverter control should switch to the FOM. The reactive and active power references should be changed within the voltage sag level and duration, as well as the inverter rating current [2]. The proposed control scheme of the inverter in NOM and FOM is given by Figure 6.

1) Voltage loop: The voltage loop is composed of two modules which ensure the control of the dc-link voltage and the calculation of the reference currents. In NOM, the first module supply a dc current allowing the calculation of the reference active power injected into the grid. As indicated by Figure 6, it is given by $P^* = i_e^* v_{dc} \approx P_{pvmax}$ whereas the reference reactive power (Q^*) should be zero in order to obtain the line current in phase with the grid voltage. The objective of the voltage control loop is to regulate the dc-link voltage at a specified value and to provide the reference current. The closed loop control of the dc-link voltage is needed because the output power of the PV panel varied with irradiance and temperature. The inverter input reference current i_e^* is described by the following relation [37]:

$$i_e^* = i_{dc} - R_{dc}(v_{dc}^* - v_{dc}) \quad (4)$$

To control the dc-link voltage, a Proportional-Integral (PI) corrector has been used. It is parameterized according to the capacitor and the dynamic of the regulation loop [40]. The dc-link voltage reference (v_{dc}^*) is set to 515V. Under SGVD, the required active and reactive power references should change. According to [41], they are given by:

$$\begin{cases} P^* = \frac{3}{2} v_g I_{2d} \\ Q^* = \frac{3}{2} v_g I_{2q} \\ P_{pv}^* = P^* + \sum P_{swi} \end{cases} \quad (5)$$

$\sum P_{swi}$ are the switching losses in the converters $P_{boost} + P_{inv}$, V_g is the amplitude value of the grid voltage at PCC and P_{pv}^* is the reference output power which should be provided by the PVG when the boost command switches to the non-MPPT control. The new required active power was lower than the maximum PV power delivered in normal conditions ($P_{pv}^* < P_{pvmax}$). The second module of the voltage loop is devoted to the calculation of the reference currents i_{2d}^* and i_{2q}^* . Reference currents i_{2d}^* and i_{2q}^* are calculated from the grid voltage and the reference active and reactive powers delivered by the switcher block according to the operation mode.

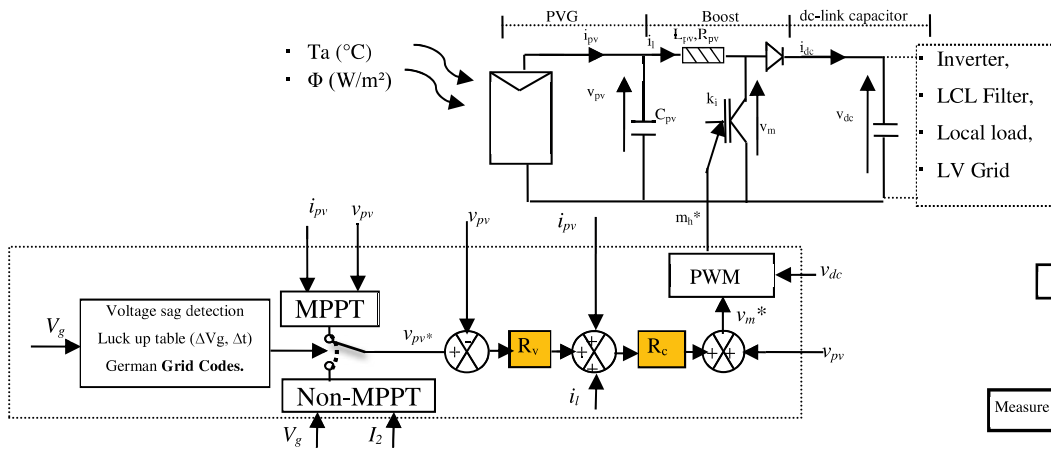


Fig. 3. Control structure of the dc-dc converter under various operation modes

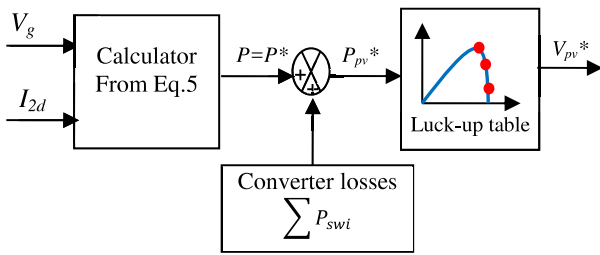


Fig. 5. Non-MPPT diagram

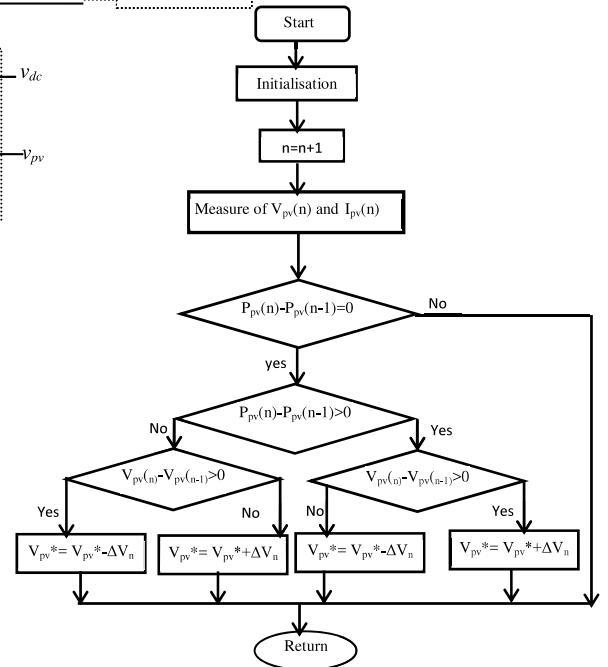


Fig. 4. Flowchart of the P&O-MPPT algorithm

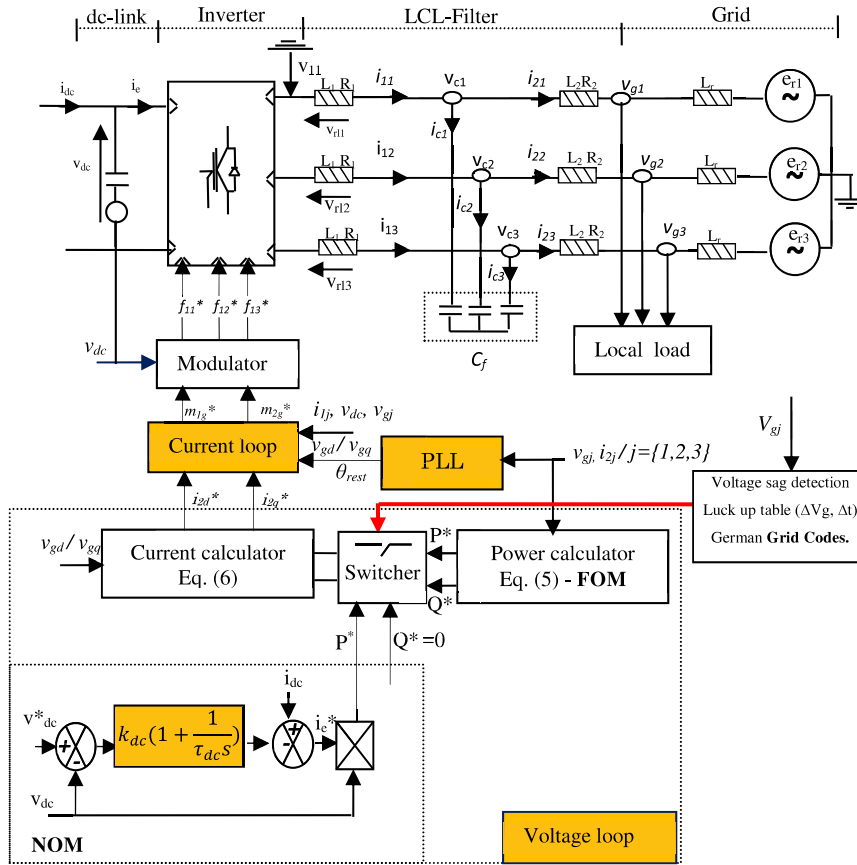


Fig. 6. Block diagram of the inverter command scheme

These currents, according to [42], are expressed in the synchronous reference dq-frame by:

$$\begin{Bmatrix} i_{2d}^* \\ i_{2q}^* \end{Bmatrix} = \frac{1}{v_{gd}^2 + v_{gq}^2} \begin{pmatrix} P^* & -Q^* \\ Q^* & P^* \end{pmatrix} \begin{pmatrix} v_{gd} \\ v_{gq} \end{pmatrix} \quad (6)$$

Where P^* can be equal to P_{pvmax} or $\frac{3}{2}v_g I_{2d} + \sum P_{swi}$ and Q^* can be equal to zero or $\frac{3}{2}v_g I_{2q}$ according to the operation mode. V_{gd} and V_{gq} are the grid voltage components at the PCC.

2) PLL loop: According to Eq.6, reference currents injected into the grid, are deduced from the measurement of grid voltages. Indeed, the network voltages at the PCC can contain various faults (voltage dips, harmonics, short interruptions...) which can pass into the current provided by the inverter. To mitigate this problem, several methods are developed in the literature [43, 44]. Among those methods we are interested in PLL expressed in dq- frame. This method is able to provide the grid frequency and phase information. The grid phase provided by the PLL will be used in the current loop unit. The PLL regulator should be designed to respond within a minimum of overshoot under grid frequency and voltage variations. When the difference between grid phase angle and inverter angle is reduced to zero, the PLL became active and we obtain; $v_{gd}=0$ and $v_{gq}=-\sqrt{3}v_g$ [43]. The model of the PLL is strongly non-linear. However, to synthesize the PLL corrector, we considered a linearized model for weak variations of grid phase angle (θ_r). According to Figure 7, the closed loop transfer function of the linearized PLL model is equivalent to a transfer function of second order system. The dynamic of this loop is obtained according to the desired response time T_r (i.e. $T_r = 10ms$). To avoid any oscillation type of the PLL response, the damping factor should be equal to 1 ($\xi = 1$). This choice of T_r and ξ permits consequently to deduce the various regulator parameters k_θ and τ_θ .

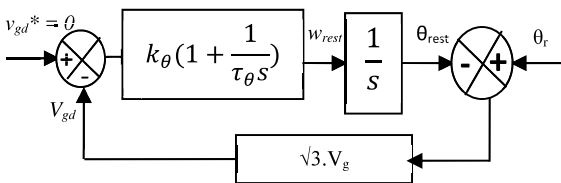


Fig.7. Structure of linearized PLL model

2.2.3. Current loop

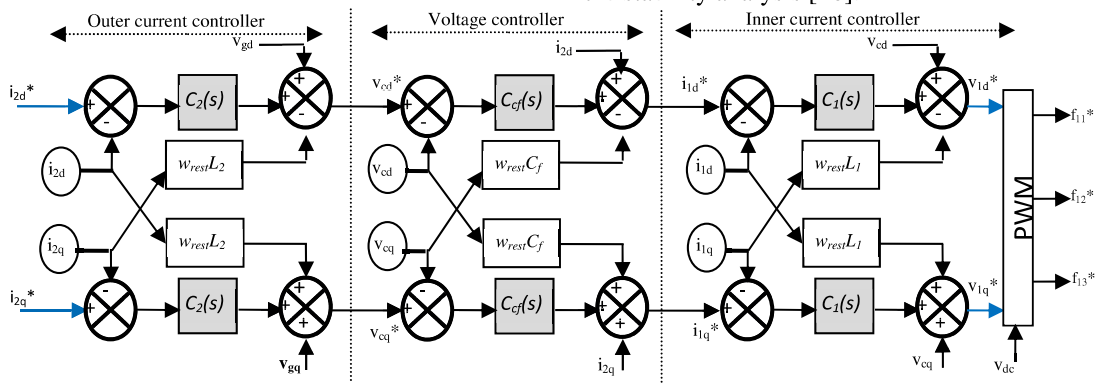


Fig. 8. Scheme of the current loop

The ac current controller is considered particularly suitable for active inverters for its safety and stability performance. It consists of a model based cascade controllers. It is composed of an outer current controller (C_2) for the network line current, i.e. current i_{2j} , an intermediate voltage controller (C_{cf}) for the filter capacitor voltage and an inner current control loop (C_1) for the output inverter current i_{1j} . The outer current loop should drive the output current i_{2d} and i_{2q} to the desired steady state current, namely to the shape and phase of the utility grid voltage by generating control signals m_1^* and m_2^* for PWM. The line current is implemented in the synchronously rotating reference dq-frame.

Hence, individual controllers for the active and reactive quantities with additional compensation for the cross coupling of the d and q axis components are obtained. This current controller block was common for both NOM and FOM. Its inputs are the dq-current component references generated by the voltage loop (i_{2d}^* and i_{2q}^*). According to the state space description of the output LCL-filter model [38], the reference voltages are given by:

$$\begin{cases} v_{cd}^* = L_2 \frac{d}{dt}(i_{2d}^*) + R_2 i_{2d} - \omega_{rest} L_2 i_{2q} + v_{gd} \\ v_{cq}^* = L_2 \frac{d}{dt}(i_{2q}^*) + R_2 i_{2q} + \omega_{rest} L_2 i_{2d} + v_{gq} \end{cases} \quad (7)$$

The inverter output reference currents are given by:

$$\begin{cases} i_{1d}^* = C_f \frac{dv_{cd}^*}{dt} - C_f \omega_{rest} v_{cq} + i_{2d} \\ i_{1q}^* = C_f \frac{dv_{cq}^*}{dt} + C_f \omega_{rest} v_{cd} + i_{2q} \end{cases} \quad (8)$$

The inverter output voltage references are given by:

$$\begin{cases} v_{1d}^* = L_1 \frac{d}{dt}(i_{1d}^*) + R_1 i_{1d} - \omega_{rest} L_1 i_{1q} + v_{cd} \\ v_{1q}^* = L_1 \frac{d}{dt}(i_{1q}^*) + R_1 i_{1q} + \omega_{rest} L_1 i_{1d} + v_{cq} \end{cases} \quad (9)$$

According to [45], terms 7, 8 and 9 should be elaborated by control loops as given by Figure 8. The controller structure consists of three cascade regulators with additional feed-forward and feed-back terms given by the LCL -filter model. In order to stabilise regulators, the gains of the proportional parts are altered from the dead beat gain by the constants k_{i1} , k_{uc} and k_{i2} . Their values are obtained from the stability analysis [46].

Table 1: Parameters of the grid connected PV system

Parameter	value	Parameter	value
Cell series resistance R_s	0.011 Ω	Output PV filter resistance R_{pv}	1 Ω
Cell parallel resistance R_p	10.35 Ω	Output PV filter capacitance C_{pv}	0.005F
Ideal constant of diode n	1.25	DC link Capacitance C_{dc}	0.009F
Cell reverse saturation current I_s	$13.89 \cdot 10^3 \exp(-13.2 \cdot 10^3 / T)$ A	Filter inductance L_1	19mH
Photo current of PVG I_{ph}	$[2.807 + 1.4 \cdot 10^{-3}(T - T_{ref})] \Phi$ A	Filter resistance R_1	0.5 Ω
Cell reference temperature T_{ref}	298.15 °K	Filter capacitance C_f	10 μ F
Series cell n_s	40	Filter inductance L_2	20mH
Parallel cell n_p	1	Filter resistance R_2	0.5 Ω
Series modules N_s	20	Grid inductance L_r	0.005H
Parallel modules N_p	3	Grid resistance R_r	1 Ω
Short circuit current of PVG: I_{sc}	8,37A	Maximal PV current I_{pvmax}	7.6A
Open circuit voltage of PVG: V_{pv0}	428V	Maximal PV voltage V_{pvmax}	340V
Boost losses $\sum P_{boost}$	0W	Inverter losses $\sum P_{inv}$	0W

III. SIMULATION

A. Normal operation mode

Under normal grid conditions, the grid connected PV system is operating in the MPPT mode, in order to deliver as much energy as possible to the grid network and to obtain a power factor near the one. The most important waveforms simulated are shown in Figures 9 and 10. These simulations have been obtained under constant irradiance ($\Phi=1000W/m^2$) and ambient temperature ($T_a=25^\circ C$). They are selected to demonstrate the most significant aspects of the system behaviour. The reference and measure are respectively represented by dotted and continuous line. Salient parameters of the system and regulators are presented in Tables 1 and 2.

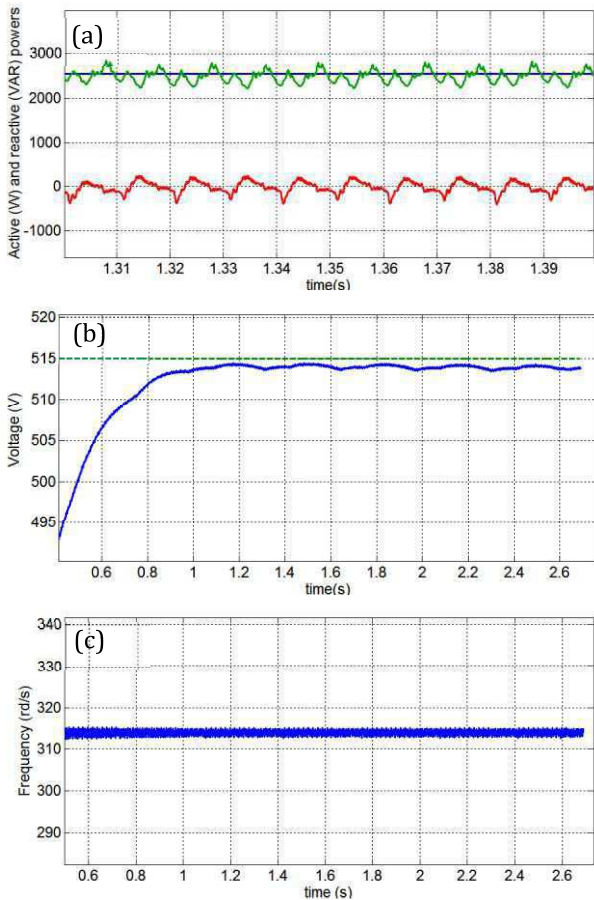


Fig. 9. Simulation results under constant climatic conditions: (a): Maximal PV power (blue), inverter output active (green) and reactive (red) powers, (b): dc-link voltage (measure and reference), (c): Grid frequency provided by the PLL

Figure 9 shows some characteristics of the PV system provided during normal conditions. Figure 9(a) presents the maximal PV power supplied by the PVG, as well as the reactive and active powers injected into the grid. At steady state, real power through the inverter is controlled and reactive power is forcefully made zero. The reactive power oscillates around its reference showing unity power factor operation and control performance of the grid current. The active power supplied by the inverter oscillates around its maximum reference. It can be seen that, in NOM, the inverter output power follows its reference and that average power control has been established. The maximal PV power is approximately equal to the inverter output power because the converter losses are neglected. The dc-link voltage, maintained at a constant level, followed instantaneously its deadbeat reference voltage V_{dc}^* (Figure 9(b)). As a consequence, the active power extracted from the PVG is completely injected into the grid. Figure 9(c) presents the grid frequency estimated by the PLL. It oscillates around its nominal value equal to 314rd/s.

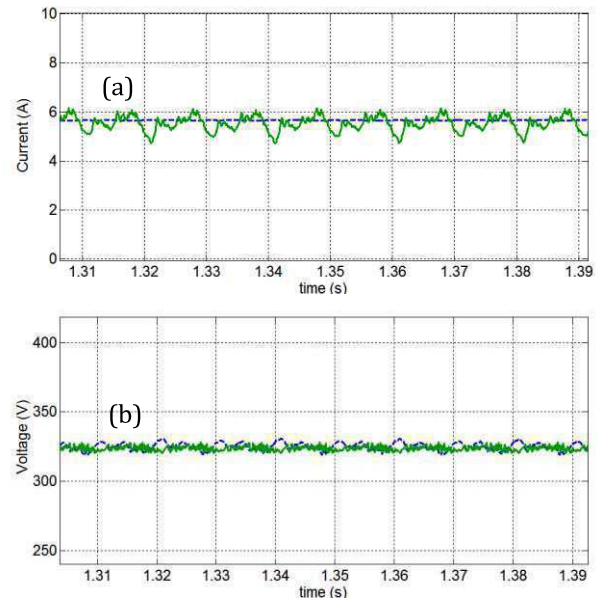


Fig. 10. Simulation results under constant climatic conditions: (a): Inverter current d-component (measure and reference), (b): Inverter voltage d-component (measure and reference)

In the inverter side, the current and voltage d-components, as depicted in Figure 10, followed their references. Those results show the good performances of the various control loops under normal grid conditions.

B. Grid fault operation mode

In order to study the behaviour of the proposed control strategy in the FOM, a symmetrical grid voltage dip is applied at the PCC. The following paragraphs illustrate the response of the grid connected PV system under 50%-100ms SGVD. Two states of the MPPT control are discussed. The first studies the impact of the grid fault on the stability of the overall system when the MPPT control is actuated. The second case discusses the disabling of the MPPT and the switch from the NOM to the FOM control.

1) Case 1: Actuation of the MPPT command.

The voltage sag duration is for 0.1s from 1s to 1.1s. In the PV converter side, PV current and the PV voltage are also as the same because the MPPT control stay enabled. As indicated by Figure 11, the PV current and voltage remain nearly their references. The voltage dip doesn't have an influence on the maximum power provided by the dc-dc converter. This is due to the dc-link capacitor which acts as a buffer zone between continuous and alternative parts. The impact of the SGVD appears only on the grid side. If a transient fault occurs, the average active and reactive powers deviate from their nominal values. As indicated by Figure 12(a), the average active power injected by the inverter decreases to 1.8 kW while the reactive power rises up to 280VAR in order to withstand the voltage dip. When the grid voltage at PCC decreased to 50% ($\approx 110V$), the inverter output current increases during the fault and reaches to the maximum rating inverter current (6.5A). Then, the inverter output power becomes lower than the maximum power injected by the PVG. Thus, the difference between these powers has been stored in the dc-link capacitor. Consequently, the dc-link voltage (V_{dc}) increases to a high level which can destroy the capacitor (Figure 12(b)).

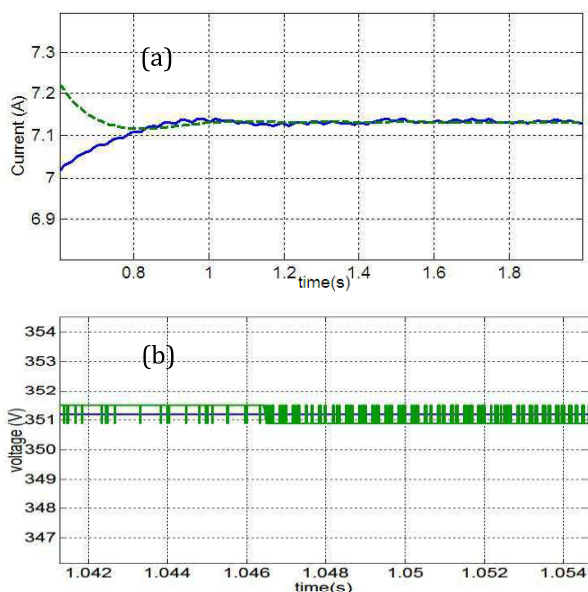


Fig. 11. Simulation results under 50%-100ms SGVD: (a): PV current (measure and reference), (b): PV voltage (measure and reference)

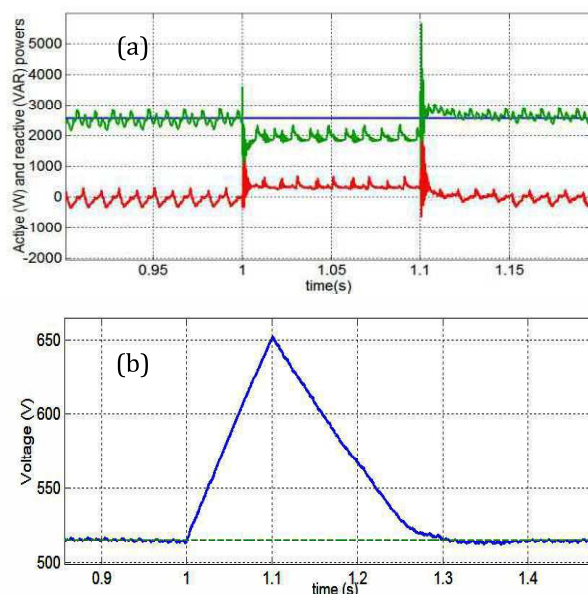


Fig. 12. Simulation results under 50%-100ms SGVD: (a): maximal PV power (blue), inverter output active (green) and reactive (red) powers, (b): dc-link voltage (measure and reference)

Figure 12(a) shows that, after the clearance of fault, the inverter output power (P) decreases slowly and reaches the maximum PV power (P_{pvmax}). As indicated by Figure 12(b), the dc-link voltage decreases progressively discharging the energy into the grid and reaches its reference in 200ms.

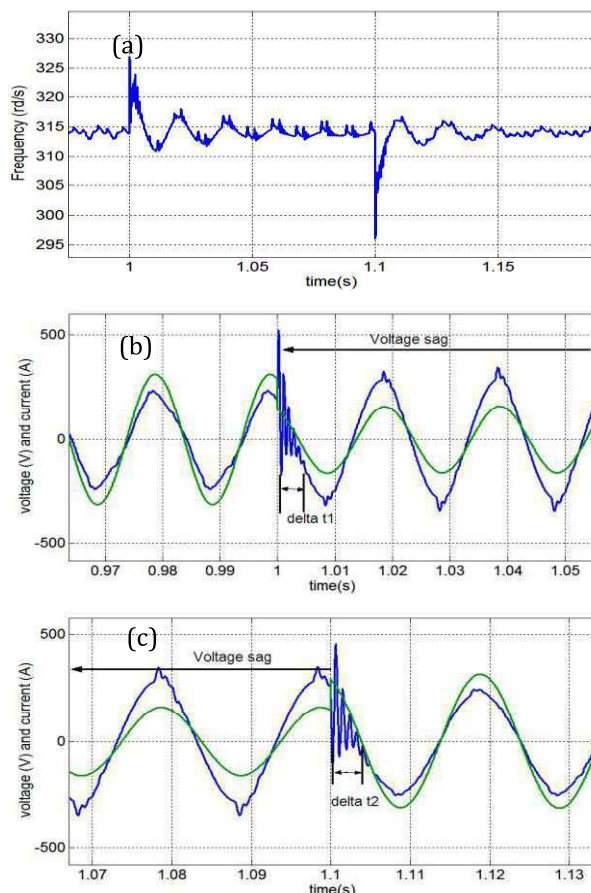


Fig. 13. Simulation results under 50%-100ms SGVD: (a): grid frequency provided by the PLL, (b,c) : grid voltage (green) and (*40) inverter current (blue)

Figure 13(a) illustrates the grid frequency estimated by the PLL. It presents some overshoot at the start and the clearance of the grid disturbance. As it can be seen by this figure, the PLL dynamics present a significant role in transient behaviour of the grid connected PV system. Figures 13(b) and 13(c) show the ac side voltage and the inverter output current. As it might be noticed in those figures, there is a phase leading/lagging between grid side line current and voltage. A low displacement can be noticed between the synthesized current, current effectively injected into the grid, and the line voltage. As a result, the unit power factor is not achieved during the grid voltage dips and for instance, the inverter should provide a reactive power. Both the start of the voltage dip and the end of that present a transient current oscillations, respectively, δt_1 and δt_2 as indicated by Figures 13(b) and 13(c).

❖ Grid connected PV system under various SGVD

The utility of the dc-link capacitor, to support and to dump the SGVD is discussed in this part. To analyze the necessity of the capacitor, various symmetrical grid voltage dips characterized by their level and duration [1-8] are simulated. The corresponding dc-link voltages, inverter output active and reactive powers are recorded in table 3.

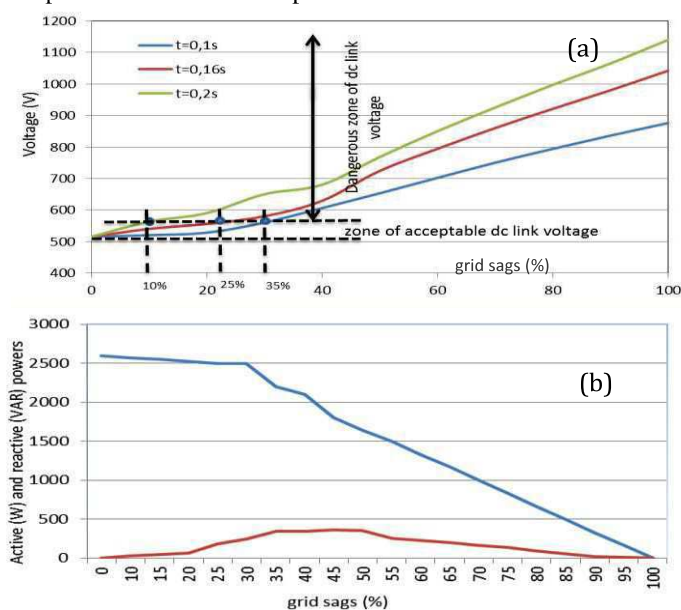


Fig. 14. Characteristics of the grid connected PV system under various SGVD; (a): dc-link voltage, (b): inverter output active (blue) and reactive (red) powers for 100ms voltage dip duration

As indicated by Figure 14(a), for various duration of grid voltage sags, the dc-link voltage increases progressively and moves away to the internal protection fixed at 110% of V_{dc} . Thus, the dc-link control loop based on PI regulator loses its performance because the energy produced by the PVG is accumulated in the continuous bus. Consequently, the dc-link voltage increases to a high level which can destroy the capacitor. According to Figure 14(a), both the duration and the level of the SGVD present an impact on the dc-link voltage. For a voltage limit equal to 560V, the system can support a SGVD equal to 10% in 0.2s, 25% in 0.16s and 35% in 0.1s with activation of the MPPT control. After those limits, this fault becomes dangerous because the PV power can't be totally

transferred into the grid side. To resolve this problem and to ensure safety as well as stability of the overall system, the control strategy should switch to the FOM. In this case and in absence of storage system, the MPPT command should be deactivated in order to limit the injection of the PV power, and thus the dc-link voltage decreased and reached its reference. The dc-link voltage becomes controlled indirectly by the active power delivered by the inverter at PCC. For this mode, the reference active and reactive powers used to control the inverter change to their new values according to Eq. 5. This solution ensures balance between production and consumption powers and thus a safety of the overall system has been realized. Figure 14(b) illustrates the power-grid voltage sags response curve. It explains that in case of voltage sags region; there should be a reduction of active power by 500W for each 15% of step voltage dip. However, when the SGVD is less than 20%, the active power injected by the inverter is approximately equal to the maximal PV power (P_{pvmax}) and the reactive power is zero. The less difference between the dc and ac powers is stored in the dc-link capacitor making a safe increase of the dc-link voltage. For this reason, it is necessary to oversize the bus capacitor in order to damp the low level of the voltage dip. Moreover, it is necessary to deactivate the MPPT control when the level (ΔV) and duration (Δt) of the symmetrical grid voltage dips exceed the limit fixed by the grid codes [1,2].

2) Case 2: disabled of the MPPT command

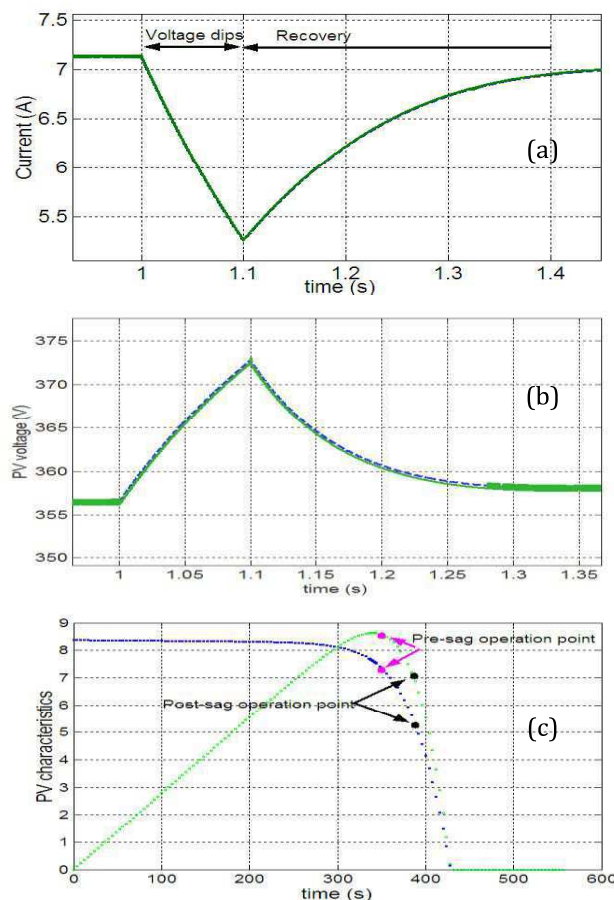


Fig. 15. Simulation results under 50%-100ms SGVD: (a): PV current (measure and reference), (b): PV voltage (measure and reference), (c): ($P_{pv}/280$)-V (green) and I-V (blue) characteristics

Table 2: Parameters of the system regulators

Parameter	Value	Parameter	Value
Gain of PV voltage regulator R_v	10	Gain of the inverter output current regulator k_{i1}	50
Gain of PV current regulator R_c	34	Const. time of the inverter output current regulator τ_{i1}	0.002
Gain of dc link voltage regulator k_{dc}	0.001	Gain of the voltage regulator k_{v_c}	0.1
Const. time of dc link voltage regulator τ_{dc}	0.1	Const. time of the voltage regulator τ_{v_c}	0.002
Gain of PLL regulator K_{θ}	10	Gain of the filter output current regulator k_{i2}	10
Constant time of PLL regulator τ_{θ}	0.1	Const. time of the filter output current regulator τ_{i2}	0.003

Table 3: dc-link voltage and inverter output powers for various duration and level of SGVD

Grid voltage dips (%)	0	10	20	30	40	50	60	70	80	90	100
Inverter output active power (kW)	2.6	2.6	2.55	2.5	2.1	1.64	1.33	1	0.66	0.33	0
Inverter output reactive power (kVAR)	0	0.03	0.07	0.25	0.35	0.355	0.23	0.17	0.09	0.025	0
dc-link voltage (duration of fault: 0.1s)	515	520	528	565	586	653	702	750	794	836	876
dc-link voltage (duration of fault: 0.16s)	515	540	556	580	629	724	794	860	921	980	1042
dc-link voltage (duration of fault: 0.2s)	515	553	575	598	656	768	850	925	997	1065	1140

In NOM, the maximum PV power is 2552W; the PV voltage and the PV current at the maximum power are 357V and 7.15A, respectively (Figure 15). Once a SGVD appears at 1s, the control system switches instantaneously to the FOM. In this case, the PV power, the voltage and the current reach progressively new values. The current, provided by the PVG, decreases in order to maintain the dc-link voltage lower than the limit value (560V).

According to Figure 16 (a), the control system ensures a safe dc-link voltage lower than the limit value fixed at 560V. Its maximum value is equal to 520V.

Figure 16(b) shows the variation of the dc current provided by the boost during the FOM between 1 and 1.1s. If the control system switches to the FOM, the current decreases progressively until 3.4A in order to ensure a balance between the PV power and the ac power provided at the PCC. After 100ms, the fault is cleared and the grid connected PV system goes back to its NOM. In the same time, the MPPT unit continues to track the optimal PV power.

As it shown by Figures 15 and 16, the system takes some time to join its normal state because of the MPPT process.

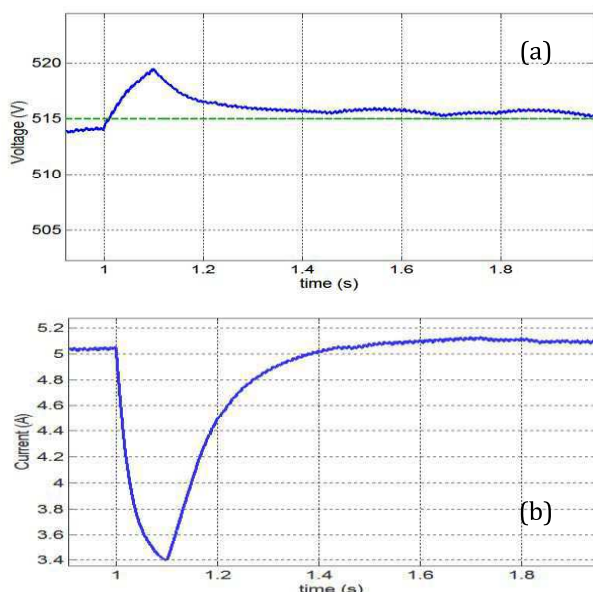


Fig. 16. Simulation results under 50%-100ms SGVD: (a): dc-link voltage (measure and reference), (b): dc current injected by the dc-dc converter

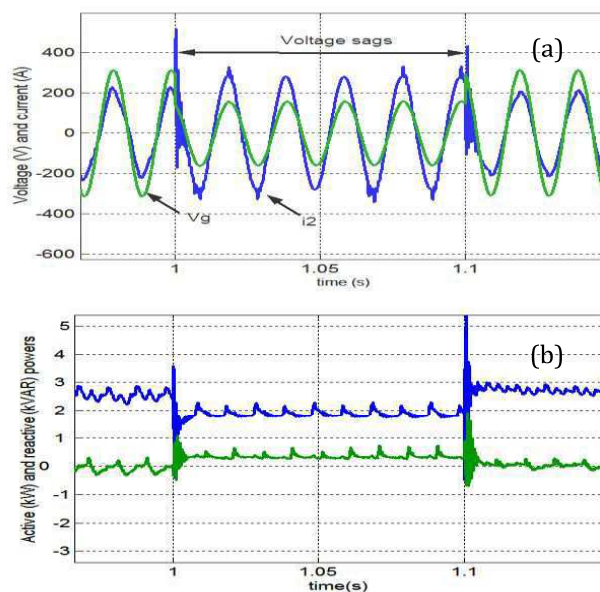


Fig. 17. Simulation results under 50%-100ms SGVD: (a): grid voltage (green) and (*40) current (blue), (b): inverter output active (blue) and reactive (green) powers.

Figure 17 illustrates the response of the grid connected PV system to 50%-100ms voltage dip which can occur on the grid voltage. The inverter starts to inject reactive power to support the grid voltage and limits the active power output to prevent the inverter from over current protection. The operating point is severely affected by the SGVD (reduction of about 40%). It is shown that during the fault, the PV system is controlled to limit the active power ($\approx 1800W$) and to inject some reactive power ($\approx 280VAR$) into the grid. As illustrated by Figure 17(a), the voltage waveform collapses and the inverter current magnitude becomes high during faults. This is to keep a balance power between the PVG and the grid. During the step transient in the grid voltage, there is a phase leading/lagging between grid side line current and voltage.

Figures 15, 16 and 17 illustrate the performances and dynamics of the command approach in FOM between 1 and 1.1s. It permits to the inverter to support the grid within a short time when it presents a SGVD. They show that the command approach provides a high performance, safety and stability of the overall system. Moreover, it allows a stable connection to 50%-100ms symmetrical grid voltage dip.

IV. CONCLUSION

In this paper a control strategy approach has been developed around a double-stage grid connected PV system functioning under normal conditions and symmetrical grid voltage dips. This command is dedicated to improve the reliability during the grid fault operation and to avoid catastrophic failure. Its validity to ride-through symmetrical voltage dips has been performed by simulations.

In NOM, the proposed control raises the PV power to the maximum power point and maintains the dc-link voltage. Meanwhile, it injects a PV power into the grid at unity power factor and a current with low harmonic distortion. In FOM, the control strategy injects the adequate amount of active and reactive power into the grid and disabled the MPPT control in order to reduce the inverter output power to the target value delivered by the PVG.

Hence, it has been demonstrated that the proposed control scheme in various operation modes presents high performances in transient and permanent phases. It improves the safety of the overall system and increases the connection time when grid faults occur. Moreover, it provides ride through capability and contributes to the system stability.

ACKNOWLEDGMENT

This work is part of the project "Projet Jeunes chercheurs" funded by the Tunisian Ministry of High Education and Scientific Research. The support of the ministry is kindly acknowledged.

REFERENCES

- [1] Baabjerg, F., and Ionel, D. M., "Renewable energy devices and systems – state-of-the-art technology, research and development, challenges and future trends," *Electrical Power Components and Syst.* Vol. 43, No.12, pp. 1319-1328, 2015.
- [2] E. ON GmbH, Grid Code-High and extra high voltage, <http://www.eon-netz.com/>.
- [3] Braun, M., Arnold, G., and Laukamp, H., "Plugging into the Zeitgeist," *IEEE Power and Energy Mag.*, Vol. 7, No. 3, pp. 63–76, 2009.
- [4] Comitato Elettrotecnico Italiano, "Reference technical rules for connecting users to the active and passive LV distribution companies of electricity," CEI 0-21, (2011).
- [5] Kobayashi, H., "Fault ride through requirements and measures of distributed PV systems in Japan," *Proceeding of the IEEE PES General Meeting*, pp.1–6, 2002.
- [6] F. Qiang, F., Nasiri, A., Ashishkumar, S., Abedalsalam, B. A., Luke, W., and Vijay, B., "Microgrids: Architectures, Controls, Protection, and Demonstration," *Electrical Power Components and Sys.*, Vol. 43, No. 12, pp. 1453-1465, 2015.
- [7] Blaabjerg, F., Teodorescu, R., Liserre, M., and Timbus, A. V., "Overview of control and grid synchronization for distributed power generation systems," *IEEE Transactions on Industrial Elec.*, Vol. 53, No. 5, pp.1398–1409, 2006.
- [8] Kjaer, S. B., Pedersen, J. K., and Blaabjerg, F., "A review of single phase grid-connected inverters for photovoltaic modules," *IEEE Transactions on Industry App.*, Vol. 41, No.5, pp.1292– 1306, 2005.
- [9] Al-Shetwi, A., Sujod, M. Z., and Ramli, N. L., "A review of the fault ride through requirements in different grid codes concerning penetration of PV system to the electric power network," *ARNP journal of engineering and applied sciences*, Vol. 21, No. 10, 2015.
- [10] Milanovic, J. V., and Djokic, S. Z., "Equipment sensitivity to disturbances in voltage supply," International electrical equipment conference JIEEC, Bilbao, (2003).
- [11] Bollen, M. H. J., and Zhang, L. D., "Different methods for classification of three-phase unbalanced voltage dips due to faults," *Renewable Energy*, pp. 59–69, 2009.
- [12] Yang, Y., Wang, H., and Blaabjerg, F., "Reactive power injection strategies for single phase photovoltaic systems considering grid requirements," applied power electronics conference and exposition, 29 annual IEEE, pp. 371-378, 2014.
- [13] Yang, Y., Blaabjerg, F., and Zou, Z., "Benchmarking of grid fault modes in single-phase grid-connected photovoltaic systems," *IEEE Trans. Ind. Appl.*, Vol. 49, No.5, pp. 2167–2176, 2013.
- [14] Cadaval, E. R., Spagnuolo, G., Franquelo, L. G., Paja, C. A. R., Suntio, T., and Xiao, W. M., "Grid-connected photovoltaic generation plants: components and operation," *IEEE Ind. Electron. Mag.*, Vol. 7, No. 3, pp. 6–20, 2013.
- [15] Yang, Y., Enjeti, P., Blaabjerg, F., and Wang, H., "Suggested grid code modifications to ensure wide-scale adoption of photovoltaic energy in distributed power generation systems," *Proc. of IEEE-IAS annual meeting*, pp. 1-8, 2013.
- [16] Carnieletto, R., Brandao, D. I., Farret, F.A., Simoes, M.G., "Smart grid initiative: A multifunctional single-phase voltage source inverter," *IEEE Ind. Appl. Mag.*, Vol. 17, No.5, pp. 27–35, 2011.
- [17] Rodriguez, P., Luna, A., Munoz-Aguilar, R., Corcoles, F., Teodorescu, R., and Blaabjerg, F., "Control of power converters in distributed generation applications under grid fault conditions," *Proceedings of the European Conference on Cognitive Ergonomics*, pp. 2649–2656, 2011.
- [18] LI, Y., and NEJABATKHAH, F., "Overview of control, integration and energy management of micro-grids," *Journal of Modern power, systems and clean energy 2*, pp. 201-212, 2014.
- [19] Teodorescu, R., Liserre, M., and Rodriguez, P., "Grid converters for photovoltaic and wind power systems", Wiley-IEEE press, 2011.
- [20] Bo, Y., Oruganti, R., Panda, S. K., and Bhat, A. K. S., "An output-power control strategy for a three-phase PWM rectifier under unbalanced supply conditions," *IEEE Trans. Ind. Electron.*, Vol. 55, pp. 2140-2151, 2008.
- [21] Junyent-Ferre, A., Gomis-Bellmunt, O., Green, T. C., and Soto-Sanchez, D. E., "Current control reference calculation issues for the operation of renewable source grid interface VSCs under unbalanced voltage sags," *IEEE Trans. Power Electron.*, Vol. 26, pp. 3744-3753, 2011.
- [22] Lee, C. T., Hsu, C. W., and Cheng P. T., "A low-voltage ride through technique for grid-connected converters of distributed energy resources," *IEEE Trans. Ind. Appl.*, 47(2011), pp. 1821-1832.
- [23] Magueed, F. A., Sannino, A., and Svensson, J., "Transient performance of voltage source converter under unbalanced voltage dips," *Proceeding of IEEE Annual Power Electronics Specialists Conference*, pp. 1163-1168, 2004.
- [24] Azevedo, M. G. S., Rodriguez, P., Cavalcanti, M. C., Vázquez, G., and Neves, F. A. S., "New control strategy to allow the photovoltaic systems operation under grid faults," Power Electronics Conference, Brazilian, pp. 196-201, 2009.
- [25] Mirhosseini, M., Félix, P., Baburaj, J. K., and Vassilios, A., "Positive- and negative-sequence control of grid-connected photovoltaic systems under unbalanced voltage conditions," AUPEC, Tasmania, Australia, pp. 1-6, 2013.
- [26] Banu, I. V., and Istrate, M., "Study of three-phase photovoltaic system under grid faults," International conference and exposition on electrical and power engineering, Romania, 2014.
- [27] Kai, D., Cheng, K. W. E., and Xue, X. D., "A novel detection method for voltage sags," *Proceedings of the International Conference on Power Electronics Systems and Applications*, pp. 250–255, 2006.
- [28] Lee, D. M., Habetler, T. G., Harley, R. G., Keister, T. L., and Rostron, J. R., "A voltage sag supporter utilizing a PWM-switched auto transformer," *IEEE Transactions on Power Elect.*, Vol. 2, No. 22, pp.626–635, 2007.
- [29] Bae, B., Lee, J., Jeong, J., and Han, B., "Line-interactive single phase dynamic voltage restorer with novel sag detection algorithm," *IEEE Transactions on Power Delivery*, Vol. 4, No. 25, pp. 2702–2709, 2010.
- [30] Fitzer, C., Barnes, M., and Green, P., "Voltage sag detection technique for a dynamic voltage restorer," *IEEE Transactions on Industry Applications*, Vol. 1, No. 40, pp.203–212, 2004.

- [31] Hernandez, O. C. M., and Enjeti, P. N., "A fast detection algorithm suitable for mitigation of numerous power quality disturbances," *IEEE Transactions on Industry Applications*, Vol. 6, No. 41, pp. 1684–1690, 2005.
- [32] Chou, S.F., Lee, C.T., Cheng, P.T., and Blaabjerg, F., "A reactive current injection technique for renewable energy converters in low voltage ride-through operations", in Proceedings of the IEEE-PES General Meeting, pp. 1–7, 2011.
- [33] Lee, C. T., Hsu, C. W., and Cheng, P. T., "A low-voltage ride through technique for grid-connected converters of distributed energy resources," *IEEE Transactions on Industry Applications*, Vol. 4, No. 47, pp.1821–1832, 2011.
- [34] Bae, Y., Vu, T. K., and Kim, R. Y., "Implemental control strategy for grid stabilization of grid-connected PV system based on German grid code in symmetrical low-to-medium voltage network," *IEEE Trans. Energy Conversion*, Vol. 3, No. 28, pp. 619–631, 2013.
- [35] Arnold, G., "Challenges of integrating multi-GW solar power into the German distribution grids," (2011) Available: <http://www.iwes.fraunhofer.de/>.
- [36] Hamrouni, N., Jraidi, M., and Cherif, A., "New control strategy for 2-stage grid-connected photovoltaic power system," *Renewable Energy*, No. 33, pp. 2212–2221, 2008.
- [37] Mogos, E. F., "Production dans les réseaux de distribution, étude pluridisciplinaire de la modélisation pour le contrôle des sources Thèse de doctorat," ENSAM, Lille (2004).
- [38] Hamrouni, N., Modélisation et commande des systèmes photovoltaïques connectés au réseau électrique basse tension," Thèse de doctorat, ENIT, Tunisie, 2009.
- [39] Mahmoud, A. M. A., Mashaly, H. M., Kandil, S. A., El Khaseb, H., and Nashed, M. N. F., "Fuzzy logic implementation for photovoltaic maximum power tracking," *Proceedings of the 9th IEEE international workshop on robot and human interactive communication*, pp. 155–60, 2000.
- [40] Hamrouni, N., Jraidi, M., Chérif, A., "New control strategy for 2-stage grid-connected photovoltaic system," *Renewable Energy*, Vol. 33, pp. 2212–2222, 2008.
- [41] Yang, Y., and Baabjerg, F., "Low voltage ride through capability of a single phase photovoltaic system connected to the low voltage grid," *International Journal of Photo energy*, 2013.
- [42] Akagi, H., Nabae, A., "Control strategy of active power filters using multiple voltage source PWM converters," *IEEE Transactions on industrial electronics*, Vol. 22, No. 3, pp. 460–465, 1986.
- [43] Pankow, Y., "Etude de l'intégration de la production décentralisée dans un réseau basse tension, application au générateur photovoltaïque," Thèse de Doctorat, ENSAM, Lille 2005,
- [44] Liadjidemetriou, L., Kyriakides, E., and Blaabjerg, F., "An adaptive tuning mechanism for phase locked loop algorithms for faster time performance of interconnected renewable energy sources," *IEEE Transactions on Industry Applications*, Vol. 51, No. 2, pp. 250–261, 2015.
- [45] Alali, M. A. E., "Contribution à l'étude des compensateurs actifs des réseaux électriques basse tension," Thèse de doctorat, Université Louis Pasteur, Strasbourg, France, 2002.
- [46] Bojrup, M., "Advanced control of active filters in a battery charger application," PHD Thesis, Lund Institute of Technology, 1999.



Nejjib Hamrouni received his engineering degree from the National Engineering School of Sfax, in 2000 and the PHD from the National Engineering School of Tunis, in 2009, both in electrical engineering. He is an Assistant professor at National Engineering School of Gabés from 2010 to 2015.

Since September 2015 he is an assistant professor at ISSAT of Mateur. He has participated in several research and cooperation projects, and is the author of more than 20 international communications and publications.

Analysis of the pv efficiency according to the characteristics of silicon solar cells

Souad Merabet*, Bilal Djelil, Boubekeur Birouk
Laboratoire des énergies renouvelables
University of MSB Jijel
City of Ouled Aissa, BP98, 18000Jijel, Algeria
msouad03@yahoo.fr

Abstract— The analysis of the obtained results from the variation of the technological parameters of two solar cells with silicon, on their photovoltaic production, worth knowing the one designed by two structures polycrystalline and monocrystalline (region N and P) called cell1 and the other one designed by two monocrystalline structures called cell2 showed a narrow relation between the initial conditions of manufacturing of cells, and the photovoltaic parameters resulting during their functioning.

Keywords- Efficiency, polycrystalline Silicon, monocrystalline Silicon.

I. INTRODUCTION

Solar PV cells are electronic devices that use P-N junctions to directly convert sunlight into electrical power [1]. A complex relationship between voltage and current is exhibited by the P-N junction in the solar cell. The voltage and current both, being a function of the light falling on the cell, and experimental conditions of manufacturing of cells. The use of a digital simulation highlights the optimization of the dominating parameters to obtain a maximal efficiency for two photovoltaic cells having for structure : poly-Si(N)/c-Si(P) called Cell1 et c-Si(N)/c-Si(P) called Cell2. For this we used an applied SILVACO program for equations and relative relations for the structures used in the conception of the photovoltaic cells.

The parameters that will be improved in this work are the technological parameters, the size's thickness and the doping. This optimization includes the influence of these parameters on the two cells in order to obtain a structure with a high efficiency.

At first, we use the SILVACO software to determine the photovoltaic current considered practically equal to current of short circuit. And, secondly we use the MATLAB software to determine the parameter's photovoltaic such as photocurrent, open circuit-voltage and efficiency.

II. METHOD

The simulation by SILVACO is based on the digital resolution of three fundamental equations of transport of carriers in semiconductors which are respectively the equation of Poisson and the equations of continuity and transport for electrons and holes [2]. After the definition of the meshing of the studied structure the materials and models, the simulator estimates numerically the resolution of these equations in every knot of the meshing [3, 4], and determine the current of

*Corresponding author.

short circuit under the standard conditions of illumination (AM1.5G) in 300°K.

The simulation by MATLAB, consists in drafting a program into which we introduce the equations of a real model to the solar cell, by exploiting the results obtained from the software SILVACO. All the work is based on the study of the influence of the thickness size (that is in the zone N or in the zone P) on the photovoltaic parameters for every cell. Three parameters are important in analyzing the performance of solar cells: the short-circuit photocurrent, the open-circuit photovoltage, and the efficiency [5, 6], and the influence of the variation of the doping in every region on these parameters.

III. RESULTS AND DISCUSSION

Fig. 1, presents the technological structures of the studied cells obtained from the software SILVACO [7].

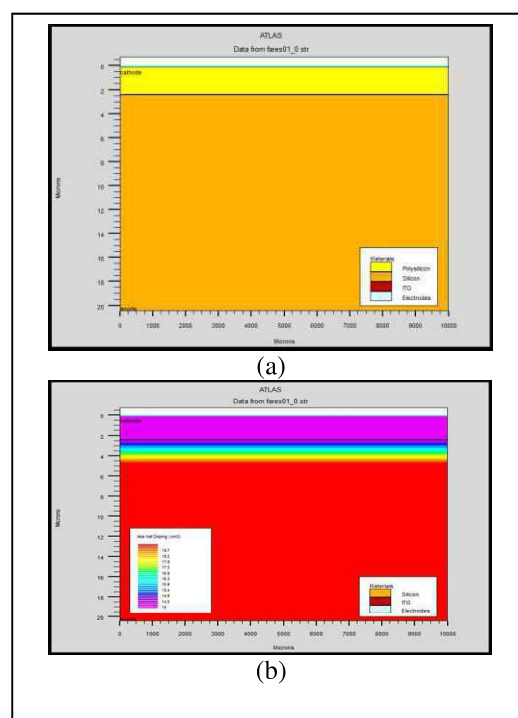


Fig. 1. Technological structures with the software SILVACO, (a) Cell1: Si-poly(N)/c-Si(P), (b) Cell2 : c-Si (N)/c-Si(P).

The characteristics of these cells are included in the Table 1:

Table 1: Characteristics of Cells

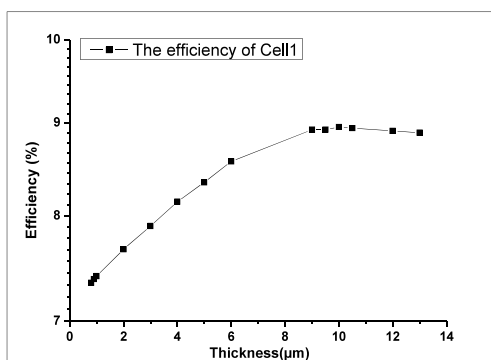
	Zone	Thickness (μm)	Dopage (cm^3)
Cell1	N	0.8	$10\text{E}14$
	P	20	$10\text{E}16$
Cell2	N	0.1	$10\text{E}14$
	P	20	$10\text{E}16$

A. Impact of thickness

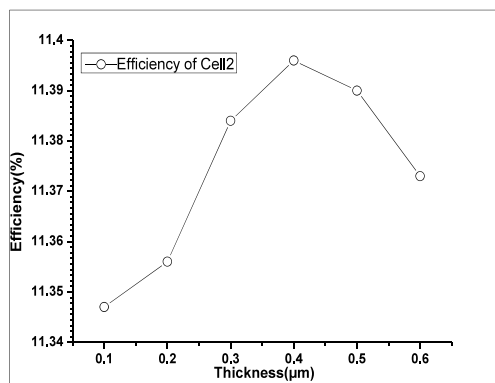
1) Influence of the thickness in the zone N

We arrange the thickness of $0.8\mu\text{m}$ until $13\mu\text{m}$ of the layer N, by maintaining the other constant parameters.

In Fig. 2, we show the evolution of the photovoltaic efficiency according to the variation in thickness of layer N of the cell1. For the varying values of thickness from 0.8 to $10\mu\text{m}$, there is an increase of short circuit current ~ photovoltaic current and open circuit voltage, the current crosses from 14.317 mA to 17.287 mA , and the voltage appears constant. For the values of thickness varying from 10 to $13\mu\text{m}$, we notice a decrease into two parameters; the efficiency obtained for a thickness of $0.8\mu\text{m}$ is 7.35% as for the thickness of $10\mu\text{m}$, it gives a 8.96% efficiency. Reaching $13\mu\text{m}$, it falls in 8.89% . The maximal efficiency is 8.9557% , corresponds to the value of thickness $10\mu\text{m}$.



(a)



(b)

Fig. 2. Influence of the thickness in the zone N. For (a) Cell1 and (b) Cell2 on the efficiency.

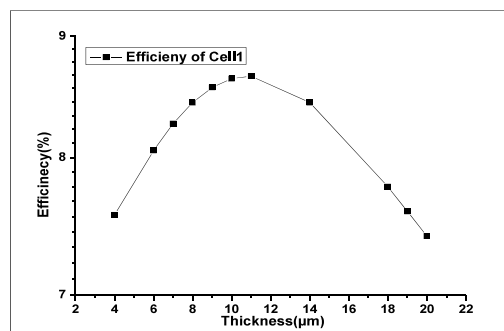
For the cell2, we vary the thickness of $0.1\mu\text{m}$ until $0.6\mu\text{m}$. For the values of thickness varying from 0.1 to $0.4\mu\text{m}$, we notice an increase of photocurrent; it passes from 20.497 mA to 20.58 mA . And from 0.4 to $0.6\mu\text{m}$, the photocurrent decrease; it spends 20.58 mA to 20.541 mA .

We notice that the obtained efficiency for a thickness of $0.1\mu\text{m}$ is 11.35% as for the thickness of $0.4\mu\text{m}$, it gives 11.4% . Reaching, we notice that the efficiency obtained for a thickness of $0.1\mu\text{m}$ is 11.35% as for the thickness of $0.4\mu\text{m}$, it gives 11.4% efficiency. Reaching $0.6\mu\text{m}$, it falls to 11.37% . The maximal efficiency is 11.396% , corresponds to the value of thickness $0.4\mu\text{m}$. At $0.6\mu\text{m}$, it falls in 11.37% .

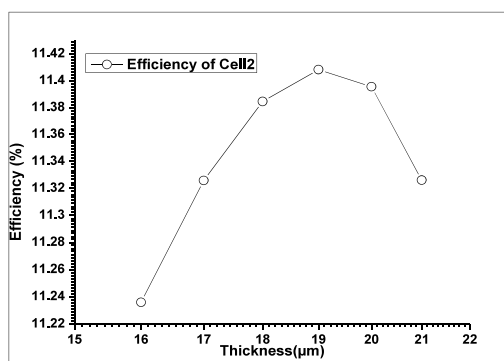
2) Influence of the thickness in the zone P

For the cell 1, we vary the thickness of $4\mu\text{m}$ until $20\mu\text{m}$ of the P layer, by maintaining the other parameters constant (see Fig.3). A proportional increase of the photovoltaic parameters with the thickness of the P layer is noticed, and it until the value $11\mu\text{m}$, after, all the values decrease. So, the obtained best efficiency is 8.6585% for the value of $11\mu\text{m}$.

For the cell2, we arrange the thickness of $4\mu\text{m}$ until $20\mu\text{m}$, the maximal values of the photovoltaic parameters are reached when the value of the thickness in the P layer achieves $19\mu\text{m}$ (11.4083%), beyond this value, it decrease.



(a)



(b)

Fig. 3. Influence of the thickness in the zone P. For (a) Cell1 and (b) Cell2 on the efficiency.

B. Impact of the dopage

1) Influence of the dopage N

For the cell1, we arrange the doping $N_d=1 \times 10^{10} \text{ cm}^{-3}$ until $1 \times 10^{14} \text{ cm}^{-3}$ ($N_a=1 \times 10^{16} / \text{cm}^3$). According to obtained curves on Fig. 4, we notice that the photovoltaic parameters increase with the increase of the dopants concentration N_d (N_d $N_a=1 \times 10^{16} / \text{cm}^3$). The increase of the doping allows a remarkable improvement of the photovoltaic conversion. This can be explained by the fact that the increase of doping increases the life expectancy of the minority carriers, as well as their mobility.

The best obtained efficiency is 8.9557 % for the values of doping $N_a=1 \times 10^{16} / \text{cm}^3$ and $N_d=1 \times 10^{14} / \text{cm}^3$. For the cell2, we vary the doping N_d of $1 \times 10^{10} / \text{cm}^3$ until $1 \times 10^{14} \text{ cm}^{-3}$ ($N_a=1 \times 10^{16} / \text{cm}^3$). We notice that the increase of the concentration of the doping N_d , led an increase in the values of the various photovoltaic parameters; the best efficiency obtained with this structure is 11.3903 % for the values of doping $N_a=1 \times 10^{16} / \text{cm}^3$ and $N_d=1 \times 10^{14} / \text{cm}^3$.

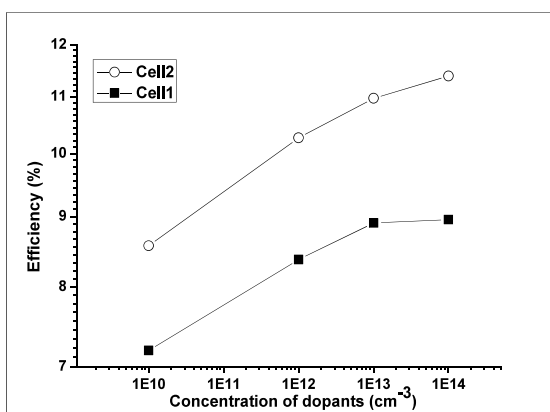


Fig. 4. Influence of the amount of dopants in the zone N on the efficiency

2) Influence of the dopage P

We vary the doping $N_a=1 \times 10^{15} \text{ cm}^{-3}$ until $1 \times 10^{20} \text{ cm}^{-3}$ ($N_d=1 \times 10^{14} / \text{cm}^3$). The results illustrated on Fig.5, show a progressive increase of the photovoltaic parameters according to the doping of the zone P in cell1 and cell2. The optimal values are obtained at concentration of $1 \times 10^{17} \text{ cm}^{-3}$ (8.7962%) in the cell1. After this concentration, all parameter's photovoltaic decrease at the same time following by decreasing, and decrease after this concentration.

For the cell2, we vary the doping $N_a=1 \times 10^{16} \text{ cm}^{-3}$ until $1 \times 10^{19} \text{ cm}^{-3}$, and take the doping $N_d=1 \times 10^{14} / \text{cm}^3$. We notice that all the photovoltaic parameters undergo a reduction during the increase of the dopants concentration in the P layer of $1 \times 10^{16} / \text{cm}^3$ to $1 \times 10^{19} / \text{cm}^3$ by maintaining constant the layer N at $1 \times 10^{14} / \text{cm}^3$.

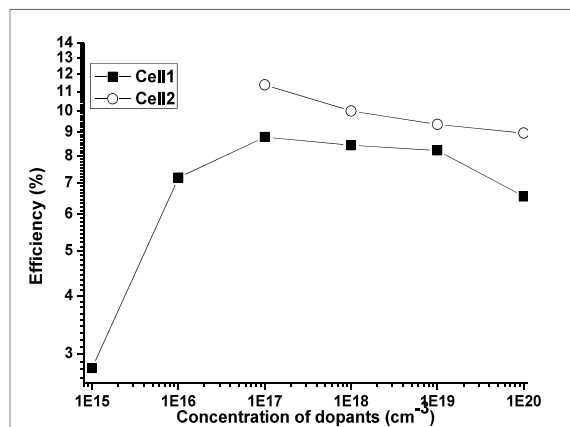


Fig. 5. Influence of the amount of dopants in the zone P on the efficiency

The comparison between the efficiencies obtained from both studied cells such as represented on Figures, show a clear difference between curves, the photovoltaic quality of cell2 is better than that obtained for cell1.

The analysis of the results obtained from the variation of the thickness for every zone of the junction, showed that when the lengths of distribution of the photo-generated carriers are upper to the traveled distances, the photovoltaic conversion increases until a maximal value in a certain value of thickness, then for high values of thickness, the length of distribution of the photo-carriers becomes small compared with the thickness [6-8]; The photo-generated carriers have to travel distances bigger than their lengths of distribution, what leads drives to a strong rate of recombination because of their weak life expectancy decreasing the photovoltaic quality [9,10].

While the increase of the doping improves all the photovoltaic parameters occurring in the efficiency on conversion of every studied solar cell; Indeed the variation as well of the open circuit voltage as the density of photo-current, evolve in the same sense as the evolution of the values of the doping of the layer N. However, the increase of the doping of the layer P shows an inverse phenomenon for cell2. This is may be due to the gradient of concentration raised between both N layers and P layer ($N_d=1 \times 10^{14} \text{ cm}^{-3}$ and $N_a=1 \times 10^{16} \text{ cm}^{-3}$ to $1 \times 10^{18} \text{ cm}^{-3}$) [8]. For cell1, the obtained results are better for a doping of $1 \times 10^{17} \text{ cm}^{-3}$, and beyond this value they fall. That confirms our results which are in good agreement with other work [11].

IV. CONCLUSION

The obtained results in this work, allowed to determine the influence of two important parameters: the size and the rate of doping characterizing two solar cells; the analysis showed that an important improvement of the photovoltaic efficiency is possible from an adequate choice of the material and these two parameters.

REFERENCES

- [1] P. Arjyadhara, A. S.M2, J. Chitralekha, "Analysis of Solar PV cell Performance with Changing Irradiance and Temperature", *J. of Engineering And Computer Science*, Vol 2 (1) pp. 214-220, (2013).
- [2] T. Markvart and L. Castaner, *Practical handbook of photovoltaics: fundamentals and applications*, Elsevier Ltd, (2003).
- [3] R.N, Hall, «Electron Hole Recombination in Germanium», *Physical Review*, vol. 87, p.387, (1952).
- [4] J. Dziewior, W. Schmid, « Auger coefficient for highly doped and highly excited silicon », *Appl. Phys. Lett*, Vol 31, pp. 346-348, (1977)
- [5] A. K. Ghosh, C. Fishman, and T. Feng « SnO₂/Si solar cells—heterostructure or Schottkybarrier or MIS type device », *J. Appl. Phys.* 49, 3490 (1978); doi: 10.1063/1.325260
- [6] A.Goetzberger, V.U.Hoffmann, « photovoltaic solar energy generation » Springer Series in optical sciences, (2005).
- [7] <https://www.silvaco.com/>
- [8] Goodrich, A., P, Hacke, Q, Wang, B, Sopori, R, Margolis, T, James, M, Woodhouse, "A wafer-based monocrystalline silicon photovoltaics road map: Utilizing known technology improvement opportunities for further reductions in manufacturing costs". *Solar Energy Materials & Solar Cells* 114: pp. 110–135, (2013).
- [9] Priety and V, Garg., "To perform matlab simulation of battery charging using solar power with maximum power point tracking (MPPT)", *International journal of electronic engineering*, ISSN 0974-2174, 7(5): 511-516, (2014).
- [10] D. Hocine, M.S. Belkaïd and K. Lagha, "Influence of interfacial oxide layer thickness on conversion efficiency of SnO₂/SiO₂/Si(N) Solar Cells", *Revue des Energies Renouvelables* Vol. 11 N°3, pp.379 – 384(2008).
- [11] Md Faysal Nayan, S. M.Safayet Ullah, S. N. Saif, "Comparative Analysis of PV Module Efficiency for Different Types of Silicon Materials Considering the Effects of Environmental Parameters", *Conference Paper* . September 2016, DOI: 10.1109/CEEICT.2016.7873089

Editors biographies:



Dr. Georges Descombes (France)

Professeur des universités au Cnam

Ingénieur motoriste diplômé du Cnam, spécialiste en conversion d'énergie dans les machines thermiques, professeur des universités au Cnam en énergétique.

descombesgeorges@gmail.com



Dr. Ahmed Rhif (Tunisia)

Ingénieur en génie Electrique diplômé de l'Ecole Nationale d'Ingénieurs de Tunis (ENIT)

Directeur du Centre International for Innovation & Development (ICID).

ahmed.rhif@gmail.com

The International Publisher & C.O (IPCO) is an organization that promotes science & engineering research worldwide without any discrimination. It acts as a bridge between young and experienced professionals through scientific journals. IPCO depends on researchers, academicians and corporate support for bridging relationships with existing scientific & engineering organizations and customizing relationships with standard bodies. The main purpose of this organization is to promote new research and scientific applications in the field of Control, Energy, Engineering, Computer Science and allied fields. IPCO provides high quality and flexible information solutions to researchers. We currently publish international journals and we provide online solutions to help researchers to achieve better results. Active Peer Review: All our journals, which are run by a group of experienced professional editors, are subject to an efficient, fair, and constructive peer review process. Maximum Global Distribution: Our website guarantees visibility, including social bookmarking services, so that your article reaches those people who need to read and cite it. High Quality, Reliable Rapid Production: Our production teams work together to continuously improve and enhance our services, building issues online and our new, even quicker production workflows. We deliver these innovations without compromising our high quality standards.

International Publisher & C.O (IPCO), in its new aspect, represents a new contribution between North African & International researchers and institutions and cover a wide range of academic disciplines. IPCO serves the world's research and scholarly communities, and aims to be one of the largest publishers for professional and scholarly societies. IPCO's journals maintain the highest standards of peer review, with some internationally-recognized editors serving on the editorial boards of IPCO's journals.

Maghreb Arab Street
Khzema East Sousse - Tunisia
Email : ipco.direction@gmail.com
Phone: (+216) 31 121 155
www.ipco-co.com
ISSN: 1737-9334

Editors biographies:



Dr. Georges Descombes (France)

Professeur des universités au Cnam

Ingénieur motoriste diplômé du Cnam, spécialiste en conversion d'énergie dans les machines thermiques, professeur des universités au Cnam en énergétique.

descombesgeorges@gmail.com



Dr. Ahmed Rhif (Tunisia)

Ingénieur en génie Electrique diplômé de l'Ecole Nationale d'Ingénieurs de Tunis (ENIT)

Directeur du Centre International for Innovation & Development (ICID).

ahmed.rhif@gmail.com